INTERACTION OF WEAK SHOCK WAVES AND DISCRETE GAS INHOMOGENEITIES

Thesis by

Jean-Francois Luc Haas

In Partial Fulfillment

of the Requirements for the Degree of

Doctor of Philosophy

California Institute of Technology

Pasadena, California

1984

(Submitted 15 June 1983)

To my parents,

Christiane and Ferdinand Haas

ACKNOWLEDGEMENTS

I would like to sincerely thank all those who have helped me in this research effort, which was undertaken under the guidance of Professor Bradford Sturtevant. His insight, interest and patience during the length of this project are gratefully acknowledged.

The project benefitted from the contributions of many individuals at Caltech: my fellow graduate students for their stimulating discussions, the technical staff of the Aeronautics Department for the realization of some of the apparatus and their constant friendly help, Miss Deanna Deeds and Mrs. Virginia Chan for their participation in the project in the summer of 1982, Mrs. Marcia Hudson for the typewriting of the manuscript and Mrs. Betty Wood for the drawings, and again, Professor Sturtevant for his editorial assistance.

Finally, I am grateful to my parents and my friends, at Caltech and elsewhere, who have contributed to this effort by their constant encouragements and support.

This work was supported by the National Science Foundation under Grant Number MEA 81-20092.

ABSTRACT

An experimental investigation of the interaction of shock waves with discrete gas inhomogeneities is conducted in the GALCIT 15 cm diameter shock tube. The gas volumes are cylindrical refraction cells of 5 cm diameter with a 0.5 μm thick membrane separating the test gas (helium or Freon 22) from the ambient air and large spherical soap bubbles containing the same gases. The incident wave Mach numbers are nominally 1.09 and 1.22. The wave pattern and the deformation of the gas volumes are documented by shadowgraphs. The transmitted and diffracted wave pressure profiles are recorded by pressure transducers at various distances behind the cylinders. The basic phenomena of acoustic wave refraction, reflection and diffraction by cylindrical acoustic lenses, with indices of refraction appropriate to the gases used in the experiments, are illustrated with computer-generated ray and wave-front diagrams.

In the case of a Freon 22-filled cylinder, the wave diffracted externally around the body precedes the wave transmitted from the interior which goes through a focus just behind the cylinder, while in the case of the helium-filled cylinder the expanding transmitted wave runs *ahead* of the diffracted wave. Both sets of waves merge a few cylinder diameters downstream. The wave patterns inside the cylinder, showing initially the refracted waves and later the same waves reflected internally, present some interesting phenomena.

The mechanisms by which the gas volumes are transformed into vortical structures by the shock motion are observed. The unique effect of shock acceleration and Rayleigh-Taylor instability on the spherical volume of helium leads to the formation of a strong vortex ring which rapidly separates from the main volume of helium. Measurements of the wave and gas-interface velocities are compared to values calculated for one-dimensional interactions and for a simple model of shock-induced Taylor instability. The behavior of thin liquid membranes accelerated by shocks under varying conditions is documented by high speed photography.

In a related experiment, shock waves of Mach number between 1.005 and 1.36 interact with a dense random array of 2 mm diameter helium filled soap bubbles. Experimental results (based on shadowgraphs and pressure measurements) show that very weak shock waves ($M_s \leq 1.01$) are strongly scattered by the array, which is left undisturbed by the shock, and that stronger shock waves, only locally disturbed by each bubble, maintain undisturbed pressure profiles because of nonlinear effects, while the array undergoes shock-induced mixing. A simple criterion for multiple scattering shows that the combined effect of many bubbles is necessary in order to produce important modifications on the shock wave pressure profile.

TABLE OF CONTENTS

Chapter	Title	Page
	Copyright	ii
	Dedication	iii
	Acknowledgements	iv
	Abstract	v
	Table of contents	vii
	List of figures	xi
	List of tables	xvii
1.0	INTRODUCTION	1
1.1	Multiple scattering of weak shock waves	1
1.2	Scattering by a single discrete inhomogeneity	3
2.0	DESIGN OF THE MULTIPLE SCATTERING EXPERIMENT	9
2.1	Generation of the discrete helium scatterers	9
2.2	Design of the bubble cloud chamber	13
2.3	Characterisation of the helium bubble array	16
3.0	EFFECT OF THE BUBBLE CLOUD COMPONENTS	25
3.1	Scope	25
3.2	Inefficiency in the bubble production	25
3.3	Mean acoustical properties of the scattering medium	26
3.4	Experimental results	28
3.5	Effect of the bubble film solution	29
3.6	Transversal effects	30

3.7 Experimental verification 30

4.0 THEORETICAL PREDICTION OF THE MULTIPLE SCATTERING 32
4.1 Introduction 32
4.2 Estimation of the volume of influence 33
4.4 Instrumental limitation 39
4.5 Expected modifications of the pressure profiles 40

5.0 EXPERIMENTAL PROCEDURE 41
5.1 Shock tube 41
5.2 Pressure transducers 42
5.3 Shadowgraph 43
5.4 Control electronics 43
5.5 Sequence of events in the experiment 44
5.6 Measured data 46

6.0 EXPERIMENTAL RESULTS 48
6.1 Outline of the experiments 48
6.2 Strong scattering of very weak waves: $M_s \leq 1.01$ 49
6.3 Partial scattering of weak waves: $1.015 < M_s < 1.025$ 62
6.4 Interaction of the bubble array with stronger waves 66

7.0 INTERACTION OF AN ACOUSTIC PULSE WITH A CYLINDRICAL LENS 73
7.1 Introduction 73
7.2 Physical principles 73
7.3 Wave fronts and ray diagrams 77

8.0 EXPERIMENTAL APPROACH TO THE TWO-DIMENSIONAL INTERACTION 87
8.1 Cylindrical refraction cell 87
8.2 Secondary effects of the refraction cell 92

9.0 FLOW VISUALISATION 97
9.1 Helium filled cylinder 97
9.2 Freon filled cylinder 102

10.0 VELOCITY MEASUREMENTS 110
10.1 Methodology 110
10.2 Helium cylinder 111
10.3 Freon cylinder 115

11.0 PRESSURE MEASUREMENTS 119
11.1 Pressure measurements inside the refraction cell 119
11.2 Pressure measurements behind the cylinders 120

12.0 EXPERIMENTAL APPROACH TO THE THREE-DIMENSIONAL INTERACTION 133
12.1 Introduction 133
12.2 Experimental procedure 134

13.0 INTERACTION OF SHOCK WAVES WITH HELIUM-FILLED SOAP BUBBLES 138
13.1 Strong shock wave, $M_s = 1.25$ 138
13.2 Interaction with weaker waves 144
13.3 Velocity measurements from the x-t diagrams 151
13.4 Growth of circular holes in the soap film 148
13.5 Pressure measurements behind the bubble 157

14.0 INTERACTION OF SHOCK WAVES WITH HEAVY AND NEUTRAL BUBBLES 160

14.1 Freon 22 bubbles 160

14.2 Argon-filled bubbles 169

14.3 Nitrogen and helium-argon bubbles 173

15.0 DISCUSSION OF THE INTERFACE VELOCITIES 185

15.1 Shock-induced acceleration of curved interfaces 185

15.2 Subsequent behavior of the gas inhomogeneity 196

15.3 Effect of the membrane and of the contamination by air 201

16.0 SUMMARY 203

16.1 Interaction with a single discrete inhomogeneity 203

16.2 Multiple scattering of weak shock waves 208

References 212

APPENDICES

A MODEL OF BUBBLE POPULATION 215

B MEAN PROPERTIES OF A MIXTURE OF SEVERAL GASES 220

LIST OF FIGURES

Figure	Title	Page
2.1	Diagram of the Bubble Generator	10
2.2	Diagram of the Bubble Flow Control System	12
2.3	Diagram of the Square Test Section	16
2.4	Visualization Set-up of the Bubble Array	20
2.5	Visualization of the Bubble Array	21
2.6	Streak Photographs of the Bubble Array	23
4.1	Schematic Transmitted and Diffracted Waves behind the Helium Scatterer	35
4.2	Volumes of Influence for Various Incident Shock Waves	39
5.1	Diagram of the Instrumentation	46
6.1	Schematic Typical Pressure Profiles	51
6.2	Histograms of Precursor Size	53
6.3	Pressure Profiles of Very Weak Incident Waves ($M_s \leq 1.01$)	54
6.4	Pressure Profiles from the Control Experiments ($M_s \leq 1.01$)	56
6.5	Shadowgraph Pictures of the Interaction with Very Weak Waves	58
6.6	Shadowgraph Pictures of Very Weak Reflected Waves	61
6.7	Pressure Profiles of Weak Incident Waves ($1.015 < M_s < 1.025$)	63
6.8	Shadowgraph Pictures of Weak Incident Waves ($1.015 < M_s < 1.025$)	65
6.9	Pressure Profiles of Stronger Incident Waves ($1.05 < M_s < 1.36$)	67
6.10	Sequence of Shadowgraph Pictures ($M_s = 1.07$)	69
6.11	Shadowgraph Pictures of Stronger Incident Waves ($M_s = 1.05$ & 1.15)	71
6.12	Shadowgraph Pictures of Strong Waves ($M_S = 1.15$ & 1.36)	72
7.1	Definition of the Rays for the Helium Cylinder	78

7.2	Ray Diagram for the Helium Cylinder	79
7.3	Wavefront Diagram for the Helium Cylinder	80
7.4	Definition of the Rays for the Freon 22 Cylinder	82
7.5	Ray Diagram for the Freon 22 Cylinder	83
7.6	Wavefront Diagram for the Freon 22 Cylinder	85
7.7	Ray and Wavefront Diagram for the Air Cylinder	86
8.1	End View of the Test Section with the Cylindrical Cell	89
8.2	Side View of Two Cylindrical Cells	90
8.3	Pressure Profiles from the Interaction with Various Cylinders (M_s = 1.085)	93
8.4	Pictures of the Interaction with a Nitrogen Cylinder (M_s = 1.085)	95
9.1	Interaction of a Mach 1.22 Shock Wave with a Helium Cylinder	98
9.2	Interaction of a Mach 1.085 Shock Wave with a Helium Cylinder	100
9.3	Schematic Representation of the Deformation of the Helium Volume	101
9.4	Interaction of a Mach 1.03 Shock Wave with a Freon 22 Cylinder	103
9.5	Interaction of a Mach 1.085 Shock Wave with a Freon 22 Cylinder	104
9.6	Interaction of a Mach 1.22 Shock Wave with a Freon 22 Cylinder	106
9.7	Schematic Representation of the Deformation of the Freon 22 Volume	108
10.1	Schematic x-t Diagram for the Helium Cylinder	112
10.2	Schematic x-t Diagram for the Freon Cylinder	116
11.1	Diffracted and Transmitted Shock Waves behind the Helium Cylinder	121
11.2	Pressure Profiles behind the Helium Cylinder (M_s = 1.085)	122
11.3	Pressure Profiles behind the Helium Cylinder (M_s = 1.22)	124
11.4	Effect of the Secondary Transmitted Wave	126
11.5	Pressure Profiles behind the Freon 22 Cylinder (M_s = 1.22)	128

11.6 Pressure Profiles behind the Freon 22 Cylinder (M_s = 1.085) 130

11.7 Pressure Profiles behind the Freon 22 Cylinder (M_s = 1.03) 131

13.1 Interaction of a Mach 1.25 Shock Wave with a Helium-Filled Soap Bubble 139

13.2 Mixing of an Initially Spherical Helium Volume Processed by a Mach 1.25 Shock Wave 140

13.3 Disintegration of the Soap Film (Helium Bubble, M_s = 1.25) 143

13.4 Interaction of a Mach 1.10 Shock Wave with a Helium-Filled Soap Bubble 145

13.5 Interaction of a Mach 1.05 Shock Wave with a Helium-Filled Soap Bubble 146

13.6 Disintegration of the Soap Film (Helium Bubble, M_s = 1.05) 147

13.7 Schematic Representation of the Wave Pattern (Helium Bubble) 148

13.8 Schematic Representation of the Deformation of the Helium Bubble 150

13.9 Pressure Profiles behind the Helium Bubble 158

14.1 Interaction of a Mach 1.25 Shock Wave with a Soap Bubble Filled with Freon 22 161

14.2 Shock Wave Focusing by a Soap Bubble Filled with Freon 22 (M_s = 1.25) 162

14.3 Interaction of a Mach 1.07 Shock Wave with a Soap Bubble Filled with Freon 22 164

14.4 Schematic Representation of the Deformation of the Freon 22 Bubble 165

14.5 Disintegration of the Soap Film (Freon 22 Bubble, M_s = 1.095) 167

14.6 Disintegration of the Soap Film (Freon 22 Bubble, M_s = 1.25) 168

14.7 Interaction of a Mach 1.25 Shock Wave with an Argon-Filled Soap Bubble 170

14.8 Interaction of a Mach 1.10 Shock Wave with an Argon-Filled Soap Bubble 171

14.9 Interaction of a Mach 1.25 Shock Wave with a Nitrogen-Filled Soap Bubble 174
14.10 Interaction of a Mach 1.25 Shock Wave with a Bubble Filled with a Mixture of 1/3 He, 2/3 Ar 175
14.11 Interaction of a Mach 1.10 Shock Wave with a Nitrogen-Filled Soap Bubble 178
14.12 Interaction of a Mach 1.08 Shock Wave with a Soap Bubble Filled with a Mixture of 1/3 He, 2/3 Ar 179
14.13 Disintegration of the Soap Film (Nitrogen Bubble, $M_s = 1.05$) 181
14.14 Disintegration of the Soap Film (Nitrogen Bubble, $M_s = 1.25$) 182
14.15 Pressure Profiles Behind the Helium-Argon Bubble ($M_s = 1.25$) 183
15.1 Shock-Induced Acceleration of a Wavy Interface 187
15.2 Shock-Induced Acceleration of a Cylindrical Interface 189

LIST OF TABLES

Table	Title	Page
3.1	Modifications of the properties of the mixture	29
4.1	Volumes of influence for various incident shock waves	38
5.1	Shock tube diaphragms (thickness in μm)	41
10.1	Measured velocities from the interaction with the helium cylinder	113
10.2	One-dimensional interaction with air-helium interfaces	113
10.3	Relative velocities of the helium volume	114
10.4	One-dimensional interaction with air-Freon interfaces	117
10.5	Measured velocities from the interaction with the Freon cylinder	117
11.1	Measured and calculated refracted wave Mach number	120
13.1	Wave and interface velocities for a helium bubble	151
13.2	Relative velocities of the bubble interfaces	152
13.3	Piston and vortex ring parameters	154
13.4	Expected behavior of the vortex rings	155
13.5	Merging distance behind a helium sphere (in mm)	159
14.1	Wave and interface velocities for a Freon 22 bubble	166
14.2	Wave and interface velocities for an argon bubble	172
14.3	Calculated velocities of the air-argon interfaces	172
14.4	Wave and interface velocities for neutral bubbles	177
15.1	Upstream interface velocities of the helium cylinder	193
15.2	Upstream interface velocities of the helium sphere	194
15.3	Downstream interface velocities of the helium cylinder	194
15.4	Downstream interface velocities of the helium sphere	195
15.5	Upstream interface velocities of the Freon cylinder	196
15.6	Upstream interface velocities of the Freon sphere	197
15.7	Predicted helium bubble and vortex velocities	198
15.8	Measured velocities of the short helium cylinder	199
15.9	Measured velocities of the helium sphere	199
15.10	Predicted Freon bubble and vortex velocities	200
15.11	Measured velocities of the Freon 22 cylinder	201
15.12	Measured velocities of the Freon 22 sphere	201
15.13	Effect of density increase on the velocity ratios	202

Chapter 1

INTRODUCTION

1.1. Multiple scattering of weak shock waves

The interaction of shock waves and nonuniform media occurs in a variety of situations such as the propagation of a sonic boom in a turbulent atmosphere and the interaction of shock waves and the lasing medium in repetitively pulsed high energy gas lasers. This interaction which causes some modifications on the shock (focusing and scattering) as well as on the medium (creation of vorticity and enhanced mixing of the gas inhomogeneities) is difficult to model numerically and experiments in controlled laboratory conditions are needed to understand some of the phenomena involved. One such experiment has been carried out at GALCIT by L. Hesselink (1977 and 1978). It was a study of the scattering of a weak shock wave by a turbulent mixture of two gases, helium and a fluorocarbon (Freon 12) of vastly different properties: speed of sound, density, and acoustical impedance. The modifications on the shock wave front, recorded by pressure transducers and observed with flow visualization were connected to the strength of the incident shock wave and to the decay of the turbulent mixture, therefore to the length scales in the fluid. The modifications brought by the shock wave on the random medium were also documented by flow visualization and quantitative optical techniques (Sturtevant et al., 1980, 1981).

The initial ambition of the present experiment was to create a random array of discrete scatterers, which could be thought of as simplified random mixture with inhomogeneities of controllable size and spacing and of controllable properties, acoustical index of refraction and density and then to study its scattering effect on the shock wave with the hope of correlating the better defined scales and properties of the inhomogeneities with the shock front topology, documented by flow visualization and pressure profiles from transducers.

Ideally, the turbulent mixture of the earlier experiment would have been replaced by a three component medium, with air as a host fluid and an array of well-defined gaseous inhomogeneities, some made of a light gas such as helium with high speed of sound and low density and the others made of a heavy gas such as Freon 12 with low speed of sound and high density. Under these circumstances, the scattering medium would have been in fact a random juxtaposition of gaseous inhomogeneities where no mixing was allowed between themselves and the host fluid. The shock wave would meet on its path a random distribution of accoustical lenses, some convergent, the other divergent, introducing positive or negative shifts in the local wave front position. The combined effect of a large number of these closely packed lenses is expected to have an effect on the shock wave comparable to the effect of the turbulent mixture of two gases with air as a host fluid.

Because of the diffusion process between gases the scatterers have to be enclosed in some kind of light membrane, thus introducing a second phase in the scattering medium with some possible effect on the wave propagation. The need to produce an array as dense as possible requires the production of a very large number of scatterers with, therefore, a production technique as simple as possible.

Soap bubbles represent the simplest form of gas enclosure with their naturally spherical shape, ideal for a three dimensional problem and their thin and fragile soap membrane. In addition, a method of producing them at a very large rate had been developed recently and was easily implemented for use in the shock tube. However, only helium filled soap bubbles could be produced to create a dense array in the shock tube test section. If the volume fractions of helium and air were comparable the medium would still have divergent and convergent inhomogeneities. As in this experiment the volume fraction of helium is very small (1% to 3%) each bubble acts as an isolated divergent acoustical lens for the shock wave. Therefore the random array cannot be considered as a true discretisation of the earlier turbulent mixture and shock wave focusing cannot be observed.

The primary goal of this first experiment (Chapters 2 to 6) is therefore reduced to a study of the combined effect on the shock wave of the weak diverging transmitted waves generated by each scatterer. A secondary goal is a qualitative study of the shock-induced mixing of the helium in the scatterer.

1.2. Scattering by a single discrete inhomogeneity

The second experiment is a detailed study of the interaction of weak shock waves with a single gas inhomogeneity of simple shape. The interaction of the shock wave with a single spherical helium scatterer, namely a large helium filled soap bubble, is an obvious complement to the first experiment but the scope of this study is more general: both types of scatterers, acting on the shock wave either as diverging or converging lenses, are investigated and the experimental study is made in two and three dimensions with cylindrical and spherical gas scatterers. The two facets of the interaction, the effect of the scatterer on the shock wave and the deformation of the scatterer under shock-induced acceleration, present several interesting phenomena which have not been observed before.

The propagation of a shock wave through a spherical or cylindrical volume of gas of a different density and speed of sound than the surrounding medium involves the phenomena of shock wave reflection, refraction, diffraction and in the case of a converging lens, focusing. The refraction of shock waves at plane gas interfaces has been the object of considerable interest both experimentally and numerically. Jahn (1956) and Henderson's group, (Abd-El-Fattah et al., 1976 and 1978 b), studied the slow-fast interface where the gas downstream of the interface has a higher speed of sound and lower density than the gas upstream, and have recognized basically two types of refraction depending on the angle of incidence of the shock on the membrane. At low angles regular refraction occurs where the refracted wave and incident wave intersect the interface at the same point. At higher angles various aspects of irregular refraction are observed where usually the intersection of the refracted wave with the interface runs ahead of the intersection of the incident wave or the Mach stem resulting from the Mach reflection of the incident wave. A weak shock wave, incident on a cylindrical interface, will cover the complete range of angle of incidence and therefore will undergo both types of refraction.

On a fast-slow interface, it has also been shown (Abd-El-Fattah et al., 1978 a) that depending on the strength of the wave, different types of refraction also appear but the refracted and incident wave always intersect the interface at the same point.

In view of the intricacies of the seemingly simple plane refraction problem, no specific theoretical or experimental study of the interaction of plane shock waves with curved gas interface has yet been made, although some aspects of the phenomenon have been observed in more complex configurations. One of them is the study of shock wave and flame interaction (Markstein, 1957 a & b and Rudinger, 1958) when pictures were made of the propagation of a shock wave through a curved flame front enclosing hot combustion products, thus acting as a slow-fast interface. Precursors and lateral shocks associated with the phenomenon of irregular refraction were identified.

When a shock wave interacts with a slow-fast gas interface, the resulting reflected wave is an expansion at small angle of incidence (regular refraction) but may be a reflected shock at higher angles (irregular refraction). Similarly, the reflected wave from a fast-slow interface is usually a shock but may be an expansion for a small range of angle of incidence and for weak waves (Abd-El-Fattah, 1978 a & b). Inside the acoustical lens, when the refracted wave reaches the interface, some of its energy is refracted outside, thus forming a transmitted wave and some are internally reflected. The internally reflected wave later intercepts the interface again. On the outside the incident wave, after it has reached the top of the lens, propagates on the downstream side as a diffracted wave and it will be seen in Chapter 7 how some of its energy may be refracted inside in the fast-slow case. Shock wave focusing is expected to occur in the case of a strongly convergent acoustical lens just as it has been observed after reflection of a plane shock wave on a concave reflector (Sturtevant and Kulkarny, 1976). Other occurrences of shock focusing will be seen after reflection of the refracted wave on the concave cylinder interface.

Refraction, reflection and diffraction are well understood phenomena for linear waves such as harmonic acoustic waves and acoustic pulses (Pierce, 1981, Friedlander, 1958). The combination of all these phenomena can be intriguing even for the simple configuration of a cylindrical acoustic lens. In addition, more extraordinary wave phenomena such as tunneling or glory could be seen in this kind of interaction (Jones, 1978, Marston and Kingsbury, 1981). Ray and wave front geometries for acoustic pulses are presented in Chapter 7 and will be compared with the shadow photographs of the interaction of a relatively weak shock wave with a circular cylinder (Chapter 9).

Two waves are generated downstream of the lens by the interaction process: the transmitted and the diffracted wave, in that order for a diverging lens, in the reverse order for a converging lens. The delay, or distance between the two waves, which is constant for an acoustic pulse, decreases to zero for a finite strength wave because of nonlinearity. One of the goals of the experiment is the study from the shadowgraphs and pressure measurements of that merging process (Chapter 9 for cylindrical lenses).

The other facet of the present investigation is the study of the motion induced by the shock of the gas initially inside the lens and its subsequent mixing with the ambient medium.

An arbitrary interface separating two gases of different properties will be distorted by a shock wave by two different mechanisms which may be coupled. The first one, usually called the initial compression, results from the velocity field created locally by the shock refraction and reflection. The velocity V at the interface is a function of the refracted wave in the gas downstream of the interface and of the combination of the incident and reflected wave in the gas upstream. This can be easily calculated in the one dimensional case where the interface is parallel to the shock front and will be used in this work for the upstream and downstream edges of the scatterer. The velocity of the interface results in the distortion of its shape. For example, in the case where the two gases are the same, an initially cylindrical (and massless) interface of diameter D will be deformed into an elliptical cylinder of major axis D and minor axis $D(1 - \frac{V_2}{V_s})$ where V_s is the shock velocity and V_2 is the gas velocity behind the shock. This is illustrated on figure 8.4 and in the spherical case with the neutral bubbles described in § 14.3.

The second mechanism of interface deformation is the shock-induced Taylor instability (Taylor, 1950) developing on any curved or corrugated interface separating gases of different density. According to a model called the simple impulsive theory (Markstein, 1957 a and Meyer and Blewett, 1972), its growth rate is proportional to V, the initial corrugation amplitude and wave number, and the ratio $\frac{\rho_2 - \rho_1}{\rho_2 + \rho_1}$ where ρ_1 and ρ_2 are the gas densities upstream and downstream of the interface. For high curvature interface and very different gases the growth rate or perturbation velocity v is comparable to V and important and widely different distortions are expected early in the interaction process. It is clear that the behavior of the gas inhomogeneity at the early time contributes to the subsequent motion and mixing pattern of the inhomogeneity with the host gas.

The shock induced instability has been recognized early in the above-mentioned shock wave-flame interaction experiments. Curved flame fronts, when accelerated by a shock wave, undergo heavy distortions such as shape reversal and spike formation (Markstein, 1957 b). Simple impulsive theories such as the one mentioned above have been used with some success. More sophisticated numerical methods taking compressibility into account, have been developed (Richtmyer, 1960), and the deformation (under shock-induced acceleration) of a sinusoidal interface separating gas pairs such as air-helium and air-Freon 22 has been investigated with experimental conditions rather close to the work presented here (Meshkov, 1970). The lower than expected deformation velocities were attributed to experimental difficulties (imprecision in the measurements, gas contamination) and the neglect of some factors such as viscosity in the theoretical calculations (Meyer and Blewett, 1972). Other possible effects such as drag force on the spike, and turbulence have also been mentioned (Baker and Freeman, 1981).

Since the present experiment involves some interface shapes rather different than the low amplitude corrugations of the previous experiments and numerical models, the measured interface velocities (Chapter 10 for the cylinder, 13 and 14 for the sphere) are compared only with the prediction of the simple impulsive theory (Chapter 15).

The experiment has been designed to provide a qualitative understanding of the second phase of the motion of the gas inhomogeneity : the formation and subsequent motion of vortical structures which are thought to be the means by which a turbulent medium is regenerated by a shock wave. It has usually been expected but never checked under controlled experimental conditions that a spherical inhomogeneity should become a vortex ring and a cylindrical inhomogeneity a linear vortex pair with positive or negative velocities relative to the surrounding medium depending on the density and the initial shape (Rudinger and Somers, 1960). The flow visualization (Chapter 9 for the cylinders, 6, 13 and 14 for the spheres) illustrates how different the motion looks like in two and three dimensions and the measured vortex velocities are compared with a simple theoretical model and previous experiments obtained on a much smaller scale (Chapters 10, 13 and 15).

Finally, another curious phenomenon is observed in the three dimensional case by means of high speed photography: the behavior of thin liquid membranes, which constitute the interface in that case, appears to be quite dependent on the shock strength and the density of the gas inhomogeneity (Chapters 13 and 14).

Chapter 2

DESIGN OF THE MULTIPLE SCATTERING EXPERIMENT

2.1. Generation of the discrete helium scatterers

2.1.1. *Introduction.* Helium filled soap bubbles have been used by a several investigators (Hale et al., 1969, 1971) as a flow visualization tool. The positive buoyancy of the helium can compensate for the weight of the soap membrane. Therefore, for various combinations of bubble size and soap film thickness the bubbles can be made neutrally buoyant and can be used as particles following closely the streamlines in low velocity flow applications. If the bubbles are illuminated for a known duration with a collimated light source, the light reflected by the soap membrane is recorded as streaks on the film of a camera whose optical axis is perpendicular to the light source axis. The direction and length of the streaks define the direction and magnitude of the velocity components in a plane perpendicular to the camera axis. The apparatus for this flow visualization technique was developed and is commercialized by SAGE ACTION Inc.

2.1.2. *Description of the bubble generator.* The bubble generator used in the present experiment is a modified version of the low speed bubble generator developed by SAGE ACTION with the same internal geometry and performance but with an external configuration identical to the one of the piezoelectric transducer KISTLER 606 so that the bubble generator can be mounted on the standard type of instrument port used on the shock tube.

Figure 2.1 shows a cut away drawing of the generator. The tip of the bubble generator is made of three concentric tubes. The inner one of internal diameter

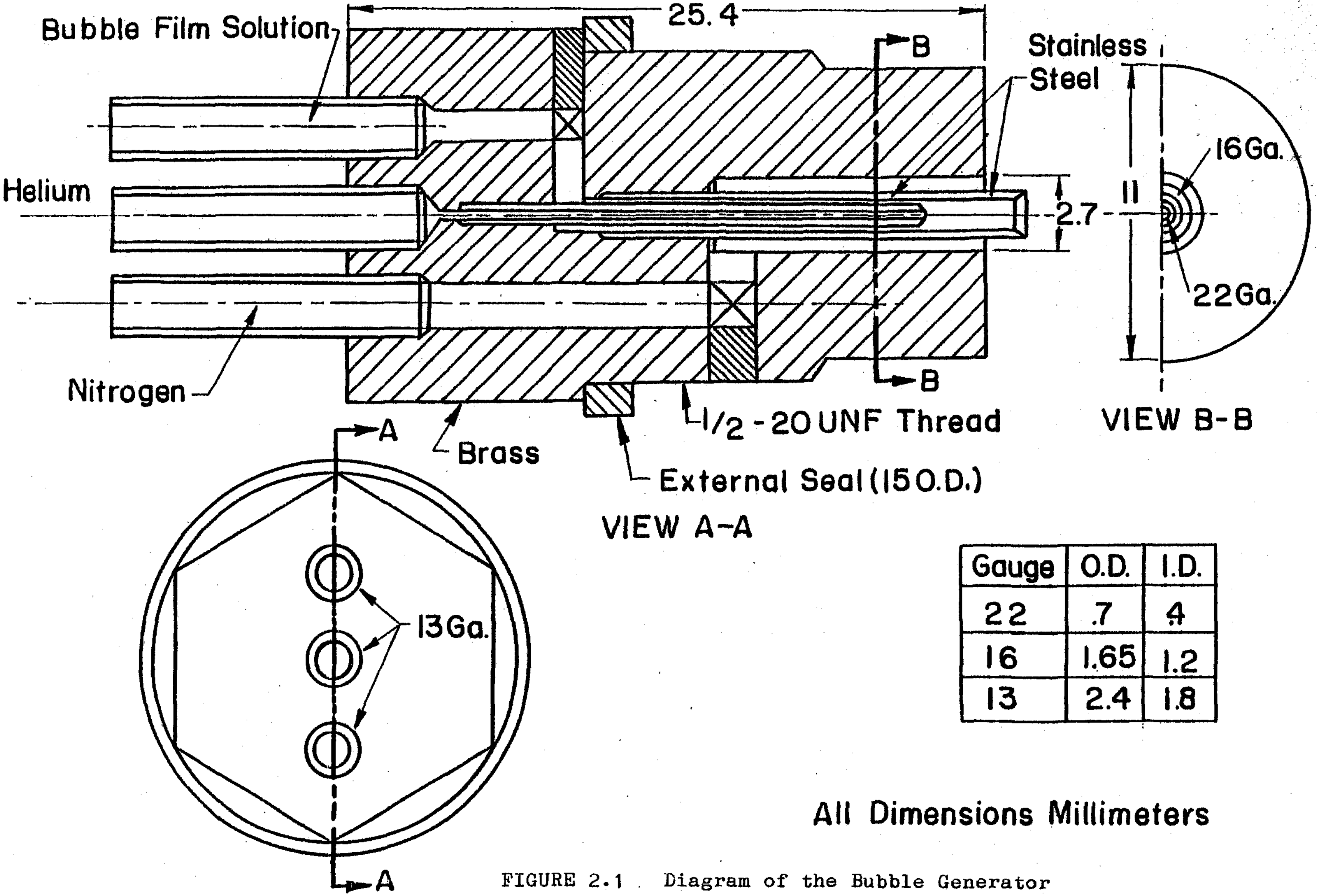

Gauge	O.D.	I.D.
22	.7	.4
16	1.65	1.2
13	2.4	1.8

FIGURE 2.1 Diagram of the Bubble Generator

.04 mm supplies the helium, the intermediate channel with the inner diameter .7 mm and outer diameter 1.2 mm supplies the soap, called bubble film solution by SAGE ACTION. A bubble is formed at the tip of the second tube and is blown away by the outflow of nitrogen when the bubble diameter has grown to the point where the drag on the bubbles overcomes the surface tension on the tip of the second tube. The nitrogen channel has an inner diameter of 1.6mm and an outer diameter of 2.75 mm. The bubble generator or bubble head is supplied with the three components, helium, soap, and nitrogen by a console with metering values so that each flow can be adjusted for the desired generator performance. The soap which is manufactured by SAGE ACTION under the brand name 1035 BFS is a mixture of a 15% solution in water of a surface active agent AEROSOL OT from the American Cyanamid Corporation and glycerin to the proportion 1/3, 2/3.

This bubble film solution, which would be quite unsuitable for making large soap bubbles by the classical method of blowing through a wetted ring, has the high molecular mobility needed for fast film forming. This quality is required for the high bubble generation rate of this bubble head.

2.1.3. *Operation of the bubble generator.* The set-up of the supply lines of the three components is illustrated in figure 2.2. The control of the bubble production: size, weight, and rate is made by adjusting the flow rate of helium, soap, and nitrogen. It is described in detail by Hale et al. (1969) and only an outline of the process is given here.

Within the normal operating range of the bubble head, the surface of film which can be produced is proportional to the bubble film solution (BFS) flow rate. For a given BFS flow rate, the flow rate of helium has to be set at the highest value possible, just below the rate for which the film cannot be formed smoothly or where too many of the bubbles burst immediately because of the

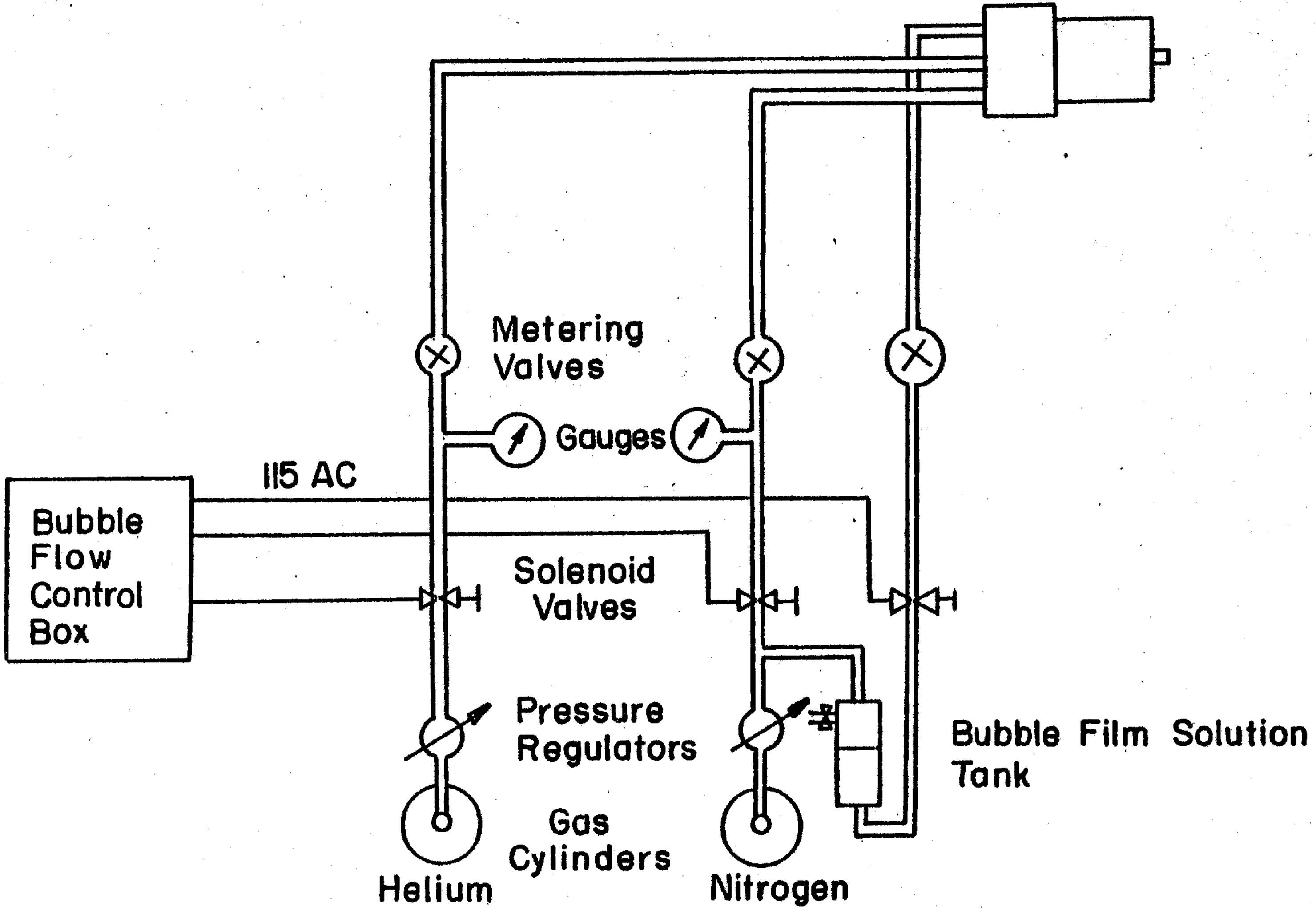

FIGURE 2.2 Diagram of the Bubble Flow Control System

too thin membrane. When the helium flow rate is significantly below the optimum, the bubbles will have a thicker membrane and will tend to be heavier or connected in chains. The size of the bubble is controlled by the flow rate of nitrogen. Hale et al. (1969) carried out some tests and found an approximate relation between d, the bubble diameter in mm and $\dot{V}_{N_2}$ the flow rate of nitrogen in cm^3/s:

$$d \simeq \left(\frac{110}{\dot{V}_{N_2}} \right)^2$$

The production rate of bubbles of a given diameter is set by the flow rate of soap first, then, with an approximate flow rate of helium the size is controlled by adjusting the flow rate of nitrogen, and finally by fine tuning the flow rate of helium, the bubble production rate is maximized. The range of bubble diameter which could be achieved was from 1 to 4 mm with a peak efficiency at 2 mm where approximately 500 bubbles could be produced per second. About 20% percent of the bubbles are significantly heavier.

2.2. Design of the bubble cloud chamber

The bubble cloud chamber was designed to the following requirements:

i. it should contain the large number of bubbles created by one or several bubble generators in a volume as well defined as possible and small enough to achieve a sufficiently high concentration of bubbles.

ii. it should have a sufficient strength to withstand the internal pressure generated by shocks of Mach number up to 1.5.

iii. it should be compatible with the dimensions of the GALCIT 6 inch diameter shock tube and allow for flow diagnosis by flow visualization, shadowgraph or schlieren and by pressure measurements.

iv. it should be adjustable, and provide for a wide range of test time and allow easy access to the inside for cleaning the soap left on the internal walls after each shock.

The chosen test section is made of a tube of extruded aluminum with a square cross section: external side 10.1 cm, internal side 8.9 cm and wall thickness 6 mm. It is divided in three sections:

i. a 1.8 m long "cookie-cutter" which is inserted inside the cylindrical test section of the shock tube which, with an internal diameter of 15.2 cm, is barely large enough for the square tube. Its role is to slice a square section of the shock wave front and delay the arrival at the bubble chamber of the diffracted waves around the cutter's sharp lips by a time larger than any maximum desired or expected test time (5ms)
ii. a 60cm long transition section
iii. the test section or bubble cloud chamber also 60 cm long but equipped with windows and pressure transducers ports on the side walls and the end plate and an adjustable instrument plate which can be positioned at various distances upstream of the real end plate.

The windows made of schlieren grade optical glass BK7 are 150 mm in diameter and 25.4 mm thick. They are epoxied to their aluminum mounts which are bolted on the test section. The test section and the windows have been tested to a static internal overpressure of 6.7 bar corresponding to the transient pressure recorded after reflection from the end plate of a shock wave of Mach number 1.64 propagating into air at one atmosphere. The windows are mounted with their axis at 178 mm from one end and 422 mm from the other end of the section which can be inverted and exchanged with the transition section so that a wide range of the distance between the window axis and real shock tube end plate can be achieved. The bubble chamber section and the transition section are connected by toggle clamps strong enough for shock waves up to Mach number 1.25. For stronger waves, some bolts must be added. These two sections are suspended by rollers on a garage door type track and this feature combined with the quick release clamps provided the easy access to the inside of the test section. Figures 2.3 and 5.1 show the general layout of the cylindrical shock tube test section and its square extensions.

Some preliminary experiments of the injection of the bubbles in transparent boxes of the same geometry showed that when injected from the end wall, they form a dense array about 40 cm long in a few seconds preceded by a much less concentrated cloud further upstream in the tube and that the losses by impact on the walls are minimal. In the actual scattering experiment, one or four identical bubble generators were mounted on the instrument plate which was positioned usually 300 or 200 mm behind the windows axis.

1.3. Characterization of the helium bubble array

1.3.1. *Introduction.* As far as the shock wave scattering experiment is concerned, the important characteristics of the bubble cloud are its length and the distribution of the concentration of bubbles both longitudinally and transversally in the shock tube test section.

1.3.2. *Theoretical estimate of the bubble flow pattern.* Because the bubble generator creates in fact a jet of nitrogen entraining a stream of bubbles, the injection of the bubble array can be analyzed using the results known about confined jets. The capital feature of a confined jet is its recirculation eddy. The calculation of the length of that eddy will give some idea about the extension of the bubble array in the test section. The results outlined here were published by Curtet (1960) but they come from the work of Thring and Newby. These investigators measured the flow field generated by the mixing of a narrow,

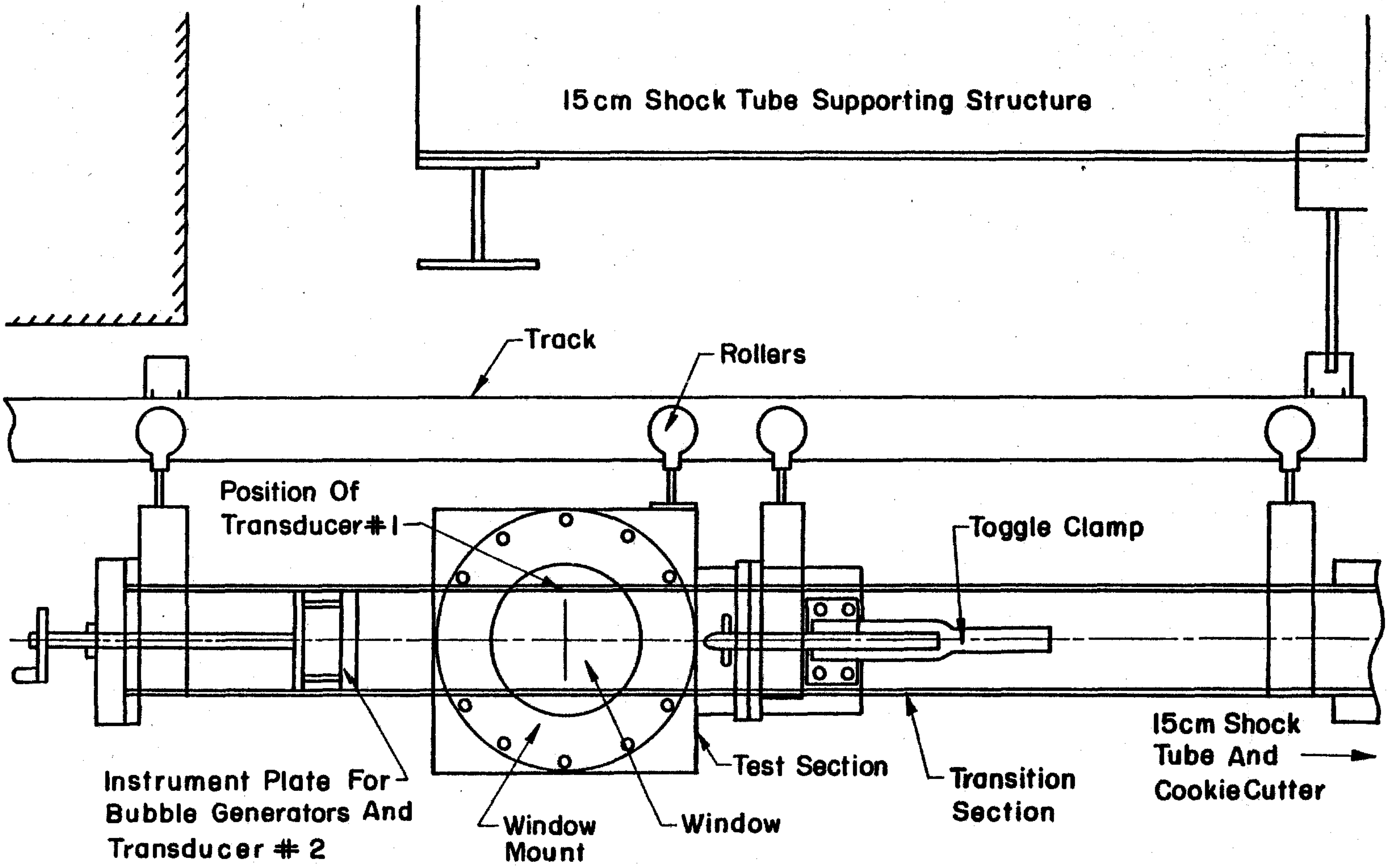

FIGURE 2.3 Diagram of the Square Test Section

strong jet (radius a, mass flow m_0) positioned coaxially with a slower outer flow (mass flow m_a) in a pipe of radius h. If it were not confined, the inner flow would spread with a half angle of 12.5° and therefore would grow to the radius h at a distance $x_e = 4.5h$. This defines the far end of the recirculation eddy of the confined jet.

The position, at a distance x_0 such that the free jet mass flow

$$m = m_0 \ (.2\frac{x}{a} - 1) \tag{2.1}$$

equals the initial outer mass flow m_a defines the beginning of the recirculation eddy

$$x_0 = 5 \ \frac{m_a + m_0}{m_0} a \, . \tag{2.2}$$

In this experiment, $m_a = 0$, $a = 1.1mm$ and $h = 43mm$ (a cylinder of this radius has the same cross-sectional area as a square tube of side length 89 mm). Therefore $x_0 = 5a = 5.5mm$ and $x_e = 4.5h = 220.5mm$. Curtet also defines as critical distance, the distance to the center of the eddy, approximately the average between x_0 and x_e : $x_c = 127.5mm$. According to this simple model the geometry of the recirculation eddy doesn't depend of the mass flow of the inner jet.

When four bubble generators are used, each one lies approximately in the center of a quarter of the end plate. Therefore each one can be thought of being at the center of a square tube of side length 44.5 mm equivalent to a cylinder of radius 24.5 mm. The four adjacent recirculation eddies are therefore twice as small as the one given above with $x_0 = 5.5mm$, $x_e = 110.2mm$, and

x_c = 68.7*mm*. With the assumption that the length of the bubble cloud is proportional to the length of the recirculation eddy, the array generated by four bubble generators is expected to be shorter than the one obtained with only one generator. Its concentration could be up to four times as high.

2.3.3. *Estimate of the velocities and mass-flow rates.* The volume flow rate of nitrogen in one generator ranges from 75 to 100 cm^3/s. With a nozzle area of 4 mm^2, the nozzle velocity ranges from 18 to 25 m/s. With an equivalent nozzle radius of 1.1mm the nitrogen jet Reynolds number ranges from 2750 to 3500. The jet is therefore turbulent. When the jet is fully developed in the test section, its mean velocity varies between 9 and 12 mm/s. When four jets are in operation, these values become 300 - 400 cm^3 for the flow rate, and 36 to 48 mm/s for the average velocity of the fully developed flow in the shock tube test section.

The strength of the recirculation eddy can be evaluated with Curtet's result for the maximum recirculated mass flow m_r

$$m_r = 5(m_v + m_u) = 5m_v \tag{2.3}$$

The recirculated volume flow rate is therefore five times the injected flow rate. It is expected that most of the bubbles will initially stay in the eddies during the few seconds it takes the latter to grow to their final strength, but after that time, the bubbles should escape from the eddies at a rate equal to their generation rate. The volume of maximum concentration of scatterers includes but is probably not limited to the recirculation eddies

2.3.4. *Flow visualization experiments.* In order to test the bubble injection method, to observe the flow pattern inside the test section and to estimate the distribution of bubble concentration, a transparent full scale model of the test section was built. The bubbles were injected by one bubble generator located on one end plate of the 8.9 x 8.9 x 120 cm lucite box and a light source, either continuous or instantaneous (electronic flash) was located at the other end. A 35 mm camera, located 1.5 m away from the side of the box was used to record the light reflected by the bubble membrane. When the electronic flash was used, the bubble motion was frozen with each bubble appearing on the recorded picture as a pair of bright spots. These spots are images of the light source formed by the two areas of the bubble membrane acting as spherical mirrors with their axis bisecting the right angle formed by the bubble to light source axis and the bubble to camera axis. The visualization setup is shown on figure 2.4. Several pictures of the bubble cloud, taken at 2 s interval show that the dense part of the cloud takes about 5 seconds to reach a steady bubble concentration and that its length is approximately 40 cm. Beyond that distance, the bubble concentration is lower but the length of this less dense cloud increases as the bubbles keep being injected.

The number of bubbles in the concentrated part is estimated to be between 1000 and 1500 corresponding to a volume available per bubble between 3.2 and 4.75 cm^3 or a mean interbubble spacing between 1.8 and 2.1 cm. When the bubble generator is turned off the number of bubbles drops and almost all bubbles have disappeared 2s later. The photographs in figure 2.5 illustrate this evolution.

With a slide projector used as a continuous light source, and the camera shutter usually set at a low speed between 1/60 and 1/4 s, the bubble flow becomes apparent as each bubble is imaged as two parallel streaks of light which define the direction and magnitude of the projection of the bubble velocity on a vertical plane perpendicular to the camera optical axis. The streaks of light from many bubbles combine to create an image of the recirculation eddy of the confined nitrogen jet which carries the bubbles. This pattern is shown on

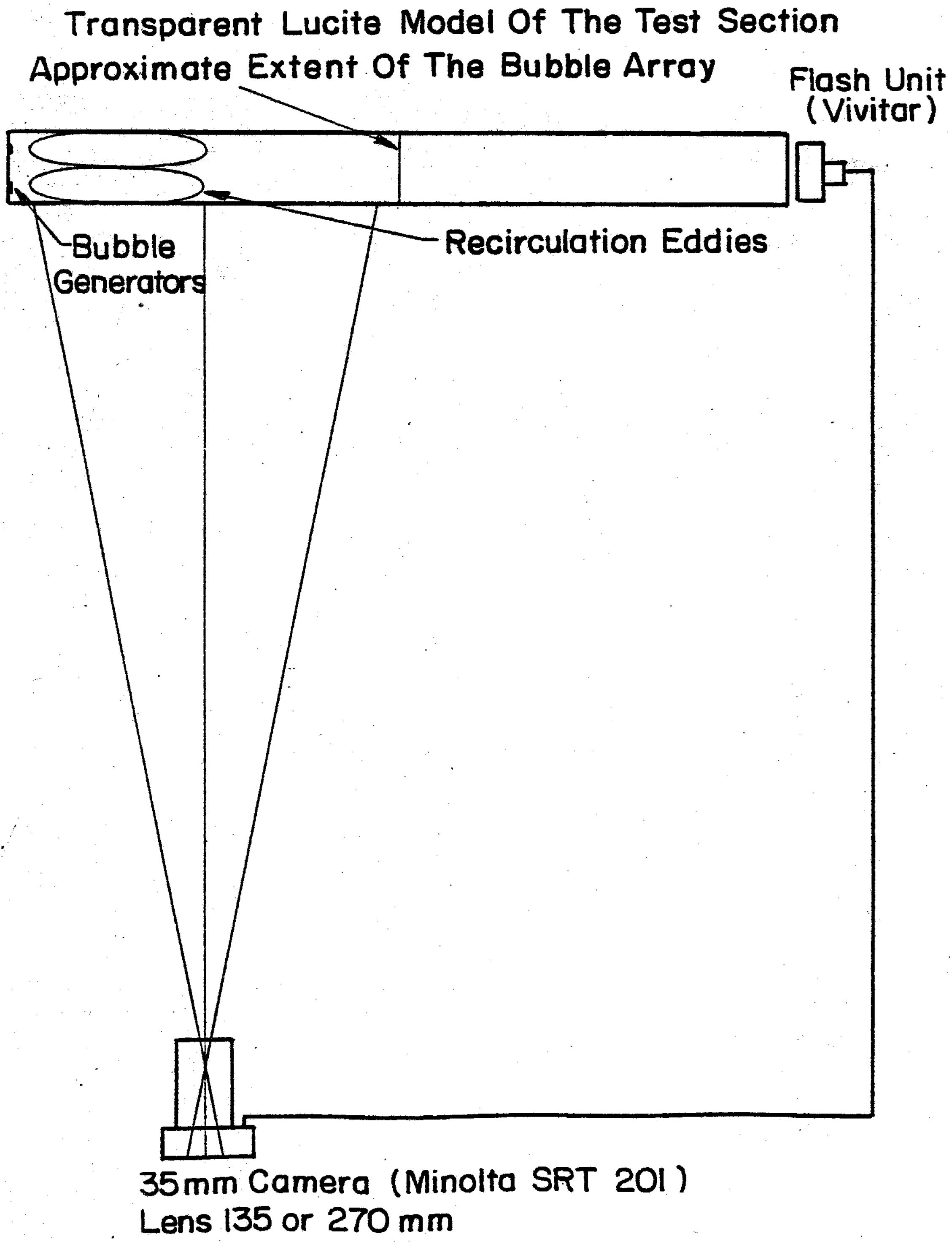

FIGURE 2.4 Visualization Set-up of the Bubble Array

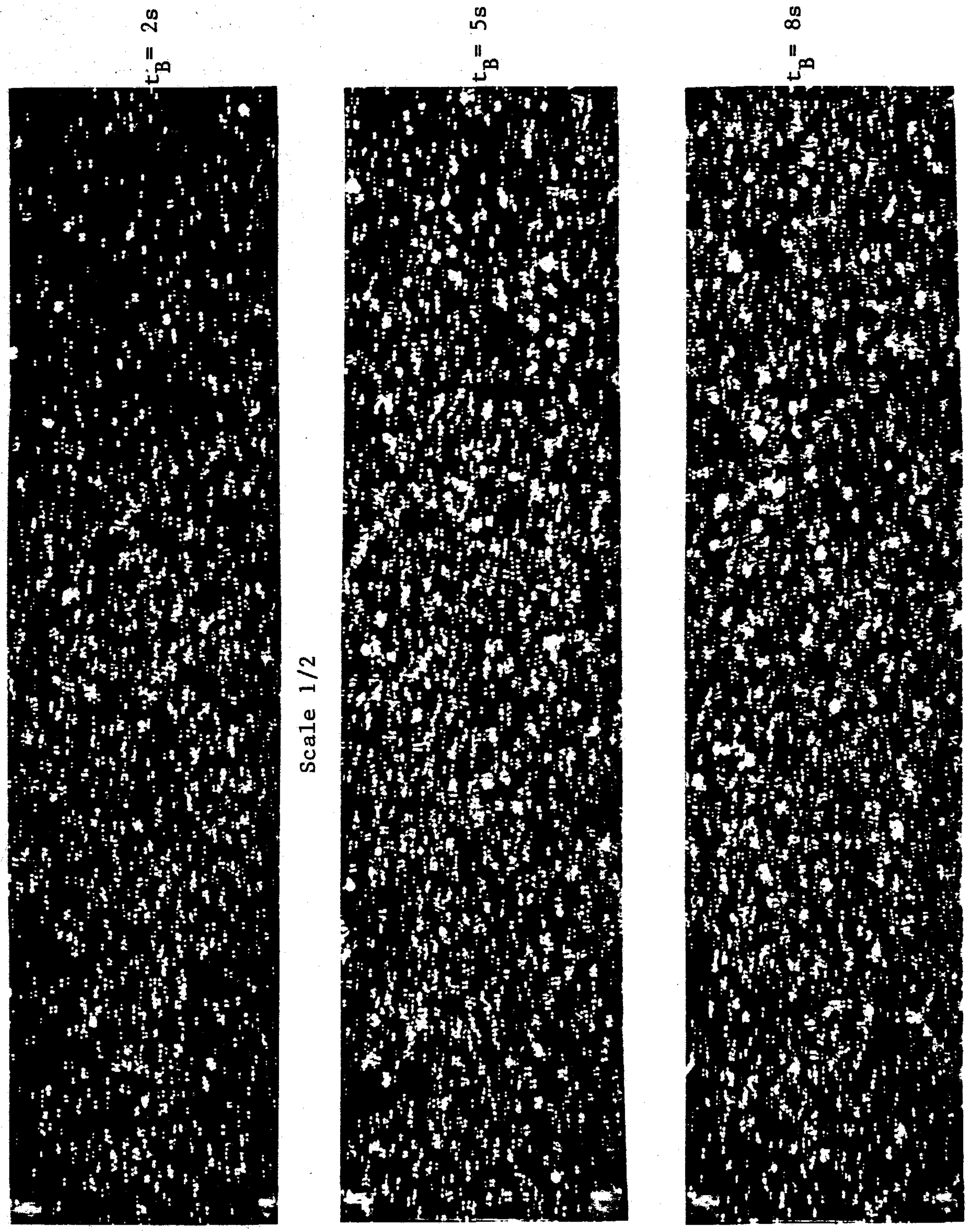

$t_B = 2s$

$t_B = 5s$

$t_B = 8s$

Scale 1/2

FIGURE 2.5 Visualization of the Bubble Array figure 2.6. The recirculation eddy seems to start right at the end plate and to end at a distance of 30 cm which is 50% more than predicted by Curtet's method. In the first 10 cm of the eddy and beyond its outer limit at 30 cm the bubble concentration seems to be lower than in the center of the eddy but that is probably an effect of the lower average velocity in these outer areas. From the average length of the streaks, the bubble velocity in the jet close to the generator is a few meters per second. The bubble velocity in the eddy, seems to be around 25 cm/s near the end wall and around 15cm/s at the outer limit. Beyond the eddy the bubble velocity is around 10 cm/s. When the bubble generator is turned off, the remaining bubbles fall towards the bottom plate with a velocity ranging from 2 to 5 cm/s.

2.3.5. *Extension to 4 bubble generators.* No such measurements were made when four bubble generators were used. However, visual observations which were made in that experimental setup confirm that the bubble cloud is shorter and denser when four generators are used instead of one. A model of the bubble population dynamics in an enclosed volume, transposed from elementary kinetics theory of gases was used to estimate the concentration limit and time to reach it for one or four bubble generators. It is given in Appendix A. This model, supported by the observation of the bubble cloud behavior in the transparent test section confirms the increase of concentration observed when going from one to four bubble generators.

2.3.6. *Observations on the shock tube.* In the experiments on the real shock tube test section, it was found that the best shadowgraph pictures of the scattering array created by one bubble generator were of the section of the bubble cloud located between 250 and 350 mm from the false end plate. The highest concentration recorded there was 200 bubbles in an observed volume of

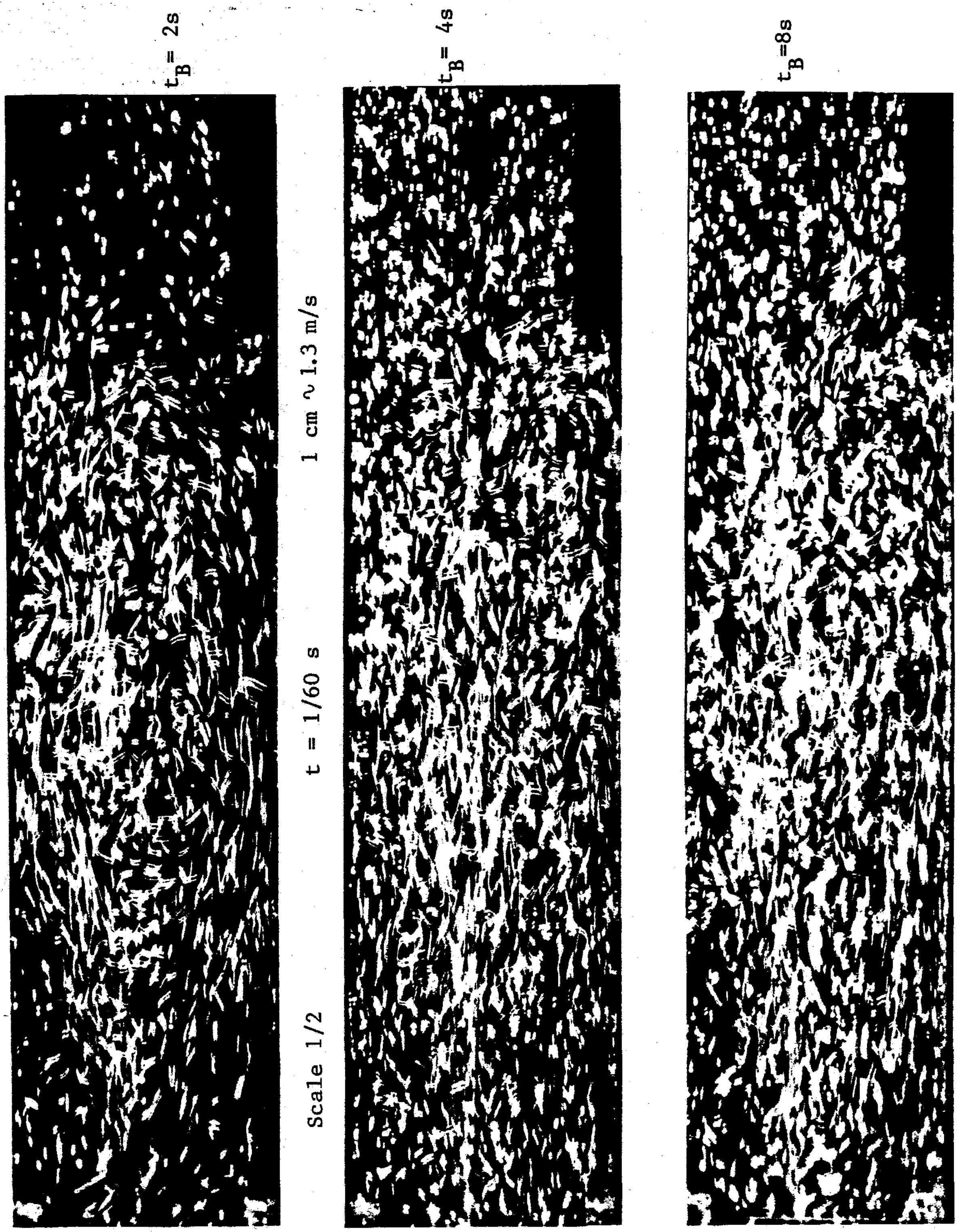

FIGURE 2.6 Streak Photographs of the Bubble Array

610 cm^3 corresponding to a volume available per bubble of 3 cm^3 equivalent to a sphere of diameter 1.8 cm. When the bubble generator was located at the real end plate 422 mm away from the window axis, the concentration of bubbles was much lower and when the end plate with the bubble generator was located 178 mm away from the window axis, the shadowgraph quality was very degraded because of the soap droplets which are spattered on the window by the bubble generator.

With four bubble generators mounted on the false end plate the best results were obtained with the plate located 200 mm from the window axis. The maximum number of bubbles recorded on the shadowgraph picture of that section of the cloud was 500. This corresponds to a volume available per bubble of 1.22 cm^3 equivalent to a sphere of diameter 1.3 cm.

In both cases, the bubbles had been injected for 4 seconds when the shadowgraph picture was recorded but in general the higher steady state concentation plateau is reached faster with four generators than the lower concentration plateau with a single generator.

2.3.7. *Transversal distribution of the bubbles*. Normally, because of the neutral buoyancy of the bubbles there should not be any transversal variation of the bubble cloud concentration except perhaps very near the end plate. In reality about 20% of the bubbles are too heavy and these would tend to create a higher concentation at the bottom of the test section. However, this was not observed either in the transparent box or in the actual test section.

Chapter 3

EFFECT OF THE BUBBLE CLOUD COMPONENTS

3.1. Scope

Because of some inefficiencies in the production and the destruction of many bubbles in the test section, a large amount of excess film solution and helium is present in the test section besides the bubble themselves. Nitrogen gas is also injected in large amounts. In this section these quantities and their effect on the mean acoustical properties and the shock wave propagation are estimated.

3.2. Inefficiency in the bubble production

The volume flow rates of each of the three components in one bubble generator were not constant throughout this investigation and the optimum behaviour of each one of the four generators required some different metering valve setting thus introducing some differences in volume flow rates. Therefore, only a range of volume flow rates is given here. Gas flow rates were calculated from the pressure drop across the metering valves, using the manufacturers calibration (Hoke metering valves, series 1300 c_v 0.028). The soap flow rate was directly measured:

Helium flow rate $\dot{V}_{He}$	: 11	*to* 17 cm^3/s	*av.* 14 cm^3/s	
Nitrogen flow rate $\dot{V}_{N2}$	: 75	*to* 100 cm^3/s	*av.* 87 cm^3/s	
Bubble film solution $\dot{V}_{BFS}$	: *average*	65 mm^3/s		

One bubble of radius r and soap thickness Δr has a membrane volume $v_{BFS} = 4\pi r^2 \, \Delta r$ and internal volume $V_{He} = \frac{4\pi}{3} r^3$. A helium filled soap bubble is neutrally buoyant if $\Delta r = .43 \, 10^{-3} \, r$ Therefore for the bubbles used in this experiment:

$$r \simeq 1\ mm \quad \Delta r \simeq .43\ \mu m$$

$$V_{BFS} \simeq 5.4\ 10^{-3}\ mm^3 \quad V_{He} \simeq 4.2\ mm^3$$

Under the best conditions, 500 bubbles are generated in one second. The helium volume initially included in the bubbles is 2.1 cm^3, between 12% and 20% of the helium injected. The soap volume included in the bubbles is 2.7 mm^3 therefore, only 4% of the soap injected.

In the previous section it was shown that the bubble cloud obtained after 4 seconds of generation from one head contains between 1000 and 1500 bubbles and that the one obtained in the same time with 4 bubble generators contains between 2000 and 3000 bubbles. In the one generator case, between 50 and 75% of the bubbles have survived and they contain between 6 and 15% of the helium and between 2 and 3% of the soap injected. In the four generator case only 3 to 7.5% of the helium and 1 to 1.5% of the soap are in fact included in the bubbles. In the calculation of the mean properties of the medium on the test section, it will thereore be assumed that all these components helium, bubble film solution and nitrogen are mixed with the air over a length L_{mix} of the test section.

3.3. Mean acoustical properties of the scattering medium

A linear relation for the calculation of the speed of sound of a mixture of air and small amounts of helium and nitrogen is derived in Appendix B. For a volume concentration C_{He} of helium and C_{N_2} of nitrogen mixed in air, the speed of sound of the mixture a_{mix} is given by the formula:

$$\frac{a_{mixt}}{a_{air}} \simeq 1 + 0.488\ C_{He} + 0.017\ C_{N_2} \qquad (3.1)$$

The density is given by:

$$\frac{\rho_{mixt}}{\rho_{air}} \simeq 1 - 0.862\ C_{He} - 0.034\ C_{N_2} \qquad (3.2)$$

and the acoustic impedance $(\rho a)_{mix}$ is

$$\frac{(\rho a)_{mixt}}{(\rho a)_{air}} \simeq 1 - 0.374\ C_{He} - 0.017\ C_{N_2}. \qquad (3.3)$$

The above relations are applicable locally in the mixture and for the average value of the concentration in the mixing volume. However, the concentation profiles in the mixing volume are not measured: within the recirculation eddy, the concentrations are probably maximum and constant and they are expected to decrease linearly beyond the eddy. As a simplification, a constant concentration profile is assumed throughout the mixing volume V_{mixt} of length L_{mixt}, then the concentrations are:

$$C_{He} = \frac{n\ \dot{V}_{He} t_{He}}{V_{mixt}} \qquad (3.4)$$

$$C_{N_2} = \frac{n\ \dot{V}_{N_2} t_{N_2}}{V_{mixt}} \qquad (3.5)$$

and $V_{mixt} = S\ L_{mixt}$ where S is the cross sectional area of the test section, t_{He} and t_{N_2} are the flow time of helium and nitrogen respectively and n is the number of generators used.

3.4. Experimental results

The average speed of sound over the densest part of the bubble cloud is calculated for every shock by measuring independently the shock wave velocity and its Mach number (§ 5.6). Taking, as a simplification that value as the average speed of sound throughout the mixing volume makes it possible to estimate the average concentations C_{He} and C_{N_2} , the mixing length L_{mixt} and the mean acoustical impedance $(\rho a)_{mixt}$. With $S = 89\ cm^2$, $\dot{V}_{He} = 14\ cm^3/s$, $\dot{V}_{N_2} = 87\ cm^3/s$,

$$\frac{\Delta a}{a_{air}} = \frac{a_{mixt} - a_{air}}{a_{air}} \simeq \frac{0.09 n t_{He}}{L_{mixt}} + \frac{.02\ n t_{N_2}}{L_{mixt}}. \tag{3.6}$$

The flow of nitrogen was usually started 1 second early in order to clear the bubble generator of any excess soap which creates too heavy bubbles in the initial instant of bubble flow ($t_{N_2} = t_{He} + 1$).

The speed of sound measurements, averaged over many shocks of various Mach number and for different values of t_{He} and n lead to a value of 80 cm for the length of the mixing volume. Table 3.1 gives the speed of sound change $\frac{\Delta a}{a}$, the concentrations C_{He} and C_{N_2}, the density and acoustic impedance changes $\frac{\Delta \rho}{\rho}$ and $\frac{\Delta \rho a}{\rho a}$ for the configurations commonly used: 4 bubble generators operating during 4s or 2s or 1 bubble generator operating for 4s.

For the more frequent configuration where 4 generators are operated for 4 seconds, we calculate that the medium has a slightly higher speed of sound +2%, a lower density -3.65%, and lower acoustical impedance, -1.65%. The gas mixture in the test section therefore weakens slightly the incident shock wave and a very

Table 3.1. Modifications of the properties of the mixture

n	t	C_{He}	C_{N_2}	$\frac{\Delta a}{a}$	$\frac{\Delta \rho}{\rho}$	$\frac{\Delta \rho a}{\rho a}$
4	4	0.0315	0.244	0.0197	-0.0365	-0.0165
4	2	0.0157	0.147	0.0103	-0.0185	-0.0082
1	4	0.0078	0.061	0.0049	-0.0088	-0.0039

weak expansion wave is reflected upstream. For very weak shock waves, where the acoustical approximation can be used, the pressure jump decrease is just 1.65% when measured at the side wall of the shock tube, and 3.3% when measured at the end plate. In fact, these changes are difficult to detect on the traces obtained from the pressure transducers in the measurements done with and without the gas mixture in the test section.

3.5. Effect of the bubble-film solution

Most of the bubble film solution injected doesn't belong to the bubbles surviving at the time of the interaction. About 20% of the bubbles produced are too heavy and drop on the lower wall of the test section. A significant proportion of the soap injected is spattered as small droplets and either impacts on the walls near the instrument plate, where the bubbles are generated or is kept suspended in the test section in the form of fog. One possible reason for which the bubbles become heavier and eventually drop on the base plate is that they could be collecting the fog droplets. Assuming, for the the moment, that the bubble film solution is very finely dispersed in the test section over a length of 80 cm, its volume concentration C_{BFS} would be 0.016% and mass fraction α_{BFS} 11%. This would decrease the mean speed of sound by 11% (from 345 to 306 m/s at 25° C) and contribute to an increased thickness of the shock wave. While this is clearly a worst case situation, since most of the soap injected is deposited on the walls, the remaining is contained in the film and in larger droplets and a fraction could have evaporated, there is a possibility of an important decrease of the speed of sound. However, the experiments indicate that this is not the case (§ 6.2.4.3 and § 6.2.6).

3.6. Transversal effects

The bubbles are initially neutrally buoyant but they probably grow heavier by accumulating fog particles and they should have a tendency to fall down in the test section. The large amount of helium present in the shock tube could create a vertical concentration gradient since it is lighter than air. However, all indications are (§ 3.7.1) that the violent mixing caused by the strong nitrogen jets is able to keep the concentration constant.

3.7. Experimental verification

3.7.1. *Helium and nitrogen jets.*

Shock wave tilt is a very sensitive indicator of sound speed gradients. In the actual experiment of the interaction of a shock wave with the bubble array, it was observed that the shock front is not significantly tilted which indicates that any vertical speed of sound or concentration gradient must be very small. To check that some of the shock wave pressure profile disturbances are caused by discrete scattering from the bubbles, a mixture of helium and nitrogen was injected without flow of bubble film solution in the generator. Most of the incident or reflected shock shadowgraphs show no tilt indicating again that there is no significant speed of sound gradient. The pressure profiles are slightly modified but much less so than with soap bubbles present. With only the (weaker) helium jets turned on, a significant vertical speed of sound gradient was observed because in the absence of the turbulent nitrogen jets, the helium rises to the top.

3.7.2. ***Nitrogen bubbles.*** The liquid phase, in the form of the bubble film solution, can in principle cause some disturbance on the shock wave. In order to estimate the effect of the bubble film solution on the shock wave, nitrogen bubbles are injected in the test section with the same component flow rate on the bubble generators. The pressure profiles are undisturbed: the rise time is still less than 1 μs which is the resolution of the transducer, but the incident and reflected wave look straight but slightly thicker on the shadowgraphs. The detailed results are reported in § 6.2.4.

Chapter 4

THEORETICAL PREDICTION OF THE MULTIPLE SCATTERING

4.1. Introduction

The interaction of a shock wave with a single helium-filled soap bubble is described in Chapter 13. The wave pattern is discussed in Chapter 7 in the acoustical case and in Chapter 9 for the two-dimensional interaction. Therefore only the outline of the physical process is given here.

When the incident shock wave of Mach number M_s intercepts a bubble, two waves are generated: a reflected shock followed by an expansion, with an approximately spherical front propagating upstream, and a transmitted wave, also approximately spherical, initially inside the bubble, later propagating downstream of the bubble with a Mach number M_T. The incident wave diffracts around the bubble and eventually catches up with the weaker spherical transmitted wave. The space downstream of the bubble within which the diffracted wave is still behind the transmitted wave can be called the volume of influence of the bubble on the shock wave. An ideal point pressure transducer with infinite time resolution would detect both downstream waves if it is located within the volume of influence and only a single one if it is located outside.

If the bubble cloud is not dense enough, such that the volume of influence of any bubble does not contain any other bubble downstream, which means that the volumes of influence do not overlap, the shock only experiences a succession of independent, similar interactions and the ideal pressure transducer can only record either an unperturbed shock or the shock perturbed by only one scatterer, depending on its position relative to the closest bubble. If the bubble cloud is dense enough, such that the average volume of free space available per bubble is smaller than the volume of influence, the shock wave will propagate through one or several other bubbles before the perturbation created upstream disappears. In that case, the shock is subjected to multiple scattering and a significant modification of the pressure profile should be recorded by a pressure transducer at any position in the scattering cloud.

4.2. Estimation of the volume of influence

The surface which limits the volume of influence is generated by the locus of the points where the expanding transmitted wave intersects the incident wave. These points are located on a circle, thus the limiting surface describes a body of revolution whose axis lies on the bubble diameter perpendicular to the unperturbed shock front. The model developed here applies in the case of weak incident shock waves, where the strongest scattering can be observed experimentally. The wave pattern can be seen easily on the shadowgraph sequence obtained from the interaction of a stronger shock (M_s = 1.25) with a large helium-filled soap bubble (figure 13.1, frames 50 μs to 169 μs) but the calculation relies for the most part on the results of acoustics. The model uses several approximations:

i. The incident wave is weak, i.e., $m = M_s^2 - 1 << 1$ and when diffracting around the bubble is unperturbed outside of the bubble by the reflected wave;

ii. The transmitted wave, when it just appears downstream of the bubble, is weaker than the incident one. Measurements on the large bubble gave this approximate relation

$$M_T - 1 = 0.25\ (M_s - 1) \tag{4.1}$$

Furthermore its strength decreases as the inverse of its distance from the bubble. To a first approximation in m, it was found that it could be considered exactly sonic everywhere;

iii. The transmitted wave front is considered here to be exactly spherical.

The spherical scatterer of acoustical index of refraction n (ratio of the speed of sound outside and inside) and radius r is taken to be a lens of focal length

$$f = -1/2 \frac{n\,r}{1-n} \tag{4.2}$$

which is exact for paraxial rays.

For a negative lens such as a helium sphere in air,

$$n = \frac{344}{1010} = 0.34 \quad , \quad f = -0.257r$$

Therefore, the center of the transmitted wave is located upstream of the bubble center at a distance equal to one quarter of the radius of the bubble.

At the time t = 0, chosen when the transmitted wave first appears outside of the bubble, the plane of the incident wave intersects the longitudinal bubble axis at a distance

$$l = -r \left[1 - 2\,\frac{V_s}{V_R} \right] \tag{4.3}$$

from the bubble center where V_R and V_s are the velocities of the refracted and incident wave respectively . For weak waves $l \simeq -r(1-2n)$. For helium, n =0.34 and $l \simeq -0.32r$. This configuration is illustrated in figure 4.1.

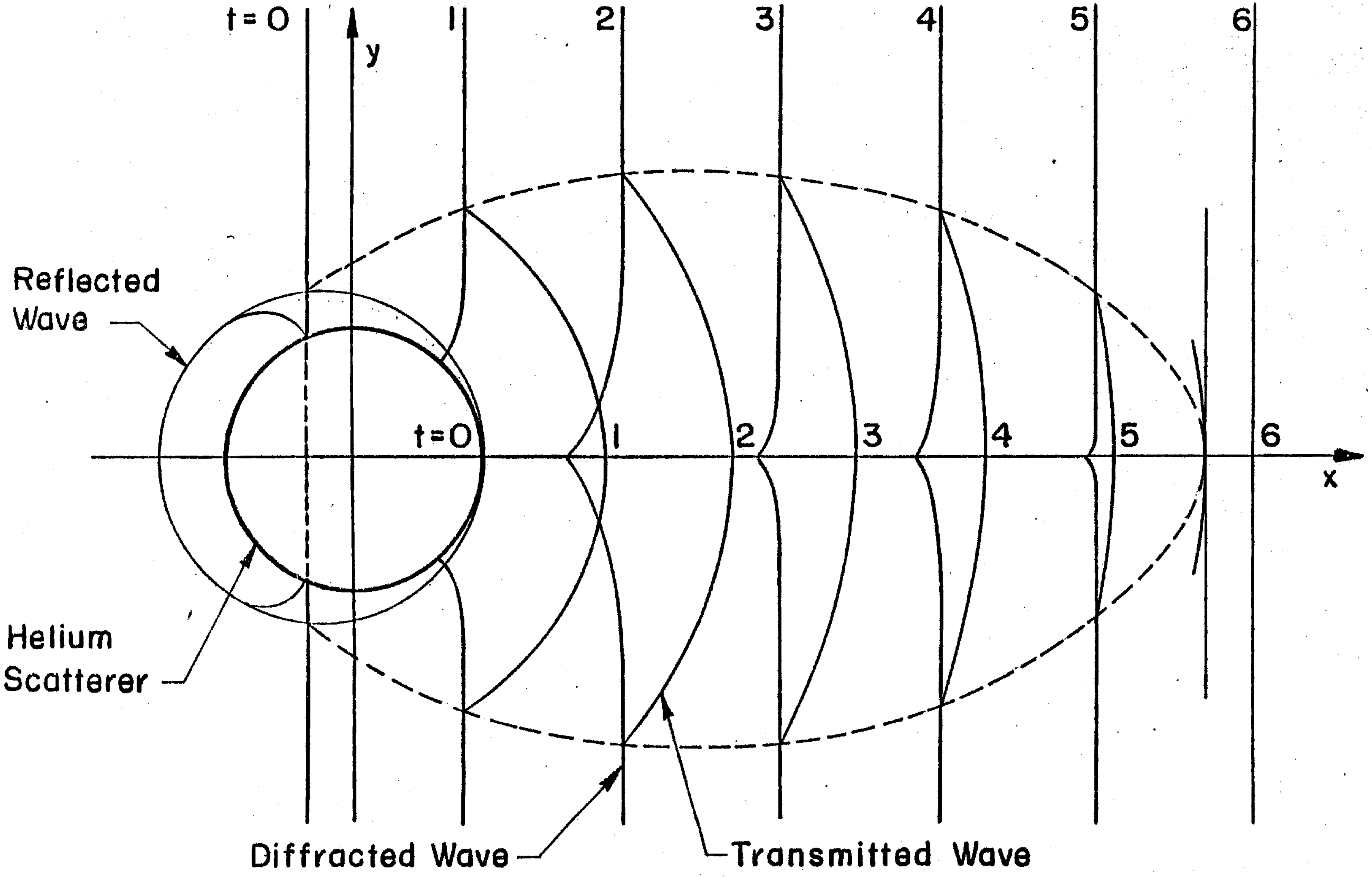

FIGURE 4.1 Schematic Transmitted and Diffracted Waves behind the Helium Scatterer

In the cylindrical coordinate system formed by the longitudinal bubble axis Ox and the perpendicular diametral axis Oy, the incident shock wave position is given by:

$$x_s = M_s\, a\, t - r(1 - 2n) \quad where \quad M_s \simeq 1 + \frac{m}{2} \tag{4.4}$$

and the transmitted shock wave by

$$\left[\left(x_T + \frac{1}{2}\frac{n}{1-n} r \right)^2 + (y_T)^2 \right]^{1/2} = a\, t + r\left(1 + \frac{1}{2}\frac{n}{1-n}\right) \quad \text{for } t \geq 0. \tag{4.5}$$

After eliminating the time between the two equations, the equation describing the limiting surface of the volume of influence is

$$\left(\frac{y}{r}\right)^2 = -m\left(\frac{x}{r}\right)^2 + 4(1-n)\left(\frac{x}{r}\right) + 4n^2 - 6n + 4 \tag{4.6}$$

where $m << 1$. This is the equation of a closed surface of revolution of length,

$$\left[\frac{x_{\max}}{r}\right] \simeq \frac{4(1-n)}{m}\ ; \tag{4.7}$$

of maximum radius,

$$\left[\frac{y_{\max}}{r}\right] \simeq \frac{2(1-n)}{m^{1/2}} \quad \text{at} \quad \left(\frac{x}{r}\right) \simeq \frac{2(1-n)}{m} \tag{4.8}$$

and of internal volume,

$$\frac{V_i}{r^3} \simeq \frac{32\pi}{3} \frac{(1-n)^3}{m^2} \simeq 33.5 \frac{(1-n)^3}{m^2}. \qquad (4.9)$$

The scattering efficiency of any interaction of a weak shock wave with a discrete array of negative acoustical lenses can be defined as the number of scatterers N_s within the volume of influence V_i in terms of the shock parameter m and the scattering medim parameters: n index of refraction, r scatterer radius, and N the number of scatterers per unit volume.

$$N_s = N\ V_i \simeq 33.5\ N\ \frac{(1-n)^3 r^3}{m^2} \qquad (4.10)$$

When N_s is of the order of 10 or 100, some strong scattering is expected; when N_s is of the order of unity, only weak scattering should be observed; when N_s is of the order 1/10, no scattering is expected except in the immediate vicinity of the scatterer.

4.3. Application to the helium scatterers

With n =0.34 and r = 1 mm the dimensions of the volume of influence are:

$$\textit{Length}: \ \frac{2.64}{m} \text{ mm}$$

$$\textit{Maximum diameter}: \ \frac{2.64}{\sqrt{m}} \text{ mm}$$

$$\textit{Volume}: \ \frac{9.63}{m^2} \text{ mm}^3.$$

Table 4.1 gives the length, width and volume of the volume of influence for various values of the shock Mach number.

Table 4.1. Volumes of influence for various incident shock waves

M_s	1.005	1.007	1.01	1.02	1.03	1.04	1.05	1.07	1.15
Length (mm)	264	188	132	65	43	32	26	18	8
Width (mm)	26.4	22.3	18.6	13.2	10.7	9.2	8.2	6.9	4.6
Volume (cm^3)	96	49	24	5.9	2.6	1.44	0.92	0.46	0.09

With a mean volume available per bubble of the order of 1 cm^3, strong multiple scattering occurs up to Mach 1.02, weak multiple scattering from 1.02 to 1.04, and only single scattering above 1.04. Some of the volumes of influence are sketched in figure 4.2.

4.4. Instrumental limitation

Since both the spark gap shadowgraph and the pressure transducers have a time resolution of 1 μs, corresponding to a spatial resolution of .4 mm, the practical volume of influence is defined as the volume within which the shock wave thickness is more than .4 mm and the shock wave rise time more than 1 μs.

On the longitudinal axis, the maximum time delay between the transmitted wave and the unperturbed incident wave is

$$\Delta t_0 = 2r\left[\frac{1}{a_{air}} - \frac{1}{a_{He}}\right] \tag{4.11}$$

Δt decreases linearly from Δt_0 near the bubble to 0 at $x_{\max}$, the end of the volume of influence. With a response time of τ, a time delay between the two

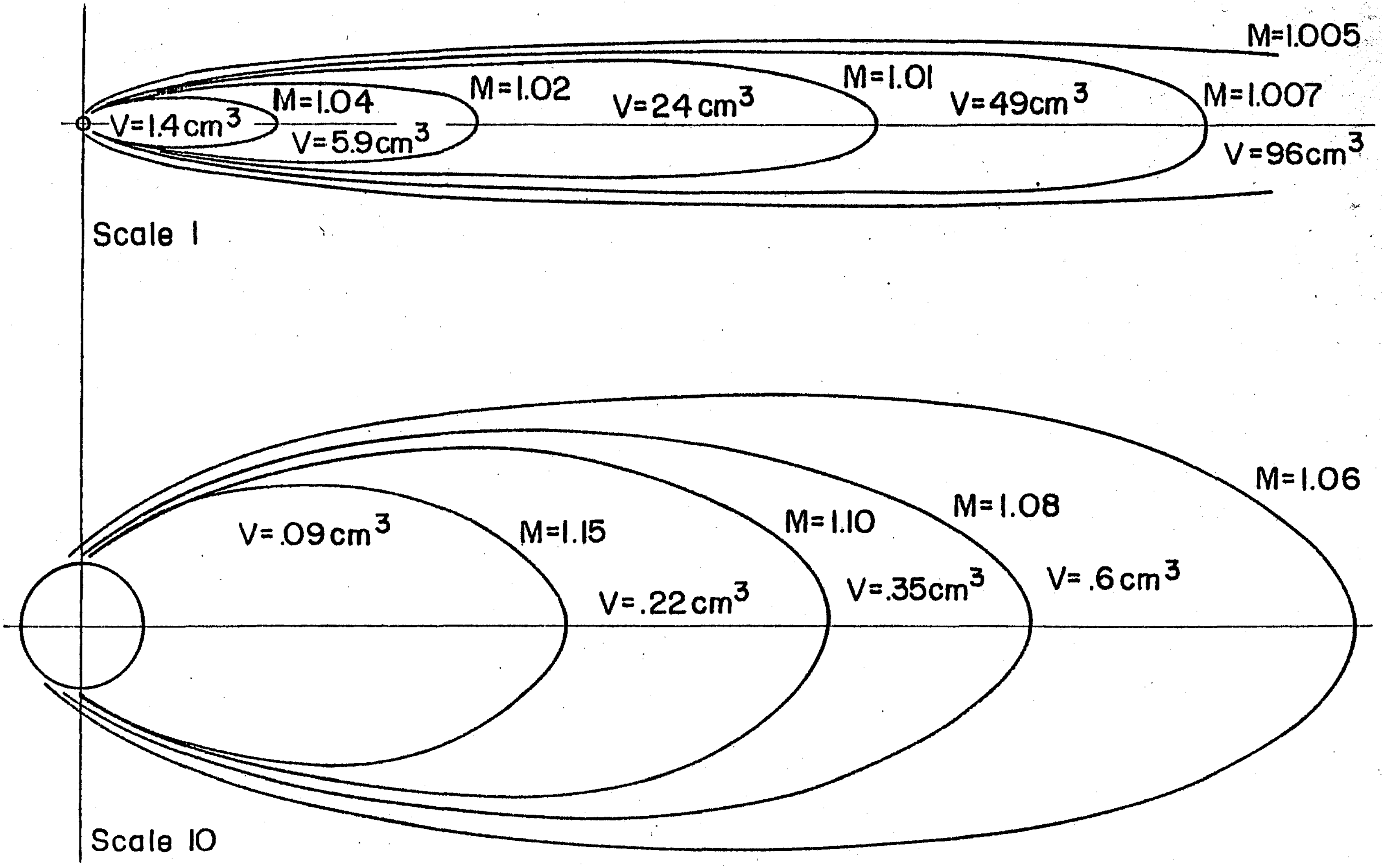

FIGURE 4.2 Volumes of Influence for Various Incident Shock Waves

waves equal to τ will be measured at a distance x_{prac}

$$x_{prac} = x_{\max} \frac{\Delta t_0 - \tau}{\Delta t_0}. \tag{4.12}$$

For the helium scatterer of radius 1 mm, $\Delta t_0 = 3.8 \mu s$ and for $\tau = 1$ μs, $x_{prac} = .74\, x_{max}$. Hence the practical volume of influence is defined by: its length, $1.95/m$; its width, $1.95/m^{1/2}$; and its volume, $3.9/m^2$, which is 40% of the previous value.

4.5. Expected modifications of the pressure profiles

Some pressure profiles were recorded at various distances behind a large helium filled soap bubble (§ 13.5). A more systematic survey was done in the case of helium cylinders (§ 11.2.1). These profiles show the weak transmitted shock followed by a peak due to the diffracted wave. This model assumes that at some distance from the bubble the diffracted shock has become plane again, thus would be recorded as a second steep front on the profile, preceded by the very weak transmitted shock at most 3.8 μs earlier. This is called a precursor. This experiment should show how the size of the precursor increases as more individual precursors are combined by the multiple scattering process. The steep shock front is expected to be modified by its downstream or low pressure side in this type of discrete scattering experiment with diverging acoustical lenses. A precursor is shown in the profile obtained for an incident shock Mach number of 1.05 in figure 13.10.

Chapter 5

EXPERIMENTAL PROCEDURE

5.1. Shock tube

The square test section has been designed to facilitate the injection of the helium soap bubbles, to use flow visualization and to provide a simple disconnecting system for cleaning purposes (§ 2.2). In this experiment the incident wave Mach number ranges from 1.004 to 1.36.

The shock tube was always used with air at one atmosphere in the test section and a mixture of air and nitrogen in the driver. The driver initially contains air at one atmosphere and is pressurized by nitrogen from cylinders. The basic shock tube is described by Smith et al. (1967). It contains no mechanism for automatic diaphragm bursting; however after increasing the flow capacity of the nitrogen supply line, the shock wave could be produced within a fraction of a second by opening a control valve on that line with a TTL signal from the bubble flow control box. This accuracy was sufficient because the time scale involved with the bubble cloud generation is on the order of a few seconds. The diaphragm used for various wave strengths are given in table 5.1.

Table 5.1. Shock tube diaphragms (thickness in μm)

Mach #	1.35	1.20	1.15	1.10	1.07	1.05	1.02
Diaphragm Thickness	Al 305	Al 152	Mylar 51	Al 38	Mylar 6	Al 25	Paper 50

Aluminum diaphragms did break at the same pressure difference $P_4 - P_1$ for a given thickness. The mylar diaphragms were not as consistent. In an attempt to obtain very weak waves $M_s < 1.04$, various papers were tried as diaphragms: wax paper gave shock waves of Mach 1.03; lightweight paper (airmail type) from foreign newspapers like 'Le Monde'' and 'Ha Aretz'' gave Mach 1.02 and the same papers heated for 15 min at 200° C provided diaphragms for the weakest shock between 1.004 and 1.01. The Israeli newsprint 'Ha Aretz'', more consistent in its performance, was the final choice.

5.2. Pressure transducers

The square test section has an instrument port on the upper horizontal wall between the two windows. The piezoelectric transducer mounted there was used as a triggering signal for the control circuitry of the flow visualization system and pressure trace recording oscilloscopes. A high sensitivity was needed to detect the weakest waves and the rise time and vibration characteristics were less important. A Kistler K-606 with the charge amplifier set at the sensitivity of 100 mV/psi was chosen for the weakest wave; otherwise a PCB-112 A21 of sensitivity 45.6 mV/psi was in place. The test section end wall or the movable instrument plate were equipped with one or two pressure transducers, PCB-113 A21 of lower sensitivity (17.4 and 23.2 mV/psi) and shorter response time (1 μs) in order to record the pressure rise from P_1 to P_5, the value behind the reflected shock wave, which was used to calculate the shock Mach number.

The travel time of the shock wave between the side wall transducer (# 1) and the end wall transducers (#2 and #3) was also recorded on a Hewlett Packard counter 5326 B in order to calculate the shock velocity. The distance was 422 mm when the real end plate was used in conjunction with a single bubble generator or in the range 200 - 300 mm when the movable instrument plate was in use, with four bubble generators mounted on it. The pressure traces were obtained on one or two oscilloscopes, Hewlett Packard 1741 A, operated in the delayed sweep mode at 5 μs/div and triggered by the transducer #1. The pressure traces were recorded on Polaroid film type 667.

5.3. Shadowgraph

A simple shadowgraph system was assembled using a locally-built point source spark gap of standardized design based on the Condensor Product Corp. EC 104 10'M capacitor (10 kV . 1 μF). It was used at 2 kV. The duration of the spark is estimated to be 1 μs.

A spherical mirror with a 20 cm diameter and a 147.3 cm focal length collimated the light from the spark gap into a parallel beam which after reflection on a flat mirror was perpendicular to the test section windows. The light illuminated the film, Polaroid type 667, 3000 ASA, located 25 cm away from the shock tube window. The spark gap condenser was discharged by a high voltage trigger pulse, generated with a variable time delay after the signal from transducer #1. The minimum delay was 70 μs and it could be increased with the delayed sweep capability of a Hewlett Packard 1340 oscilloscope externally triggered by the transducer #1 signal.

5.4. Control electronics

5.4.1. *Bubble flow control.* The control electronics performed two functions; to control of the duration of flow of nitrogen, bubble film solution and helium, and to trigger the shock wave. In one approach the duration of the flow of bubble fluid is directly controlled by the electronics. In the other approach the bubble control box sends a signal to the electronics controlling the flow of gas to the shock tube driver section which triggers the shock wave and the arrival of the shock wave at the location of transducer #1 generates the signal which stops both the bubble flow and the driver gas flow. The second method was normally used. In both cases the bubble flow time is recorded by a counter built in the control box and the bubble flow is still on when the interaction takes place. Nevertheless, the bubble motion can still be considered frozen in the time scale of the shock wave propagation.

5.4.2. *Driver gas control.* The driver gas valve was controlled via a solid state relay, either directly by the operator, or by an external TTL signal from the bubble flow control box. The driver gas valve is turned off by the TTL signal from the transducer #1 via a voltage comparator. The same signal controls the rest of the instrumentation.

5.5. Sequence of events in the experiment

1) The flow of nitrogen in the bubble head is initiated by a switch on the bubble flow control box. About one second later the helium and bubble film solution start flowing and the bubbles are injected in the test section.

2) After a variable delay set beforehand (2 - 5 s), the driver gas valve is turned on and the pressure in the shock tube driver increases from P_1 to P_4 in about 1 second. When the diaphragm breaks, a shock wave is formed and propagates in the test section.

3) When the shock wave passes the first transducer, a TTL pulse is created which turns off the bubble flow: the bubble flow duration is displayed on the bubble flow control box. The same TTL pulse starts the delay circuitry of the two oscilloscopes and the two timers.

4) After a time delay t_S set on one oscilloscope and measured on one counter, the spark gap is discharged and the shadowgraph is recorded (before the run, the room lights are turned off and the shutter in front of the film holder is opened).

5) After a different time delay t_D, the delayed sweep in the storage oscilloscope is triggered and the pressure trace from the end plate transducer is recorded. When two end plate transducers are used, the same sequence applies for the two storage oscilloscopes with the same delay t_D. The delay t_D is measured by another counter. The instrumental set-up is illustrated in figure 5.1.

5.6. Measured data

In each run the following time delays are directly measured: t_B : bubble flow duration, t_S : spark gap discharge delay, t_D : delay before sweep of the storage oscilloscope. From the recorded pressure trace of the end plate transducer the time delay t_P before the pressure rise, the rise time t_R, and the value $P_5 - P_1$ are obtained. The shock wave Mach number M_s is calculated from the value of P_5 / P_1. The travel time of the shock between the transducers #1 and #2 is $t_{21} = t_D + t_P$ and the shock velocity is obtained from the distance d_{21} between the two transducers:

$$V_s = d_{21}/t_{21} \ . \tag{5.1}$$

The ratio V_s/M_s gives the average speed of sound a_{mixt} in the shock tube between the two transducers from which the concentration of Helium C_{He} and length of mixing zone L_{mixt} are calculated.

Since the time delay t_{21} includes some delays due to the circuitry, an effective distance d_{21} has been measured for each shock wave strength and after each change of position of the end plate. It is obtained with a calibration run: where a shock is generated in air without any bubble components injected. From that run, M_s is obtained from $P_5 - P_1$, t_{21} is measured and the distance obtained from the formula

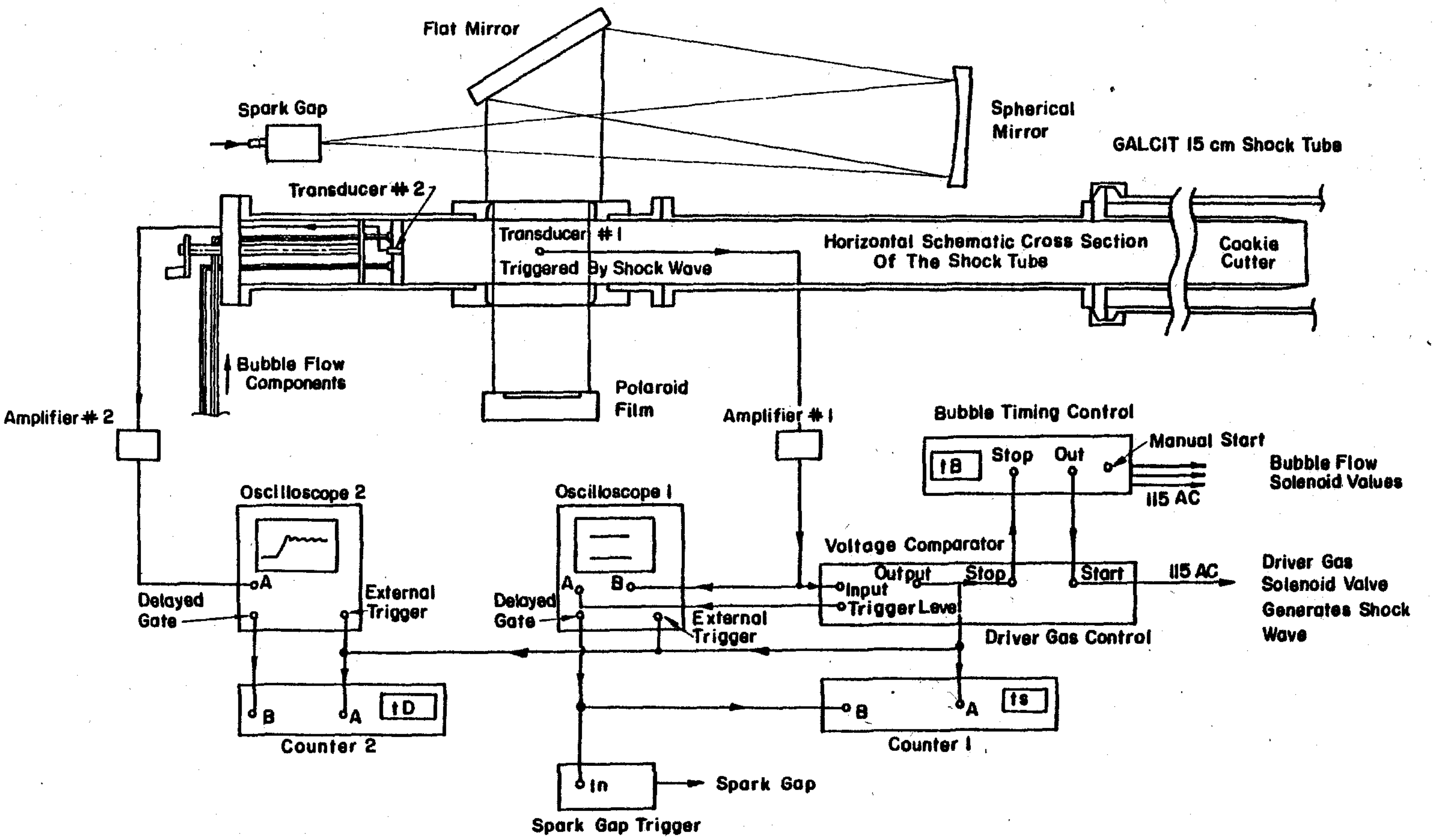

FIGURE 5.1 Diagram of the Instrumentation

$$d_{21} = M_s \, a \, t_{21} \tag{5.2}$$

The same value of d_{21} is then used for all the runs made at this configuration.

Chapter 6

EXPERIMENTAL RESULTS

6.1. Outline of the experiments

A criterion for strong or weak scattering has been derived in Chapter 4. The range of shock strengths and bubble concentration covered by this experiment is such both phenomena are observed.

The experiments were carried out in two phases: In the first one, only one bubble generator was used to create the array of scatterers and the shock wave strength ranged from $M_s = 1.02$ to $M_s = 1.35$. The bubble cloud concentration observed was relatively low. With the instrument end plate located 300 mm downstream of the axis of the shock tube windows, the shadowgraph covered a volume of 610 cm^3 in which typically 150 to 200 bubbles could be counted. This corresponds to a volume per bubble between 3 and 4 cm^3. For the weakest shock, $M_s = 1.02$, the scatterer volume of influence is 5.9 cm^3 (section 4.3), which means that on the average, the shock front, locally deformed by one scatterer, would be further perturbed by another scatterer before it could be restored to its unperturbed shape by the nonlinear effects inherent to shock wave propagation. Therefore, at best, partial shock wave scattering could be measured.

The goal of the second phase of the experiment was specifically to obtain more extensive scattering of the shock wave by increasing the concentration of the scatterer array and by triggering still weaker shocks. The denser bubble cloud was obtained with 4 bubble generators and with the instrument plate located 200 mm downstream of the axis of the windows, between 300 and 500 bubbles could be counted on the shadowgraph prints corresponding to a mean volume available per scatterer, betweeen 1.2 and 2 cm^3. As the use of specially cured paper diaphragms allowed a decrease of the minimum shock Mach number to 1.005 for a scatterer volume of influence of 100 cm^3, a rather strong scattering of the shock wave could clearly be expected and was in fact observed.

For the cases involving strong scattering of the shock wave, the key experimental evidence is the shape of the end plate pressure trace, particularly the rise time between P_1 and P_5. For stronger waves the emphasis is more on the flow visualization where the local perturbation on the shock wave front is more apparent and the bubble deformation, break up and subsequent gas mixing can be observed.

The results are presented here with the order of increasing shock strength.

6.2. Strong scattering of very weak waves: $M_s \leq 1.01$

6.2.1. *Conditions of the experiment.* The four bubble generators were operating for 2 - 5 s. The diaphragm was made with heat-cured "Ha Aretz" producing shock waves of Mach number between 1.004 and 1.010.

The corresponding volume of influence ranges from 24 to 150 cm^3. As the volume of test section space available per bubble varies between 1.23 and 2.47 cm^3 (between 250 and 500 bubbles are visible in the shadowgraph), the number of bubbles participating in the multiple scattering ranges from 10 to 120. Therefore, both weak and strong multiple scattering can be observed.

The instrument end wall where bubble generators and pressure transducers are located is 200 mm downstream of the window axis, thus the shadowgraph shows a section of the bubble cloud between 150 and 250 mm from the end wall. The high bubble density observed there has been observed to remain constant up to the end wall but decreases significantly upstream of the observation area. While the incident shock wave observed on the shadowgraph has already been perturbed by the less dense cloud upstream, it is assumed that the medium downstream remains identical to the one observed on the shadowgraph as far as its influence on the shock wave is concerned. Close to the end wall much more liquid soap is suspended in the air and the bubbles have a higher velocity but this has little effect on the shock wave scattering.

The pressure trace was recorded usually in the center of the instrument end wall except for one series of runs where one was located in the bottom and the other at the top in order to measure the tilt of the plane of the shock wave front at the end of the test section.

Some measurements of the effects on the shock wave of one or two components of the bubble array: i.e., helium and nitrogen, helium or nitrogen alone, nitrogen and soap, were carried out in order to distinguish them from the effect of the discrete scatterer array.

6.2.2. *Representative pressure data profiles.* Figure 6.3 shows several pressure profiles obtained for initial shock Mach number of 1.01 or less.

Figure 6.3a is an unperturbed pressure trace (#2505) The main features are a steep pressure rise in a time of 1 μs which is the minimum response time of the transducers and the oscillations on the high pressure side due to the ringing of the transducers at the resonance frequency near 400 kHz.

The finer oscillations visible throughout the signal are electronic noise, visible here because of the high amplification of the signal. The pressure profiles of perturbed shocks fall into two categories: the partially scattered waves and the totally scattered waves. These and the unperturbed profile are shown in figure 6.1 to illustrate their differences. Profile 6.1a represents an unperturbed shock

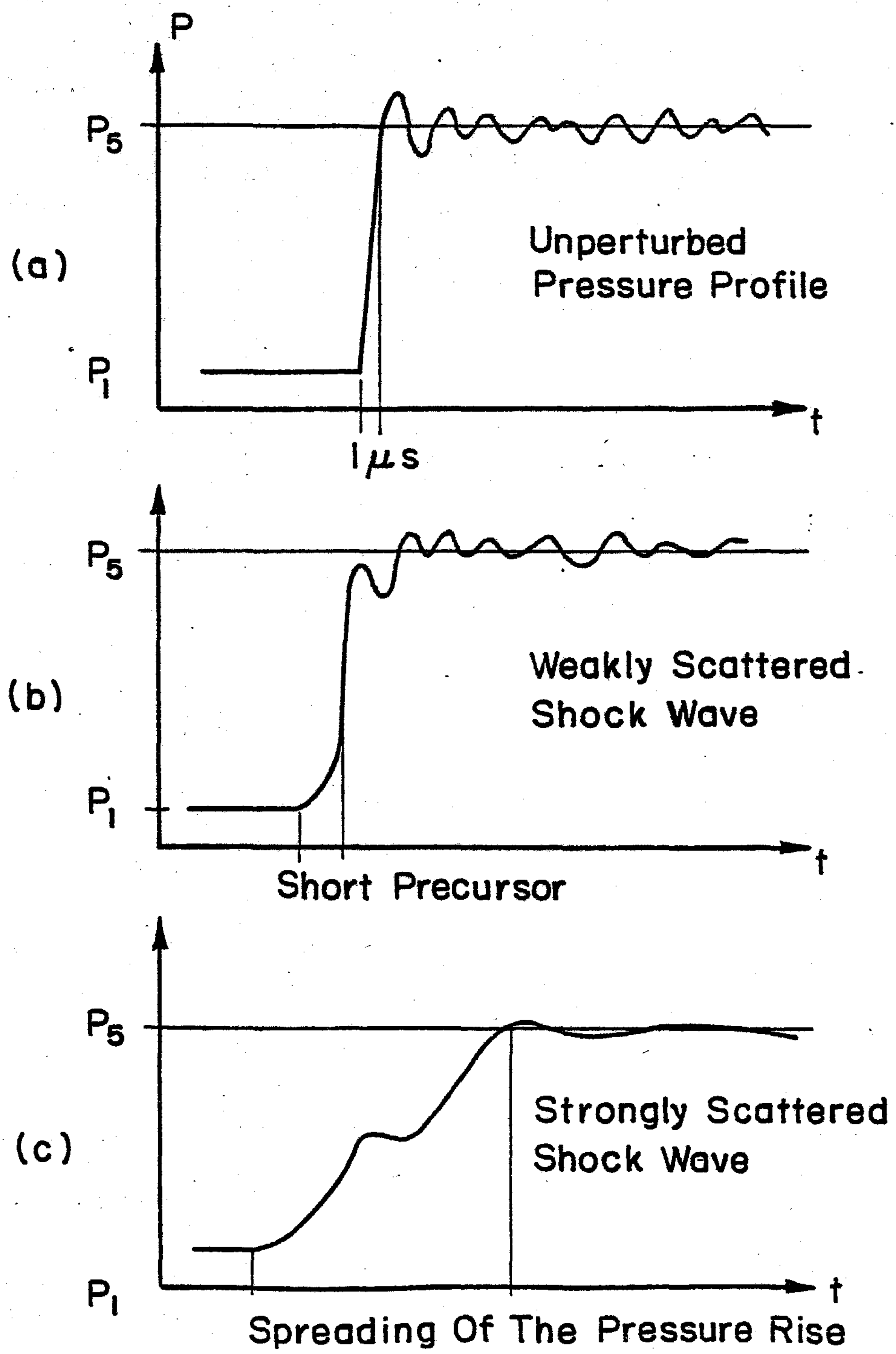

FIGURE 6.1 Schematic Typical Pressure Profiles

with a steep pressure rise and a well marked first peak of the transducer oscillation. Profile 6.1b represents a partially scattered shock with a compression precursor and a decreased first peak of the transducer oscillation. The width of the precursor could be up to 10 μs and its height 50% of the total pressure rise. Profile 6.1c represents a totally scattered shock with the disappearance of the steep pressure rise and of the transducer oscillations, and showing one or several intermediate peaks indicating a possible multiple shock front and a rise time larger than 10 μs.

The histogram in figure 6.2a shows the distribution of the rise time of the precursor among the 21 recorded pressure profiles, recorded for 21 different shocks. The decrease of height of the first peak was observed in all cases of partial scattering. Low frequency pressure fluctuations appeared after the initial rise in most partial scattering cases and all the total scattering cases.

A typical pressure trace characteristic of the weaker partial scattering is given in photograph 6.3b (#2525). The stronger partial scattering case is illustrated in photograph 6.3c (#2509). Finally, examples of pressure profiles from totally scattered shock waves are given in photograph 6.3d (#2522) and 6.3e (#2523).

The compression precursor phenomenon has been introduced above (§ 4.5) with the existence of very weak transmitted waves ahead of the main shock after interaction with a single scatterer. The decrease of height of the first peak in the transducer ringing might correspond to a rounding-off of the top of the pressure rise from a perfect, i.e., non-ringing transducer. The steep shock front would then appear to be destroyed from immediately upstream (precursor) and downstream (rounding-off).

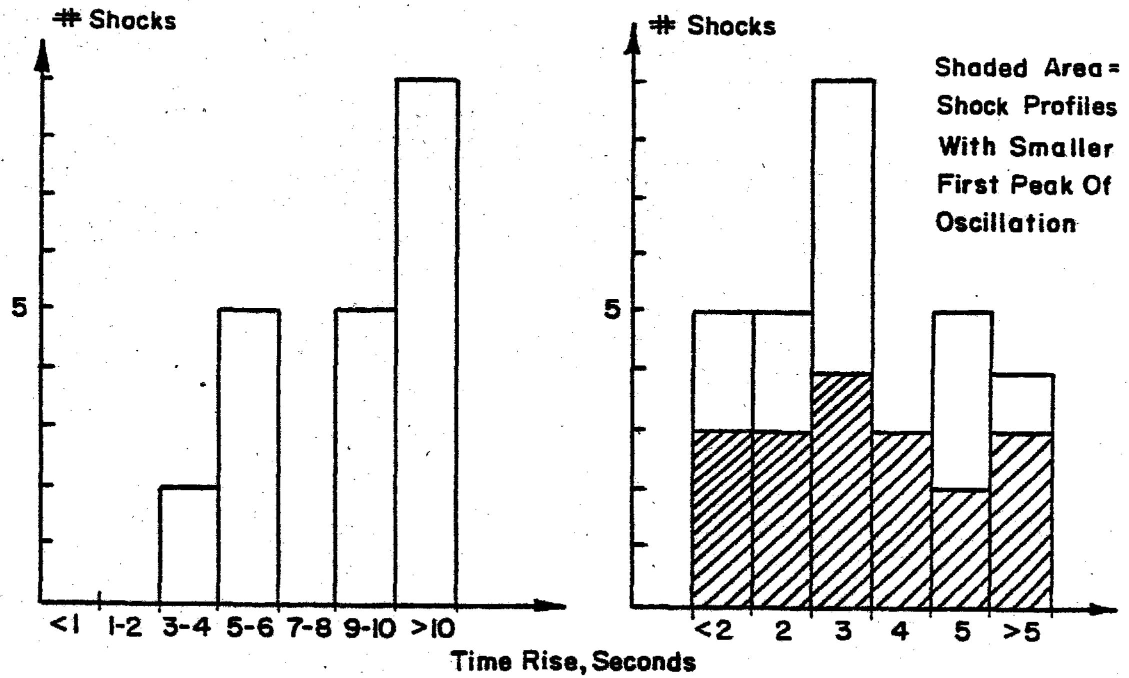

(a.) Very Weak Waves $M_s \leq 1.01$
Dense Cloud

(b.) Weak Waves $M_s \simeq 1.02$
Dense Cloud

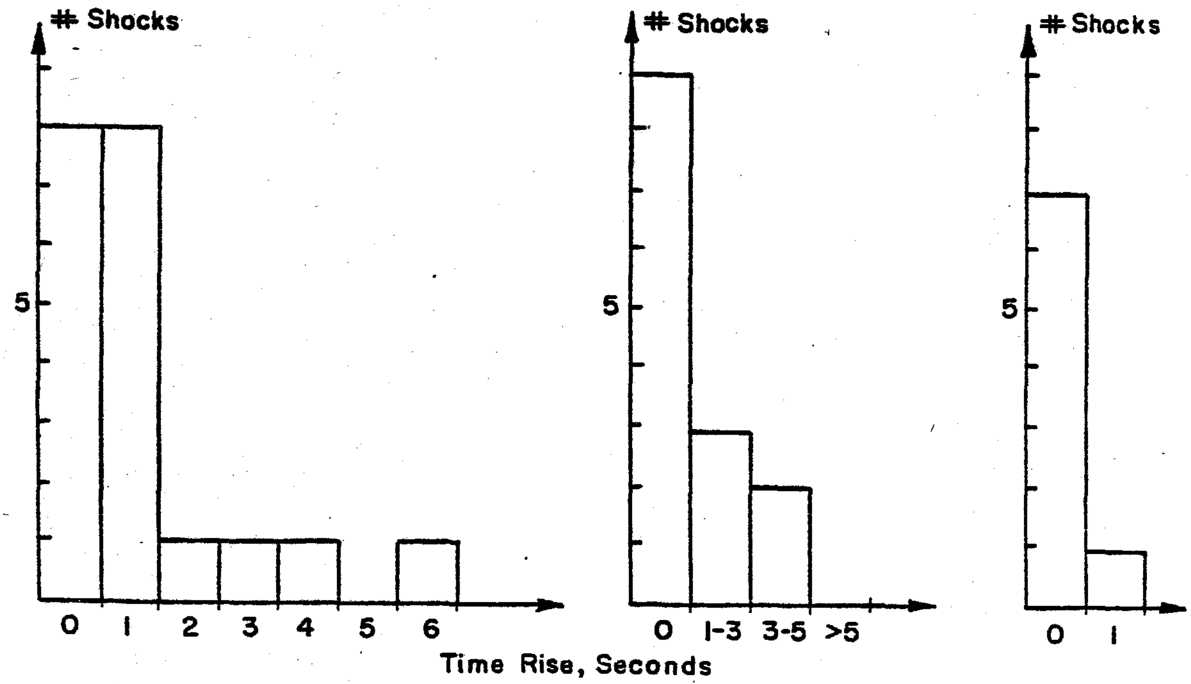

(c.) Weak Waves $M_s \simeq 1.02$
Diluted Cloud

(d.) Weak Waves $M_s \simeq 1.06$
Dense Cloud

(e.) Strong Waves
$M_s = 1.15; 1.36$

FIGURE 6.2 Histograms of Precursor Size

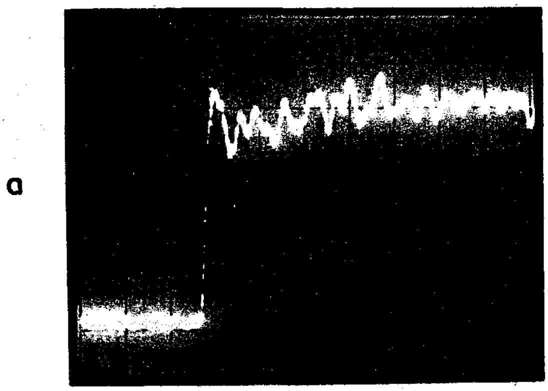

(#2505) No Scattering $M_s = 1.0085$

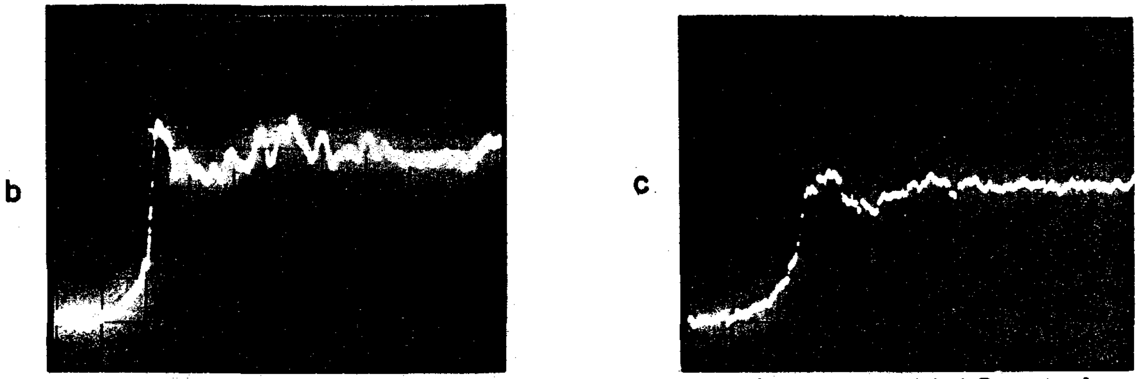

(#2525) Weak Partial Scattering $M_s = 1.007$

(#2509) Strong Partial Scattering $M_s = 1.005$

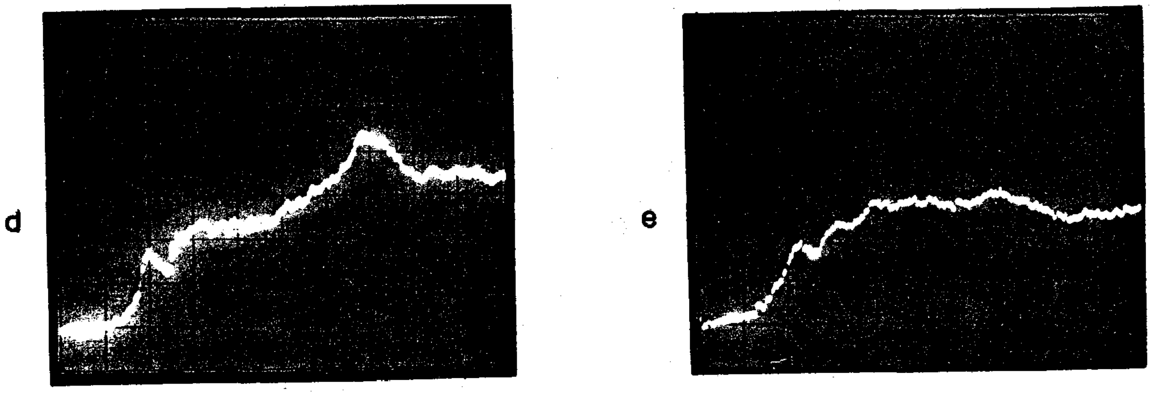

(#2522) Strong Scattering $M_s = 1.007$

(#2523) Strong Scattering $M_s = 1.005$

Horizontal Scale 5μs/div. Vertical Scale 8mbar/div.

FIGURE 6.3 Pressure Profiles of very Weak Incident Waves ($M_s \leq 1.01$)

The existence of a local shock-expansion sequence, often observed in the profile of a totally scattered wave in the form of an intermediate peak after 5 or 10 μs of rise, is unexplained.

6.2.3. *Simultaneous recording of two pressure traces.* These measurements, carried out for 8 shocks, show that the arrival time of the shock wave on the top and bottom transducers in the instrument end wall is very close with a maximum delay of 5 μs. This corresponds to a maximum shift of 1.75 mm for a separation distance of 60 mm for the two transducers. Thus, the maximum tilt from the vertical for the incident shock wave is 1.7° at most. This very small tilt can have both signs: the wave can propagate slightly faster on top or on bottom. Therefore, the assumption that the gases are well mixed by the action of the nitrogen jets is justified (§3.6 and § 3.7).

The pressure profiles from the two locations are slightly different. From the 8 pressure profile pairs observed, 6 indicated that the shock wave was slightly more scattered in the top, with a larger precursor, and a smaller first peak of oscillation. This would indicate a slightly higher bubble concentration on top or a higher concentration of helium even though this is not confirmed by the arrival time data. A typical pair is shown in photograph 6.4a and 6.4b (#2554). Both show evidence of cancellation of the steep pressure front but exhibit differences in shape.

6.2.4. *Control experiments.* In order to ensure that the observed shock wave scattering was only due to the interaction with finite size helium scatterers, three sets of control experiments were carried out: effect of the jets of helium and nitrogen; effect of the helium jets alone; effect of the nitrogen bubbles.

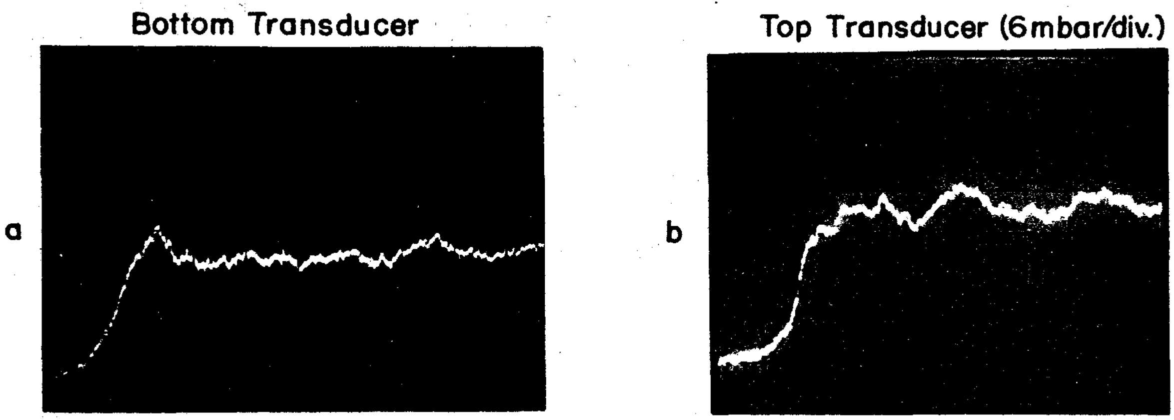

Bottom Transducer

Top Transducer (6mbar/div.)

(# 2554) Simultaneously Recorded Pressure Profiles $M_s = 1.043$

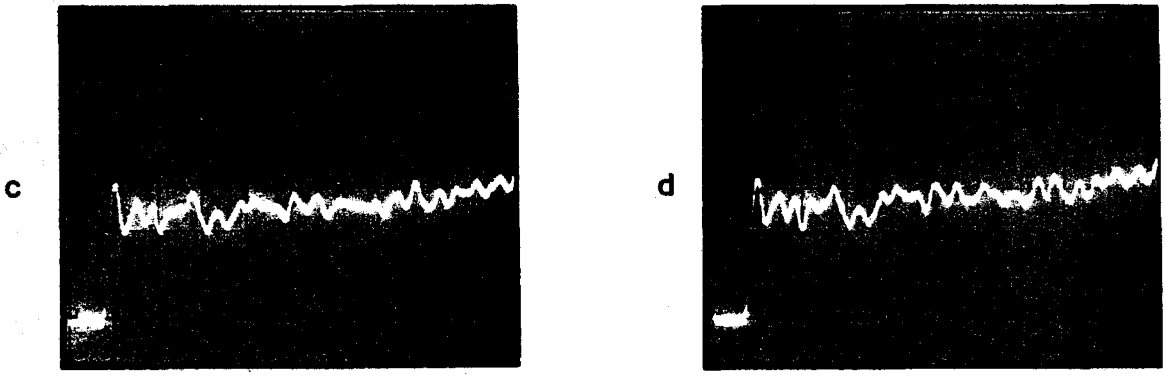

(# 2538) Helium And Nitrogen Jets, $M_s = 1.008$ (# 2539) Helium $M_s = 1.008$

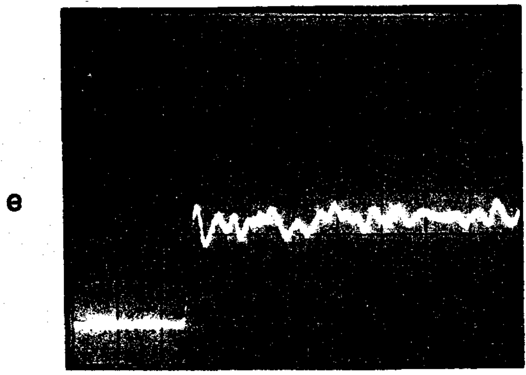

(# 2544) Nitrogen Bubbles, $M_s = 1.0075$

Horizontal Scale 5μs/div. Vertical Scale 8mbar/div.

FIGURE 6.4 Pressure Profiles from the Control Experiments ($M_s \leq 1.01$)

6.2.4.1 *Helium and nitrogen jets.* The bubble generators are used with the soap flow turned off but otherwise at the same flow rate for helium and nitrogen and for the same amount of time as during an actual scattering experiment with bubbles. Because the bubble generation process generates a large amount of helium and an even larger amount of nitrogen, their effect alone on the shock wave has to be measured.

In the five runs made, the pressure profiles were very similar to the undisturbed wave pressure profile, the difference being a small and slow variation of the pressure level behind the shock and in one case a decreased size of the first peak of the oscillation. This shows that the flow field behind the front is not totally uniform. A representative pressure profile is shown in figure 6.4c (#2538). The shadowgraph (figure 6.5d) of the incident and reflected shock waves indicate that the shock front is not exactly plane; it appears thicker at places and, on average, slightly faster on top, indicating a gradient of speed of sound and hence of helium concentration.

6.2.4.2 *Helium jets.* Without the enhancement of the mixing of helium provided by the strong nitrogen jets, most of the helium generated rises to the top of the tube and stays close to the end wall. The shock wave was observed to be more bent than in the helium-nitrogen jets experiment (figure 6.5e), but the pressure trace is very similar (figure 6.4d) (#2539). The helium concentration in the last 20 cm of the test section was also twice as high.

6.2.4.3 *Nitrogen bubbles.* In this experiment the flow of helium in the bubble generator is replaced by a flow of nitrogen at the same rate. Some nitrogen bubbles are produced, though smaller and less numerous than the helium bubbles.

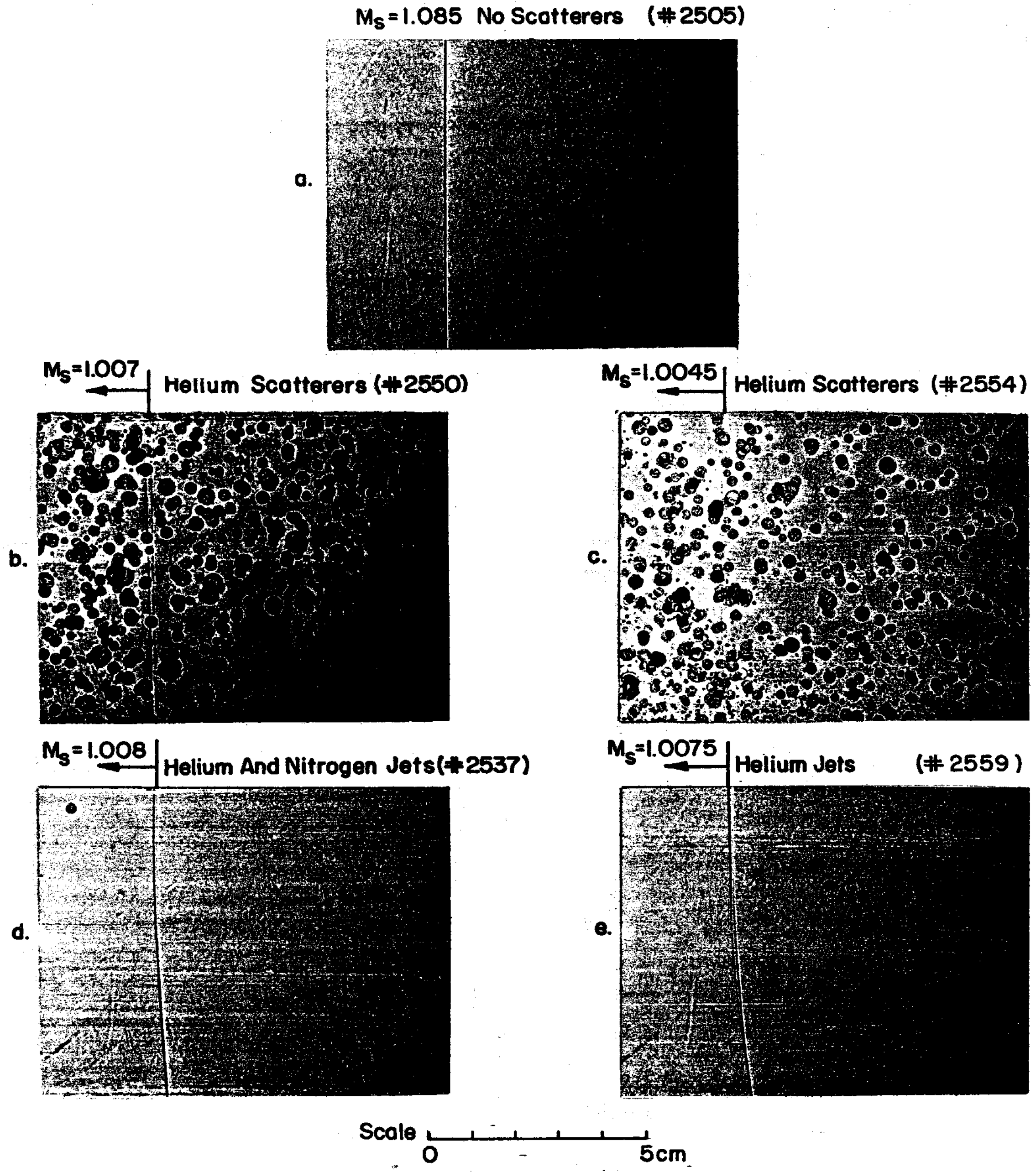

FIGURE 6.5 Shadowgraph Pictures of the Interaction with very Weak Waves

The recorded pressure profile is normal, except for the decreased size of the first oscillation peak and shadowgraphs show an unperturbed incident shock wave and a uniformly thicker reflected wave, but still planar and vertical. A representative pressure profile is shown in photograph 6.4e (#2544). This experiment was made as a check that the liquid phase introduced by the soap doesn't have an effect on the shock wave. The average speed of sound increase over the value for air was found to be less that 1% and this could be caused by the injection of nitrogen alone. The liquid phase does not contribute here to any significant speed of sound decrease (§ 3.5).

6.2.5. *Shadowgraphs ($M_s \leq 1.01$)* .

6.2.5.1 *Incident shock shadowgraph.* An undisturbed shock wave shadowgraph is shown in photograph 6.5a (#2505). In spite of its very low Mach number, 1.008, it is sharply defined. In contrast to this, shadowgraphs of shock waves processed by the scatterer array are much fainter and appear thickened or folded. The shadowgraph shown in photograph 6.5b (#2550) corresponds to a partially scattered shock according to the pressure profile recorded at the end wall. No shadowgraph picture was taken closer to the end wall but since the shock here is seen after having propagated through at least 70 mm of dense bubble cloud, it has probably acquired at this location the same structure as on the end wall.

In figure 6.5c (#2554) the shadowgraph of a shock wave, totally scattered upon arrival at the end plate, seems to be very faint and discontinuous, yet appearing neither thicker or folded. With a Mach number of 1.0045 this shock is somewhat weaker than the previous one with 1.007 and may be totally scattered in some parts of its front, already at this location 175mm away from the end plate.

6.2.5.2 *Reflected shock shadowgraph.* If the incident shock shadowgraph gives a qualitative idea of the shock structure after a relatively short propagation distance in the scatterer array, i.e., on the order of 15 cm, a reflected wave shadowgraph illustrates the state of the shock after 55 cm of bubble influence. All bubbles have survived the interaction with such a weak incident shock. As a comparison, an undisturbed shock wave is shown after reflection in photograph 6.6a (#2506). It appears to be somewhat dimmer but still as sharply defined as the incident shock wave (photograph 6.5a).

The reflected shock waves, after interaction with the bubbles, are barely visible. In photograph 6.6b (shock #2529), a faint, folded front which corresponds to a totally scattered pressure profile at the end wall, can barely be seen. Similarly, shadowgraphs of reflected waves were taken in the case of the nitrogen bubbles, photograph 6.6c (#2544), showing a faint but slightly distorted wave front and in the case of the helium-nitrogen jets combined, photograph 6.6d (#2538) showing again a tilted and apparently uniformly thickened wave front, probably due to tilt along the viewing axis.

6.2.5.3 *Influence of the shock wave on the array.* As illustrated on the shadowgraphs 6.5b, 6.5c and 6.6b, the bubbles are slightly distorted by the shock wave but they all survive intact and seem to have recovered their spherical shape 1 ms later before the arrival of the reflected shock wave which, in turn, distorts them again. The helium-filled soap bubbles are slightly compressed initially in the direction parallel to the shock propagation and probably oscillate afterwards because of the restoring force of the soap membrane.

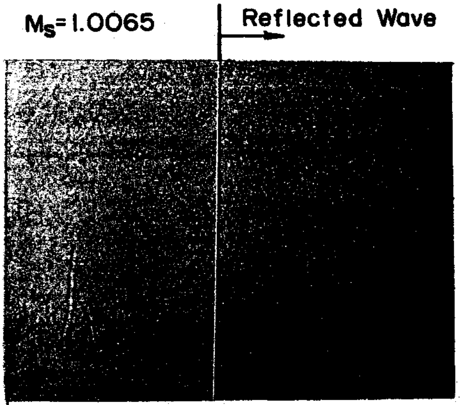

(#2506) No Scatterers

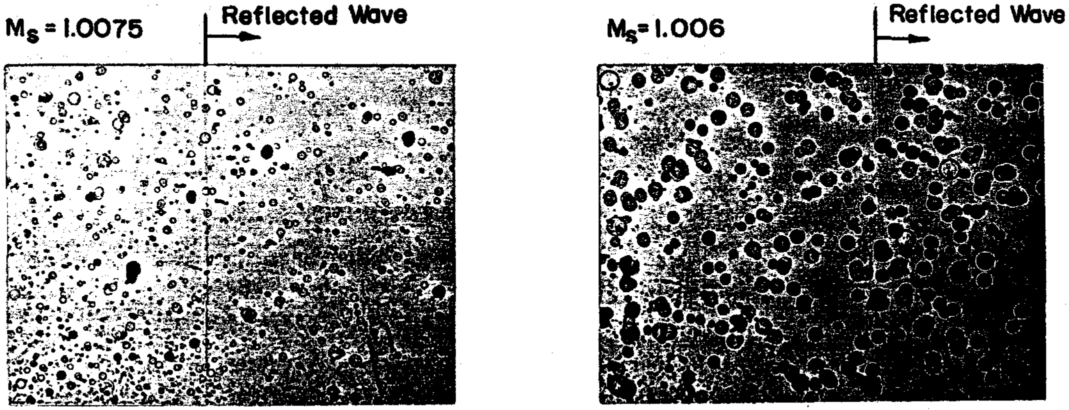

(#2544) Nitrogen Bubbles

(# 2529) Helium Bubbles

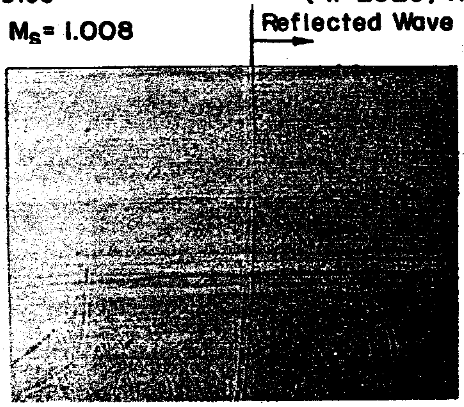

(# 2538) Nitrogen And Helium Jets

Scale 0 5cm

FIGURE 6.6 Shadowgraph Pictures of very Weak Reflected Waves

6.3. Partial scattering of weak waves: $1.015 < M_s < 1.025$

6.3.1. *Conditions of the experiment.* At $M_s = 1.02$ the volume of influence of each scatterer is 5.9 cm^3. For a dense bubble array, the volume available per scatterer is 1.5 cm^3 and there are 4 bubbles involved in the multiple scattering. For a low density cloud, such as obtained with a single bubble generator, this number drops to 1. Both 1 and 4 bubble generators were used in this sequence of experiments.

6.3.2. *Pressure profiles.* The histogram in figure 6.2b shows the distribution of the rise time of the precursor of a shock wave of Mach number $M_s \simeq 1.02$ with four bubble generators operating. Most pressure profiles show evidence of partial scattering with an average pressure rise time of 3 μs. More than half of the traces have a decreased first peak of oscillation.

From the 31 pressure profiles recorded, four are strongly scattered Figure 6.7a shows a representative profile (#2493) with a precursor of 7 μs reaching 50% of the total shock pressure and where the pattern of the first oscillations behind the pressure rise is heavily modified. Figure 6.7b (2473) shows a moderately scattered wave with a precursor of 5 μs reaching 30% of the total shock pressure rise. A weakly scattered wave is shown in figure 6.7c (#2468). Figure 6.7d (run #2484) shows another weakly scattered profile with sone lower frequency pressure oscillations behind the steep pressure rise.

In contrast, the pressure profiles obtained with a shock wave of the same initial strength processed by a less dense array generated by only one bubble generator show only signs of weak scattering, as illustrated on the histogram 6.2c. A typical weakly distorted wavefront with a short precursor (1 μs risetime) is shown in figure 6.7c (#2401).

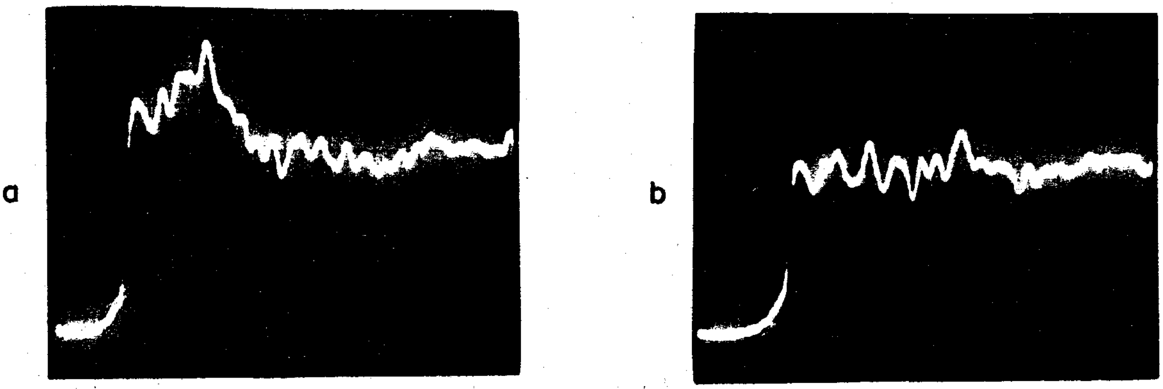

(# 2495) Dense Array M_S= 1.017   (# 2473) Dense Array M_S= 1.016

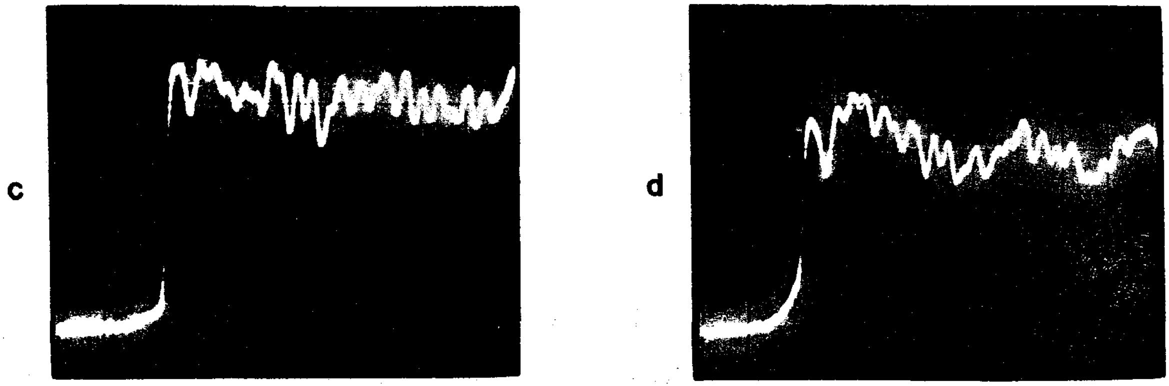

(# 2468) Dense Array M_S=1.022   (# 2484) Dense Array M_S= 1.017

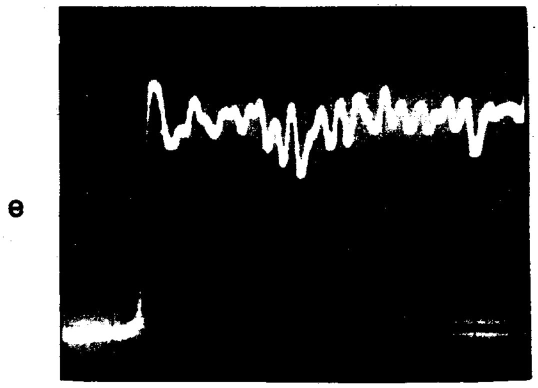

(# 2401 Diffuse Array M_S= 1.02

Horizontal Scale 5μs/div.   Vertical Scale 20mbar/div.

FIGURE 6.7 Pressure Profiles of Weak Incident Waves ($1.015 < M_s < 1.025$)

As with the weaker shocks (§ 6.1.4), there is no scattering observed from the interaction with the mixture of air, nitrogen and helium obtained when no soap is supplied to the bubble heads.

6.3.3. *Shadowgraphs.* Depending on the local concentration of bubbles, the incident shock wave may look relatively undisturbed as in photograph 6.8a (#2460) or rather folded as in photograph 6.8b (#2493). The reflected shock appears always transformed; thickened as in photograph 6.8c (#2463) or folded as in photograph 6.8d (#2473). The shock is too weak to destroy the bubbles except for a very small number (2% at most), apparent as puffs of helium on some shadow photographs of the reflected shock taken 1.1 ms after the incident shock triggered the instrumentation. Five of these can be seen on photograph 6.8c. The low density bubble cloud produced by one generator is not able to create a visible disturbance on the shock front, as shown on photograph 6.8e (#2341).

6.3.4. *Mean speed of sound and length of mixing zone.* The relative increase of the average speed of sound of the mixture over the one in air, $\Delta a/a$, and the length of the mixing zone L were measured for the different test conditions. The values averaged over many runs are: $\Delta a/a$ = .6% for one bubble generator operating during 5 seconds, $\Delta a/a$ = 1.1% for four bubble generators operating during 2 seconds, and $\Delta a/a$ = 2% for four bubble generators operating during 4 seconds.

In all cases the average mixing length was approximately 80 cm. The speed of sound increase obtained with the injection of helium and nitrogen was about the same as the one obtained with the array of bubbles, indicating again that the soap does not contribute to a measurable change of the speed of sound. The observed number of bubbles in the shadowgraph photos was approximately 100 for the tests with one generator and around 250 for the tests with four

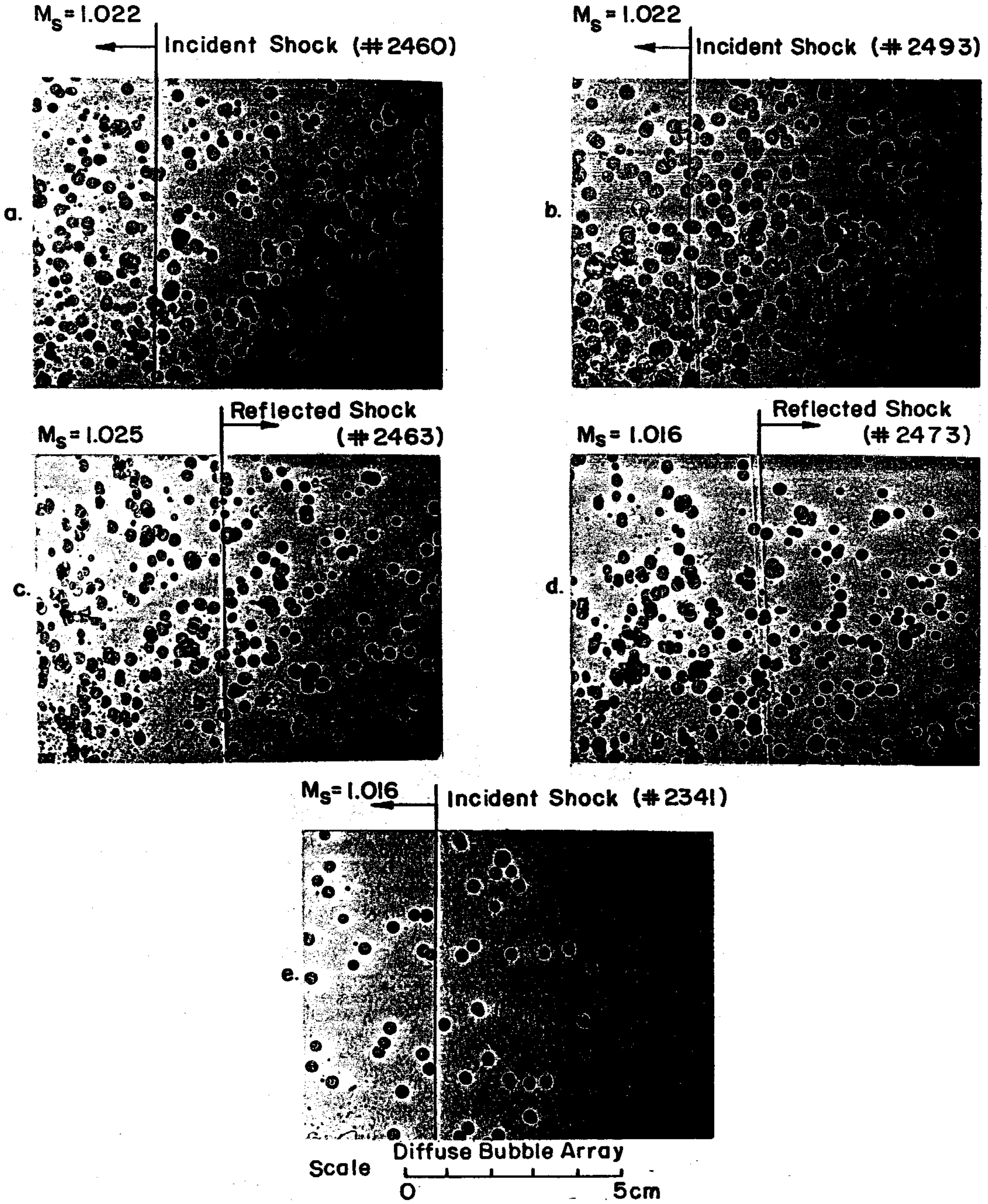

FIGURE 6.8 Shadowgraph Pictures of Weak Incident Waves ($1.015 < M_s < 1.025$)

generators.

6.4. Interaction of the bubble array with stronger waves

In this section we discuss shock wave Mach numbers of 1.06, 1.15 and 1.36. For the weakest case, M_s = 1.06, the volume of influence of one 2 mm diameter helium scatterer is .63 cm^3. For a volume available per scatterer varying between 1.5 and 6 cm^3, only weak scattering effects can be expected. For the two sets of strong shock experiments, at M_s = 1.15 and 1.36, no scattering is expected. However, the effect of this class of shock on the scatterer array is important and the shock front, as observed on shadowgraphs, is locally disturbed.

6.4.1. *Analysis of the pressure profiles.* A histogram of the precursor length in the pressure profile obtained at the lower Mach number, presented in figure 6.2d, shows that a weak scattering was measured in 5 out of 14 tests. A typical weakly scattered trace appears in figure 6.9a (#2569). Probably because of a cluster of bubbles very close to the transducer, a more perturbed profile was recorded and is shown in figure 6.9b (#2572). Probably for the same reason, one pressure profile out of eight presented a very short precursor in each of the two stronger cases: M_s = 1.15 and M_s = 1.36. With M_s = 1.16 as shown in figure 6.9c (#2560), the shock profile is not perturbed by the bubble array, while for the slightly weaker (M_s = 1.14) shock pressure profile shown in figure 6.9d (#2557) a weak precursor is present. Similarly for Mach number 1.36, most recorded pressure profiles are unperturbed, as shown in figure 6.9e (#2585), except for one profile with small precursor, shown in figure 6.9f (#2584).

6.4.2. *Shadowgraphs.*

6.4.2.1 *Mach number 1.07.* A sequence of four shadowgraphs of the interaction process of the bubble array with a Mach 1.07 wave is shown in figure 6.10

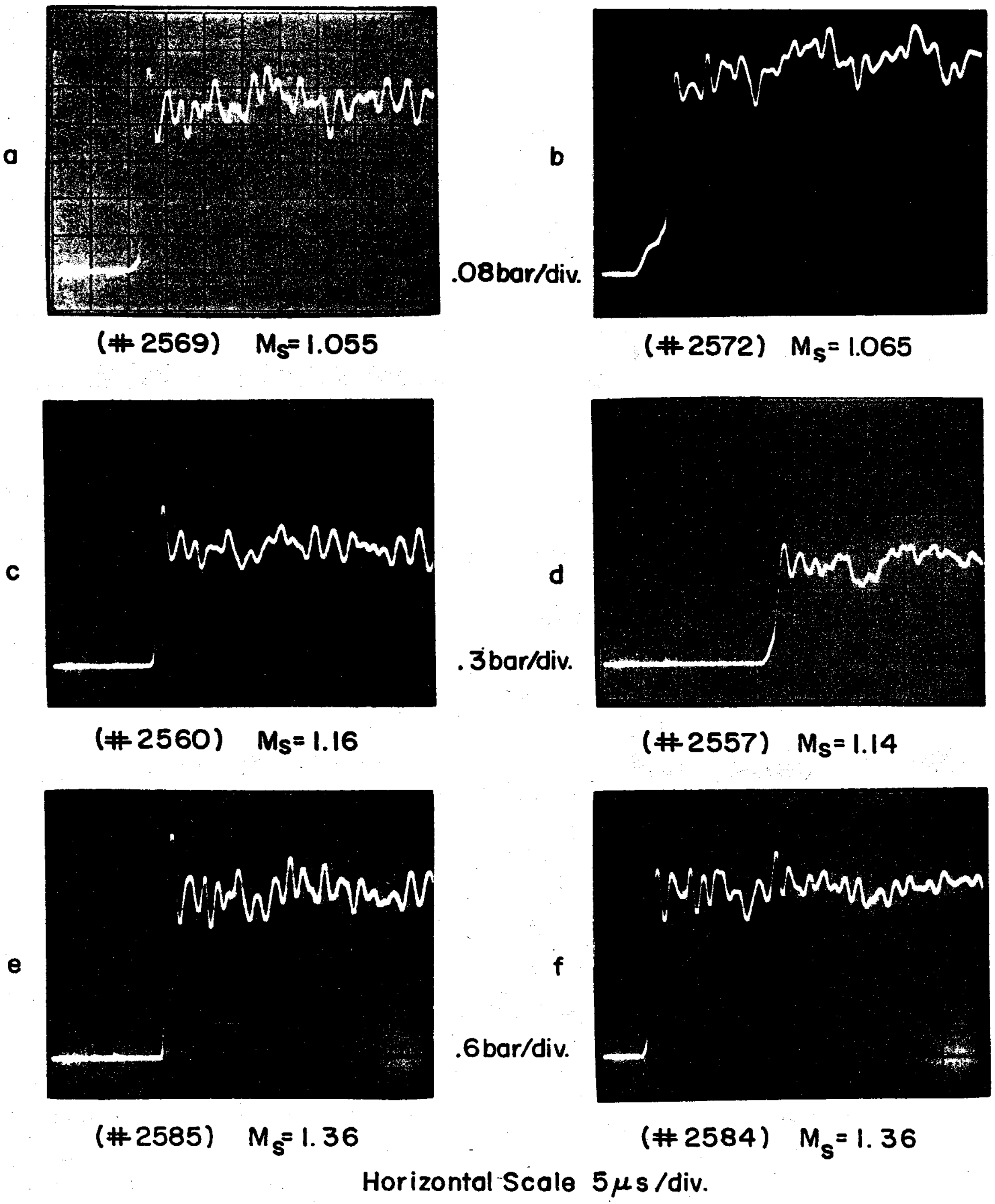

(#2569) M_s= 1.055

(#2572) M_s= 1.065

(#2560) M_s= 1.16

(#2557) M_s= 1.14

(#2585) M_s= 1.36

(#2584) M_s= 1.36

FIGURE 6.9 Pressure Profiles of Stronger Incident Waves ($1.05 < M_s < 1.36$)

where the spark gap was fired .13 ms (6.10a) (#2578), .37 ms, 6.10b (#2570), .73 ms (6.10c) (#2572) and 1.00 ms (6.10d) (#2573), after the incident shock wave triggered the first transducer. The aspect of the scatterer array at various locations behind the shock wave is therefore illustrated: between 0 and 88 mm for 6.10a, between 84 and 179 mm for 6.10b, between 220 and 315 mm for 6.10c, and between 321 and 416 mm for 6.10d.

In the shadowgraph 6.10a, the bubbles start breaking 40 mm behind the shock front, therefore about 110 μs after being processed by the shock wave, which in this picture does not appear very much perturbed. The break-up mechanism cannot be clearly understood at such a small scale, but with the hindsight of the experiment with large helium filled soap bubbles (§ 13.1.2), the ring and jet structure can be recognized. The following pictures show the evolution of the mixing of the helium structures with air. A small number of bubbles do not break until the reflected shock wave, appearing on the left of photograph 6.10d, processes them. The last shadowgraph of the sequence, recorded as the reflected wave leaves the field of view on the right 1.29 ms after the incident wave triggered the first transducer is shown in figure 6.10e, where the mixing becomes more complete with the break up of the last bubbles.

A more perturbed incident shock front is shown on the shadowgraph in figure 6.11a (#2577), while the thicker-looking reflected shock front is shown in figure 6.11b (#2574) where the break-up mechanism of the bubbles which had survived intact the incident shock wave appears more clearly. These bubbles again seem destroyed at a distance of 40 mm behind the reflected wave, but before this the jet of air penetrating inside the distorted helium enclosure, thus transforming it into a toroidal structure can be observed. The reflected shock Mach number is estimated at 1.055.

6.4.2.2 *Mach number 1.15.* The shadowgraphs obtained with Mach 1.15

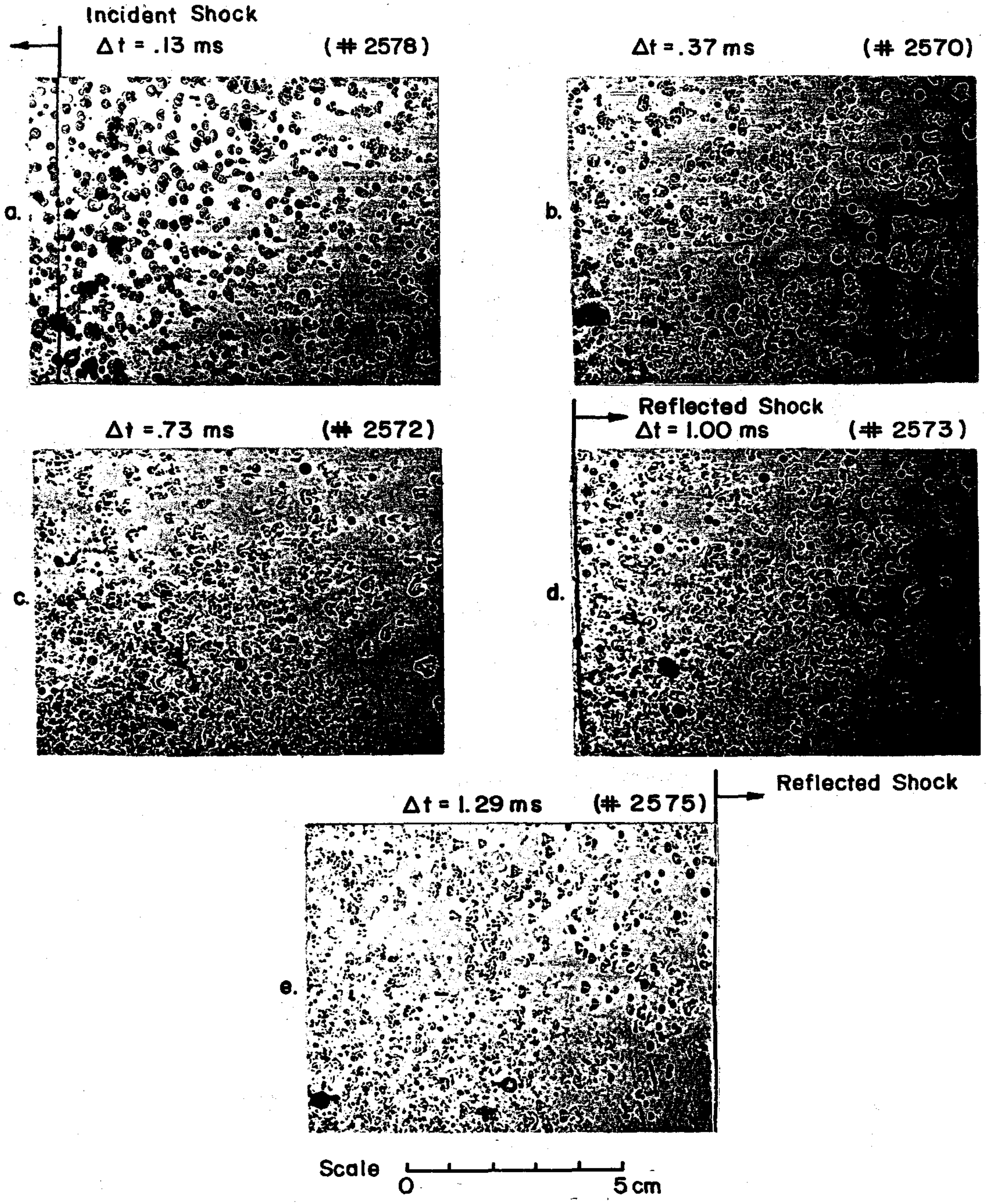

FIGURE 6.10 Sequence of Shadowgraph Pictures ($M_s = 1.07$)

shocks are shown in figures 6.11c (#2580) and 6.11d (#2561). A strongly perturbed incident shock front appears in figure 6.11c and the bubbles seem to be destroyed after 20 mm, that is, 50 μs after being processed by the shock. Again, the subsequent shape of the enclosed helium resembles the helium torus, and secondary vortex ring documented at the much larger scale in Chapter 13. The shadowgraph in figure 6.11d recorded .15 ms later, when the shock has travelled 35 mm to the left of the picture shows the further mixing of the gases. At the time of the arrival of the reflected shock wave, 1 ms later, the two gases have mixed to the point where the shape of the structures cannot be distinguished easily on the shadowgraph any more (see figure 6.11e) (#2558).

Figure 6.12a (#2293) shows the interaction of a shock wave of the same strength with a less dense array of scatterers obtained with a single bubble generator. The shadow of the shock front appears less perturbed than it was for the denser array. Figure 6.12b (#2259) illustrates the interaction of the less dense array with a slightly stronger shock ($M_s = 1.21$) which appears remarkably undisturbed. The bubbles seem to be destroyed 8mm behind the shock, i.e., after a delay of 20 μs.

6.4.2.3 *Mach number 1.35.* Finally, the shadowgraphs obtained in the strongest case ($M_s = 1.35$), figures 6.12c (#2587) and 6.12d (#2586) taken 100 μs later, with the shock 30 mm to the left of the picture show a much stronger mixing: the bubbles are destroyed within 2 mm, or 4 μs after being processed and the helium structures become unrecognizable 100 mm behind the shock. The spherical transmitted waves generated by two bubbles near the top of the shock trace on figure 6.12b and more weakly on figure 6.11a can be seen.

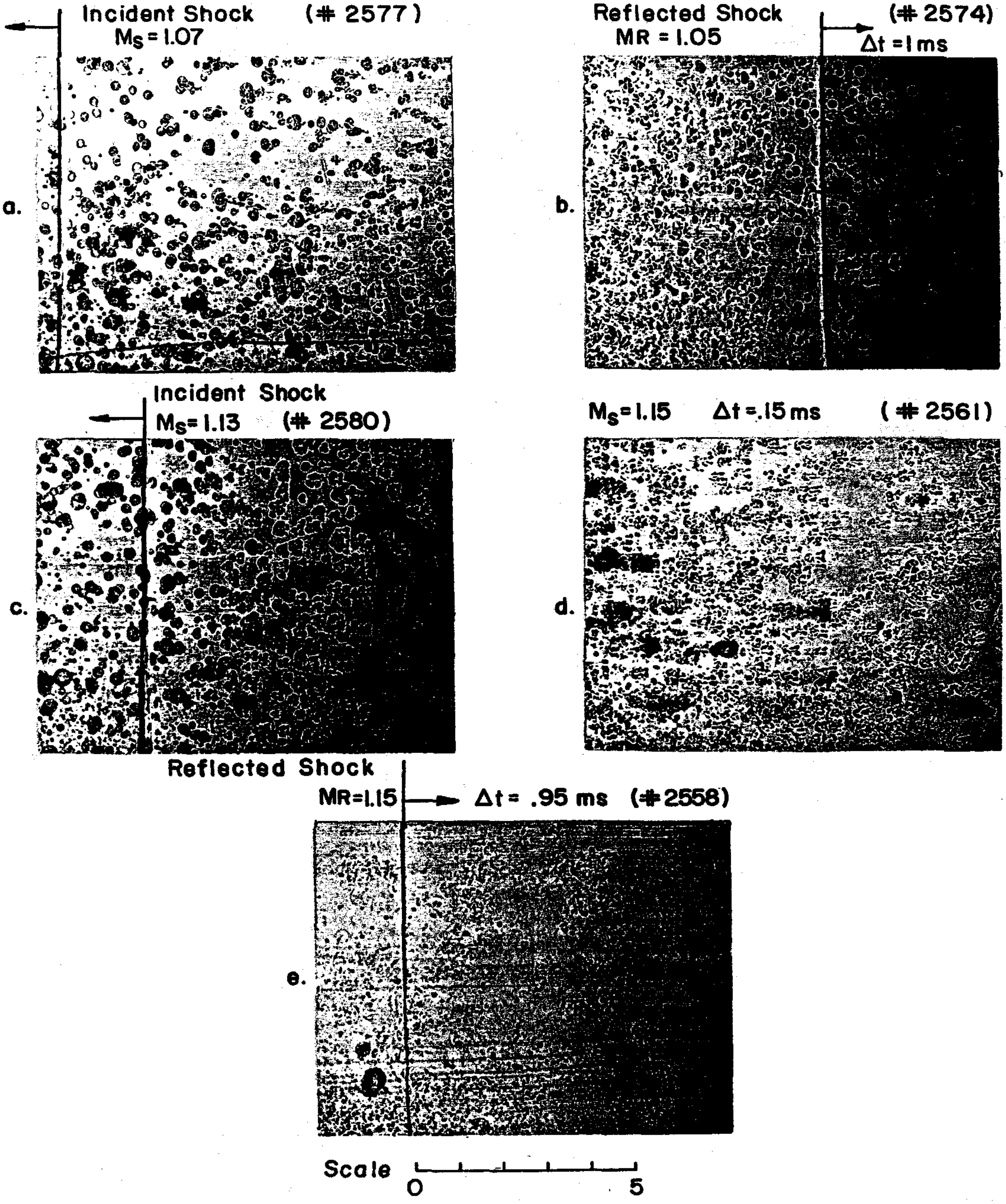

FIGURE 6.11 Shadowgraph Pictures of Stronger Incident Waves (M_s = 1.05 & 1.15)

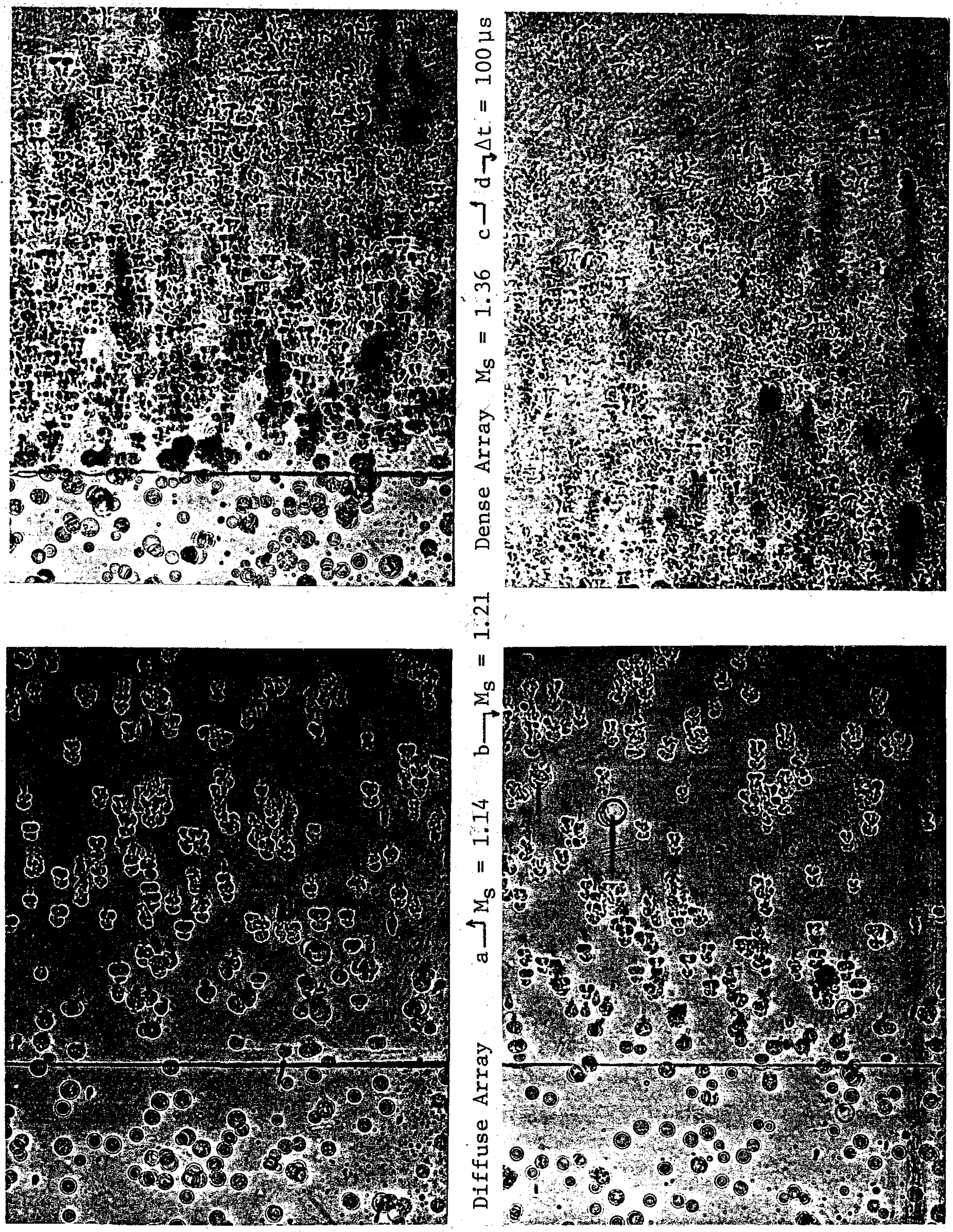

FIGURE 6.12 Shadowgraph Pictures of Strong Waves (M_S= 1.15 & 1.36)

Chapter 7

INTERACTION OF AN ACOUSTIC PULSE WITH A CYLINDRICAL LENS

7.1. Introduction

In this chapter, the results of geometrical acoustics are used to predict the rays and wave fronts associated with the interaction of a plane acoustic pulse with a cylindrical acoustic lens. The lens is made of a cylindrical gas inhomogeneity of speed of sound a_2, density ρ_2 and acoustical impedance $\rho_2 a_2$. The corresponding parameters are a_1, ρ_1 and $\rho_1 a_1$ for the surrounding air. The acoustical index of refraction is $n = a_1/a_2$. The computer-generated sketches of rays and wave fronts presented here are used to interpret the shadowgraphs obtained in the experiment of the interaction of moderately weak shock waves with cylindrical gas inhomogeneities (Chapter 9). Of particular interest are any differences between experimental observation and the predictions of geometrical acoustics that might be ascribable to the effect of nonlinear wave propagation.

7.2. Physical principles

7.2.1. *Incident wave.* The incident wave is represented in the diagrams by a family of parallel rays incident from the right onto the cylindrical boundary at various points defined by their height h vertically above the cylindrical axis. An impact parameter α is defined by the ratio h/R where R is the cylinder radius. The angle of incidence θ_i, between the ray and the normal to the interface, is related to α,

$$\sin \theta_i = \alpha = h/R \quad . \tag{7.1}$$

7.2.2. *Reflected waves.* Wave reflection occurs for the incident wave at the convex air-gas interface of the cylinder and for the various internal waves at the concave gas-air interface.

The angle of reflection is equal to the angle of incidence, $\theta_r = \theta_i$. The focal length of rays incident on the interface with an angle of incidence θ_i is given by,

$$f = -\frac{R}{2}\cos\theta_i \tag{7.2}$$

where we adopt the convention of using the − sign for convex interfaces, i.e., reflected incident waves are divergent. The radius of curvature of curved incident and reflected wave fronts (R_1 and R_2) are related by the lens formula,

$$\frac{1}{f} = \frac{1}{R_1} + \frac{1}{R_2} \quad . \tag{7.3}$$

7.2.3. *Refracted waves.* The continuity of the incident and refracted wave fronts at the interface leads to Snell's law,

$$\frac{\sin\theta_t}{\sin\theta_i} = \frac{a_2}{a_1} = \frac{1}{n} \quad . \tag{7.4}$$

For $n < 1$, a critical angle of incidence is obtained,

$$\theta_{i_{crit}} = arcsin \; \frac{a_1}{a_2} = arcsin \;\; n \quad . \tag{7.5}$$

The range of regular refraction occurs for $0 < \theta_i < \theta_{i_{crit}}$. In this case there are real waves reflected and refracted at the interface. Critical refraction occurs for $\theta_i > \theta_{i_{crit}}$. Inside the cylinder, the refracted waves are imaginary and, therefore evanescent. All the incident energy is reflected. The intersection point of the refracted wave front and the interface runs ahead of the corresponding point for the incident wave front and a lateral wave appears ahead of the incident wave as the refracted wave is refracted again to the exterior.

7.2.4. *Amplitudes of the reflected and refracted waves.* The continuity of pressure and normal velocity at the interface yield expressions for amplitude reflection (R_{fl}) and refraction (R_{fr}) coefficients in terms of the ratio,

$$r = \frac{(\rho\alpha)_1 \cos\theta_t}{(\rho\alpha)_2 \cos\theta_i} = \frac{(\rho\alpha)_1}{(\rho\alpha)_2} \left\{ \frac{1 - \left(\frac{\alpha_2}{\alpha_1^{2}} \right) \sin^2\theta_i}{1 - \sin^2\theta_i} \right\}^{1/2} . \qquad (7.6)$$

$$R_{fl} = \frac{1-r}{1+r} \quad , \quad R_{fr} = \frac{2}{1+r} . \qquad (7.7)$$

Above the critical angle, r is imaginary and the amplitude reflection and refraction coefficients become complex. The refracted wave, called in this case an evanescent wave, propagates along the interface and decays exponentially with the distance normal to the interface.

7.2.5. *Transmitted wave.* The refracted rays refract again out of the cylinder; the rays are called here the transmitted rays. The focal length of each ray passing through a cylindrical lens of radius R and index of refraction n is defined as the distance between the center of the cylinder and the intersection of the transmitted ray with the diametral axis parallel to the incident rays. It is obtained with the following formula (Davy and Blackstock,1971):

$$f = \frac{n^2 R}{2[(n^2 - \alpha^2)^{1/2} - (1 - \alpha^2)^{1/2}][(1 - \alpha^2)^{1/2}(n^2 - \alpha^2)^{1/2} + \alpha^2]} . \tag{7.8}$$

The focal length of the paraxial rays ($\alpha = 0$) is:

$$f_1 = \frac{n\ R}{2(n - 1)} . \tag{7.9}$$

For $n \geq 1$, the focal length of the rays incident near the top of the lens ($\alpha = 1$) is:

$$f_2 = \frac{n^2 R}{2(n^2 - 1)^{1/2}} \tag{7.10}$$

and for $n \leq 1$, the focal length of the rays incident near the critical angle ($\alpha = n$) is:

$$f_3 = - \frac{R}{2(1 - n^2)^{1/2}} . \tag{7.11}$$

7.2.6. *Diffracted waves.* The incident ray grazing the top of the cylinder constitutes the boundary of the shadow behind the cylinder. According to the geometrical theory of diffraction (Keller, 1955 and 1958),a surface diffracted ray propagates along the downstream cylindrical interface and sheds tangentially diffracted rays into the shadow region. For a converging lens, the surface ray also sheds critically refracted rays to the inside of the cylinder. The amplitude of the surface diffracted ray, initially a fraction of the incident amplitude, decreases exponentially as it propagates along the surface and the amplitude of the tangentially shed diffracted rays (and, for a converging lens, of the critically refracted rays) is a fraction of the local surface ray amplitude.

In the case of the converging lens, the critically refracted rays shed internally from the surface diffracted ray intercept the concave slow-fast (gas-air) surface again at the critical angle. According to Jones (1978) the external evanescent waves generated by this interaction leave from the body tangentially and become *real* outside a boundary layer. This is an example of the tunneling effect.

7.3. Wave fronts and ray diagrams.

7.3.1. *Helium cylinder.* With an index of refraction of 0.34, the helium filled cylinder is a strongly diverging lens. From equations (7.9) and (7.11) the focal lengths of the transmitted rays range from -0.257 R for paraxial rays to -0.531 R for the rays issued from the incident rays near the critical angle of refraction (20 °).

Figures 7.1 and 7.2 identify five families of rays. The parallel rays on the left are the incident rays. The reflected and transmitted rays are seen outside the cylinder. Inside the cylinder appear the refracted rays and singly reflected rays which form a caustic that begins at the critically-refracted incident ray and loops downstream all the way to the axis. (All multiply-reflected internal rays also form caustics which lie between the primary caustic and the perimeter of the cylinder.) Not shown in the exterior are the diffracted rays and the secondary transmitted rays resulting from the refraction of the internal singly-reflected rays.

Figure 7.3 is a diagram of the wave fronts associated with some of these rays. Outside the cylinder the reflected wave fronts are seen tangent to the transmitted wave fronts to the right of the cylinder and connected at the shadow boundary to the diffracted wave front to the left of the cylinder. The incident wave

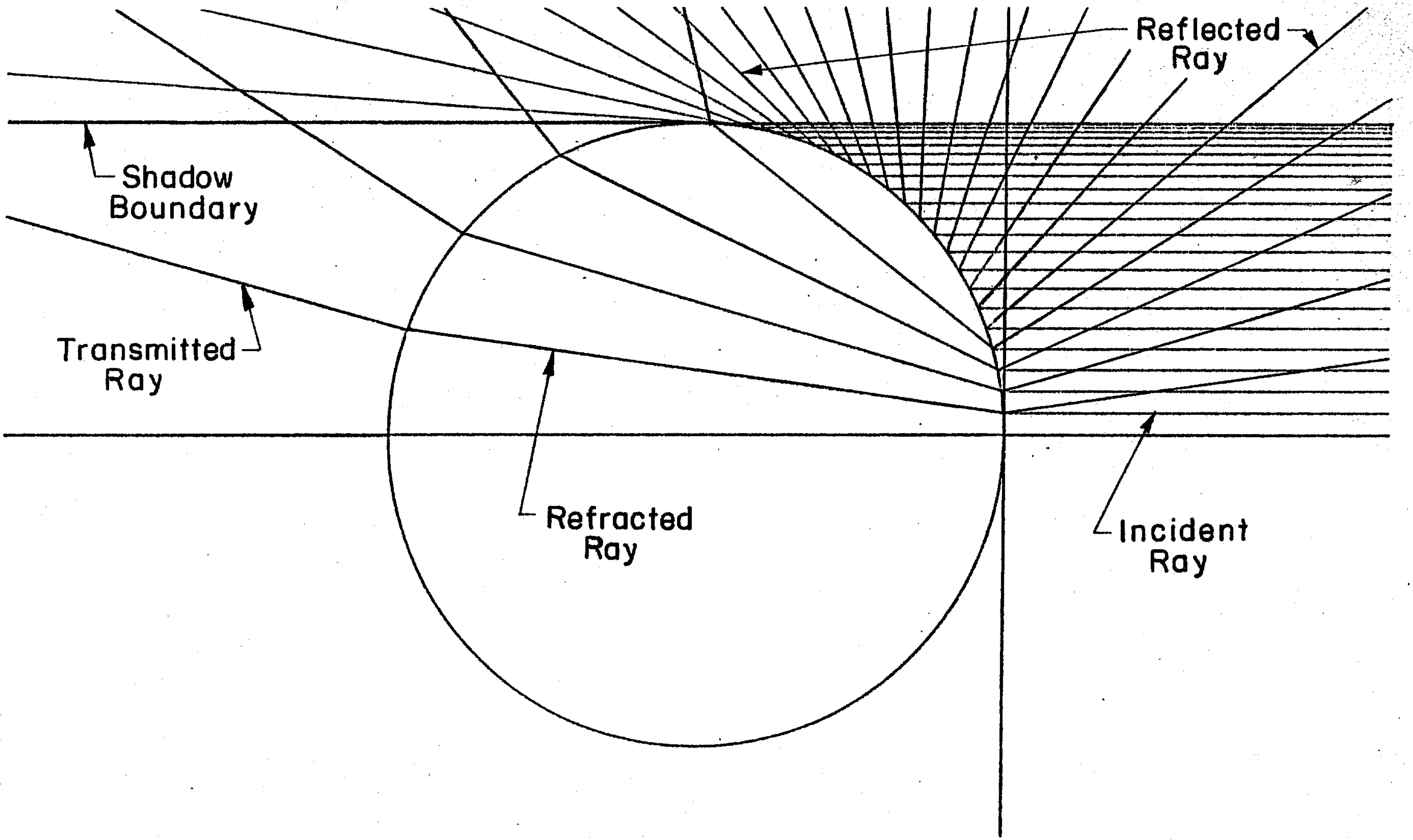

FIGURE 7.1 Definition of the Rays for the Helium Cylinder

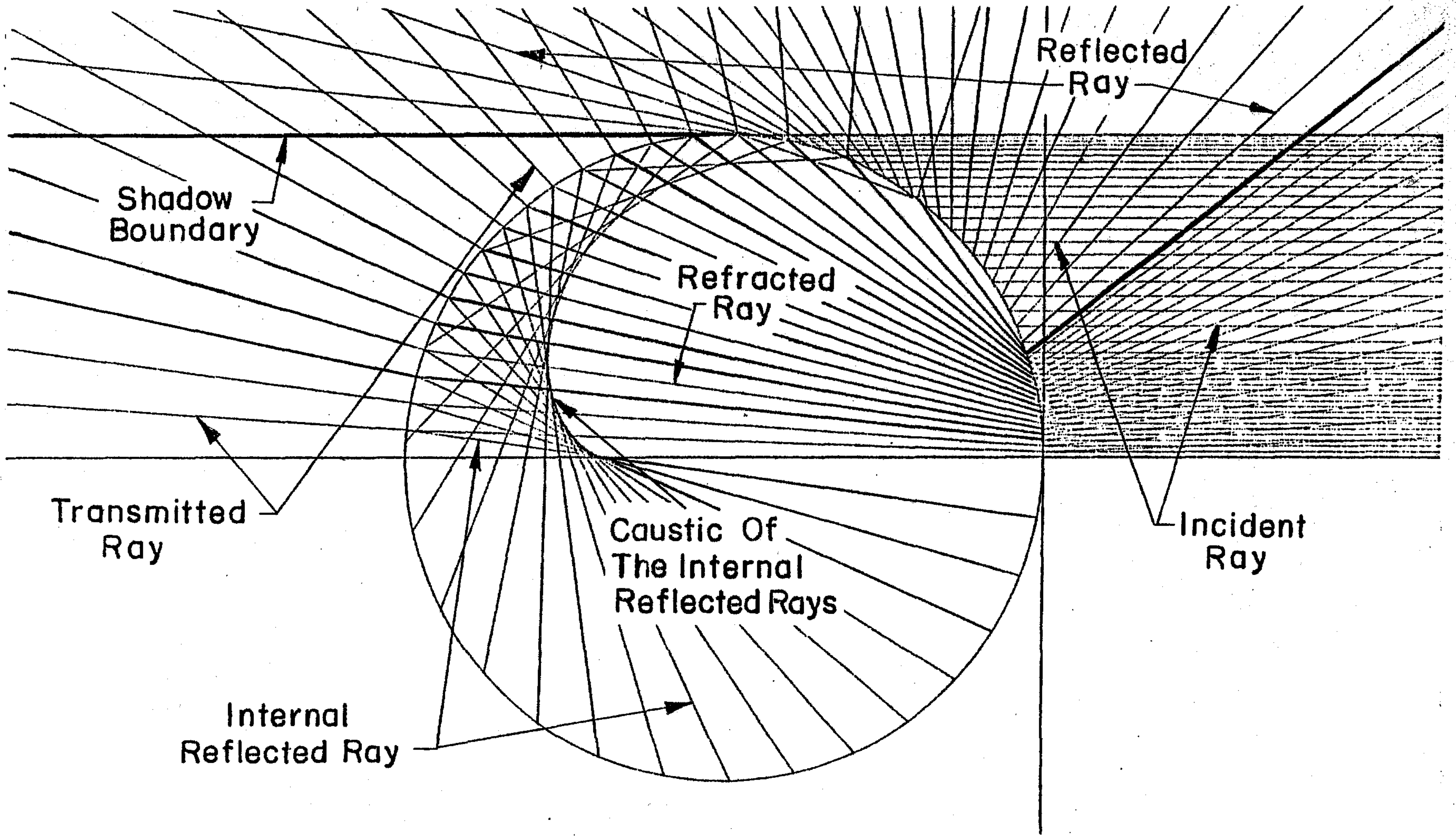

FIGURE 7.2 Ray Diagram for the Helium Cylinder

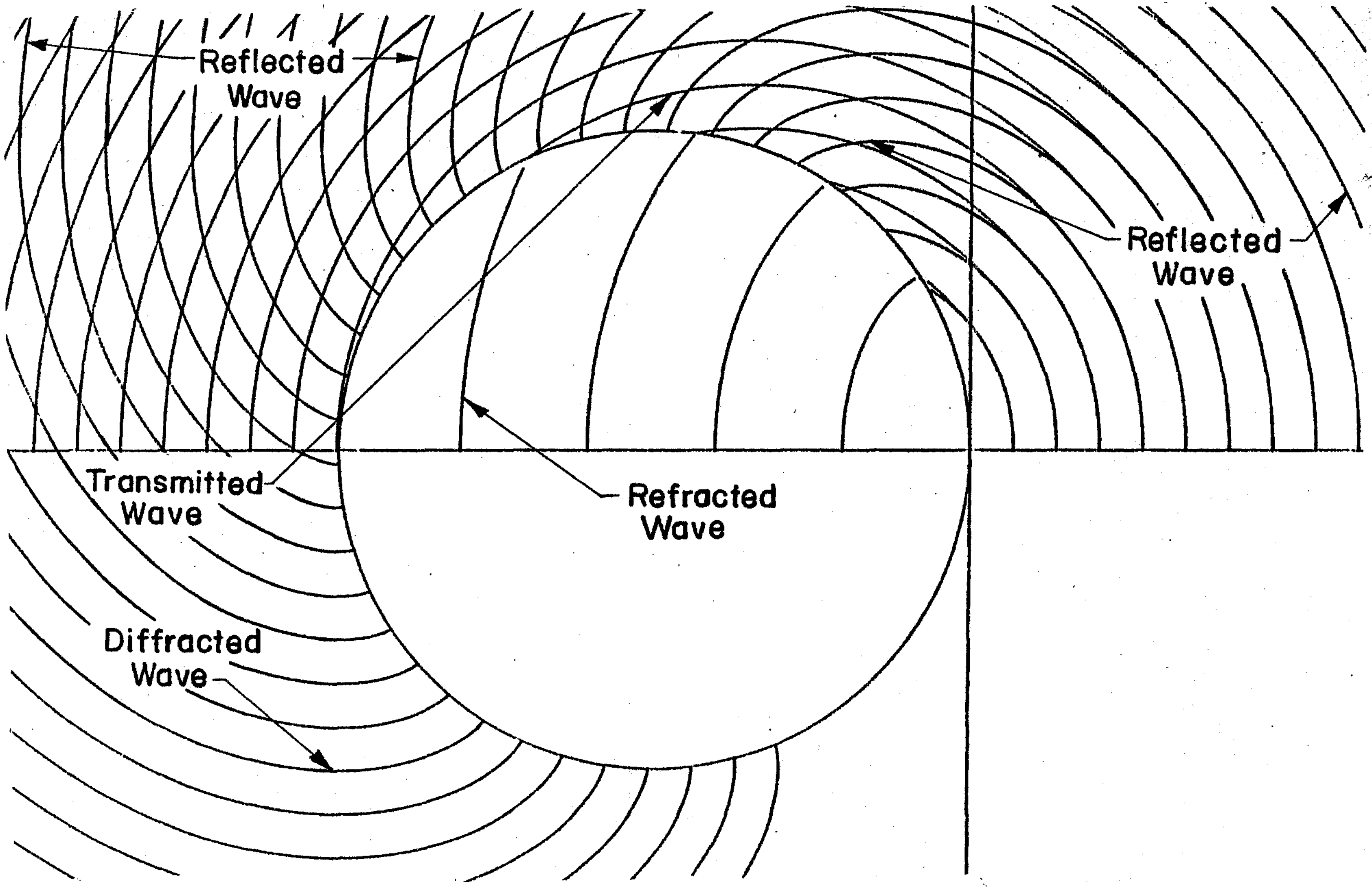

FIGURE 7.3 Wavefront Diagram for the Helium Cylinder

front, not represented here, is tangent to these two wave fronts at the shadow boundary. The transmitted wave front appears to the left of the cylinder but at a much earlier time than the diffracted wave. The fronts associated with the secondary transmitted rays follow behind the initial transmitted waves and are tangent to them at the critically reflected ray, just as are the reflected waves. They are not represented in the diagram but appear clearly on the photographs in figure 11:4.

7.3.2. *Freon 22 cylinder.* Freon 22 is a fluorocarbon (chemical formula $CHClF_2$) with a density of 4.72 kg/m^3 and a speed of sound of 182 m/s at 22 ° C. With an acoustic index of refraction of 1.89, the Freon 22 filled cylinder immersed in air is a strongly converging lens. From (7.9) and (7.10) its focal lengths are 1.06 R for the paraxial rays and 1.11 R for the rays incident near the top of the cylinder. This means that the focal area is just in front of the cylinder. The critical angle for the interior rays incident in the concave cylinder interface is 32 °. The various rays are identified in figure 7.4. The incident rays are missing but the reflected rays and diffracted rays are shown on the outside of the cylinder. Refracted rays and critically refracted rays shed from the surface diffracted rays appear inside.

Figure 7.5 shows nine families of rays. Shown in the exterior are (proceeding in a counterclockwise direction) incident, reflected, diffracted, transmitted and the critically-refracted rays originating from the refracted rays shed, also at the critical angle, by the diffracted surface ray. In the interior appear the refracted rays which form a caustic and the rays refracted internally from the surface diffracted ray which form a circular caustic joining the first caustic at an arête. Also shown are the internal reflected rays associated with the refracted rays.

The primary caustic is in the main focus of the internal front and continues for a short distance external to the cylinder on the transmitted rays. It also

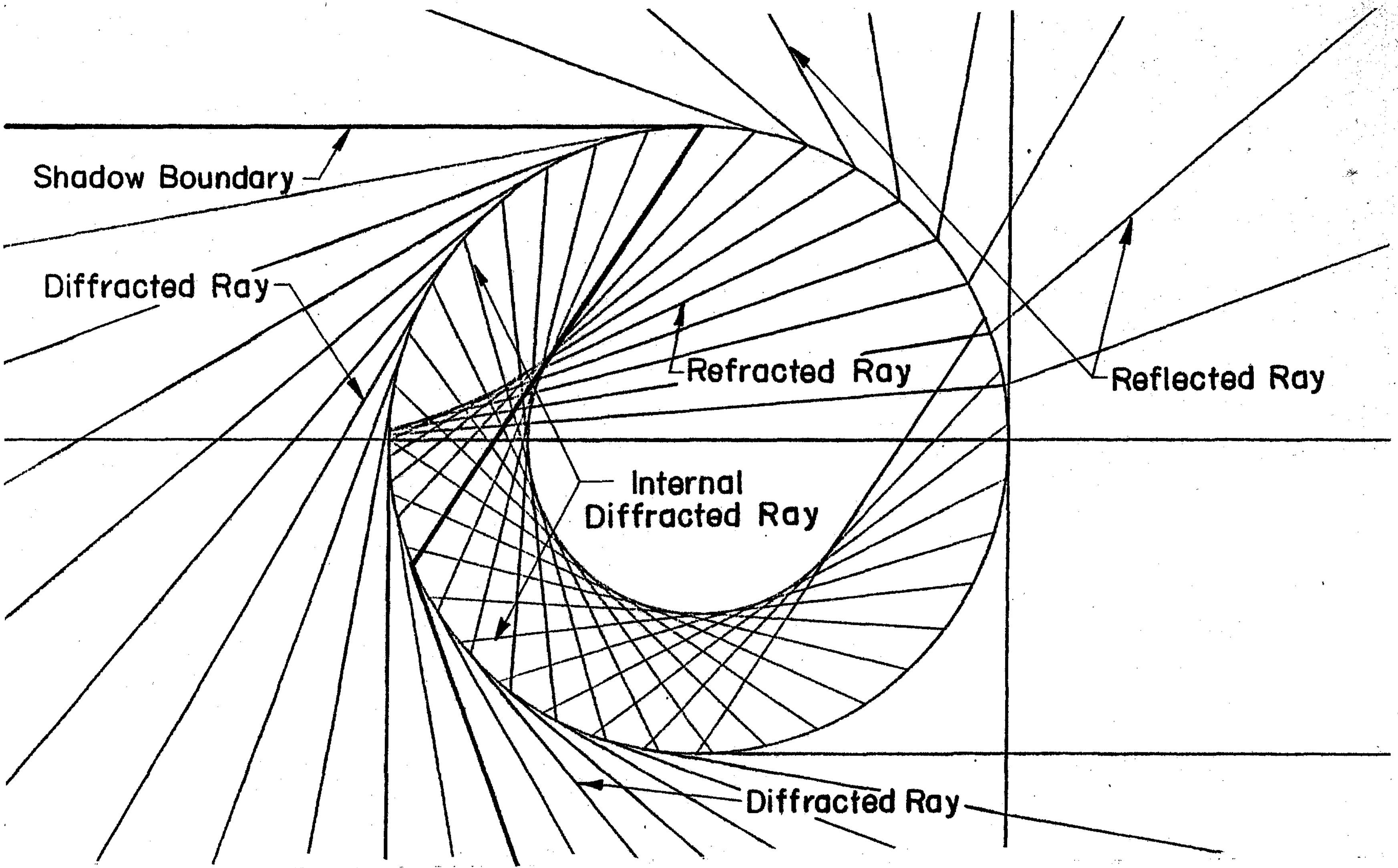

FIGURE 7.4 Definition of the Rays for the Freon 22 Cylinder

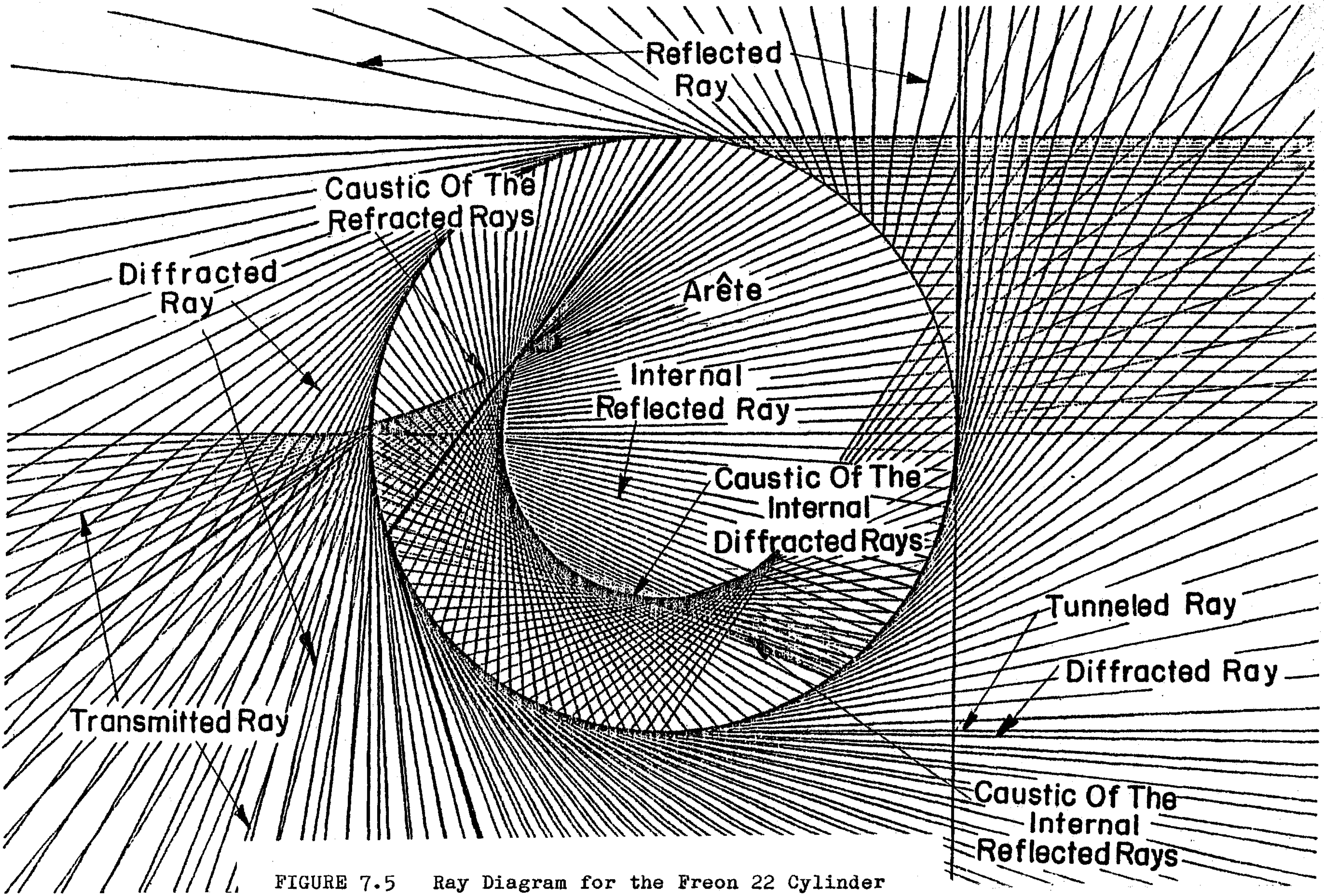

FIGURE 7.5 Ray Diagram for the Freon 22 Cylinder

continues in the interior on the reflected refracted rays which forms a third caustic beginning at, and somewhat obscured by, the circular caustic mentioned above.

The external rays generated by the interaction of the internal diffracted rays with the concave interface are first evanescent but,according to Jones (1978) they "tunnel" and after a very short distance propagate as real waves again.

The wave fronts associated with the various rays are presented in figure 7.6. It shows how the originally smooth internal fronts form two folds on the two caustics. As the circular caustic never ends, the leading (diffracted) leg of the internal wave remains folded. The external wave joined to the second fold of the refracted wave is the transmitted wave, which follows far behind the external diffracted wave, and can be followed from its junction with the reflected wave along the shadow boundary down to the bottom of the cylinder. The wave fronts, parallel to the diffracted wave front, which were drawn up to the right side of the cylinder and which join the transmitted wave in the lower left side, are associated with the second (trailing) leg of the internal diffracted wave.

7.3.3. *Effect of the membrane: air cylinder.* Figure 7.7 is shown to illustrate the effect of the membrane alone on the wave propagation. Since $n = 1$, the incident, refracted and transmitted rays are aligned but the membrane creates both internal and external reflected rays. Only the external reflected wave is shown here. As for the helium cylinder, the internal reflected rays form a caustic between the critically refracted incident ray (in this case, at the top) and the axis. Not shown are the internal reflected wave front which goes to a focus and expands as a backscattered wave and the secondary transmitted wave front, tangent to the transmitted and reflected waves along the shadow boundary and connected to the internal reflected wave front. They appear in figure 8.4 in the case of a weak incident shock wave.

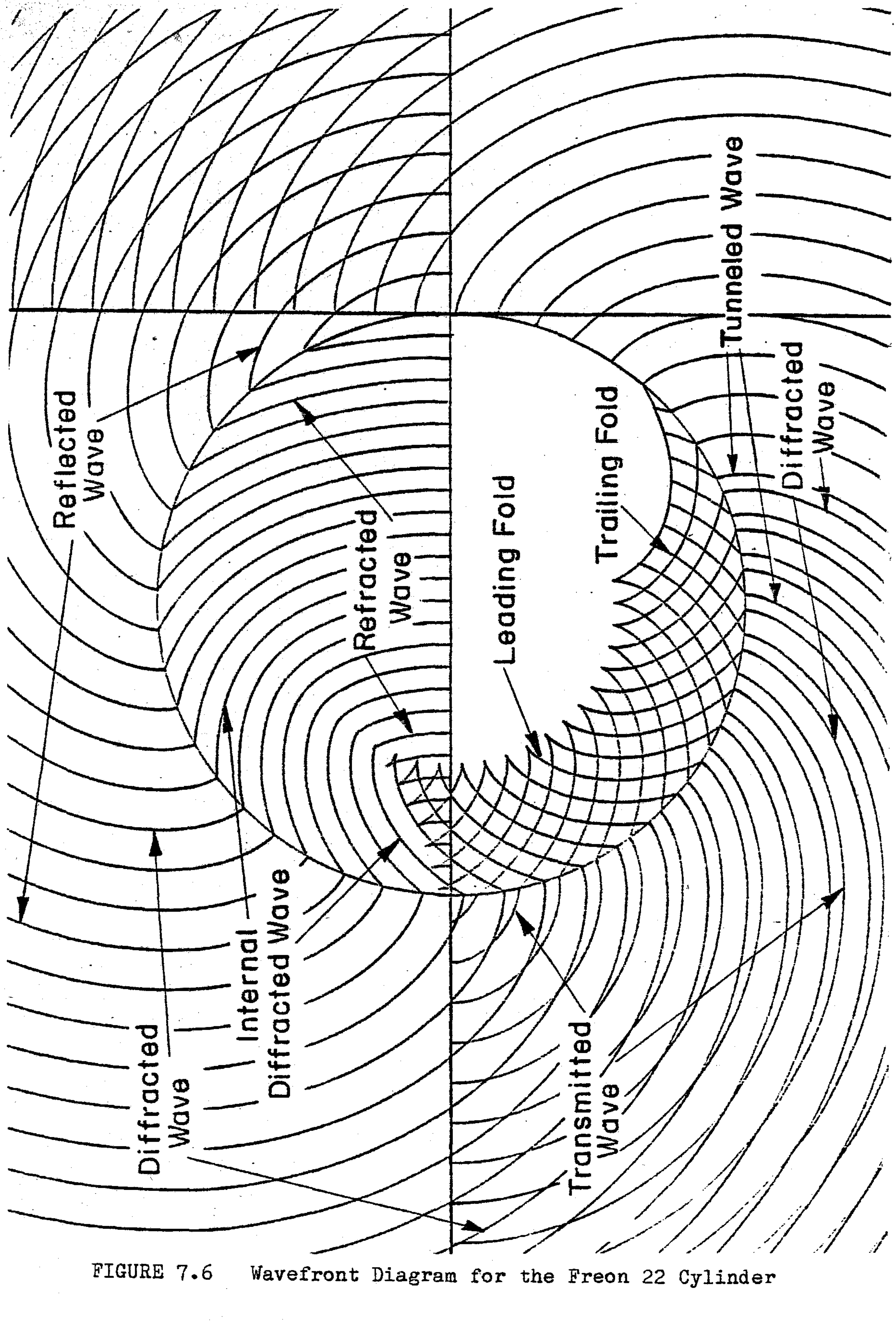

FIGURE 7.6 Wavefront Diagram for the Freon 22 Cylinder

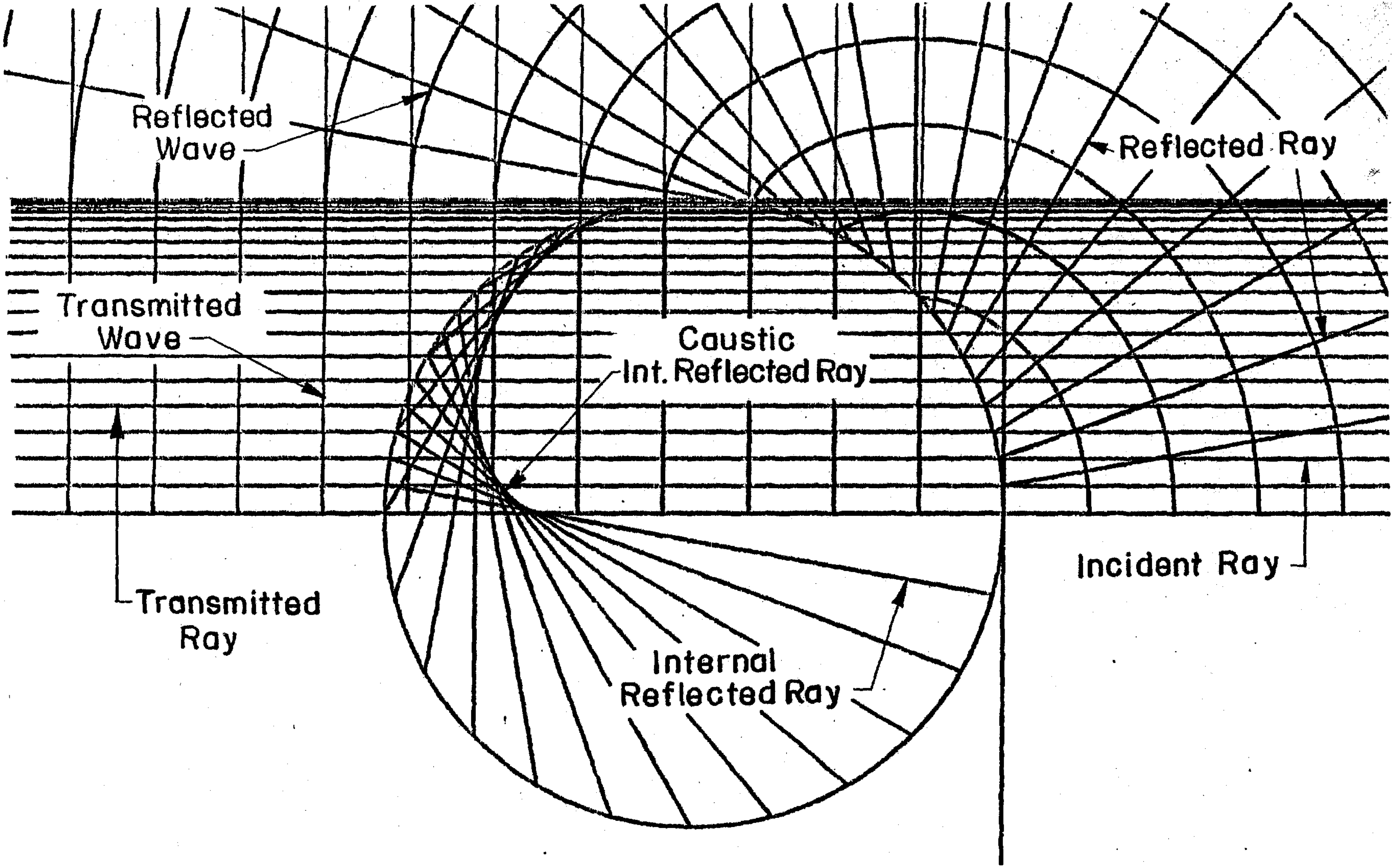

FIGURE 7.7 Ray and Wavefront Diagram for the Air Cylinder

Chapter 8

EXPERIMENTAL APPROACH OF THE TWO DIMENSIONAL INTERACTION

8.1. Cylindrical refraction cell

8.1.1. *Requirements.* The cylindrical refraction cell was designed around the following requirements:

i. It must be a cylindrical enclosure of the test gas: here helium and Freon 22, with a cylindrical membrane as light as possible to minimize its effect on the shock wave propagation and on the subsequent gas motion.
ii. It should be easily installed in the 8.9 cm x 8.9 cm test section already used in the multiple scattering experiment.
iii. It should allow visualization of the inside.

8.1.2. *Membrane.* The membrane was the key parameter in all the previous experiments on refraction of shock waves at plane interfaces. First Jahn (1956), and then Henderson's group (Abd-El-Fattah et. al. 1976 and 1978 a & b) were able to create and install on their shock tubes some membranes as thin as 0.05 μm and as light as 5 $\mu g/cm^2$, although sometimes a triple layer of membrane had to be used in order to cancel the leaks.

Henderson and his group used a solution of commercial vinyl resin VYNS in cyclohexanane. Various combinations of VYNS and SARAN resins mixed in different kinds of chemicals were tried in this laboratory and some were as thin as Henderson's membrane. But in general, they were fragile and difficult to fabricate in a large area, such as 100 cm^2. Making a cylindrical enclosure from them would have been extremely tedious.

Instead, a commercially available microfilm solution used for indoor model airplanes was chosen. This microfilm solution is nitrocellulose dissolved in a high-grade lacquer thinner (amyl acetate or butyl acetate) and plasticized with castor oil, tricresyl phosphate (TCP) or dioxybutyl phthalate (DOP) to prevent shrinking and retain flexibility. The commercial solutions used in this experiment are IMS FAA standard B and Micro x Microfilm. The membrane is formed when a few drops of microfilm solution are deposited on the free surface of water in a large tank. After most of the solvents evaporate, which takes a few minutes, the film is lifted from the water using a balsa frame (20 x 26 cm^2) and left to dry.

The membrane exhibits various colors from the interference of the reflected light from the two surfaces, indicating that its thickness is a fraction of the wavelength of light. On average, it weighs 50 $\mu g/cm^2$, corresponding to a thickness of .5 μm. That is 10 times the thickness of microfilm used for plane refraction experiments and rather resilient, indicating that it has a stronger effect on the shock wave. However, it proved to be very easy to handle and allowed a short preparation time for each experiment.

8.1.3. *Fabrication of the cylindrical cell.* The structure of the cell is illustrated in figures 8.1 and 8.2. The ends are made with Pyrex glass 51 mm in diameter and 3 mm thick for visualization of the inside. The connecting brass rod of cross section 3 x 4 mm^2, which is epoxied in the notches of the glass and the test gas inlet and outlet tubes screwed in the center are used to position the cell in the shock tube square test section.

The length of the cylinder (88 mm) is such that it fits almost exactly the width of the shock tube. The membrane is cut in a rectangle 88 mm wide and 170 mm long, on which the cylindrical cell is rolled such that the 2 short sides of the membrane rectangle overlap on the transversal beam and the long sides of

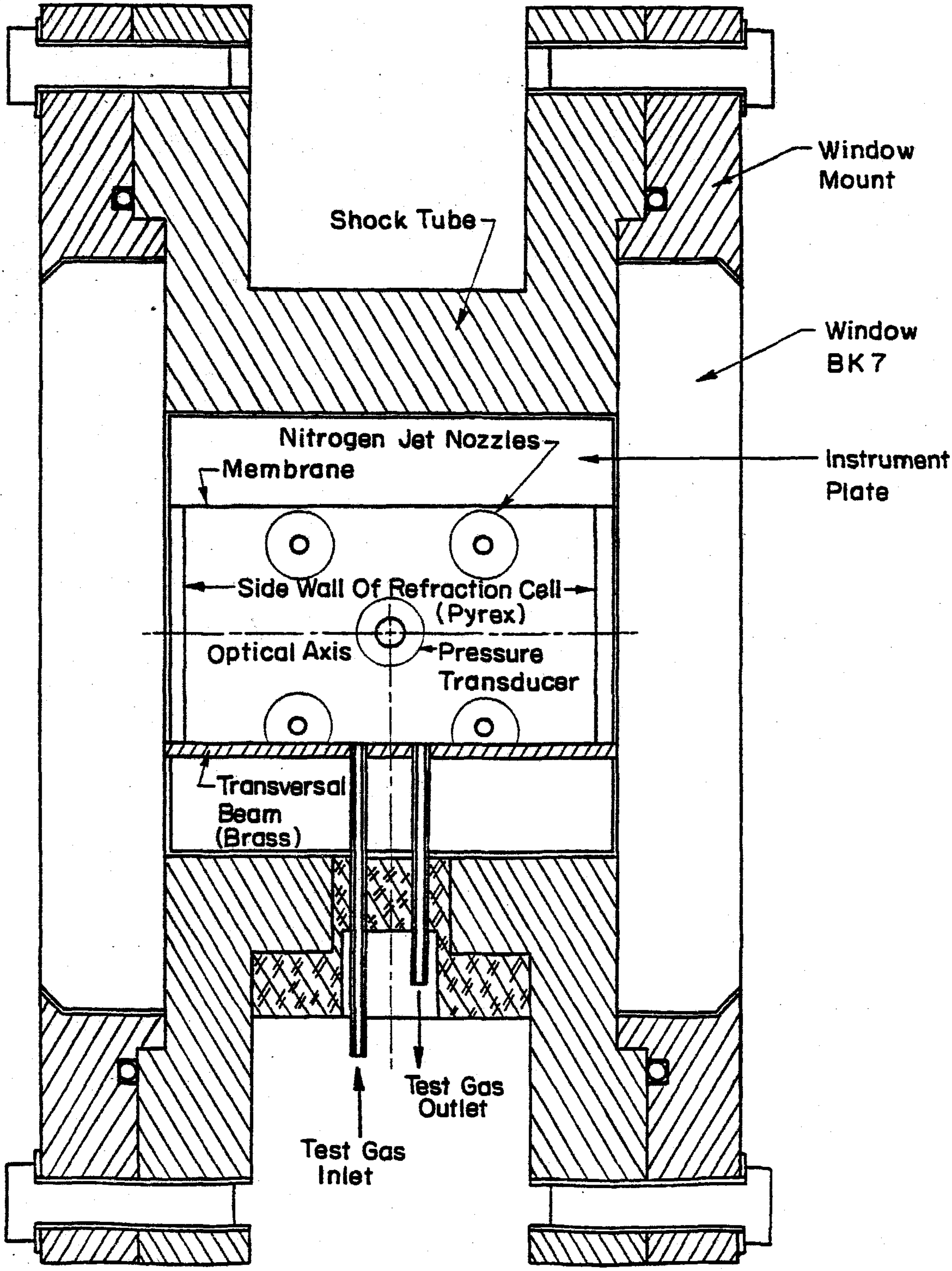

FIGURE 8.1 End View of the Test Section with the Cylindrical Cell

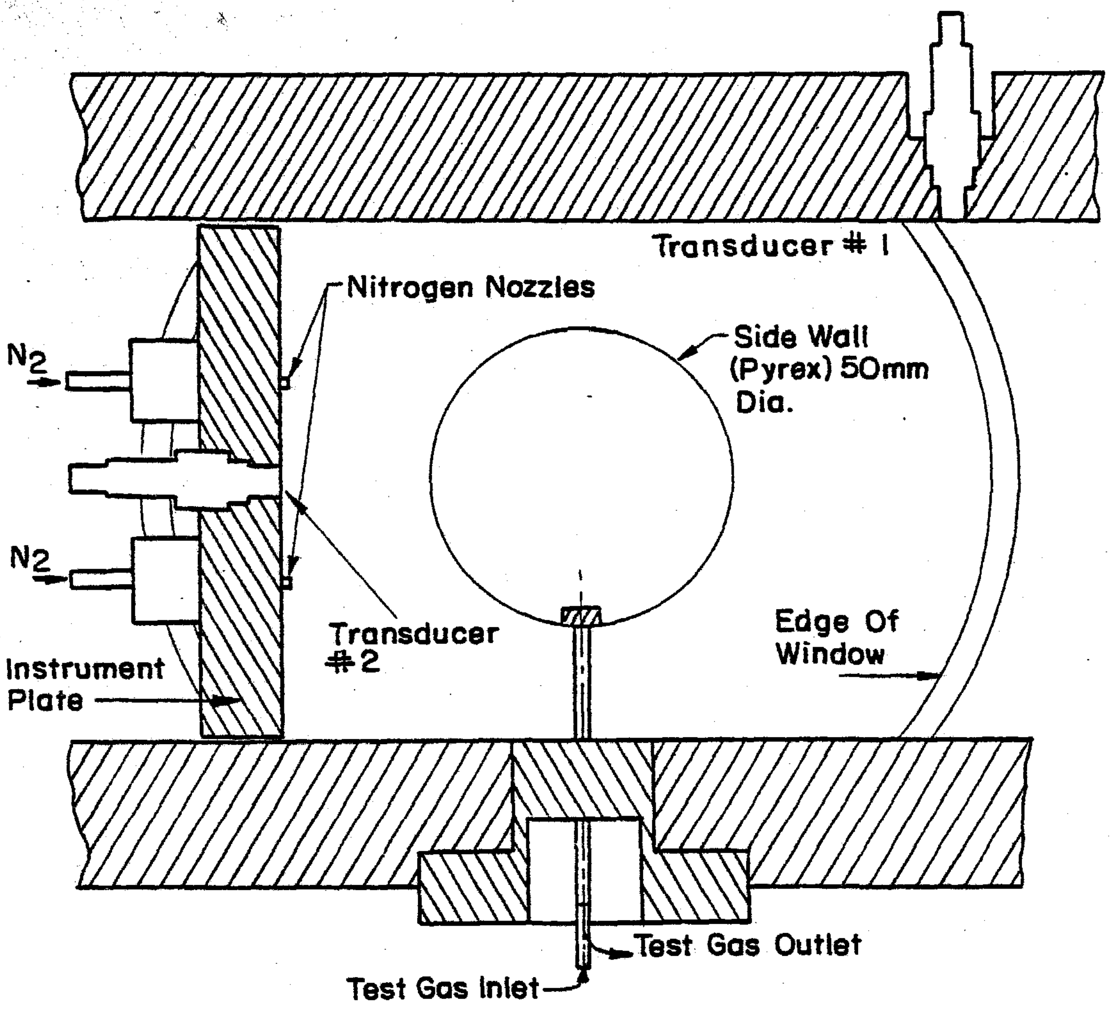

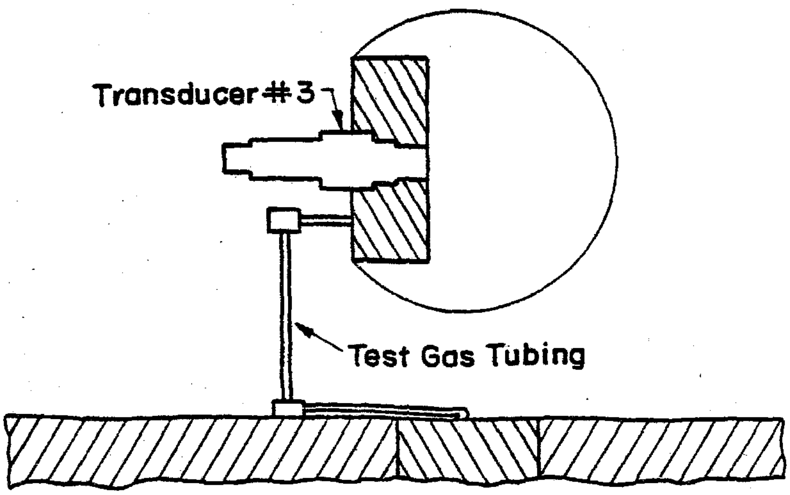

FIGURE 8.2 Side View of two Cylindrical Cells

the rectangle adhere to the previously wetted edges of the Pyrex windows. The two tubes are then screwed on the beam and inserted in the plug which is mounted in the lower wall of the test section. The positioning of the refraction cell is made with one test section window mount removed. When the mount is bolted back onto the test section it will slightly press on the cylindrical cell, thus aligning it and maintaining it in position.

When the cell has to be positioned upstream of the window in order to record the wave pattern or the gas mixing away from the cylinder's initial position, a slightly shorter cell is used which can be slid easily inside the square tube. In that case, the gas supply tubes still penetrate in the shock tube at the window position and lie on the bottom wall of the test section up to the cylinder position. The tubes actually support the cylinder in that configuration.

8.1.4. *Operation of the cylindrical cell:* The test gas is circulated inside the cell continuously: the inlet line brings the test gas at a low flow rate on the order of 10 cm^3/s. The outlet tube is directly open to the atmosphere under the test section and the slight overpressure built inside to overcome the friction on the outlet tube helps to stretch the membrane into its cylindrical shape.

Often, the test gas leaked to the outside of the cell because of some holes in the membrane and because of the gas diffusion through the intact membrane. The holes, usually created when the membrane was rolled on the cylindrical frame, could be detected because the cell would not stretch properly and could be repaired by laying some small patches of microfilm on them. The leaks due to the diffusion were impossible to eliminate. The test gas escaping the cell would normally rise to the top, in the case of helium, or drop to the bottom, in the case of Freon 22, thus creating a speed of sound gradient in the test section and therefore an oblique incident shock wave.

The solution was to cancel the concentration gradient by mixing evenly the gas which had leaked in the test section using nitrogen jets, which originate from the nitrogen nozzles of the four bubble generators mounted on the instrument plate (§ 2.1.2). A volume flow rate of several hundred cm^3/s was needed from each generator in order to cancel the tilt of the shock front when the test gas was Freon 22 and somewhat less when it was helium.

When it is desired to observe the pattern of shock waves in the vicinity of the cylinder, the instrument plate is located between 50 and 100 mm downstream of the cylinder axis, just outside the field of view of the shadowgraph. The pressure build-up due to these jets inside the test section tends to collapse the cylindrical cell, therefore it is released in the lab via a small nozzle on the main shock tube side wall.

Just as the test gas contaminates the air outside the cylinder in the test section, the air contaminates the test gas inside the cylindrical refraction cell and the experimental results indicate a slower wave speed than expected inside the helium cylinder and faster inside the Freon 22 cylinder. However, the contamination level did not change much between different shocks and thus the experiment retains some quantitative value.

8.2. Secondary effects of the refraction cell

8.2.1. *Effect on the pressure traces.* The membrane, the transversal beam and glass sides create some disturbance on the shock wave. The wave diffracts around the glass sides and beam, and is perturbed by the resistance of the membrane. Reflected waves sent by the membrane, beam and glass sides are recorded by the transducer located on the shock tube top wall, 64 mm upstream of the center of the window (figure 8.3). The pressure profile from this transducer (figure 8.3a) shows three pulses on tests made with a shock of Mach

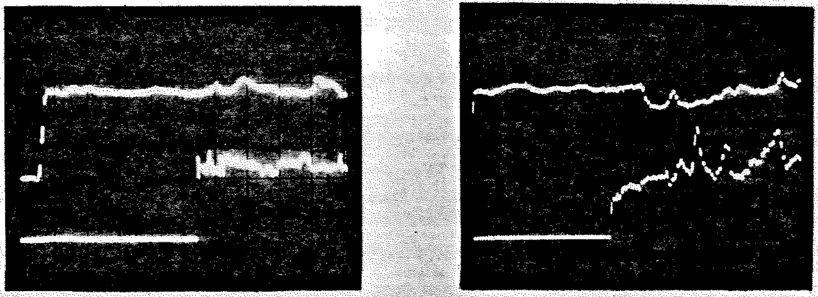

a Air Cylinder

b Helium Cylinder

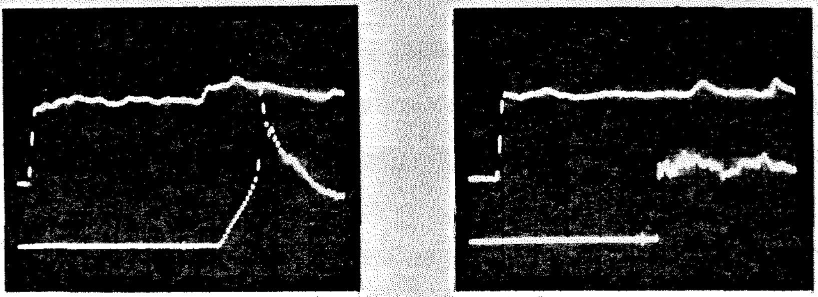

c Freon Cylinder

d Cylinder Without Membrane

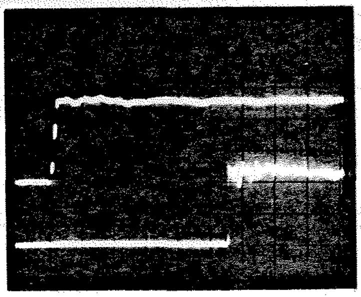

e No Cylinder

M_s=1.085 Horizontal Scale 50 μs/div.

Vertical Scale { Upper Trace (Side Wall Transducer) .08 bar/div.
Lower Trace (End Plate Transducer) .19 bar/div.

FIGURE 8.3 Pressure Profiles from the Interaction with Various Cylinders (M_s = 1.085) number 1.09 and a nitrogen-filled cylinder. The first pulse corresponds to the cylindrical reflected wave from the membrane with a Mach number of 1.005. The second and third pulses correspond to reflected waves from the glass sides and transversal beam, respectively, with a Mach number of 1.01. When the cylinder is filled with helium, the reflected shock wave from the membrane is followed by an expansion wave due to the lower acoustic impedance of helium compared to air (figure 8.3b). Upon arrival at the transducer location 52 mm away, the expansion wave has caught up with the reflected pulse which is not seen any more on the pressure profile. Similarly, for a Freon 22 filled cylinder (figure 8.3c), the reflected pulse from the membrane is combined with a reflected shock due to the higher acoustic impedance of Freon and the side wall transducer only records a single shock. For comparison, similar pressure profiles are obtained with the cylindrical cell without the membrane (figure 8.3d) where only two pulses are seen and without the cell (figure 8.3e) where none appear.

The transmitted pressure profile recorded at various distances behind a nitrogen-filled cylinder do not differ from the one measured behind a cylindrical frame without a membrane. (The effects of the membrane can only be measured very close to the cylinder.) The oscillations are due to the arrival at the transducer location of the diffracted and reflected waves from the transversal beam, the membrane and side windows. Of course, transmitted pressure profiles behind the Freon and helium cylinders are very different.

8.2.2. *Effects on the shadowgraphs.* The wave pattern is apparent on shadowgraphs of the interaction of a weak shock wave (M_s = 1.085) with a nitrogen cylinder, shown in figure 8.4. The transmitted shock is seen in the first two frames 6 mm and 13 mm behind the cylinder and appears unperturbed except at two segments at the level of the top and bottom parts of the cylinder, where it

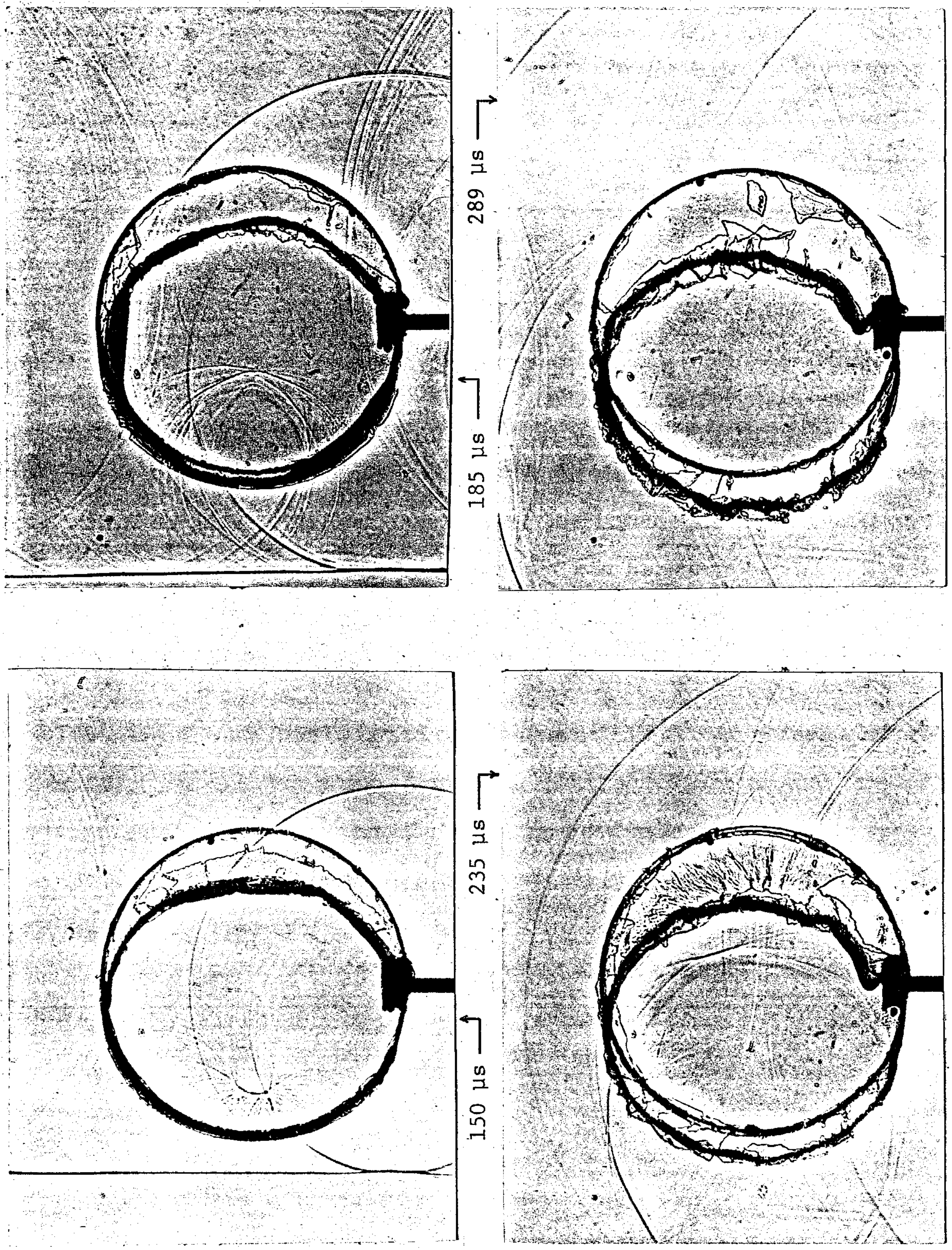

FIGURE 8.4 Pictures of the Interaction with a Nitrogen Cylinder (M_S=1.085)

is caught up with two sets of cylindrical waves. In the bottom, the diffracted wave from the transversal beam, and on top and bottom the wavefront corresponding to the rays which reflected once inside the cylindrical cavity before emerging outside. The reflected wave from the transversal beam is seen in the four shadowgraphs. This wavefront is connected to the reflected wavefront inside the cylinder which is seen just before the focus in picture 8.4a and after the focus in pictures 8.4b and 8.4c.

The membrane appears as the approximately elliptical contour which moves to the left, away from the circular shadow of the window,at a velocity V_2 equal to 42 m/s. The ratio of the major axis over the minor axis is 1.2 which would correspond to the compression by a shock wave of Mach number 1.12. The last two frames show that the displacement of the membrane is somewhat hindered by the transversal beam.

The internal wave first reflected then transmitted did not produce a measurable effect on the transducer 3 mm behind the cylinder in the case of a nitrogen-filled cylinder. In the case of helium-filled cylinders, this wave appears on the shadowgraph as well as on pressure traces (§ 11.2.1.5). Its effect is in fact stronger in the spherical case for the helium-filled soap bubbles (§ 13.5). It is very apparent as well in the pressure profiles obtained behind the bubbles filled with nitrogen or the helium-argon mixture (§ 14.3.6).

Chapter 9

FLOW VISUALIZATION

9.1. Helium filled cylinders

9.1.1. *Mach 1.23 shock wave.* The shadowgraph sequence of the interaction appears in figure 9.1 .The shock waves are moving from right to left.

9.1.1.1 *Wave pattern.* The various waves are defined in figure 7.3. The refracted wave is seen developing at time delays 12 to 52 μs and the transmitted wave is observed at delays from 62 μs to 132 μs. The internal wave resulting from the reflection of the refracted wave is seen converging at 62 μs, going through a focus at 72 μs and expanding at 82 μs, then it refracts out in air to appear at delays 102, 132 and 160 μs as a reflected back-scattered wave. The oblique wave due to the reflection of the incident and transmitted waves on the transversal beam can also be seen at delays 62 to 132 μs. The secondary transmitted wave corresponding to the rays refracted outside after one internal reflection is seen at delays 72 to 132 μs. The two converging reflected waves inside the cylinder due to these rays is connected to the secondary transmitted front as seen in the photograph taken at 62 μs and the whole pattern of secondary transmitted waves is seen connected to the backscattered wave in the photograph taken at 102 μs.

The reflected wave is shown developing from 12 μs to 82 μs and the subsequent reflected waves from the top and bottom walls are seen at time delays 102 to 245 μs. The diffracted wave is seen from 62 μs to 160 μs.

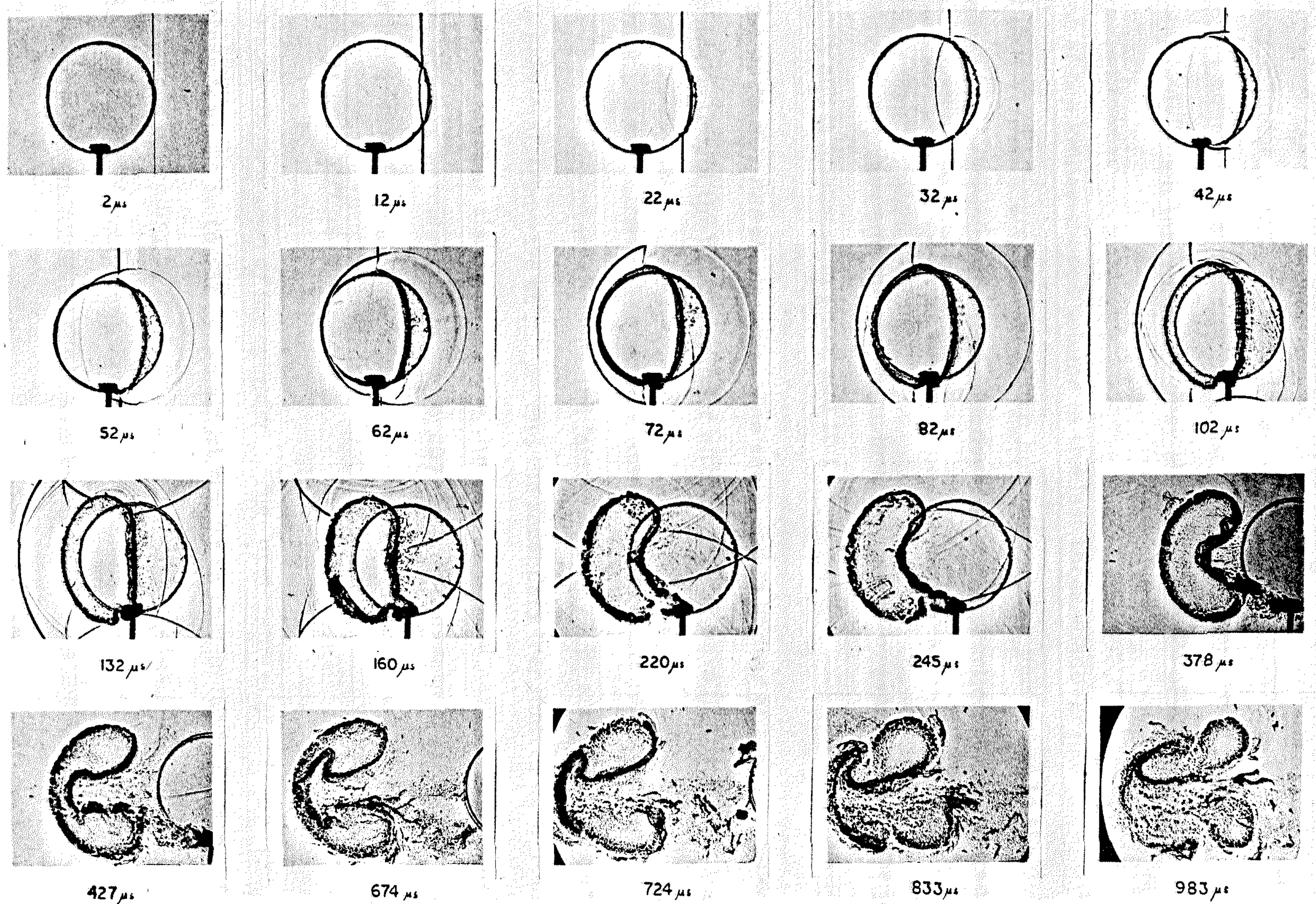
2μs 12μs 22μs 32μs 42μs

52μs 62μs 72μs 82μs 102μs

132μs 160μs 220μs 245μs 378μs

427μs 674μs 724μs 833μs 983μs

FIGURE 9.1 Interaction of a Mach 1.22 Shock Wave with a Helium Cylinder

9.1.1.2 *Deformation of the cylinder.* Flattening of the upstream edge of the helium cylinder occurs between 12 μs and 132 μs; thereafter this interface becomes concave as a spike or jet of air is growing from 160 to 427 μs in the helium body which takes now a kidney shape. The spike of air impacts on the cylinder downstream interface at 674 μs and a pair of helium vortices develop in front of the kidney shaped volume in the last three shadowgraphs (724 to 983 μs) In later shadowgraphs (not shown here) the vortex pair grows to the detriment of the two remnants of the kidney which has practically disappeared at time delays larger than 2 ms. The interpretation of the behavior of the upstream interface and the air jet implies the concept of generalized Taylor instability and is discussed in § 10.2 and 15.1.

9.1.2. *Mach 1.085 shock wave.* The same events appear at a slower pace for the interaction of the helium cylinder with the weaker wave (figure 9.2).

9.1.2.1 *Wave pattern.* The various waves seen are: the refracted wave at 13, 24 and 45 μs, the internally reflected faintly seen at 77, 87 and 109 μs appearing as a back-scattered wave at 157 μs, and the secondary transmitted wave from 77 to 157 μs which is also connected to the back-scattered wave. The transmitted wave appears at delays from 87 to 237 μs and the wave resulting from the reflection first by the cylinder and then by the shock tube side walls appears from 134 μs to 297 μs.

9.1.2.2 *Deformation of the cylinder.* The upstream edge of the cylinder flattens from 24 μs to 337 μs, an air jet similar to that in figure 9.1 grows from 438 to 1202 μs leading to the formation of a helium vortex pair seen at 1823 μs. The subsequent development of the vortex pair is similar to the stronger case. Idealized representations of the helium cylinder deformation are shown in figure 9.3.

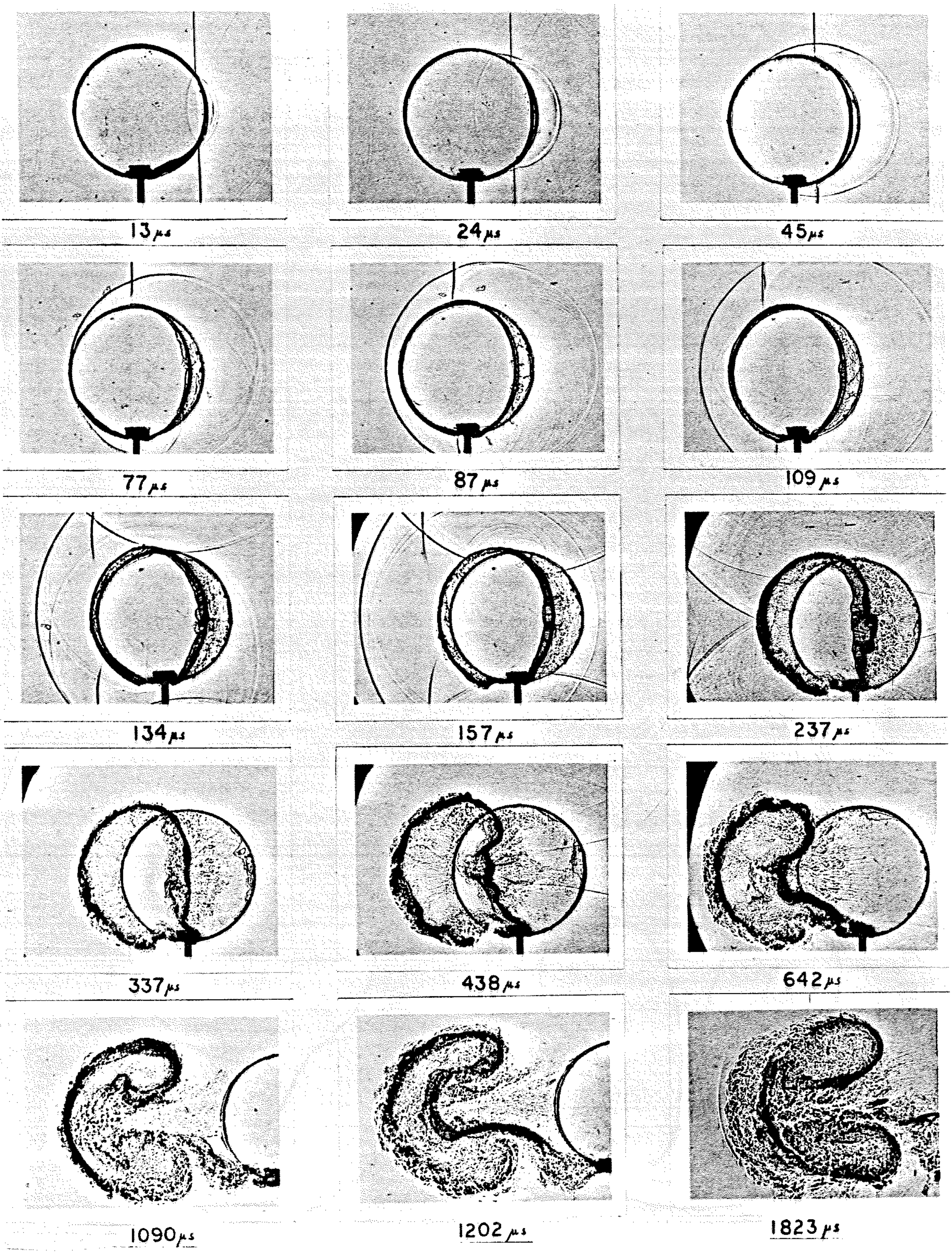

13µs

24µs

45µs

77µs

87µs

109µs

134µs

157µs

237µs

337µs

438µs

642µs

1090µs

1202µs

1823µs

FIGURE 9.2 Interaction of a Mach 1.085 Shock Wave with a Helium Cylinder

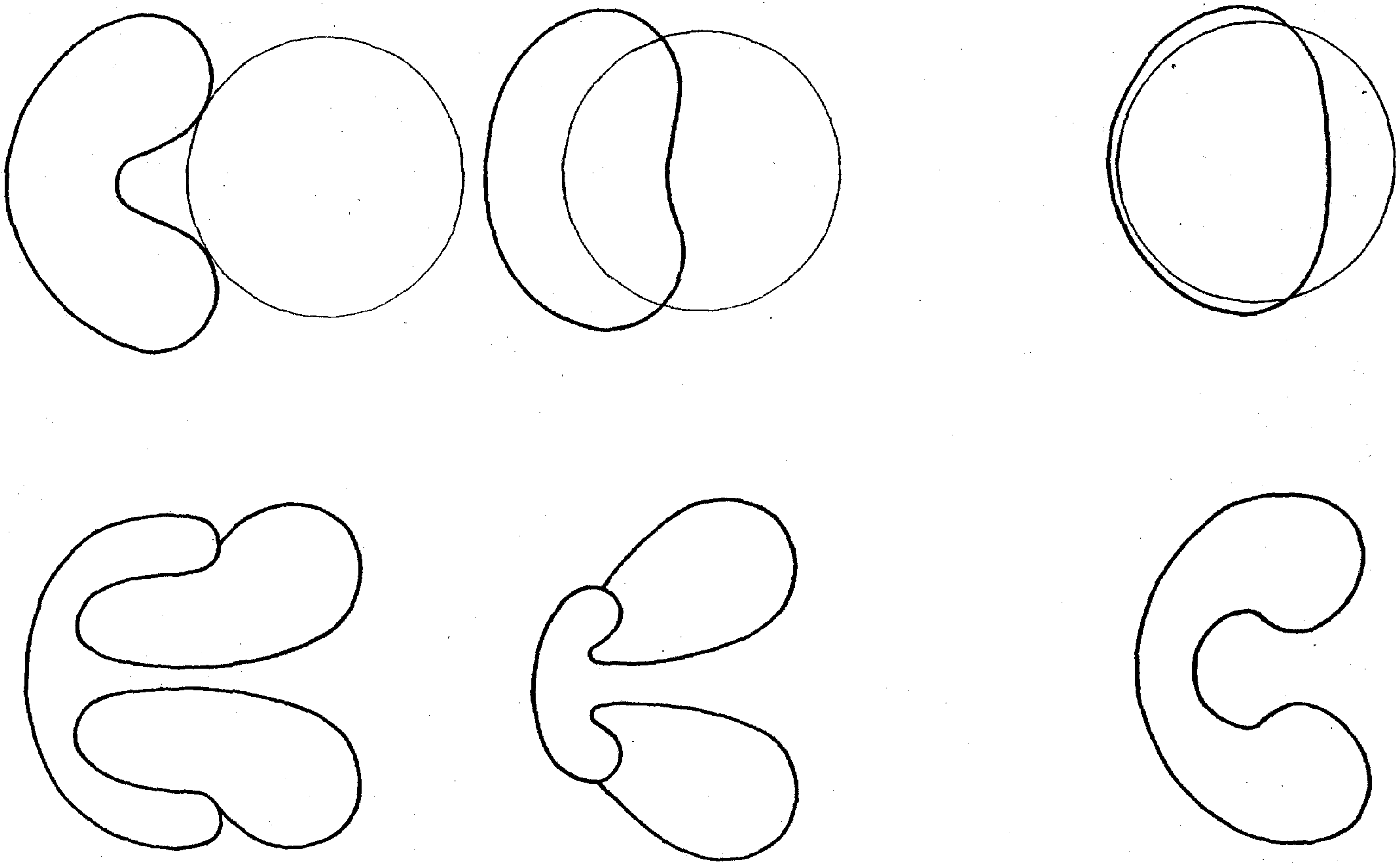

FIGURE 9.3 Schematic Representation of the Deformation of the Helium Volume

9.2. Freon filled cylinders

9.2.1. *Very weak wave:* $M_s = 1.03$ (figure 9.4). The various waves are defined in figure 7.6. This first sequence of shadowgraphs shows how the well-defined refracted wavefront inside the cylindrical volume converges to a focus from 80 μs to 275 μs while the internal diffracted wave is faintly visible next to the top and bottom extremities of the refracted wave. The transmitted wave is seen past its focus at 295 and 320 μs while the internal reflected wave with the two internal diffracted waves are seen from 295 to 370 μs.

The reflected wave from the cylinder which appears barely in the lower right corner of the picture at 80 μs creates the reflected wave from the side wall well visible inside the cylinder in all other pictures. Finally, the reflected wave from the transversal beam is seen in all the pictures from 180 to 295 μs.

9.2.2. *Weak wave:* $M_s = 1.085$ (figure 9.5).

9.2.2.1 *Wave pattern.* The converging refracted wave is seen at delays from 5 to 205 μs. The internal diffracted wave appears from 115 to 185 μs as the thick black bands connected in pictures at 156 μs by an arête, undisturbed on top and strongly modified on the bottom by the diffracted wave around the beam. The internal diffracted wave is connected to the external diffracted wave up to the time delay 185 μs when both sets of waves cross on the axis. The refracted wave is refracted out as a transmitted wave which appears at or just past its focus in the picture taken at 245 μs. It is seen subsequently as it expands behind the diffracted wave, leaving at the location of its focus a focal "hot" spot (266, 279 and 329 μs). Unfortunately, any internal wave field that might occur behind the converging refracted wave is swamped by the diffracted wave around the beam and the reflected wave from the shock tube's top and bottom walls. At time delays 266, 279 and 329 μs, the complex, two folded, internally reflected

FIGURE 9.4 Interaction of a Mach 1.03 Shock Wave with a Freon 22 Cylinder

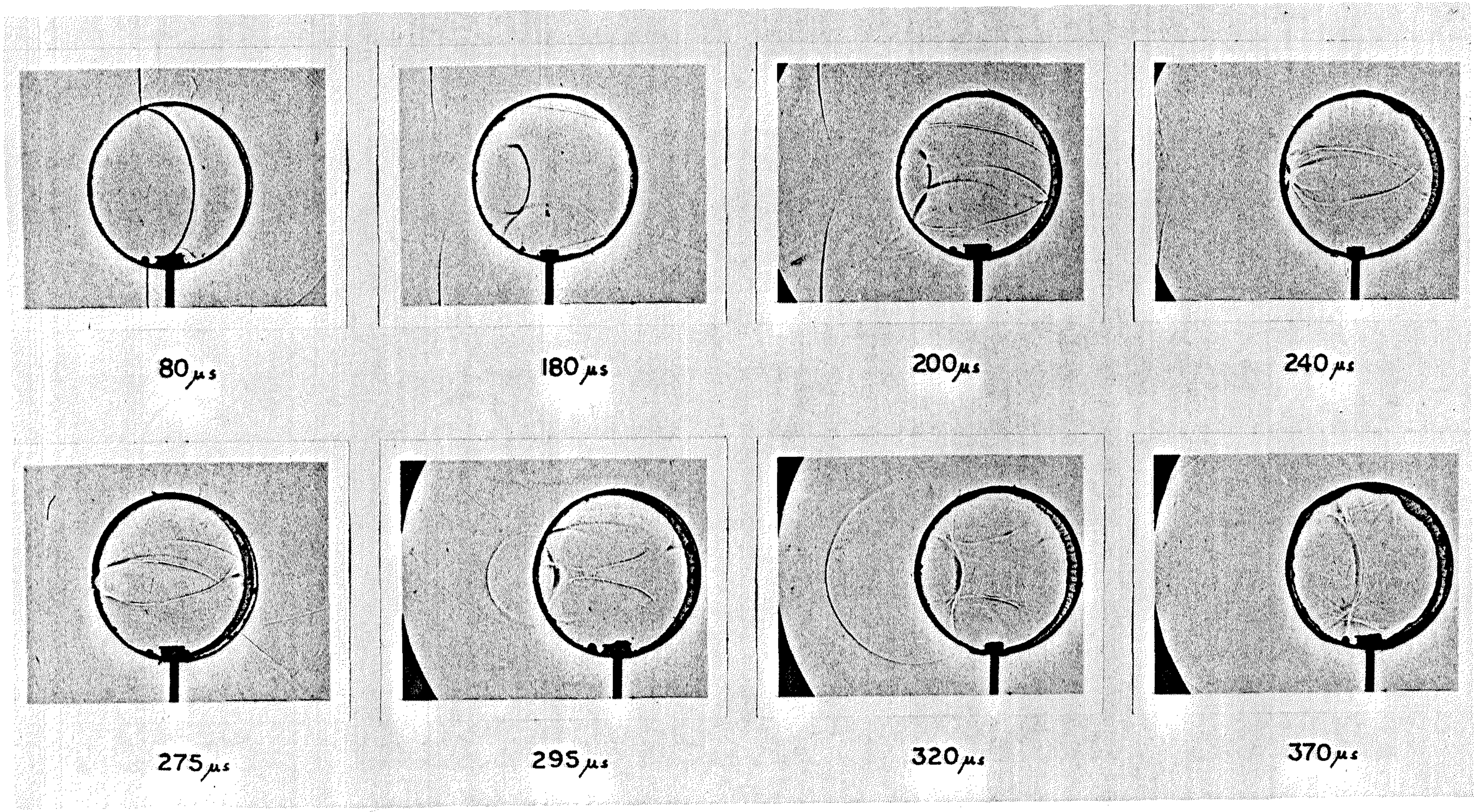

80μs 180μs 200μs 240μs

275μs 295μs 320μs 370μs

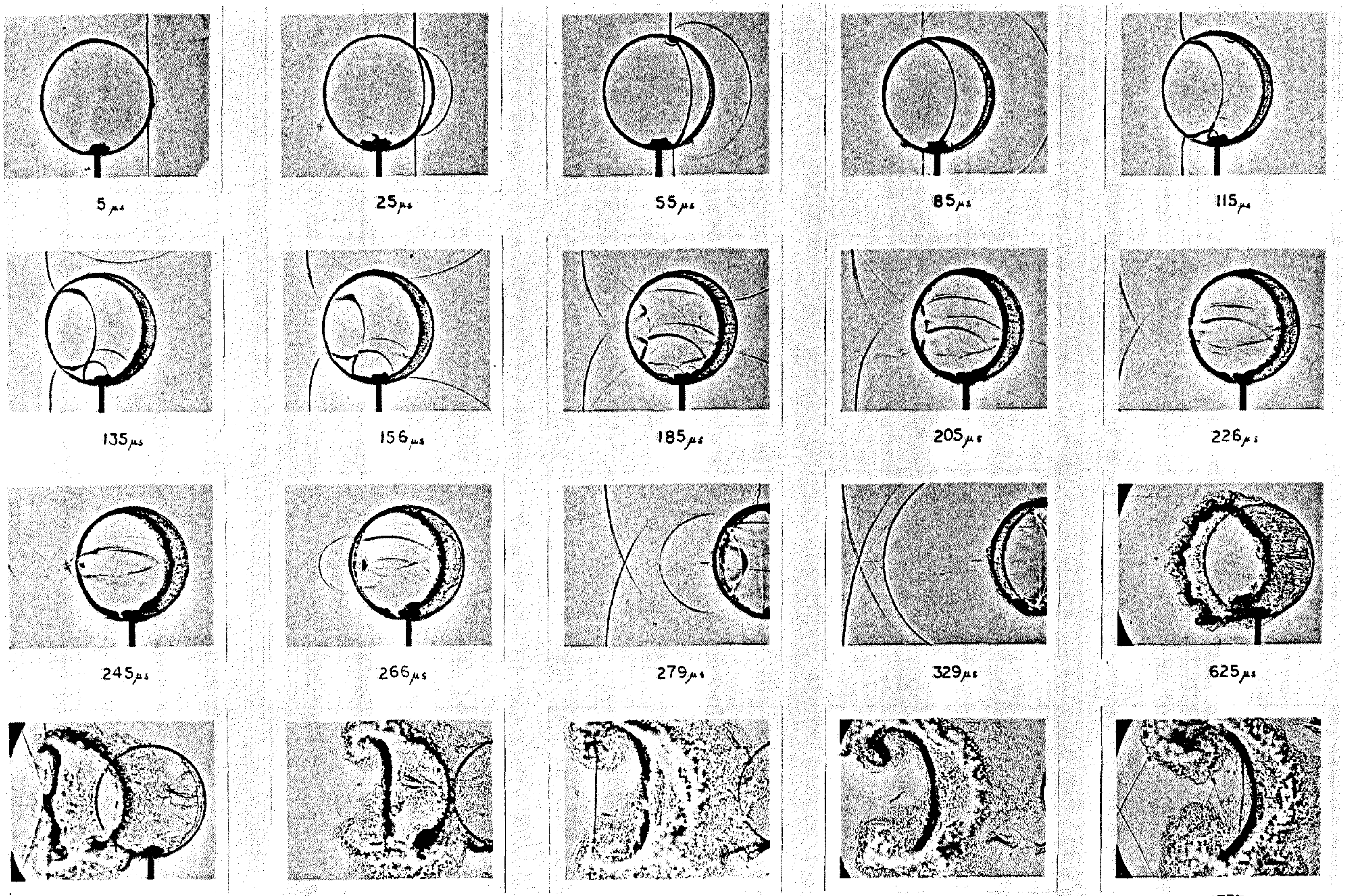

5μs 25μs 55μs 85μs 115μs

135μs 156μs 185μs 205μs 226μs

245μs 266μs 279μs 329μs 625μs

1027μs 1571μs 1972μs 2215μs 2737μs

FIGURE 9.5 Interaction of a Mach 1.085 Shock Wave with a Freon 22 Cylinder

wave pattern (from the refracted and internal diffracted waves) can be seen.

9.2.2.2 *Deformation of the cylinder.* The last six photographs illustrate the deformation of the Freon 22 cylinder with the formation of the two vortices which entrain the gas left in the center of the structure so that the downstream wedge created by the transmitted wave is eventually erased (at 625 and 1027 μs) as the waist of the structure becomes thinner (1571 μs to 2737 μs). The wave pattern seen in photographs at 1027, 1972 and 2737 μs is reflected from the shock tube end wall and has not had time to deform the Freon structure shown.

9.2.3. *Strong wave : M_s* = 1.22 (figure 9.6).

9.2.3.1 *Wave pattern.* The same pattern described above occurs for the stronger shock. Again, the bar seen at the bottom of the cylinder creates a strong thick wave propagating upwards which can be followed from the frame at 95 μs to the one at 247 μs. The contrast between the thin, well-defined refracted wave seen between the frames 25 to 167 μs and the thick black waves on the top and bottom of the cylinder converging towards the axis due to the internal diffracted waves (75 to 167 μs) is striking. The shape of the arête connecting the two waves is interesting and not fully understood (135, 167 and 187 μs). The thick internal diffracted fronts which are connected to the external diffracted wave cross each other (187 μs) well before the internal refracted wave completes its focus (217 μs). The short front, connecting the junction between the internal diffracted and refracted waves to the cylinder boundary, seen in frames from 115 to 187 μs is not understood. Similarly, the curved lines slightly ahead of the left edge of the cylinder and of the refracted wave at time 167 μs are mysterious. Perhaps it is only an optical effect. The irregular shaped waves seen inside the cylinder, in front of the refracted wave and connected to one branch of the diffracted wave (frames 25, 95 and 115 μs) and outside of the cylinder (frames 135 and 167 μs) are due to the shock propagating in the narrow gap between

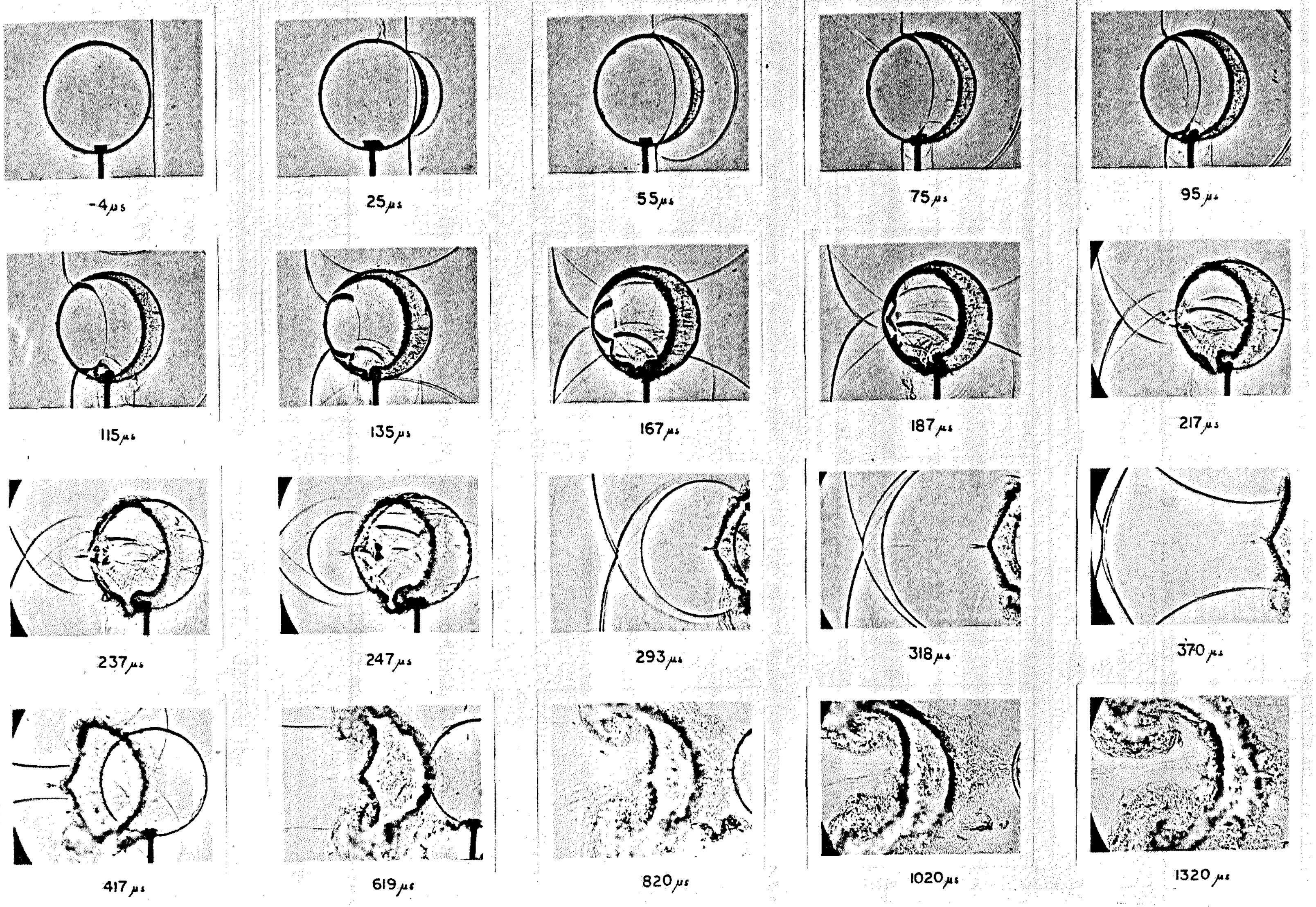

FIGURE 9.6 Interaction of a Mach 1.22 Shock Wave with a Freon 22 Cylinder

one of the cylinder side glass windows and the shock tube window where there is a mixture of air and Freon. The transmitted wave is seen expanding after its focus (217 to 370 μs) as it catches up with the diffracted wave whose two branches have combined to form a Mach disk followed by the triangular shaped set of slipstreams (293 to 370 μs). The focal "hot" spot delimited by the stronger set of slipstreams left by the transmitted wave can be seen in frames from 251 to 820 μs. The waves due to the reflection from the top and bottom walls of the shock tube of the external reflected wave are seen in the frames from 115 to 247 μs where they merge with the diffracted wave and the transmitted wave. The transversal waves observed in frames from 370 to 619 μs are due to the reflection from the shock tube walls of the transmitted wave.

9.2.3.2 *Deformation of the cylinder.* While the right side (or upstream side) of the Freon cylinder has been moving since the arrival of the incident shock, the left or downstream side is brought in motion only with the passage of the transmitted wave which creates the wedge growing just behind the focal spot (from 237 to 619 μs). When the two vortices develop (from 417 μs to 1320 μs) they entrain Freon from the core of the structure which becomes thinner. Normally, it should be more and more stretched, but the structures at later times are disturbed by the presence of the shock tube walls which forces the top vortex to pass in front of the lower one. This behavior starts to appear on the last picture at 1320 μs. The idealized representation of the Freon cylinder deformation is shown in the figure 9.7.

9.2.4. *Image distortion.* The large difference of the optical index of refraction of air and Freon 22 causes a significant distortion of the image. This is apparent in some regions of the shadowgraphs of the Freon structures at long time delays : from 1027 to 2737 μs for the weaker case (figure 9.5) and from 417 to 1320 μs for the stronger one (figure 9.6). The information about the scale of

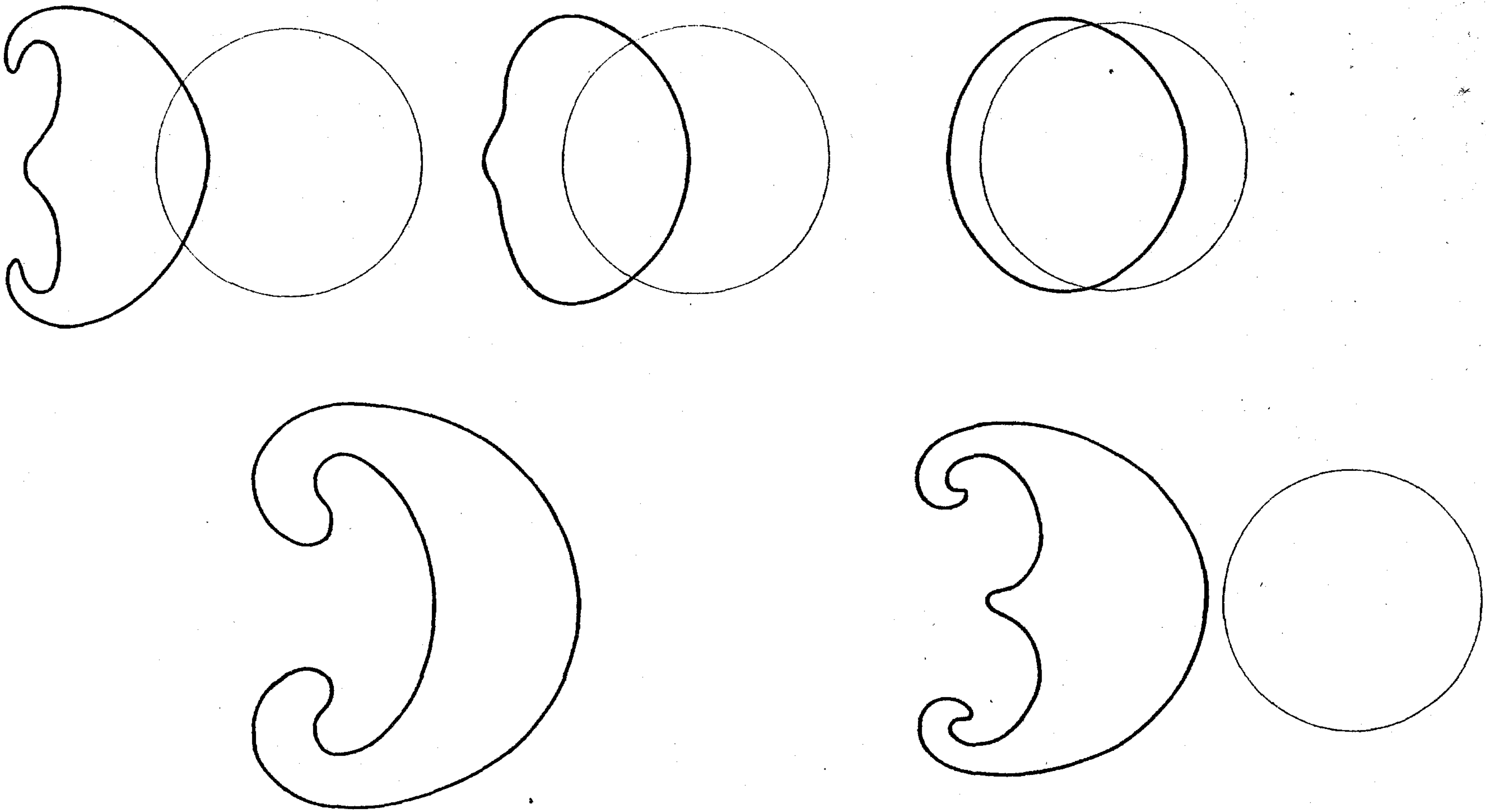

FIGURE 9.7 Schematic Representation of the Deformation of the Freon 22 Volume

the turbulence in these regions is therefore lost. Optical distortion might also create the complicated pattern near the focal region, inside and ouside the cylinder (at 217 μs in figure 9.5 and from 217 to 247 μs in figure 9.6).

9.2.5. *Comparison of shock wave focusing.* The focal hot spot obtained in the weaker case (figure 9.5, delay 279 μs) appears limited in size while the one obtained in the stronger case (figure 9.6, delay 237 and 247 μs) apparently continues downstream even though it can be distinguished only for a short distance because of the lack of sensitivity of the shadowgraph. In a study of shock wave focusing by concave cylindrical reflectors, Sturtevant and Kulkarny (1976) have found a similar difference in the geometry of the focal hot spot obtained after reflection of a Mach 1.1 and 1.2 shock wave (figure 5, op. cit.). It appears that the transition between the strong focusing and weak focusing behavior occurs roughly at the same incident Mach number for both configurations.

Chapter 10

VELOCITY MEASUREMENTS

10.1. Methodology

The various features which are observed in the shadowgraphs (shock waves, gas interfaces, etc.) move with a velocity which can be estimated by plotting their distance from a reference position against time and measuring the slope of those lines on a x-t diagram. Because the gases in the interior and exterior of the cylinder are contaminated, there is some scatter of the value of the speed of sound inside and outside. There is also a small variation of the strength of the incident wave because the diaphragms do not rupture always at the same pressure difference. Therefore a method using series of still photos from several runs at different time delays is not precise. The velocities of the various gaseous features such as interfaces, jets and vortices could not be measured simply by any other way. The measurement of the velocity of the waves is used in conjunction with the calculation of the Mach number of the waves obtained from pressure measurements (Chapter 11).

We present here two x-t diagrams, one for the helium case (figure 10.1) and the other for the Freon case (figure 10.2). The origin of distance is the upstream edge of the cylindrical cell and the zero in the time axis is the instant at which the incident shock touches that edge. In the shadowgraphs showing the early moments of the interaction, the outlines of the cylindrical cell can be seen and distances can be measured directly on the picture. When the refraction cell is positioned to the right of the window axis using holders of various lengths (55, 100, 182 and 272 mm) in order to record the gas structure as it passes in the flow visualization area at longer time delays, the times and distances for the x-t diagram are corrected accordingly.

10.2. Helium cylinder

The conceptual x-t diagram of the interaction of a shock wave with a helium filled cylinder is shown in figure 10.1 in which the features seen on the shadowgraphs are defined. As most of the x-t diagram is made of straight line segments it is convenient to discuss the features in terms of their slopes, i.e. their velocities.

The velocity of the refracted wave V_R, and of the transmitted wave V_T are measured from their positions on the shock tube longitudinal axis. The incident wave velocity V_s, then the diffracted wave velocity V_D, are measured from the shock position on the top and bottom of the shadowgraph's field of view, that is, outside the acoustical shadow of the cylinder. The velocity of the intersection of the two branches of the diffracted wave (V_D on axis) is also measured.

The gas interface velocities, except the vortex pair, are measured on the shock tube longitudinal axis: V_{u_i} is the initial upstream gas interface velocity, V_{d_i} is the initial downstream gas interface velocity, V_j is the velocity of the forward edge of the instability driven air jet in helium, and V_v is the velocity of the forward edge of the helium vortex pair which resulted from the air jet. The instant at which the transition from the air jet to the helium vortices occurs defines an important time scale t_v in the motion of the gas. V_{u_i} and V_{d_i} are valid for the velocities up to that time t_v, while V_{u_f} and V_{d_f} give the interface velocities for time delays larger than t_v. The time t_j defines the instant at which the air jet starts developing.

The measured velocities (in m/s) and the time scales t_v and t_j (in μs) are given in table 10.1. The measured values can be compared with the results (shown in table 10.2) of the calculation of the one-dimensional interaction of a

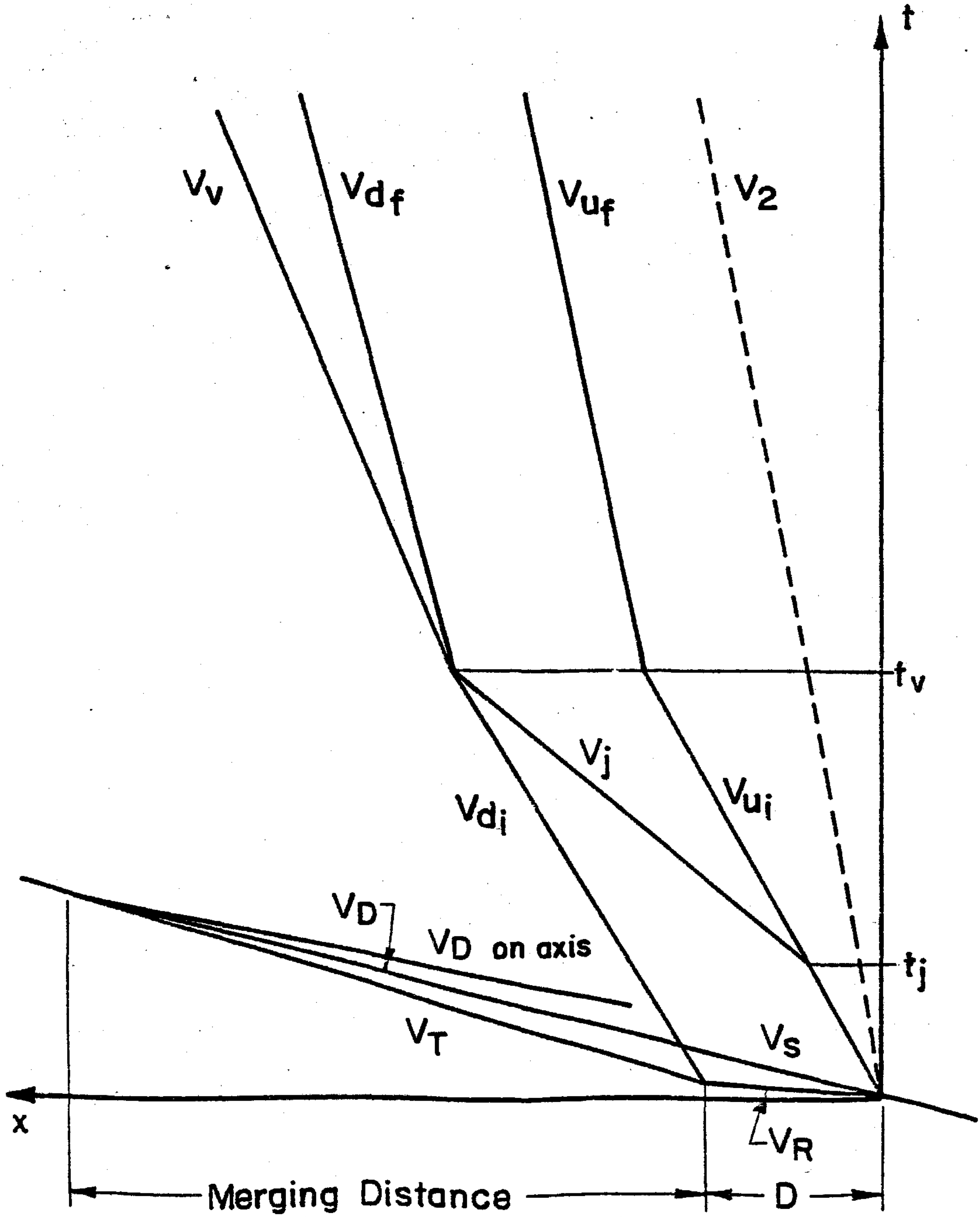

FIGURE 10.1 Schematic x-t Diagram for the Helium Cylinder

shock wave with a volume of helium, i.e., a section of the shock tube filled with helium with plane upstream and downstream interfaces. (Speed of sound in air is 342 m/s; in helium, 1010 m/s.) In table 10.2 the interface velocities are valid only at the initial times before the internal wave reflected from the downstream interface reaches the upstream interface.

Table 10.1. Measured velocities from the interaction with the helium cylinder

M_s	V_s	V_D *onaxis*	V_R	V_{u_i}	V_{d_i}	t_j	t_v	V_{u_f}	V_{d_f}	V_j	V_v
1.085	400	–	950	89	69	250	1200	43	--	125	60
1.22	410	500	900	170	145	100	700	113	97	230	128

Table 10.2. One-dimensional interaction with air-helium interfaces

M_s	V_s	V_2	M_R	V_R	M_T	V_T	V_{u_i}	V_{d_i}
1.085	371	46.5	1.035	1040	1.05	361	52	28
1.22	417	114	1.085	1090	1.13	389	123	70

The important differences between the measured and calculated wave velocities are mainly due to the imprecision of the x-t diagram method. The lower measured value of the refracted wave velocity indicates in addition that the contamination by air of the helium inside the cylinder is significant. As the Mach number of the refracted wave is approximately known (§ 11.1), a rough estimate of the speed of sound inside the cylinder can be made: 910 m/s for the weak shock case and 830 m/s for the strong one. The first value, 10 % less than the speed of sound in helium, corresponds to a air-helium mixture with a mass fraction of air of 22 %, a volume fraction of air of 3 % and a density 20 % above the density of helium.

Using a crude one-dimensional analysis, one would expect that a helium inhomogeneity is accelerated by the shock to a velocity higher than the air velocity V_2 in the adjacent ray tubes where the incident shock wave is unperturbed and that vorticity is produced on the sides of the helium volume where the velocity gradients are important. However, as the one-dimensional model predicts very low positive values for $V_{u_i} - V_2$ (5.5 and 9 m/s) and even negative values for $V_{d_i} - V_2$ (-18.5 and -44 m/s), it is inadequate in explaining the mechanism of vorticity production. Fortunately, the differences between the measured interface velocities and V_2 and the relative jet velocity ($V_j - V_{u_i}$) as well as the relative vortex velocity ($V_v - V_{u_f}$) are larger (table 10.3).

Table 10.3. Relative velocities of the helium volume

M_s	$V_{u_i}-V_2$	$V_{d_i}-V_2$	$V_{u_f}-V_2$	V_j-V_2	V_v-V_2	$V_j-V_{u_i}$	$V_v-V_{u_f}$
1.085	42.5	22.5	-3.5	80	13.5	36	17
1.22	56	31	-1	124	14	60	15

These velocity differences indicate that the upstream interface acquires initially a high velocity and this is followed by the rapid growth of the jet of air in helium. Both events can be explained by the concept of the generalized Taylor instability. The shock accelerates the interface in a stabilizing direction and this causes the flattening of the upstream interface. However, the velocity field thus created maintains itself and this leads to the formation of the spike or jet of air which therefore is in fact an instability. The mechanism is discussed in § 15.1. On the other hand, the downstream interface doesn't accelerate much. At later times, once the vortex pair starts to develop, the upstream edge of the structure slows down to a velocity close to V_2. The fact that the same relative vortex pair velocity has been measured for the two shock strengths reflects the difficulty of measuring the vortex position and an unexplained higher contamination by air inside the refraction cell for the strong shock case. A further discussion of the vortex velocity appears in § 15.2.

10.3. Freon cylinder

The x-t diagram for the Freon cylinder is shown in figure 10.2. V_s, V_T and V_R are the incident, transmitted and refracted wave velocities. V_j refers now to the velocity of the short-lived Freon jet in air which grows on the downstream edge behind the transmitted wave. The velocity of the upstream edge has an initial value V_{u_i} and final value V_{u_f}, and the transition between the two occurs at a time of approximately 400 μs. The velocity V_D is the velocity of the intersection of the two branches of the diffracted wave on the shock tube longitudinal axis. The one dimensional calculation predicts the wave and interface velocities appearing in table 10.4. (Speed of sound in air, 342 m/s; in Freon, 182 m/s) The velocities measured from the x-t diagram are shown in table 10.5. Based on the refracted wave velocity and its Mach number calculated from the pressure profiles, the mean speed of sound is estimated to be between 180 and 190 m/s, at most 4% higher than the speed of sound in pure Freon, indicating a mass concentration of air of less than 3.4% or a volume concentration of air less than 10%. As expected, the upstream and downstream edges of the Freon volume

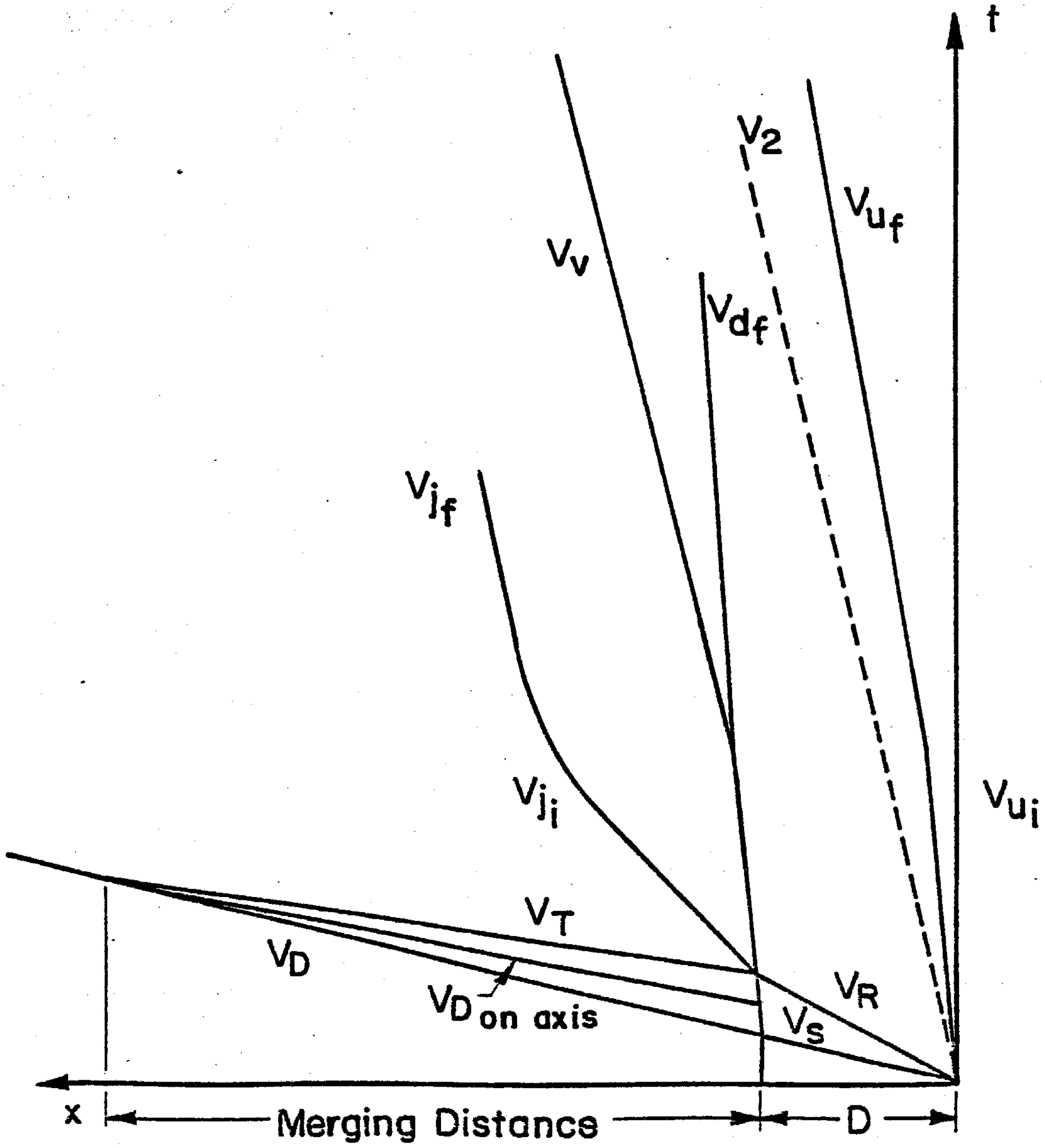

FIGURE 10.2 Schematic x-t Diagram for the Freon 22 Cylinder

Table 10.4. One-dimensional interaction with air-Freon interfaces

M_s	V_s	V_2	V_R	V_{u_i}	M_T	V_T	V_{d_i}
1.03	352	17	189	13	1.025	350	14
1.085	371	46.5	204	38	1.07	366	39
1.22	417	114	237	89	1.17	400	90

Table 10.5. Measured velocities from the interaction with the Freon cylinder

M_s	V_s	V_D *on axis*	V_R	V_T	V_{u_i}	V_{d_i}	V_{u_f}	V_{d_f}	V_j	V_v
1.03	364	--	184	447	--	--	--	--	--	--
1.085	382	450	220	510	42	0	35	35	--	60
1.22	415	470	240	540	73	0	90	78	153	130

move slower than air does behind an unperturbed shock. On the other hand the two vortices which develop at later time are marginally faster. The two vortices should move somewhat slower than the air around them because they are created by the shear of the air on an initially much slower moving Freon cylinder (§ 15.2). The fact that their velocity is higher than V_2 indicates that the diffracted and transmitted waves behind the cylinder have either accelerated the air behind them less than an undisturbed shock would have or, more likely, that the vortices have acquired a higher speed because of their interaction with the shock tube side walls (§ 9.2.3.2). The Freon jet, created by the focus of the transmitted wave, is relatively fast but quickly stops growing and disappears.

Chapter 11

PRESSURE MEASUREMENTS

11.1. Pressure measurements inside the refraction cell

11.1.1. *Modified refraction cell.* The strength of the refracted wave was measured by using a cylindrical cell in which a wide and thick plate for mounting a piezoelectric transducer replaced the connecting beam (figure 8.2). The cylinder is installed in the shock tube with the plate vertical so that the transducer measures the pressure rise after reflection of the refracted wave. The transmitted wave is not plane, but converging in the case of a Freon 22 filled cylinder, diverging in the case of the helium filled cylinder. Therefore, the refracted wave Mach number varies inside the cylindrical cell. In the case of helium it should be weaker than the one obtained with a plane interface, normal to the shock propagation, and stronger in the case of Freon 22. It is assumed that the gas composition inside the modified cell is the same as inside the original one.

11.1.2. *Results.* Table 11.1 gives, for the two gases helium and Freon 22 and for two shock strengths 1.09 and 1.22, the measured refracted Mach number and the calculated value in the one dimensional case.

The Mach numbers are calculated from the average level of the initial plateau (about 40 μs long) in the reflected wave pressure profile. It appears indeed that the measured value of the refracted wave strength in Freon 22 is higher than the calculated value. The fact that it is also the case for the refraction air/helium indicates some contamination by air inside the refraction cell, since this creates a higher acoustic impedance and consequently a stronger refracted

Table 11.1. Measured and calculated refracted wave Mach number

gas	M_s	M_R (measured)	M_R(calculated)
Freon 22	1.085	1.17	1.12
	1.22	1.37	1.31
helium	1.085	1.045	1.035
	1.22	1.08	1.085

wave.

11.2. Pressure measurements behind the cylinders

11.2.1. *Pressure profiles behind the helium cylinder.*

11.2.1.1 *Merging of the transmitted and diffracted wave.* The shadowgraph sequence (cf § 9.1) shows that the cylindrical transmitted wave (re-refracted in and out of the cylinder) runs ahead of the diffracted wave (72 μs to 160 μs in the helium cylinder sequence for M_s = 1.22, figure 9.1, and 134 μs and 157 μs for M_s = 1.085, figure 9.2). The two branches of the diffracted wave do not appear to cross each other close to the cylinder. They are caught up by the reflected wave from the cylinder after its reflection on the top and bottom walls of the test section before they can combine to become a normal shock (shadowgraphs 1 and 2 (M_s = 1.085) and 3 and 4 (M_s = 1.22) in figure 11.1).

11.2.1.2 *Pressure profiles for incident Mach number 1.085.* The pressure profiles taken at various distances behind the cylinder with a transducer mounted in the center of the instrument plate are shown in figure 11.2 for Mach number 1.085. In all cases the transmitted wave is clearly seen as a clean shock followed by a slow pressure rise leading to a triangular shaped peak

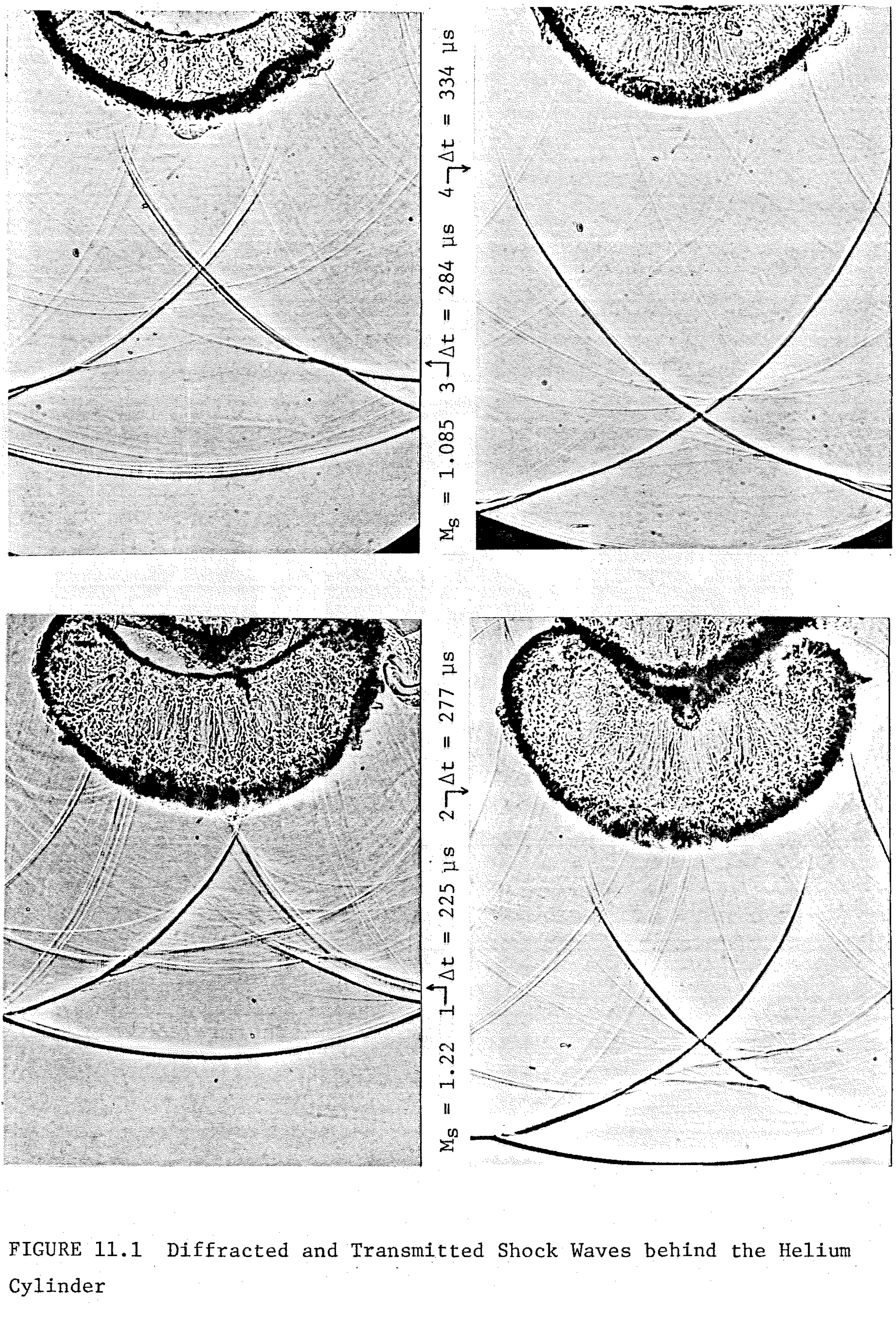

FIGURE 11.1 Diffracted and Transmitted Shock Waves behind the Helium Cylinder

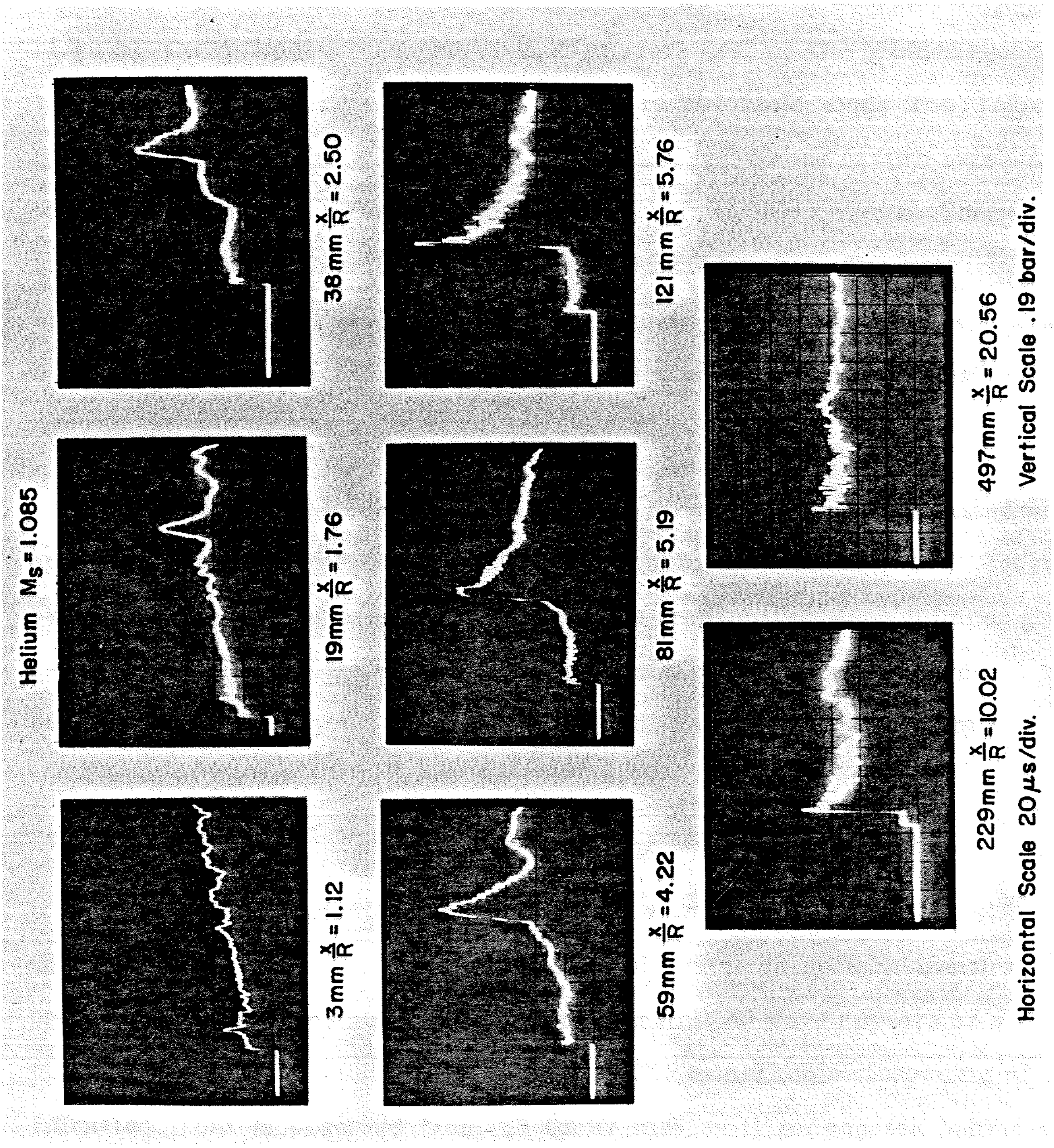

FIGURE 11.2 Pressure Profiles behind the Helium Cylinder ($M_s = 1.085$)

corresponding to the diffracted wave. On the first profile however, the diffracted wave peak doesn't appear but the small triangular peak which can be seen about 15 μs behind the transmitted shock is due to the secondary transmitted wave (§ 11.2.1.5). The diffracted wave peak which appears first on the profiles recorded 19 mm downstream of the cylinder, steepens to become a shock front followed by a rapid expansion at a distance of 81 mm and this shock in turn catches up with the transmitted wave at about 250 mm behind the cylinder. This is the merging distance of the diffracted and transmitted waves. The perturbations which appear behind the shock front on pressures profiles recorded beyond the merging distance are mostly due to the reflected waves propagating up and down in the test section.

For incident shock Mach number 1.085, the strength of the transmitted wave appears to decrease linearly from 1.045 just behind the cylinder to 1.02, 230 mm behind. A one dimensional calculation of the transmitted Mach number gives 1.054. The diffracted wave Mach number based on the pressure jump of the peak itself is 1.11. Beyond 250 mm, when the diffracted wave has caught up with the transmitted wave, the Mach number of the resulting wave is close to the incident Mach number of 1.085.

11.2.1.3 *Pressure profiles for incident Mach number 1.22.* For the stronger shock wave (figure 11.3), the diffracted wave cannot be seen in the first two profiles (2 and 23 mm) but the secondary transmitted wave appears as a small pulse 5 μs behind the initial pressure rise. The remarkable steepening of the diffracted front is observed from 33 to 97 mm as it propagates behind the transmitted wave and combines with it at 142 mm. The Mach number of the transmitted wave averages 1.12 up to 50 mm away from the cylinder, close to the estimate of 1.13 in the one dimensional case and decreases slightly to 1.10 shortly before the wave merges with the diffracted wave. Based on its local

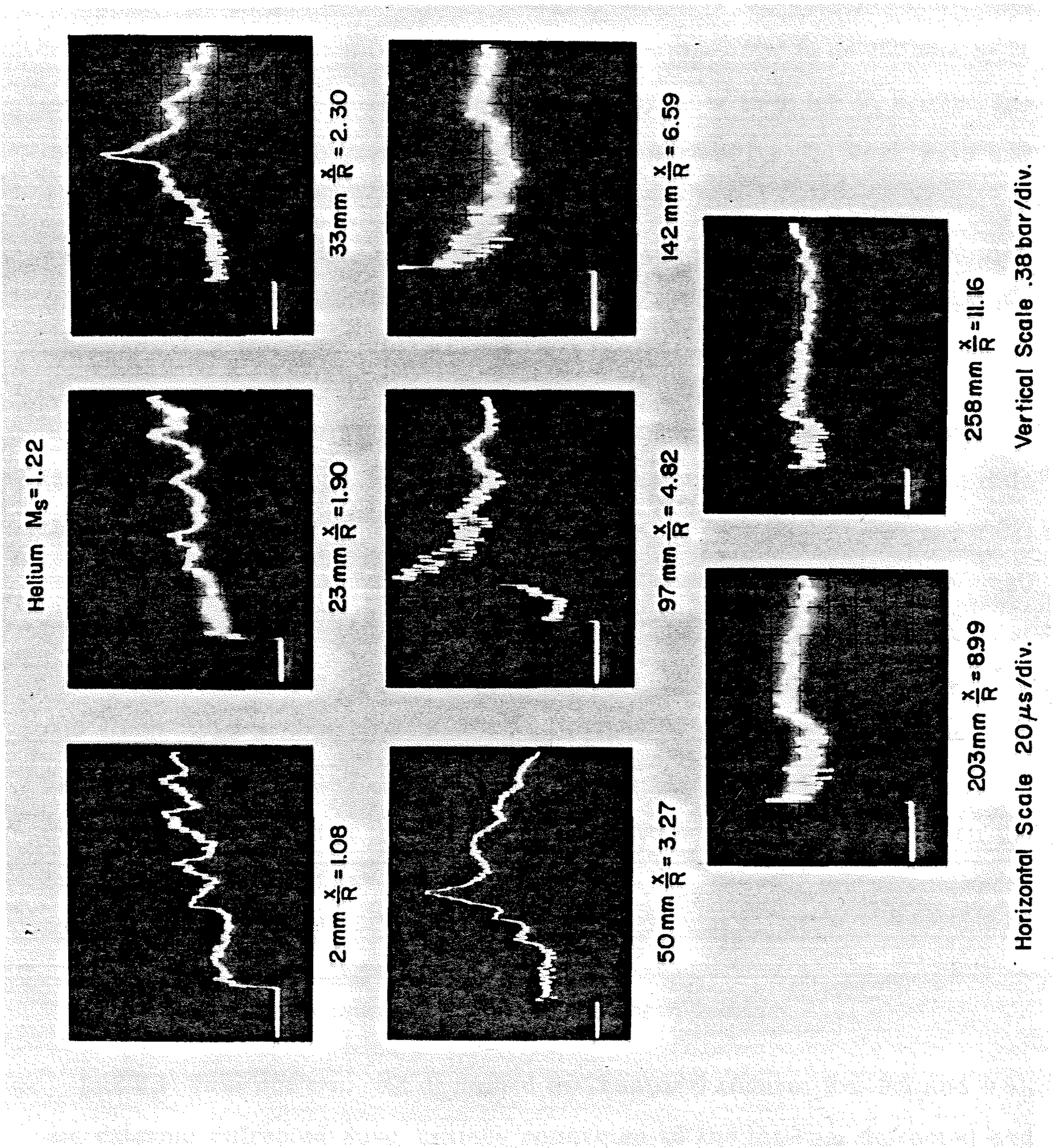

FIGURE 11.3 Pressure Profiles behind the Helium Cylinder ($M_s = 1.22$)

pressure jump, the Mach number of the diffracted shock is estimated at 1.15. When the transmitted and diffracted fronts merge, their combined Mach number is equal to the incident Mach number of 1.22.

11.2.1.4 *Merging distance.* The merging distance of the diffracted and transmitted waves behind the helium cylinder was measured to be 250 mm or 10 cylinder radii for M_s = 1.085 and 150 mm or 6 cylinder radii for M_s = 1.22. The model developed in Chapter 4 predicts 14 bubble radii for the weak wave and 4.40 bubble radii for the strong case where the approximations of the model are not justified. The shorter range of influence of the cylinder for M_s = 1.09 indicates again that the speed of sound inside the cylinder is not as high as the speed of sound of helium because of the contamination by air.

11.2.1.5 *Effect of the secondary transmitted wave.* The secondary transmitted wave corresponds to the rays which have had one internal reflection inside the cylinder. The first two pressure profiles of each case (M_s = 1.085 and 1.22) shows the presence, just behind the transmitted shock pressure rise, of a small peak, due to the secondary transmitted wave. It is most apparent on the first profile in the case M_s = 1.085 where it is half as high as the initial pressure jump and about 12 μs behind. Two shadowgraph pictures of these waves are shown in figure 11.4 with two detailed portions of the pressure profile (both recorded by a transducer 3 mm behind the cylinder), the first one after interaction with the weak shock (figure 11.4a), the other after interaction with the strong shock (figure 11.4b).

11.2.2. *Pressure measurements behind the Freon cylinder.*

11.2.2.1 *Wave pattern.* As described in Chapter 9 (figures 9.4, 9.5 and 9.6), the external diffracted wave, initially connected to the internal diffracted and the refracted shocks inside the cylinder, runs ahead of the transmitted shock

FIGURE 11.4 Effect of the Secondary Transmitted Wave

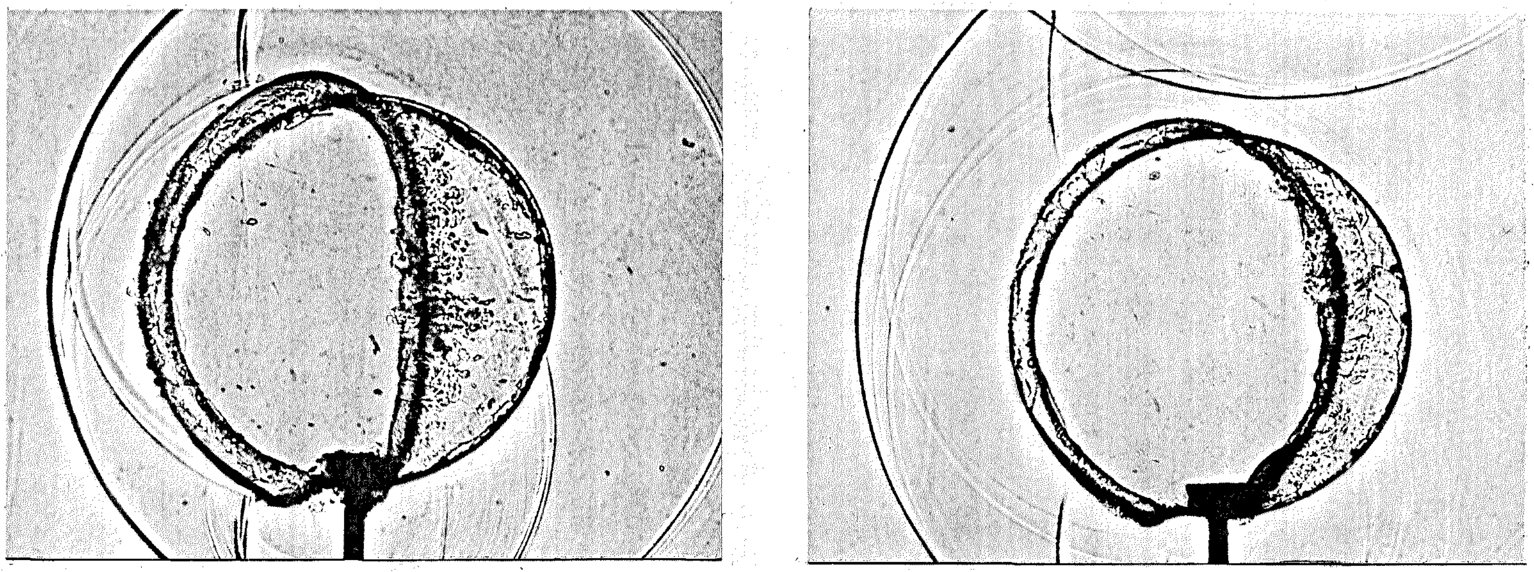

a $M_s = 1.22$ $\Delta t = 92$ µs

b $M_s = 1.085$ $\Delta t = 124$ µs

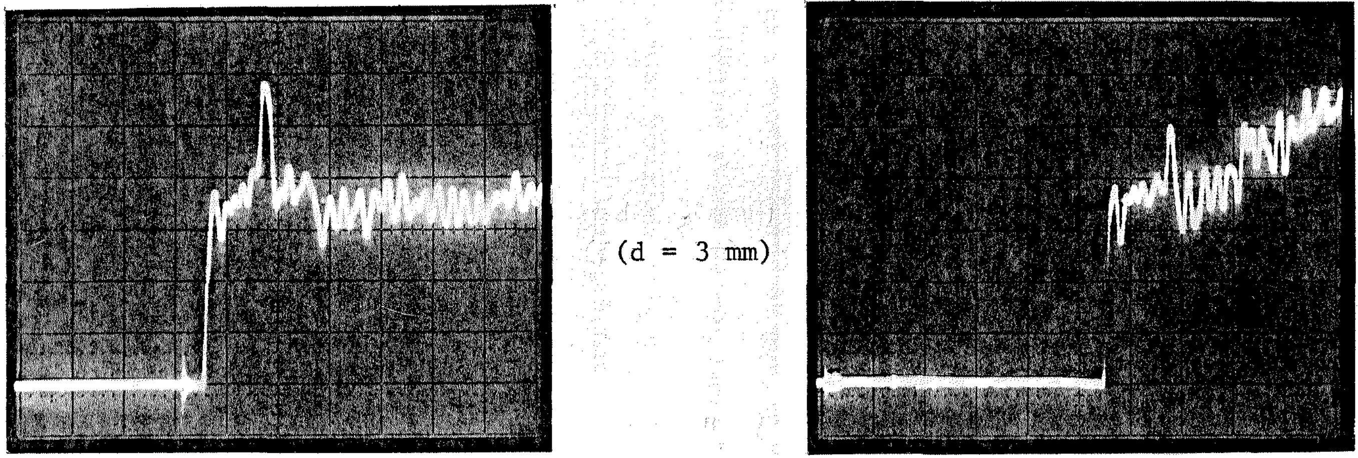

(d = 3 mm)

Vertical 190 m bar 1 div. Horizontal 10 µs/div Vertical 80 mb /div after the latter emerges outside the cylinder. The two branches of the diffracted shock cross on the axis and are caught up first by the reflected waves after reflection from the shock tube top and bottom walls and then as they have combined to form a Mach disk, by the transmitted shock.

11.2.2.2 *Strong wave*, M_s = 1.22. The formation of the Mach disk is seen at a time delay of 318 μs, or 70 mm behind the cylinder and this normal diffracted shock is caught up by the transmitted wave at a delay of 370 μs, or 96 mm behind the cylinder (figure 9.6). The pressure measurements shown in figure 11.5 indicate close to the cylinder a continuous pressure rise, due to the diffracted wave, followed by a discontinuous rise at the transmitted wave. The diffracted wave steepens (27 mm), appears as a shock (43 and 67 mm) of Mach number 1.22 and is caught up by the transmitted shock 99 mm behind the cylinder. The transmitted shock creates very high overpressures, up to 6.7 bar, directly behind the cylinder near its focus. The transmitted wave Mach number based on the pressure jump decreases from 1.22 near the focus to 1.04, just before this wave merges with the diffacted wave. The pressure profile behind the combined front beyond merging distance stays perturbed by the arrival of the various waves reflected by the shock tube side walls, the strongest one being the reflection of the transmitted wave from top and bottom walls, which appears on the profiles recorded 67, 99 and 180 mm behind the cylinder and is visualized in figure 9.6 on the frame recorded with a delay of 370 μs. For reference, the one dimensional calculation predicts a transmitted Mach number of 1.17.

11.2.2.3 *Weaker wave*, M_s = 1.085. The selection of pressure profiles given in figure 11.6 shows how the diffracted wave steepens into a shock 29 mm behind the cylinder and is caught up by the transmitted pulse before 300 mm. The diffracted wave Mach number averages 1.07 and the transmitted wave Mach number based on the pressure jump across the wave decreases from 1.065 at 29

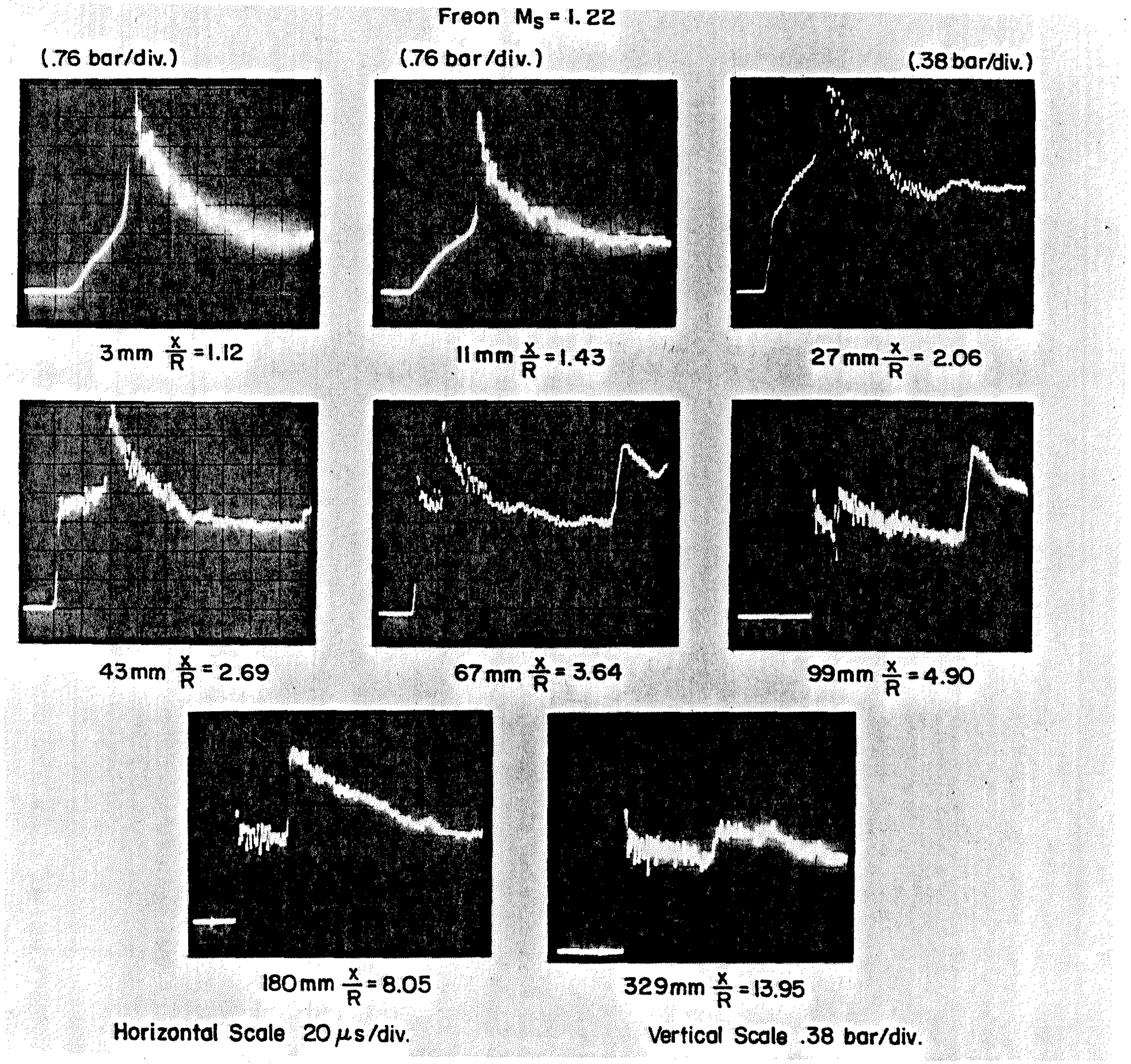

FIGURE 11.5 Pressure Profiles behind the Freon 22 Cylinder (M_s = 1.22)

mm to 1.01 at 250 mm. Beyond 300 mm, the single shock front has the Mach number of the unperturbed wave, namely, 1.085. The one dimensional calculation predicts the transmitted Mach number at 1.07. Note: the pressure profiles obtained near the cylinder are similar to the ones shown in the case of perfect line focus on figure 7 of Sturtevant and Kulkarny (1976).

The behavior of the waves can summarized by the following law:

i. the diffracted front starts weak and strengthens,
ii. the transmitted front starts strong and gets very weak,
iii. their asymptotic sum is as strong as the incident shock.

This law of course includes scattered waves which are redirected into the fluid by the walls. There are also some back reflected waves as in the one-dimensional interaction.

11.2.2.4 *Weak wave*, M_s = 1.03. The pressure jumps of the waves surveyed from the cylinder to a distance of 115 mm indicate a diffracted wave Mach number of 1.02 and a transmitted Mach number of 1.01 (figure 11.7).

11.2.2.5 *Merging distance*. The downstream range of influence or the merging distance of a Freon 22 cylinder is about 125 mm, or 5 cylinder radii, in the case of a strong wave (M_s = 1.22) and about 300 mm, or 12 cylinder radii, in the weaker case (M_s = 1.085). It is estimated to be more than 500 mm, or 20 cylinder radii, for the weakest shock (M_s = 1.03). It is an interesting fact that these values are close to the ones found for the helium cylinder.

11.2.3. *Conclusion*. A strongly converging acoustic lens such as the Freon cylinder causes the focusing of the transmitted wave very close to the downstream surface of the cylinder. Thereafter, the transmitted wave expands and the effect of the scattering fluid in the far field is reduced to the passage of two shock fronts: a relatively strong diffracted shock ahead of a weak transmitted

Freon $M_s = 1.085$

($50 \mu s$/div., Top Trace .08 bar/div.)

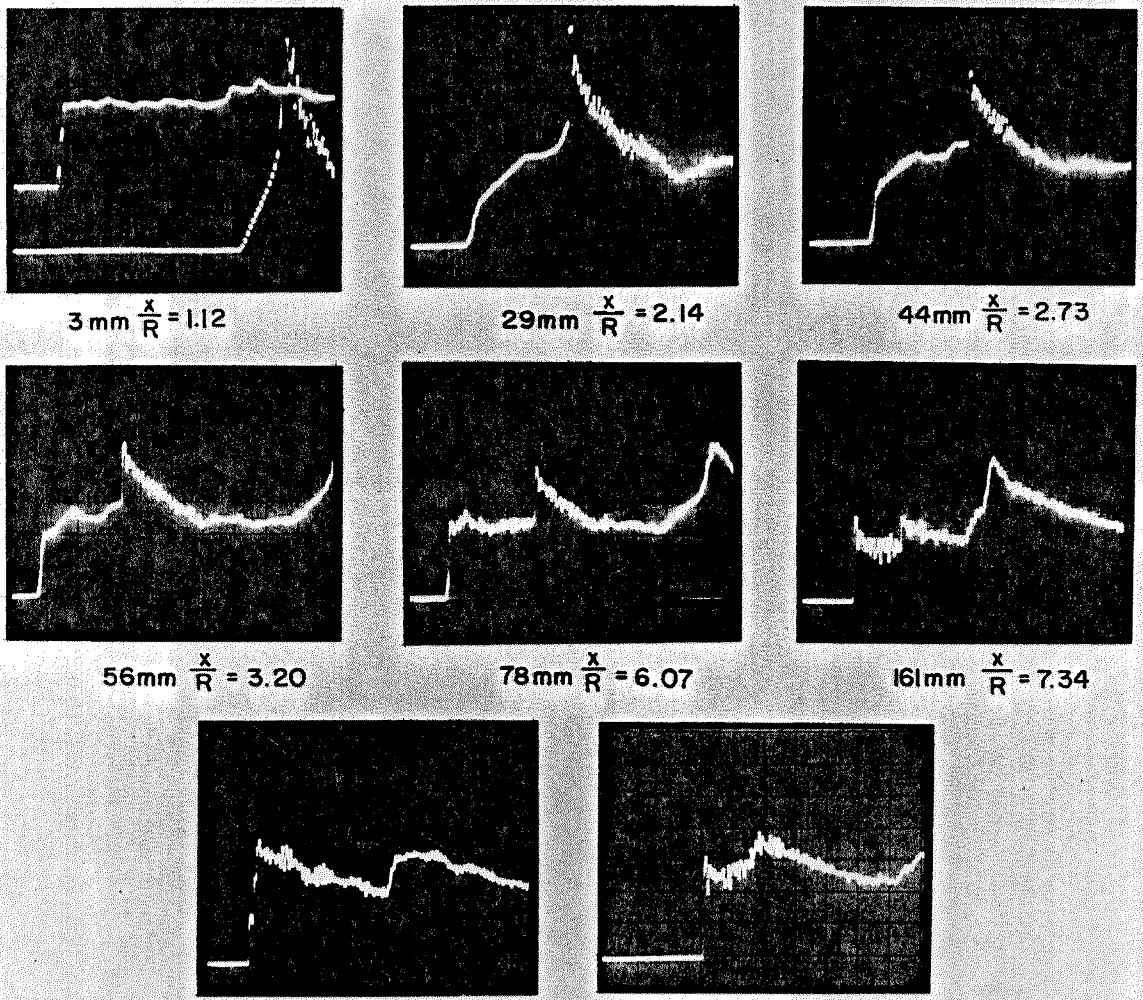

3 mm $\frac{x}{R} = 1.12$

29mm $\frac{x}{R} = 2.14$

44mm $\frac{x}{R} = 2.73$

56mm $\frac{x}{R} = 3.20$

78mm $\frac{x}{R} = 6.07$

161mm $\frac{x}{R} = 7.34$

333mm $\frac{x}{R} = 14.11$

497mm $\frac{x}{R} = 20.56$

Horizontal Scale $20 \mu s$/div.

Vertical Scale .19 bar/div.

FIGURE 11.6 Pressure Profiles behind the Freon 22 Cylinder ($M_s = 1.085$)

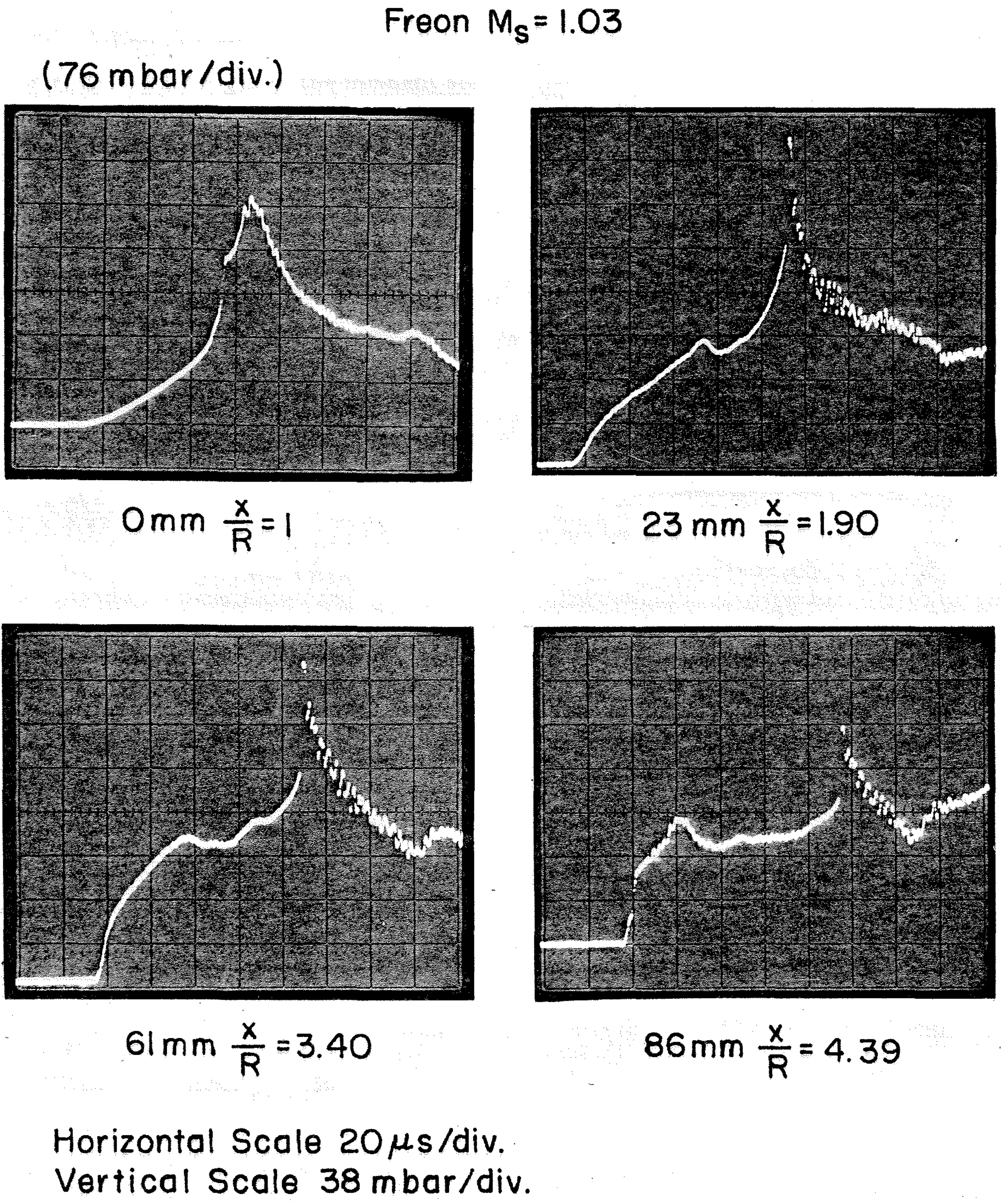

FIGURE 11.7 Pressure Profiles behind the Freon 22 Cylinder ($M_s = 1.03$)

shock. In the far field a helium scatterer has also created two shock fronts, but with a weak transmitted shock ahead of the diffracted shock which has approximately the strength of the incident shock wave.

Chapter 12

EXPERIMENTAL APPROACH TO THE THREE-DIMENSIONAL INTERACTION

12.1. Introduction

The three dimensional version of the experiment is realized with large soap bubbles filled with various gases. The technique of using soap membrane in the studies of shock wave or acoustic wave refraction is not new. The early experiments in the study of the plane shock wave refraction problem were made with soap membranes. Because of their weight and instability, these were soon replaced by the more convenient dry microfilms.

Soap bubbles were used by Davy and Blackstock (1971) in a study of the refraction and diffraction of a spark generated N wave by an argon or helium filled soap bubble. One characteristic result from this study is that the combined diffracted and refracted waveforms recorded behind the argon bubbles (a converging lens) by a microphone had the shape of a peaked N wave while the diffracted waveform measured behind the diverging lens, the helium bubble, was a rounded N wave.

In studies of shock wave and flame interaction, Rudinger (1958) observed the interaction of a helium filled soap bubble held on a ring and a shock wave and reported on a formation of a spike of air driven in the bubble which eventually becomes a vortex ring. The same behavior was found for the interaction of a shock wave with a spherical region of burnt gas which is called a flame bubble. That experiment was made by Markstein and is reported within the discussion at the end of the above-mentioned reference. The only published picture of the helium filled soap bubble (page 158, figure 2b) and the text (page 159), indicate that the bubble becomes a vortex ring. However, in the case of the flame bubble, it is seen that the spike of air in the bubble drives a jet of turbulent burnt gas on the other side of the bubble (figure 8, following page 178), but the investigator still compares the main body of burnt gas to a vortex ring. While the geometry here is perturbed by the combustion process which continuously increases the volume of burnt gas at a rate proportional to the area of the flame surface area, the same pattern should appear for the helium filled soap bubble, and the resulting structure is expected to be more complex than the single vortex ring mentioned in this reference.

12.2. Experimental procedure

12.2.1. *Bubble formation.* In Rudinger's experiment the bubbles were supported by a ring which could have some influence on the initial response of the bubble to the shock wave. In order to minimize that possible effect, the bubble in the present investigation is supported by a small (6 mm diameter) cup epoxied to the end of a stainless steel tube (OD .75 mm, ID .66 mm) inserted into the shock tube by means of a port located on the roof or floor of the test section between the windows (figure 8.2). A drop of soap is deposited on the cup and the test gas is injected through the tube, initially at a very slow rate to allow a smooth start of the bubble growth without the soap spattering, and then at a constant rate (approximately 10 cm^3/s) set by a metering valve during a few seconds (usually 5 to 10 seconds), this time being controlled electronically by the bubble timer (§ 5.4.1).

The bubble was typically 45 mm in diameter. The size of the holding cup is such that the surface tension along the cup perimeter can support the load of a bubble in the worst case; namely, a bubble filled with Freon 22 supported from above.

In the early phase of this investigation, a mixture of toy soap bubble solution and glycerin (between 10% and 40% by volume) was used with some success. Later, the soap solution originally used by Plateau (Stong, 1969) proved to be more dependable, the bubbles being able to survive a few minutes in the shock tube test section. Plateau's soap solution contains in mass concentration 78% distilled water, 2% sodium oleate and 20% glycerin.

The thickness of the soap film depends on the gas in the bubble. When a helium bubble is growing, the film has initially a thickness above 1 μm and is colorless. When the final size is reached, the soap starts flowing down toward the cup, the membrane becomes thinner and thinner and tends to have a red or yellow color due to the interference of light reflected by the external and internal surface of the soap film. At the end of the life of the bubble, just before it bursts, the film is usually blue. In his classical book on soap bubbles Boys (1911) published a chart of the interference color vs. film thickness: the colors observed here indicate a film thickness between .25 and .6 μm. Heavy bubbles filled with nitrogen, argon or Freon 22 do not have very thin films since there is always a supply of soap on the cup which drains down towards the bottom and sometimes forms a drop there. The color is either absent or pale blue, and the thickness is estimated at around 1 μm. The bubbles are nearly spherical with their height at most 5% larger than their width, with the exception of the Freon 22 bubbles which are very elongated.

Once the gas flow which inflated the bubbles is stopped, they stay at a constant size which indicates that there is no significant permeation of the gases across the membrane with the exception again of the Freon 22 bubbles, for which the supply of gas had to be kept at a low rate after the bubble formation in order to keep it from shrinking.

As was the case for the experiment with cylinders, the bubbles are initially positioned between the centers of the two windows using the straight tube through the port in the test section, or at various distances upstream of that position using some bent tubes of various lengths (positions offset by 63, 161, 251 and 366 mm) such that the structure formed from the gas initially inside the bubble can be observed a long time after it has been hit by the shock wave and swept to the window location.

12.2.2. *Expected results from the 3D experiment.* The primary goal of the three dimensional experiment is the visualization of the gas mixing after the shock has been propagating through the bubble. There is very little support structure which might hinder the gas motion, in contrast to the situation in the two dimensional experiment. Furthermore the film is self destructing. Due to the smaller gas volume contained initially in a bubble, the resulting gas structure is less likely to interact with the shock tube walls.

However, the three dimensionality of the experiment introduces a certain ambiguity into the interpretation of the shadowgraph photographs. The waves are axisymmetric, so they do not form as clear an image on the shadowgraph. Furthermore, some of the features of the axisymmetric flow field do not appear clearly as well when projected on the film plane. Fortunately, since the physics of the interactions has been better explored in the two dimensional experiment, all the features observed in this experiment can be understood by deduction. In addition, this experiment presents an interesting new facet: the observation of the behavior of thin liquid films when hit by shock waves. Visualization of the disintegration of the soap film was by shadowgraphy and reflected-light photography.

12.2.3. *Reflected-light photography.* In order to observe the behavior of the soap membrane without visualizing the gases, another set of photographs were taken of the bursting bubble, side-lit through a transparent end plate of the test section by a spark gap light source. Instead of the point spark used for the shadowgraphs, a 1 cm long spark discharged in 1 μs from a .1 μf condensor at a potential of 10 kV is now used as a diffuse light source. The internal walls of the shock tube between the transparent end plate and the windows are lined with aluminum foil in order to increase the diffuse character and the intensity of the light falling on the bubble located between the windows. Two types of cameras were used to image the bubble: a 5 x 7" view camera with Polaroid film (type 57, 3000 ASA) with a magnification 1 (for the photographs appearing in Chapters 13 and 14), and a 35 mm single lens reflex camera with a 100 mm focal length lens and set at the maximum magnification of .2, loaded with 400 ASA Ektachrome film but exposed and processed at 800 ASA. The principle of recording the light reflected by the membrane or scattered at 90° by the droplets from the broken membrane was already used in the visualization of the cloud of small bubbles (§ 2.3.4).

Chapter 13

INTERACTION OF SHOCK WAVES WITH HELIUM-FILLED SOAP BUBBLES

13.1. Strong shock wave, $M_s = 1.25$

13.1.1. *Wave pattern.* Shadowgraphs taken at various delays after the shock wave has hit the upstream edge of the bubble are shown in figures 13.1 and 13.2. There is an approximate picture-to-picture time correspondence between the figure 13.1 for the three dimensional experiment and the figure 9.1 in the two dimensional experiment. (Note: the curved lines seen on frames 0 to 8 (delays 0 - 82 μs) in the lower part of the bubbles are due to the variation of the thickness of the soap membrane apparently driven by the Marangoni effect.)

In the photographs the reflected wave is seen developing from the 10 μs frame to the 82 μs frame. After its reflection from the shock tube walls, it is seen in the frames from 102 μs to 300 μs. The fact that the reflected wave always appears on the shadowgraph as a shock wave, as well defined as the transmitted wave, indicates that the weak shock wave reflected from the soap film is not completely cancelled by the reflected expansion wave expected in the interaction of the air shock with helium. The internal refracted wave is barely seen on the original Polaroid prints taken at delays 10 to 42 μs and can be distinguished in figure 13.1 only for the frame taken at 20 μs, when the wave emerges from the interior for the first time and joins tangentially the reflected wave. The transmitted wave can be seen downstream of the cylinder from 50 μs to 169 μs. It is followed closely by the secondary transmitted wave (the wave once internally reflected and then transmitted) which is ring shaped but appears on the shadowgraph as a plane front. The edges of this wave are seen in

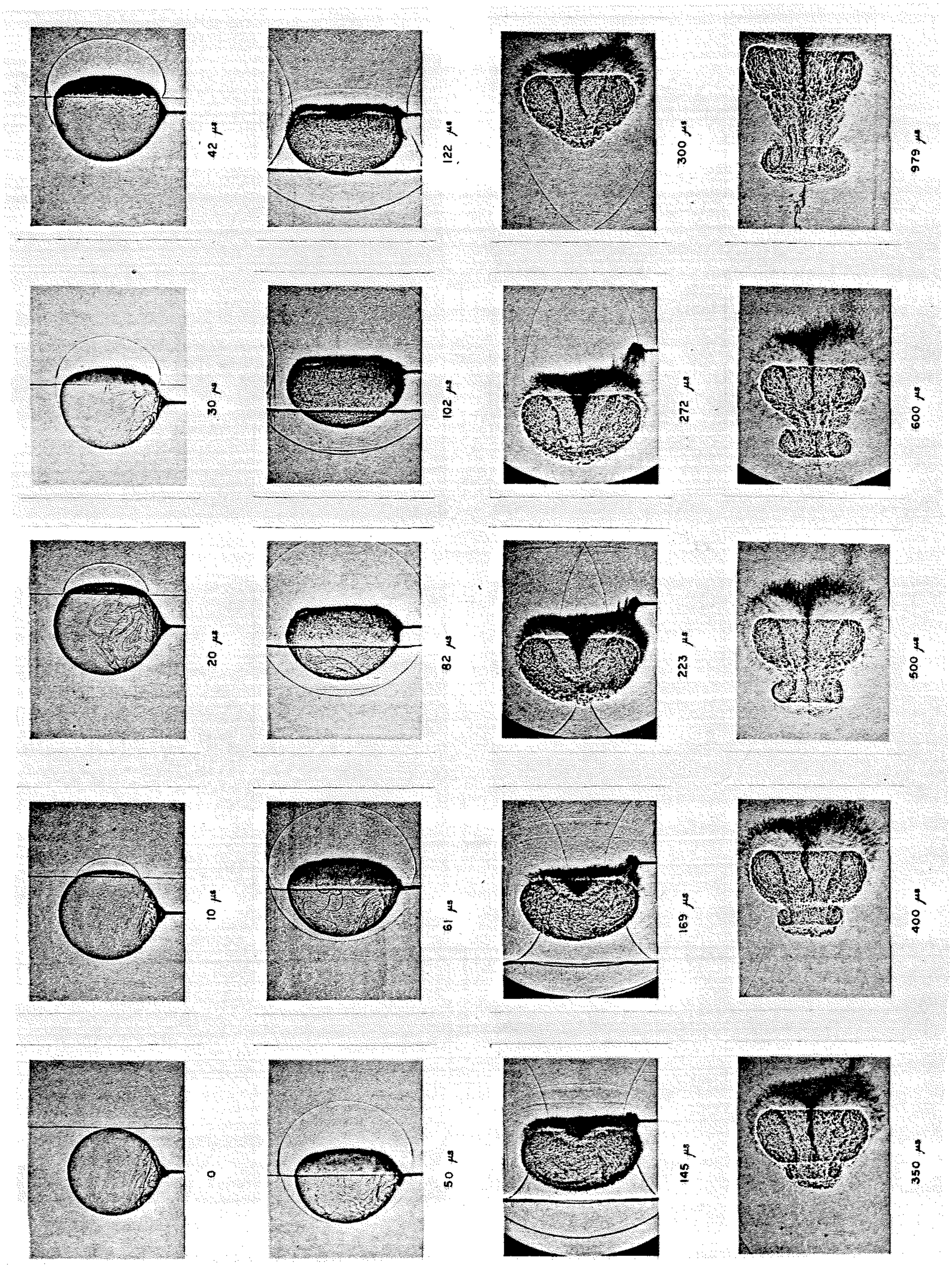

FIGURE 13.1 Interaction of a Mach 1.25 Shock Wave with a Helium-Filled Soap Bubble

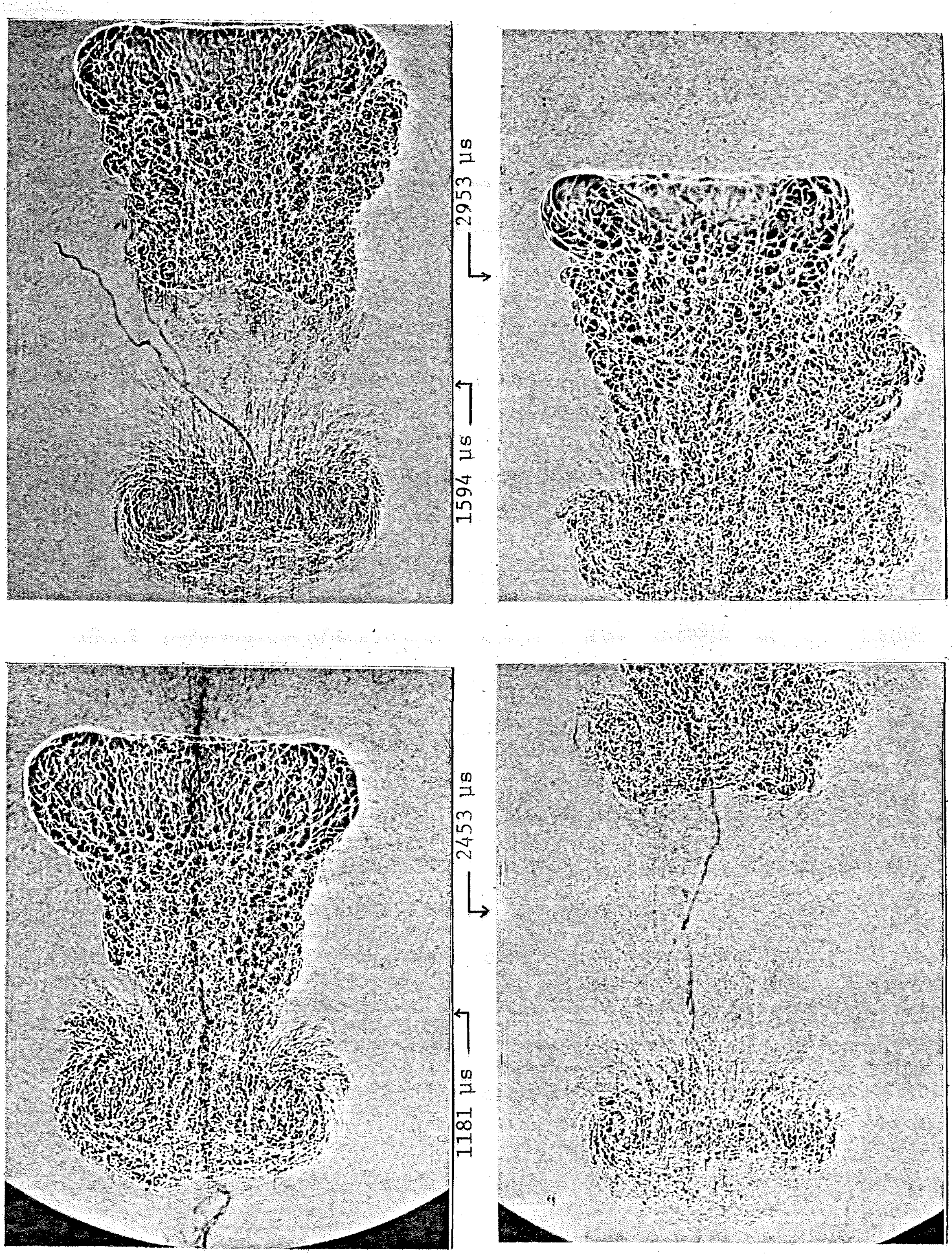

FIGURE 13.2 Mixing of an Initially Spherical Helium Volume Processed by a Mach 1.25 Shock Wave

frames at 50 μs and 61 μs. It emerges fully as a complete disk as it is catching up with the transmitted wave in frames from 82 μs to 122 μs. The diffracted wave front, also ring shaped, appears as a thicker and slightly convex wave in in frames 145 μs and 169 μs. The transmitted and diffracted waves merge about 125 mm or 5.5 bubble radii downstream of the bubble center. The range of influence predicted by the model from chapter 4 is 4.7 bubble radii.

The first backscattered wave, having been internally reflected and refracted out of the bubble, is shown in frames 122 μs to 169 μs. In spite of its similar appearance to the secondary transmitted wave, the back scattered wave is a flattened spherical wave. It is followed by the second backscattered wave which has been twice reflected inside the bubble.

13.1.2. *Deformation of the helium volume.* The motion of the helium induced by the shock wave begins with the rapid acceleration of the upstream (right) side of the bubble, which causes the flattening shown in the frames 10 μs to 82 μs. Then the front side overshoots forming a strong jet of air (frames 102 μs to 272 μs). It is shown in § 15.1 how the Rayleigh-Taylor instability of an interface accelerated by a shock causes such a behavior. The remaining frames show how the protusion of the air jet through the downstream surface of the bubble generates a helium vortex ring. Later development appears in figure 13.2 : the vortex ring separates from the main structure which itself stretches and becomes more complex, sometimes with formation of another small vortex ring (frames at 2453 μs and 2953 μs). The toroidal structure left by the primary vortex ring is seen to have little net vorticity because it is observed to be only moving at the same velocity as air behind the undisturbed shock wave. The vortex ring is noticeably faster (§ 13.3). It is interesting to note that on the two dimensional case the vortex pair grows and eventually includes all the helium initially in the cylinder while in this case the vorticity seems to be included mainly in a small portion of the volume of helium originally included in the bubble.

13.1.3. *Disintegration of the soap membrane.* Evidently, on the upstream side of the bubble the soap film film disintegrates into a fine aerosol immediatly behind the incident shock (frames 10 μs to 61 μs). However, later it is hard to distinguish it from the fine-scaled cellular structure on the boundary of the helium. On the downstream side, it is probable that the diffracted wave and the transmitted wave have a lesser effect on the membrane than the incident wave on the upstream side. The remnants of the film on the upstream side appear as fine black particles which are left behind the fast moving helium-air interface in frames 82 μs and 102 μs and which are then entrained by the strong air jet (frames 122 μs to 400 μs) through the core of the bubble and then through the vortex ring. In the last three frames (500 μs to 979 μs) they appear as a slender jet of soap droplets formed along the axis of symmetry. The fine scale cellular structure which becomes very apparent in the frame at 145 μs is due to the Rayleigh-Taylor instability on the helium-air boundary all around the bubble, which has been subjected to the unstabilizing acceleration of the transmitted wave.

13.1.4. *Observation by reflected light photography.* Reflected light pictures (figure 13.3) show how instabilities are introduced by the transmitted wave on the membrane on the downstream side of the bubble. Some perturbations appear at 80 μs and have developed into a rough pattern all around the bubble at 140 μs, at which time the incident wave has passed entirely over the outside of the bubble. Thereafter, the film disaggregates though its features remain relatively detailed up to 270 μs. After the air jet reaches the downstream side of the bubble the film is reduced to a fog of tiny droplets such as shown on the picture taken at 320 μs.

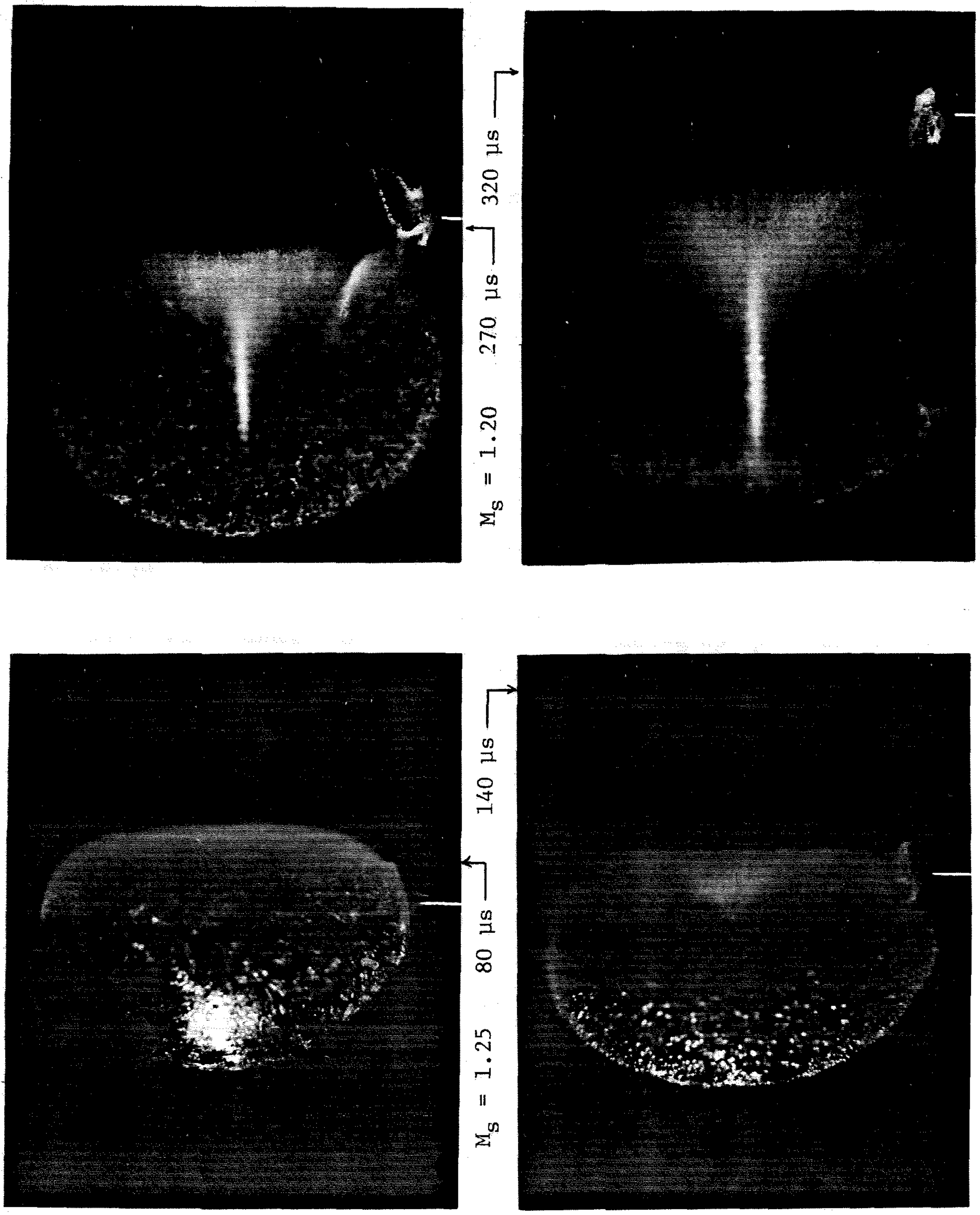

FIGURE 13.3 Disintegration of the Soap Film (Helium Bubble, M_s = 1.25)

13.2. Interaction with weaker waves

13.2.1. *Mach number 1.10.* The shadowgraphs of the interaction of a weaker wave (Mach number 1.10) with the helium bubble are presented in figure 13.4. With the weak waves, the wave pattern is hardly visible, but the same evolution of the bubble shape occurs, though at a slower pace. The upstream side of the bubble flattens, while the film rapidly disintegrates (170 μs); the air jet forms (360 to 650 μs) followed by the development of the helium vortex ring and its separation from the main helium volume (1000 to 2541 μs). The different pace is well illustrated by the fact that the helium structure on the last frame at 2541 μs is quite similar to the one obtained with the stronger shock (figure 13.2) at 1181 μs.

13.2.2. *Mach number 1.05.* The sequence of shadowgraph pictures obtained with the weakest shock wave (Mach number 1.05) is shown in figure 13.5. Although the overall evolution of the bubble shape remains very similar to the one observed for the slightly stronger case, some conspicuous large structures can now be seen in the last three pictures (1260, 1458 and 2640 μs) at the internal bondary between the spike of air and the surrounding helium torus. They are due to the Kelvin-Helmholtz instability developping at an interface between two gases moving at different velocities. Their relative velocity is given in § 13.3.2.

Figures 13.6 and 13.7 are sketches of the wave pattern and of the evolution of the helium structure representative of the two stronger shocks.

13.2.3. *Disintegration of the soap film.* The breakdown of the soap film looks quite different in the case of the weaker waves from the rapid disintegation seen in the strong wave case. In figure 13.4 (Mach number 1.10), some waves can be seen on the membrane at 170 μs and circular holes start appearing at 310 μs

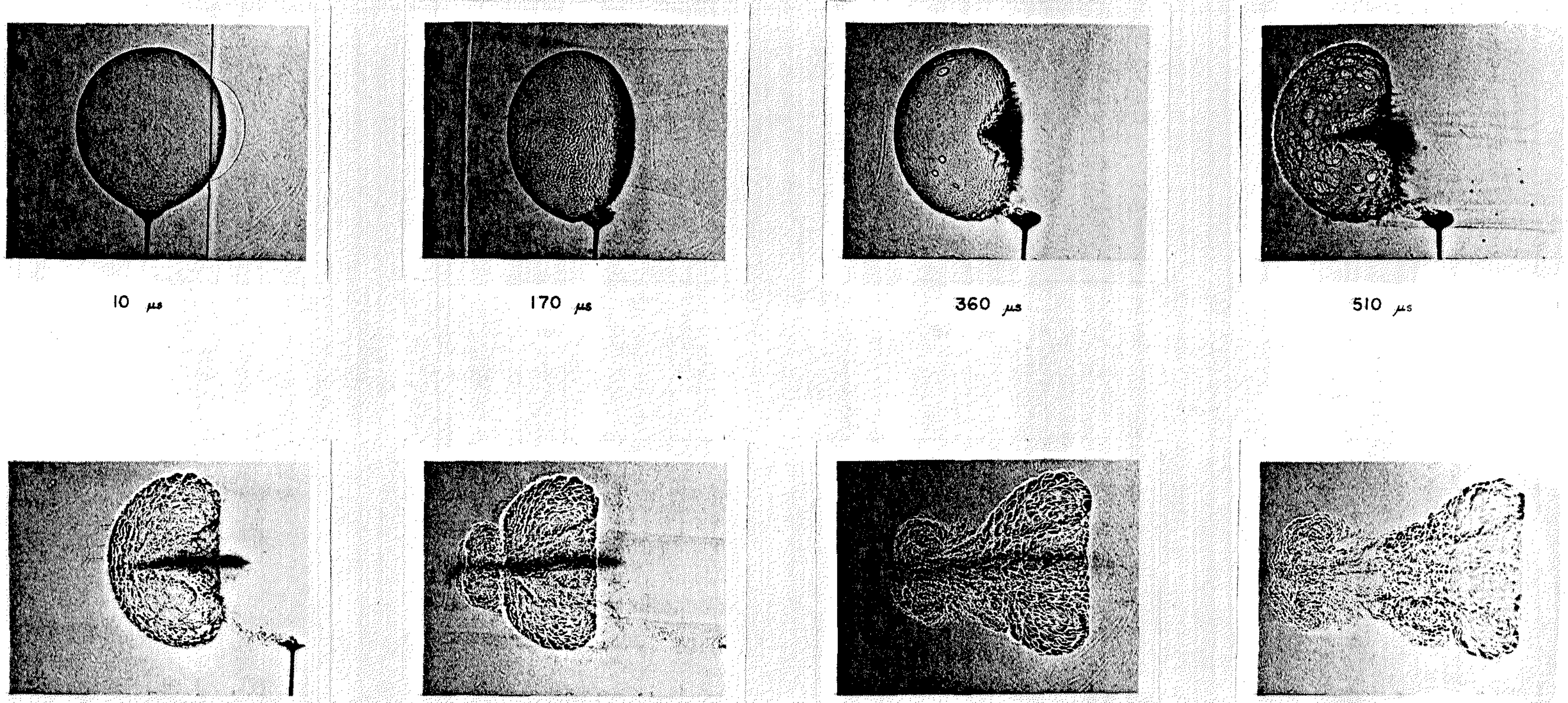

10 μs

170 μs

360 μs

510 μs

650 μs

1000 μs

1665 μs

2541 μs

FIGURE 13.4 Interaction of a Mach 1.10 Shock Wave with a Helium-Filled Soap Bubble

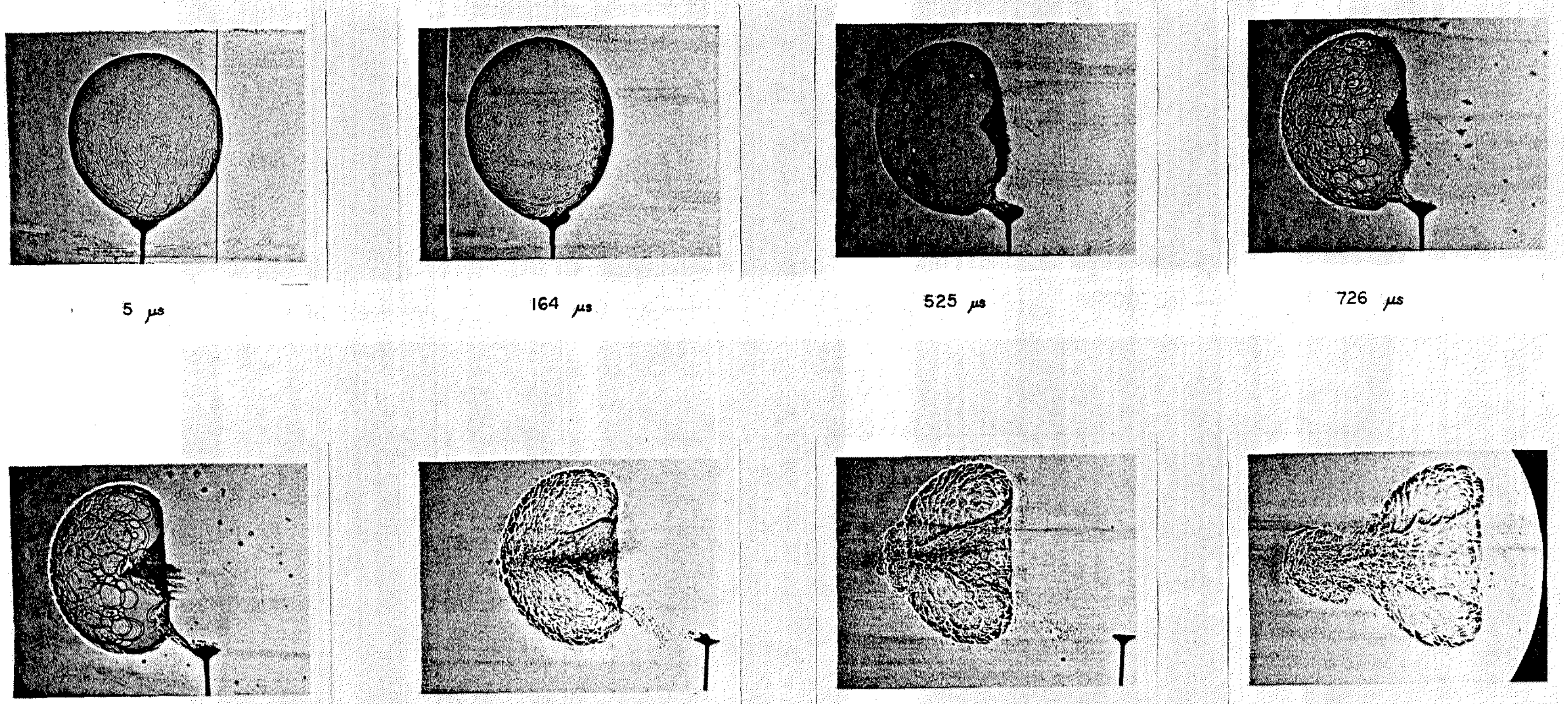

5 μs

164 μs

525 μs

726 μs

930 μs

1260 μs

1458 μs

2640 μs

FIGURE 13.5 Interaction of a Mach 1.05 Shock Wave with a Helium-Filled Soap Bubble

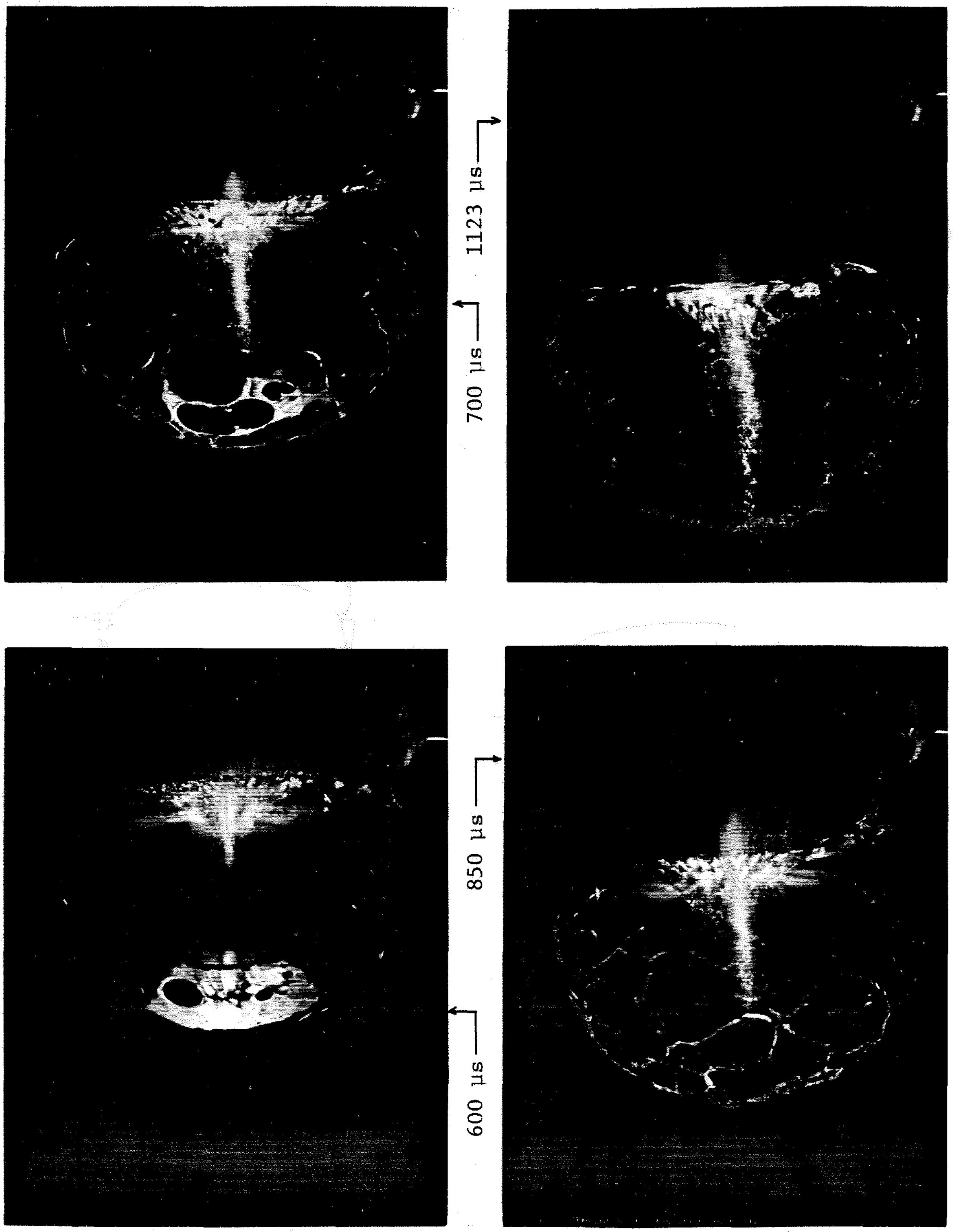

FIGURE 13.6 Disintegration of the Soap Film (Helium Bubble, M_s = 1.05)

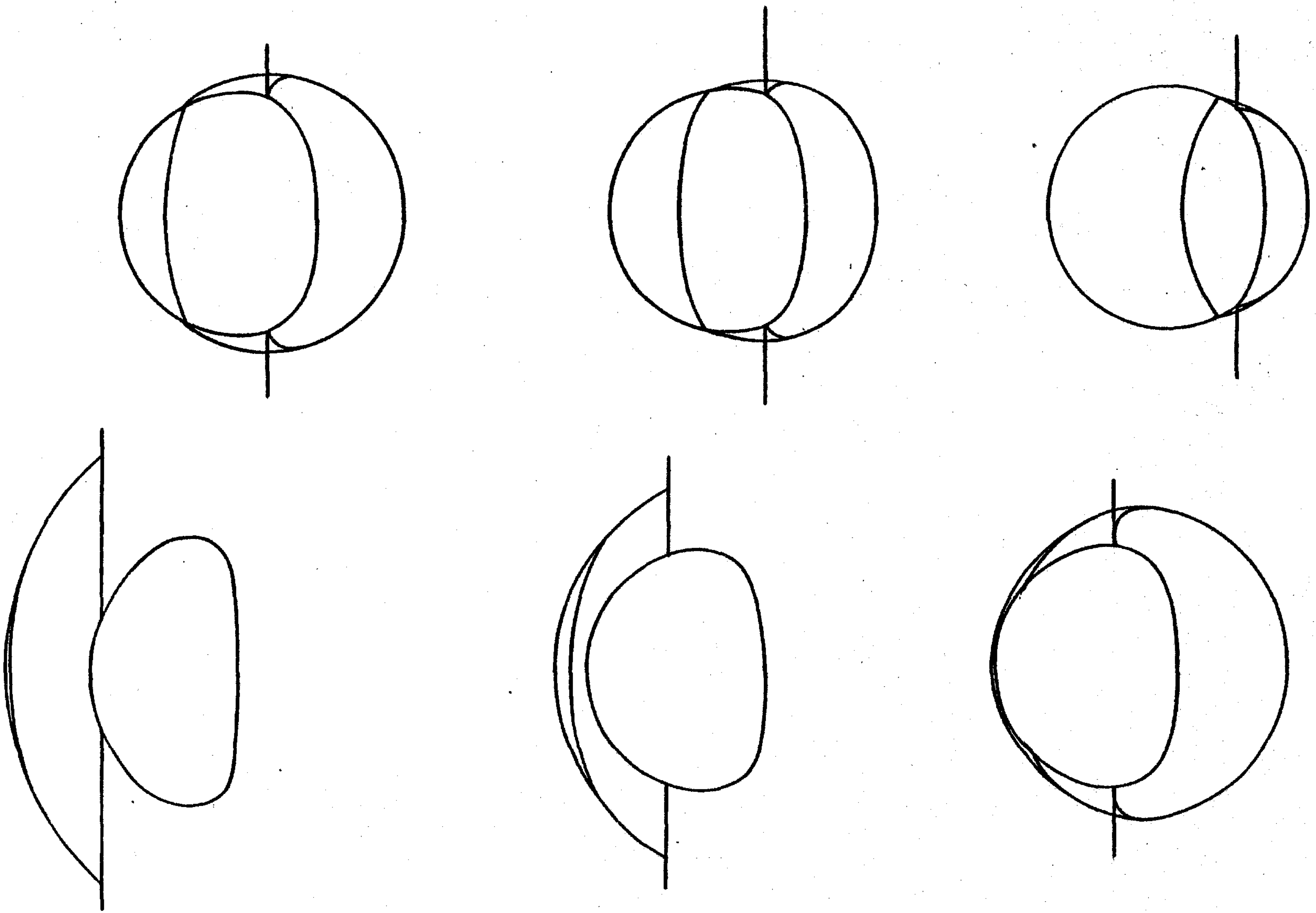

FIGURE 13.7 Schematic Representation of the Wave Pattern (Helium Bubble)

and grow in size and number up to 510 μs. Afterwards, they have all merged and the film is totally broken. In figure 13.5 (Mach number 1.05), the first holes have appeared at 425 μs and have merged at 1000 μs. Figure 13.8 shows the pictures of the breaking film obtained by the reflected light technique for an incident shock wave Mach number of 1.05. The spectacular breakdown of the bubble membrane appears here more clearly than in the shadowgraph pictures. Holes which seem to have appeared simultaneously on the downstream half of the bubble surface (600 μs) grow and merge (700 μs) such that, a little later, a spiderweb structure can be seen in which only filaments are left between the holes (850 μs) and these filaments in turn disintegrate (1123 μs). The process is faster but very similar for the stronger wave of Mach number 1.10. The soap aerosol originating from the broken upstream interface is entrained by the air jet and can be seen in the four pictures but it is interesting to see that the area of the film which remains intact for the longest time is around the entrance of the air jet.

Two mechanisms of soap membrane destruction can therefore be defined :

i. Fragmentation of the membrane occurs on the upstream cap of the bubble, where the helium has been accelerated to a high velocity.

ii. The membrane everywhere else remains smooth but circular holes appear, probably triggered by the Rayleigh-Taylor instability induced by the transmitted wave. The growth of the holes is driven by surface tension (§ 13.4). It has been observed that more holes are created by stronger shock waves and, consequently, that they grow to a smaller diameter before they merge. In the case of strong waves a very dense pattern of holes is created such that the membrane looks immediately fragmented.

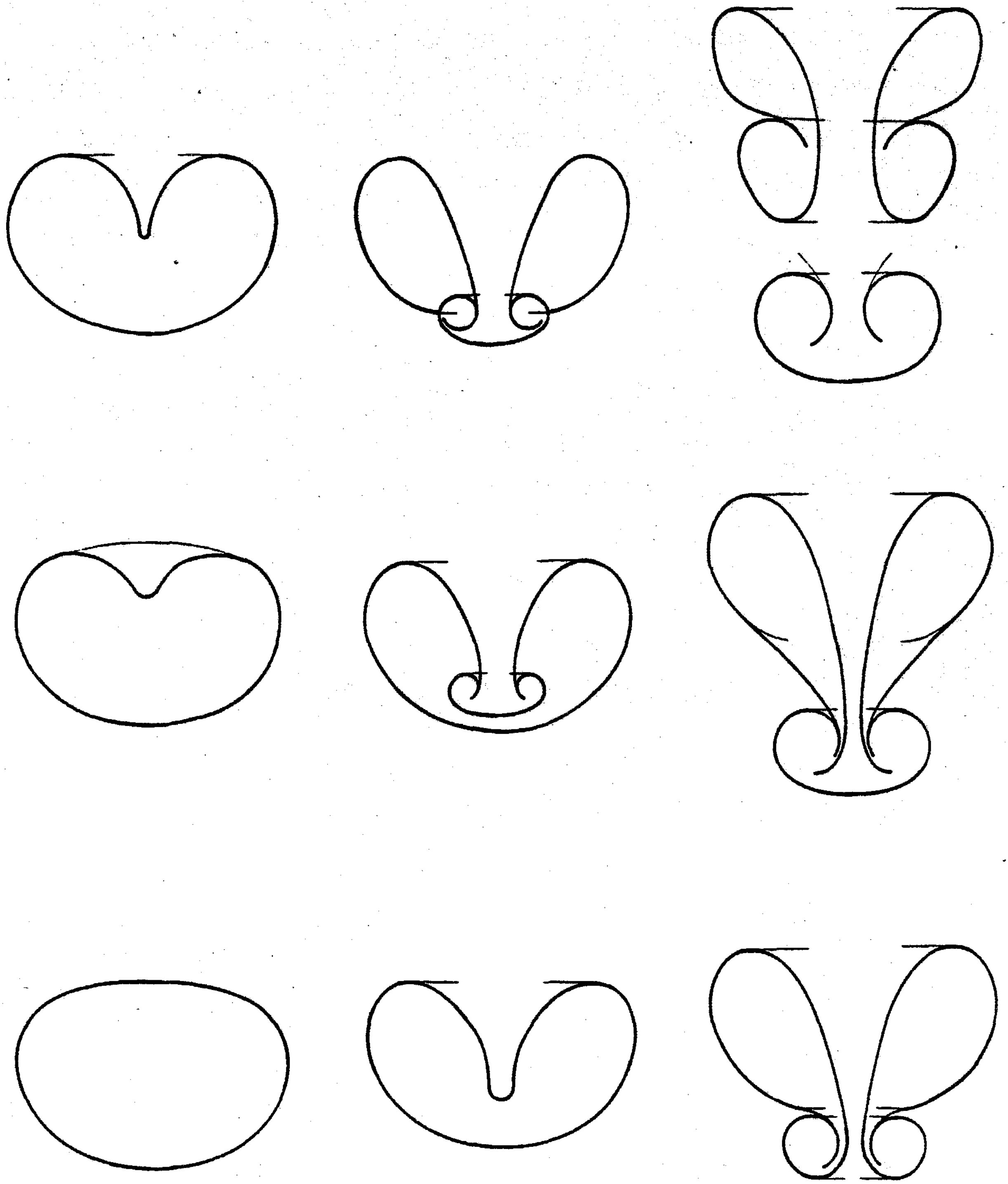

FIGURE 13.8 Schematic Representation of the Deformation of the Helium Bubble

13.3. Velocity measurements from the x-t diagrams

13.3.1. *Velocities.* The x-t diagram is similar to the one presented for the helium cylinder experiment (figure 10.1). Table 13.1 gives the velocities of the different waves and features of the helium structure measured from the x-t diagram for the three shock wave strengths (velocities in m/s). The notation is defined in § 10.2.

Table 13.1. Wave and interface velocities for a helium bubble

M_s	$V_{s_{calc}}$	$V_{2_{calc}}$	V_s	V_R	V_T	V_{u_i}	V_{u_f}	V_{d_i}	V_{d_f}	V_j	V_v
1.05	360	28	370	--	--	53	29	39	26	83	44
1.10	377	54	380	--	--	87	50	67	50	140	75
1.25	428	128	420	960	365	190	125	165	125	335	165

The transmitted shock wave speed V_T corresponds to a Mach number of 1.065 in the strongest case (M_s = 1.25). The high initial velocities of the upstream bubble edge V_{u_i} are due to the flattening of that edge which precedes the formation of the air jet. The air jet itself V_j is stronger in the three dimensional case than in the two dimensional one (§ 15.1). The time t_j defined to be the instant at which the jet appears is also the instant at which the transition from initial (V_{u_i}) to final (V_{u_f}) upstream edge velocities occurs, while t_v, the instant at which the jet reaches the downstream bubble edge corresponds to the transition from initial (V_{d_i}) to final (V_{d_f}) downstream edge velocities. These two times t_j and t_v (in μs) and the relative velocities (in m/s) with respect to the air surrounding the helium structure are given in table 13.2. We assume here that the air behind the diffracted wave moves at the velocity V_2, which is the velocity of the air behind the incident shock wave. The final upstream and downsteam edges move

Table 13.2. Relative velocities of the bubble interfaces

M_s	$V_{u_i}-V_2$	$V_{u_f}-V_2$	$V_{d_i}-V_2$	$V_{d_f}-V_2$	V_j-V_2	V_v-V_2	t_j	t_v
1.05	15	1	11	-2	55	16	450	1300
1.10	33	-4	13	-4	86	20	200	700
1.25	62	-3	37	-3	207	37	100	300

at the same velocity as the surrounding air but the vortex ring is noticeably faster. The relation between the relative air jet and vortex ring velocities is discussed in § 13.3.2.

13.3.2. *Estimation of the circulation.* The relative velocities in the bubble frame of reference of the jet of air $V_j - V_{u_f}$ and of the helium vortex ring $V_v - V_{u_f}$ are close to the ones given in table 13.2. It is possible to evaluate with them the circulation introduced by the air jet inside the bubble and the circulation of the vortex ring.

In order to estimate the strength of the vortex ring, the generation mechanism is compared with the classical method of producing vortex rings by the impulsive motion of a piston in a short cylinder ejecting a cylindrical volume of fluid which becomes the vortex ring (Maxworthy, 1977, Didden, 1979 and Glezer, 1981).

The air jet acts as a piston of velocity V_0, diameter D_0 and travel length L_0. In our case,

$$V_0 = V_{jet} - V_{u_f} \ . \qquad (13.1)$$

An impulse is defined by:

$$I = \rho\, A\ V_0 L_0 \tag{13.2}$$

where

$$A = \frac{\pi\ D_0^2}{4}. \tag{13.3}$$

A Reynolds number is defined by:

$$\mathrm{Re}_0 = \frac{I}{2\rho\upsilon A} = \frac{V_0 L_0}{2\nu} = \frac{\Gamma_0}{\nu}, \tag{13.4}$$

where Γ_0 is the initial circulation associated with the generation process,

$$\Gamma_0 = \frac{V_0 L_0}{2}. \tag{13.5}$$

The Kelvin formula for the velocity of a vortex ring of radius R and core radius a small compared to R is

$$U = \frac{\Gamma}{4\pi R}\left[\log(\frac{8R}{a}) - \frac{1}{4} + o(\frac{a}{R})\right], \tag{13.6}$$

where Γ is the circulation about the ring.

In our experiment the vortex radius R and the vortex velocity $U = V_v - V_{u_f}$ are known, but the core radius is difficult to measure. A rare shadowgraph where a core seems to be well defined is the picture 1594 μs of figure 13.2 for which R = 15 mm and a = 4 mm for the incident shock Mach number of 1.25. The core radii of the vortex rings obtained with weaker shocks can only be guessed: R = 12 mm, a = 5 mm for M_s = 1.10, and R = 10 mm, a = 5 mm for M_s = 1.05. The circulation Γ of the vortex ring calculated using (13.6) can be compared to the initial circulation Γ_0 from (13.5). The quantities associated with the generation process are measured from the shadowgraph. The piston velocity U_0 and the piston travel L_0 are well known but the diameter D_0 is harder to define since the shape of the air jet is conical when it propagates through the helium structure. An average diameter is hence chosen. Table 13.3 gives the various piston model and vortex ring quantities as well as the associated circulations (lengths in mm, circulations in m^2/s).

Table 13.3. Piston and vortex ring parameters

M_s	U_0	D_0	L_0	Γ_0	U	R	a	Γ	Γ/Γ_0
1.05	54	17.5	38	1.025	15	10	5	0.68	0.66
1.10	90	20	35	1.575	24	12	5	1.23	0.78
1.25	210	22.5	30	3.150	40	15	4	2.39	0.76

According to the approximate results of Γ_0 and Γ a major part of the circulation introduced by the air jet ends up in the vortex ring. This is consistent with the results plotted in figure 9 of Maxworthy (1977) and therefore shows that the piston model describes adequately this vortex ring generation process. However a small fraction of the circulation generated is likely to remain in the main body of helium.

Vortex rings generated by the piston method can be laminar or turbulent depending on the geometry and the Reynolds number of the generation process.

In his figures 4 and 5, Glezer (1981)identified a transition line seperating the domains of laminar and turbulent vortex rings when they are mapped in function of L_0/D_0 and Γ_0/ν which is the Reynolds number associated with the generation process. If the kinematic viscosity of helium (ν_{He} = 1.0864 10^{-4}m^2/s) is chosen, the vortex rings obtained in this experiment find themselves just across the transition line (table 13.4). However,an intermediate value of the kinematic viscosity between the value for helium and the value for air (ν_a = 1.426 10^{-5}m^2/s) should probably be chosen and because of the resulting higher Reynolds number the vortex rings would clearly be in the turbulent region. In fact their aspect on the shadowgraph pictures seems to indicate that the vortex rings obtained with the three shock strengths are turbulent.

Table 13.4. Expected behavior of the vortex rings

M_s	L_0/D_0	Γ_0/ν_{He}	behavior	Γ_0/ν_a	behavior
1.05	2.25	0.94 10^4	laminar	7.18 10^4	turbulent
1.10	1.75	1.45 10^4	transitional	11.03 10^4	turbulent
1.25	1.50	2.90 10^4	turbulent	22.07 10^4	turbulent

13.4. Growth of circular holes in the soap film

The sudden appearance and the rapid growth of holes in the soap membrane described in § 13.2.3 is a remarkable peculiarity of the membrane disintegration following the interaction with weak shock waves. The phenomenon of the growth of holes in thin liquid membranes has been the object of specialized investigation (McEntee and Mysels, 1969 and Frankel and Mysels, 1969). When for some reason (in our case the Rayleigh-Taylor instability) a tiny hole has appeared on a thin liquid film, it grows because of surface tension forces. A simple but reasonably accurate estimate of the growth rate after the early disturbances due to puncturing have died out, assumes that the film is undisturbed except at the edge of the hole where a toroidal rim has formed with the collapsed material from the disappeared membrane. The radial rim velocity V_c was derived by Culick (1960) using the conservation of momentum of the rim. The momentum increase in an increment of time dt of a section of the rim sustained by a small angle α is the product of the increment of the rim mass dm by V_c and is equal to the impulse created by the surface tension acting on the two sides of the membrane just outside the rim. The radius of the hole at the time t is r, σ_0 is the surface tension, δ_0 is the film thickness and ρ_s is the film density. The momentum balance is :

$$2\sigma_0\, r\,\alpha\, dt = \left[\rho_s \delta_o V_c dt\right] r\,\alpha\, V_c\ , \qquad (13.7)$$

hence the velocity of the rim (also called the Culick velocity) is :

$$V_c = \left(\frac{2\sigma_0}{\delta_0\rho_s}\right)^{1/2} . \qquad (13.8)$$

For the soap membrane used in this experiment,

$$\sigma_0 = 30\times10^{-3}\ \mathrm{N/m}, \quad \rho_s = 1.08\times10^{3}\ \mathrm{kg/m^3}$$

and δ_0 could range from 10^{-7} m to 10^{-6} m. Therefore, the possible range of V_c is from 7.4 m/s to 23.6 m/s.

Although in this experiment the growth rate of a given hole could not be recorded, the average size of the largest holes was measured as a function of time in the series of shadowgraph pictures obtained from the interaction of weak shocks (Mach number: 1.05 and 1.10) with the soap bubble. The Culick velocity ranges from 10 to 20 m/s. This implies a film thickness between .55 and .14 μm which is consistent with the estimates based on color of the soap film.

13.5. Pressure measurements behind the bubble

The pressure measurements were made in the conditions described for the cylinder experiment in Chapter 11. However, the survey of pressure profiles is not as complete. In figure 13.9 three pressure profiles (a,b and c) are shown with the simultaneously recorded shadowgraphs. They were obtained for a strong incident shock wave (M_s = 1.25) with the transducer located very close (2, 11 and 29mm) behind the bubble downstream edge. The first pressure profile indicate a transmitted shock of Mach 1.06 followed by a strong N shaped pulse, about 1.24 bar peak to peak, which corresponds to the secondary transmitted front (§ 13.1.1). The second and third profiles and corresponding shadowgraphs show how the secondary transmitted wave merges with the (primary) transmitted wave. The third profile also shows the pressure rise due to the diffracted wave. When measured at the real shock tube end plate, 422 mm away from the bubble center, the shock profile obtained for the strong incident shock is unperturbed.

For a weak shock wave sequence (1.05 to 1.08) and the transducer plate located 278 mm behind the bubble center, a precursor between 5 and 17 μs was usually recorded for the weakest waves (M_s = 1.05) and none for stronger ones (M_s = 1.08). This precursor, the trace of a very weak transmitted wave (M_T = 1.01) is similar to the one found in the small bubbles experiment (Chapter 6). The merging distances ($x_{\max}$) or ranges of influence predicted by the model of Chapter 4 are given in table 13.5 as a function of the incident shock wave Mach number.

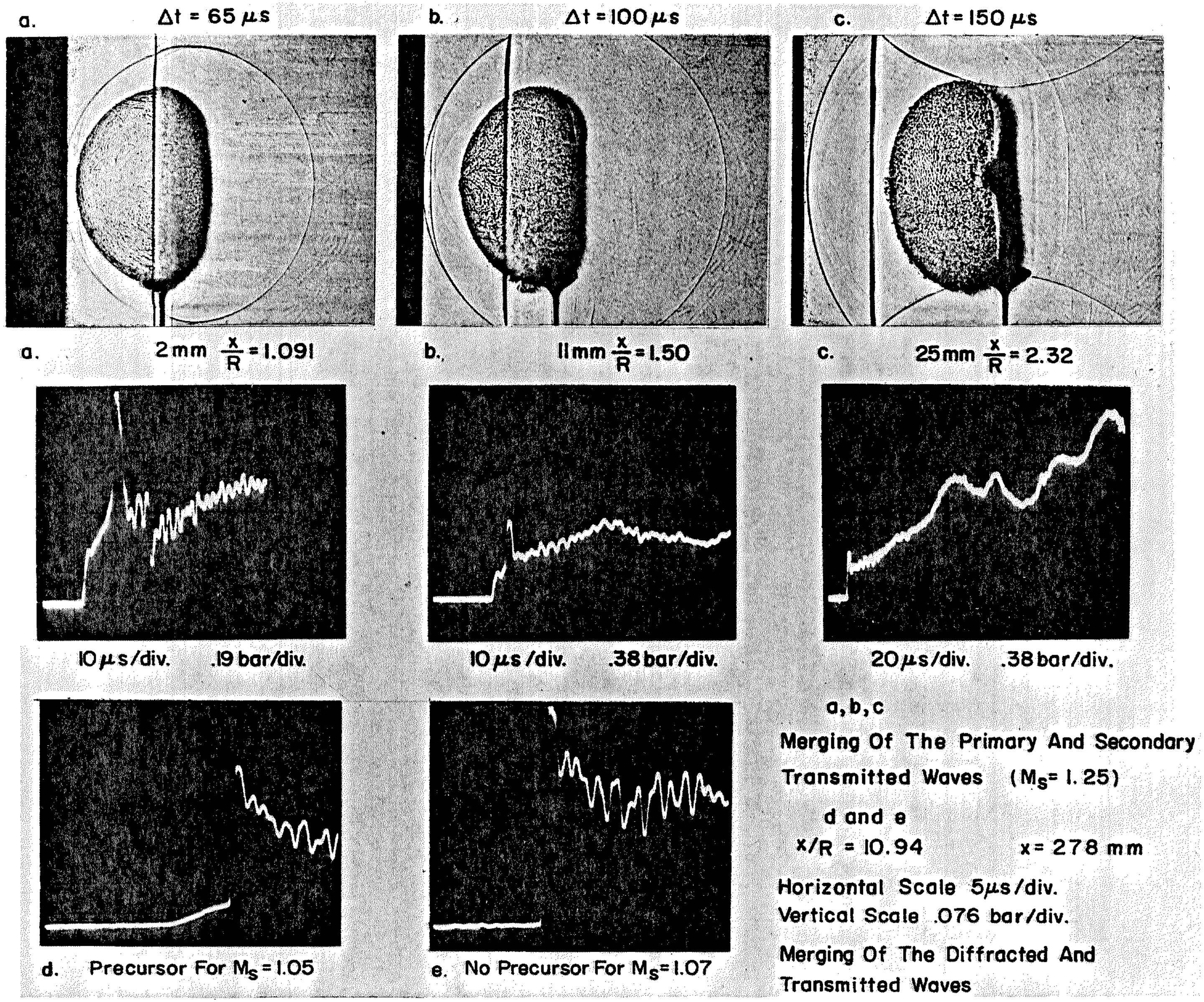

a, b, c

Merging Of The Primary And Secondary Transmitted Waves (M_S = 1.25)

d and e

x/R = 10.94 x = 278 mm

Horizontal Scale 5 μs/div.

Vertical Scale .076 bar/div.

Merging Of The Diffracted And Transmitted Waves

FIGURE 13.9 Pressure Profiles behind the Helium Bubble

Table 13.5. Merging distance behind a helium sphere (in mm)

M_s	x_{max}/r	x_{max}
1.05	25.7	578
1.07	18.2	410
1.10	12.6	283
1.25	4.7	106

The profiles d and e shown in figure 13.9 for incident shock wave Mach number of 1.05 and 1.07 were obtained at a distance of 278 mm from the bubble center. Both profiles have a rather high initial peak, but only the first, weaker one displays a precursor: therefore we see that the real range of influence for the stronger wave is shorter than 278 mm and that the one for the weaker wave is longer. This shows that the model predicts a range of influence which is too long for the weak shock waves, where the model is supposed to be applicable. The difference is partly due to some air contamination inside the bubble.

On the other hand, the range of influence predicted for the strong wave is shorter than the one deduced from the flow visualization (§ 13.1.1). The reason is that it takes a longer distance for the diffracted wave to catch up with a finite strength transmitted shock wave than with an acoustic pulse as assumed in the model.

Chapter 14

INTERACTION OF SHOCK WAVES WITH HEAVY AND NEUTRAL BUBBLES

14.1. Freon 22 bubbles

14.1.1. *Incident shock wave Mach number 1.25.* The sequence of shadowgraphs from the interaction appears in figure 14.1 and the details of the waves downstream of the bubble are shown on figure 14.2. The incident shock wave is seen as it diffracts completely over the bubble in the first six frames of figure 14.2 (35 to 119 μs) and appears noticably dished in. At 136 μs, the center of the dish flattens as the diffracted wave becomes normal. The transmitted wave appears just before its focus at 119 μs as a complex fan of weak waves and looks much sharper after its focus at 136 μs.

The asymmetry of the transmitted wave is due to the asymmetry of the bubble itself and to the thicker soap film at the bottom. The transmitted shock has almost merged with the diffracted shock on the last frame (261 μs). The same wave pattern appears in figure 14.1 with the addition of the reflected wave (25 and 65 μs) and some faint backscattered waves at 265, 305 and 407 μs.

In the initial phase of the interaction (25 to 125 μs) there is no noticeable deformation of the Freon volume, yet the soap film is completely destroyed. With the passage of the transmitted shock wave near its focus, the downstream edge of the volume is deformed and a small jet of high speed Freon develops from 166 μs to 607 μs. At the same time on the upstream side a spherical cap forms. The high-speed Freon jet is due to the localized high velocity field created by the strong transmitted shock wave near its focus. Later, this jet, which has stopped growing, remains visible. The main body grows (presumably

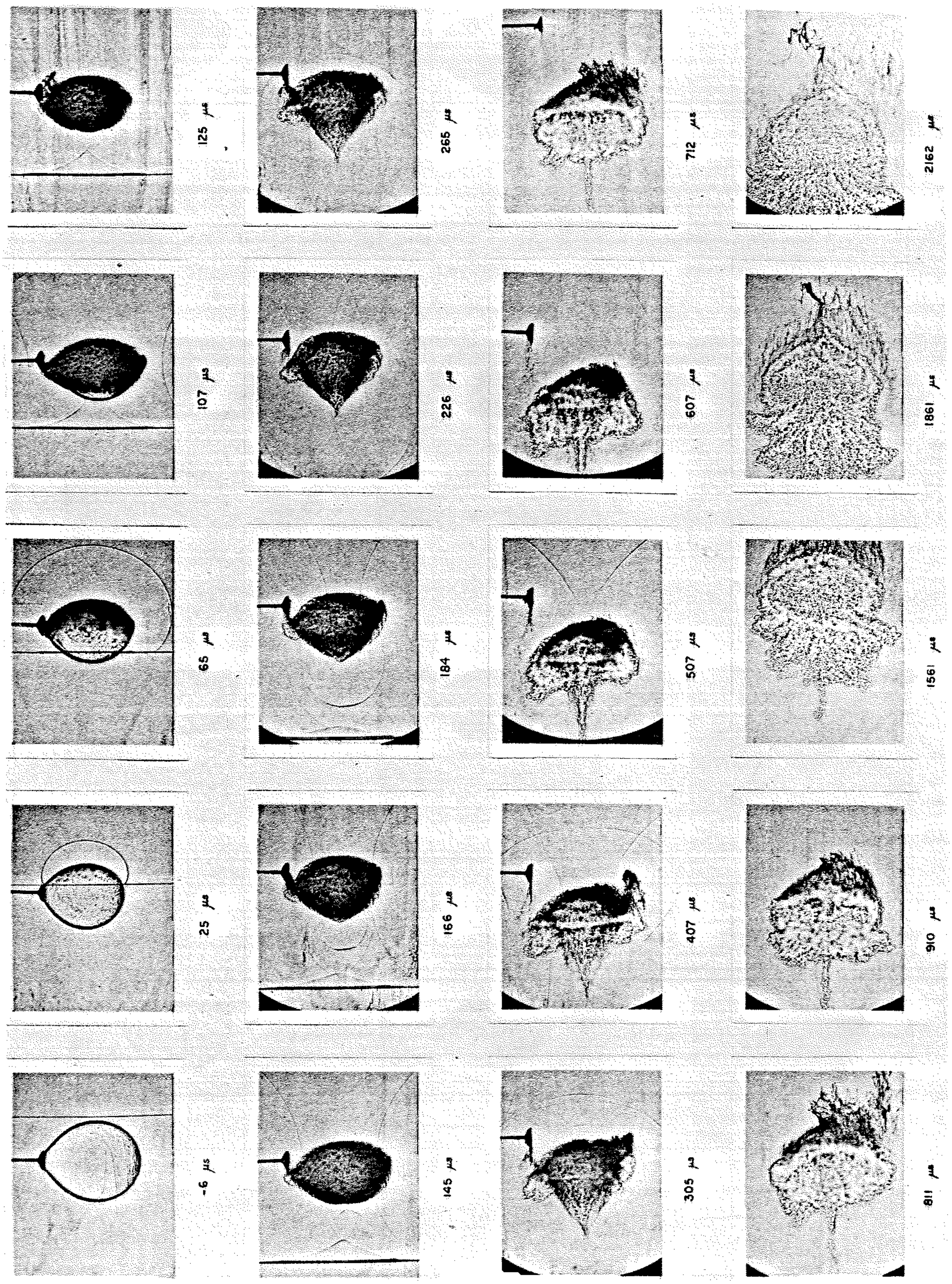

FIGURE 14.1 Interaction of a mach 1.25 Shock Wave with a Soap Bubble Filled with Freon 22

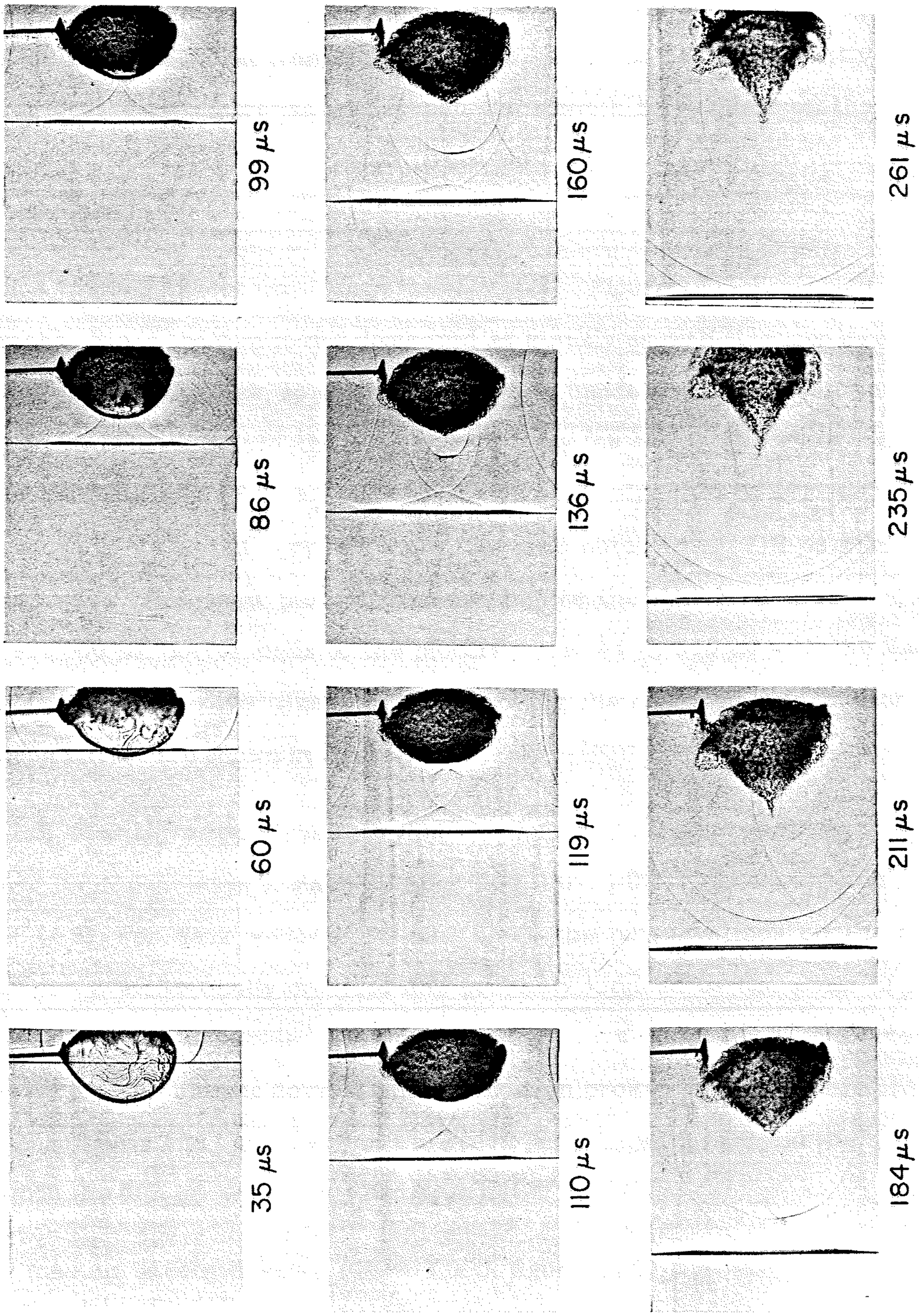

FIGURE 14.2 Shock Wave Focusing by a Soap Bubble Filled with Freon 22 (M_s = 1.25)

by entrainment) yet not much concentrated vorticity is evident. Recalling the vortex pair observed with the Freon cylinder, one might expect the large structure seen in the last three frames (1561 to 2162 μs) to be bell-shaped with a vortex ring located at the transition between the smooth half sphere on the right and the fingered structure on the left (from 1861 μs), but in fact the vortex ring is not visible.

14.1.2. *Incident shock wave Mach number 1.07.* Figure 14.3 shows eight shadowgraphs. Since the film is not destroyed as quickly as with stronger waves, it does not obscure the view, so the refracted wave inside the bubble can be seen (18 and 138 μs). As before, the transmitted wave (as shown at 198 μs) causes the development of the Freon jet at the downstream edge (299 to 1712 μs). The last picture (1712 μs) is very similar to the one obtained at 712 μs with the stronger wave. The latest picture obtained before the return of the reflected wave, at 2500 μs, corresponds to the picture obtained at 910 μs with the Mach number 1.25 shock wave. Sketches summarizing the observed deformation of the Freon bubble are shown in figure 14.4.

14.1.3. *Disintegration of the soap film.* Reflected light pictures were obtained for shock waves of Mach number 1.05, 1.07, 1.095 (figure 14.5) and 1.25 (figure 14.6). For weak waves (1.05 and 1.07), the perturbations on the film appear as waves, vertically oriented and probably induced by the shear of the faster air around the bubble. The upstream cap stays intact for a long time (1 ms for M_s = 1.05), but the downstream cap is soon broken by the passage of the transmitted wave and the growth of the Freon jet. The waves around the bubble grow until the film breaks (1.2 ms for M_s = 1.05).

For medium strength waves (M_s = 1.095, figure 14.5) the wavelength of the periodic pattern is shorter and covers more of the bubble surface. The film breaks up around 300 μs and the last film fragments can be seen on the

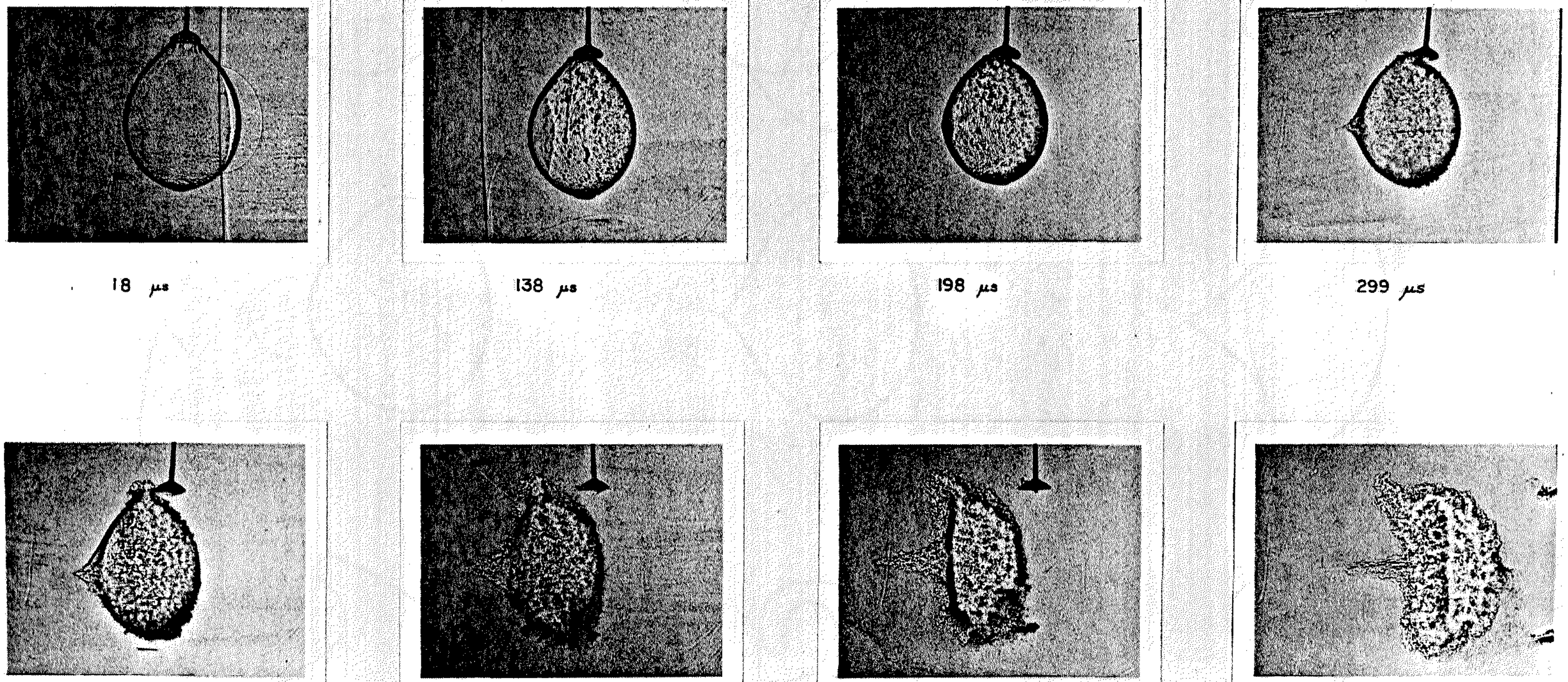

18 μs

138 μs

198 μs

299 μs

449 μs

800 μs

1096 μs

1712 μs

FIGURE 14.3 Interaction of a Mach 1.07 Shock Wave with a Soap Bubble Filled with Freon 22

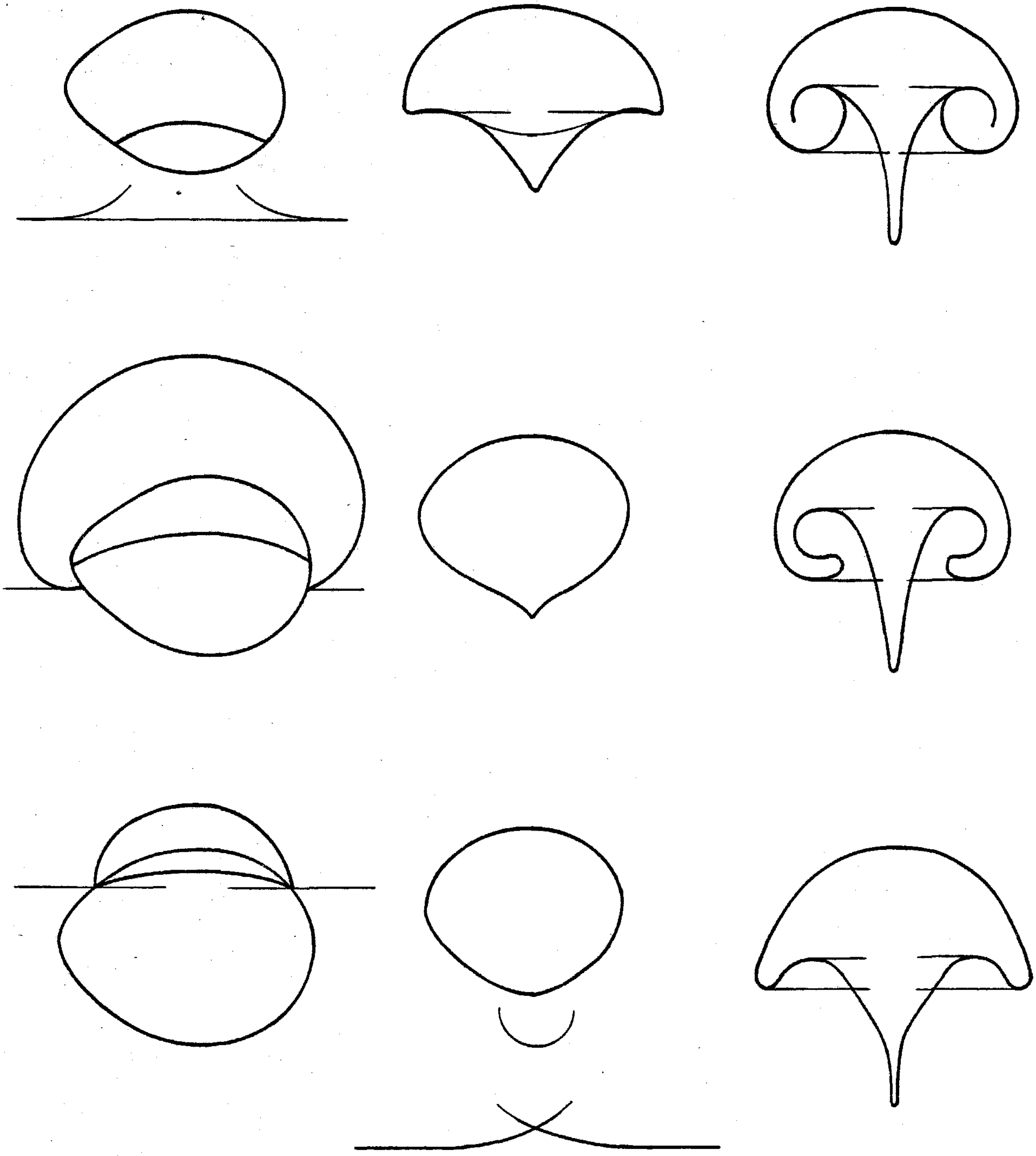

FIGURE 14.4 Schematic Representation of the Deformation of the Freon 22 Bubble

downstream side around the hole created by the Freon 22 jet. Finally, for strong waves (M_s = 1.25, figure 14.6), the film breaks up quickly from the upstream side and there is only a narrow transition section between the rough-looking broken area and the intact downstream side, in which short waves can be seen.

14.1.4. *Velocity measurements from the x-t diagrams.* The x-t diagram helped to determine the initial and final upstream edge velocity V_{u_i} and V_{u_f}, the initial and final downstream edge velocity V_{d_i} and V_{d_f}, the velocity of the Freon jet V_j, the incident wave velocity V_s, and for the weaker case the refracted wave velocity V_R and the average transmitted wave velocity V_T.

The velocities obtained for the two shock strengths are given in table 14.1. The Freon 22 speed of sound is 182 m/s and its density is 4.72 kg/m^3.

Table 14.1. Wave and interface velocities for a Freon 22 bubble

M_s	$V_{s_{calc}}$	$V_{2_{calc}}$	V_s	V_{u_i}	V_{d_i}	V_{u_f}	V_{d_f}	V_{j_i}	V_{j_f}	V_R	V_T
1.07	367	39	372	18	27	24	27	--	32	222	440
1.25	428	128	421	60	83	99	100	165	123	239	574

The range of influence of the Freon bubble on the shock wave, defined as the distance behind the bubble center at which the transmitted wave has caught up with the diffracted wave, is equal to 119 mm or 8.5 bubble radii (measured on the horizontal axis) for M_s = 1.25. For the weak wave, M_s = 1.07, that distance appears to be much longer.

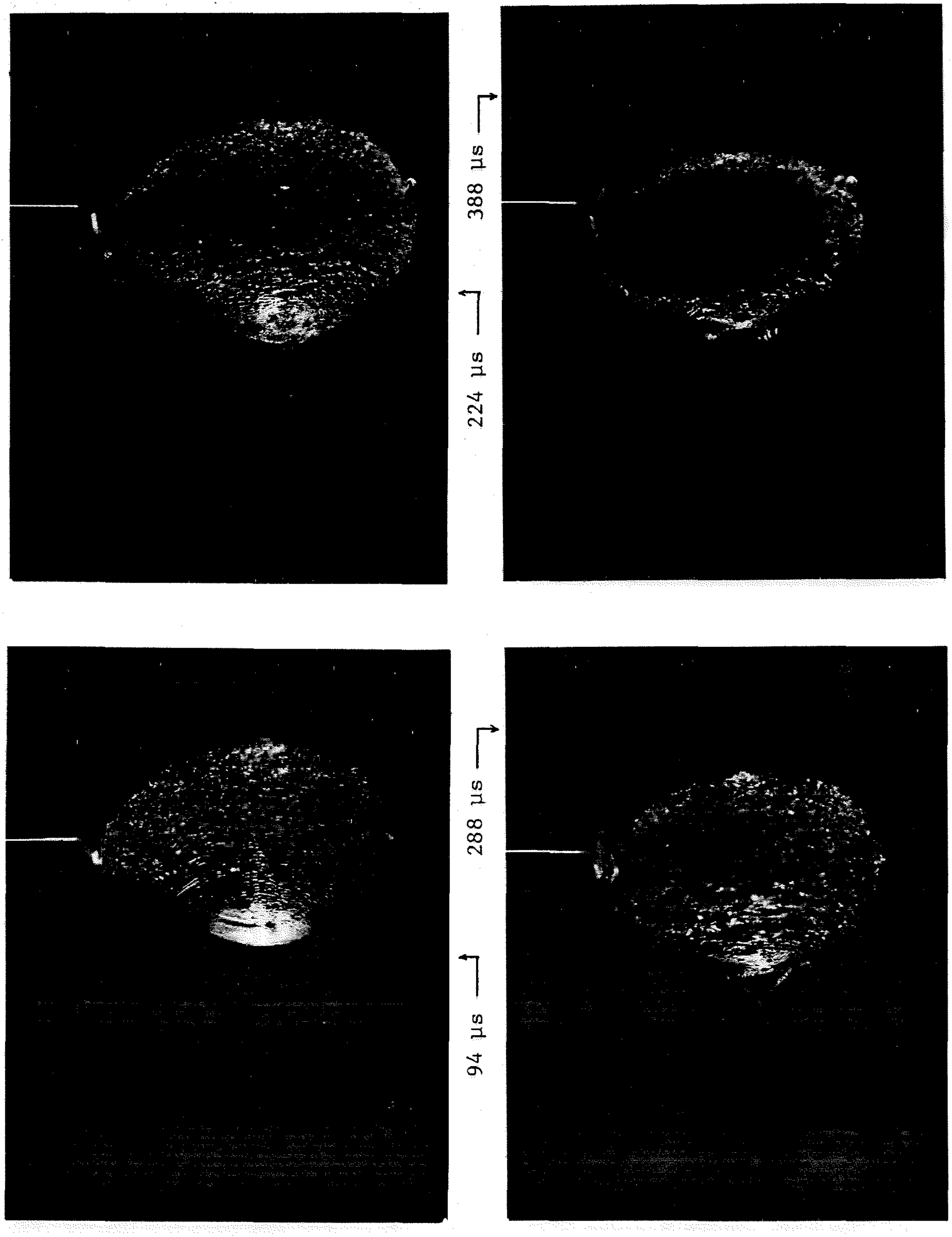

FIGURE 14.5 Disintegration of the Soap Film (Freon 22 Bubble, M_S= 1.095)

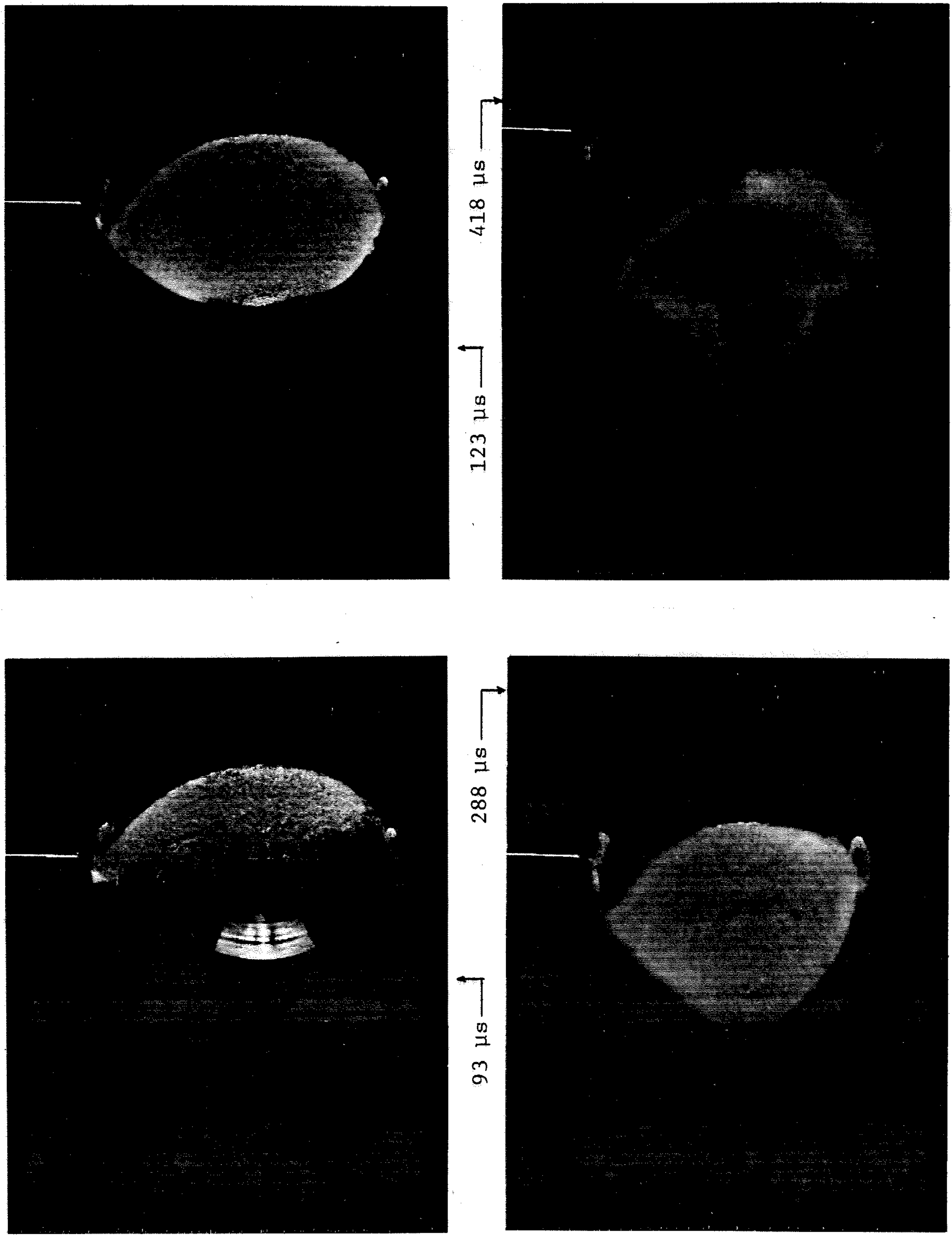

FIGURE 14.6 Disintegration of the Soap Film (Freon 22 Bubble, $M_S = 1.25$)

Taking the speed of sound in the interior of the bubble to be 182 m/s, the measurements show that the Mach numbers of the refracted wave are 1.22 and 1.31 for the incident wave Mach numbers of 1.07 and 1.25, respectively.

14.2. Argon filled bubbles

In figures 14.7 and 14.8, a few shadowgraphs of the interaction of shock waves of Mach number 1.25 and 1.10 with argon-filled bubbles are presented.

14.2.1. *Incident shock Mach number 1.25.* In figure 14.7 the refracted wave is seen on frames 40 μs and 80 μs, just behind the incident shock wave. Then the disk due to the concave transmitted wave is seen as it flattens in the next three frames: 120, 139 and 170 μs. Two backscattered waves appear in frames 221 and 320 μs. The first one (to the right) is due to the primary internally reflected wave, and the second one to the twice internally reflected wave. The destruction of the film is almost complete 5 mm behind the incident shock. Due to the small density difference between argon and air, there should be little vorticy produced and the deformation of the argon volume does not present any remarkable features.

14.2.2. *Incident shock Mach number 1.10.* The six shadowgraphs in figure 14.8 mainly illustrate the destruction of the film starting from the upstream face with very fine waves (157 μs) which grow and break the film, and leaving the downstream cap remarkably intact for a very long time. The cap is eventually destroyed by the growth of holes rather than the progression of the breaking front (1309 μs). The refracted wave appears remarkably flat when it propagates through the downstream portion of the bubble (85 to 140 μs), and the disk shaped transmitted wave is observed until 210 μs as it flattens. An argon bubble is only a weak convergent acoustical lens. Unlike what was seen for the Freon bubble, the diffracted wave and the transmitted wave are directly connected, and because of the strengthening of a convergent shock, the central part of the

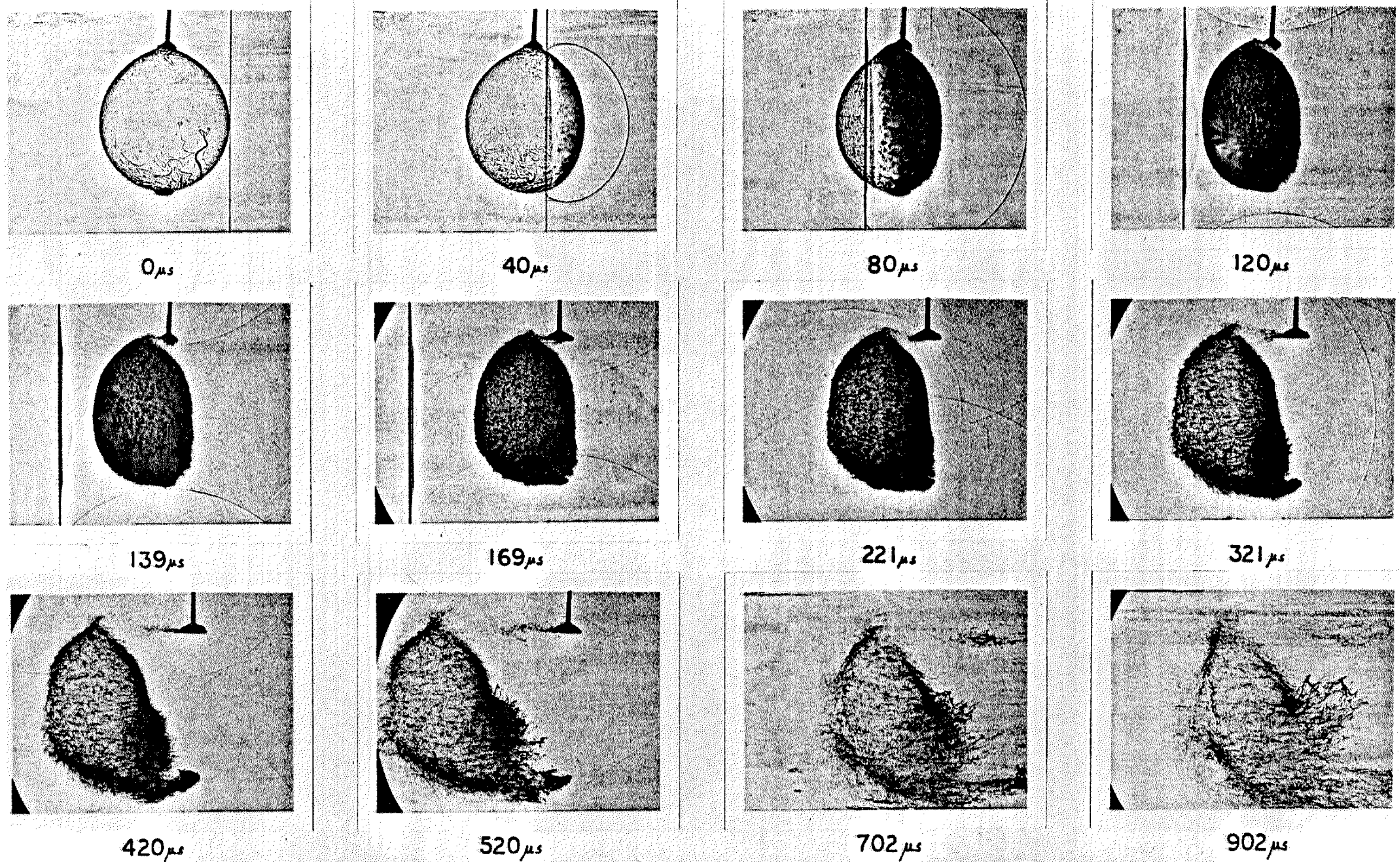

0μs 40μs 80μs 120μs

139μs 169μs 221μs 321μs

420μs 520μs 702μs 902μs

FIGURE 14.7 Interaction of a Mach 1.25 Shock Wave with an Argon-Filled Soap Bubble

FIGURE 14.8

INTERACTION OF A MACH 1.10 SHOCK WAVE WITH AN ARGON-FILLED SOAP BUBBLE

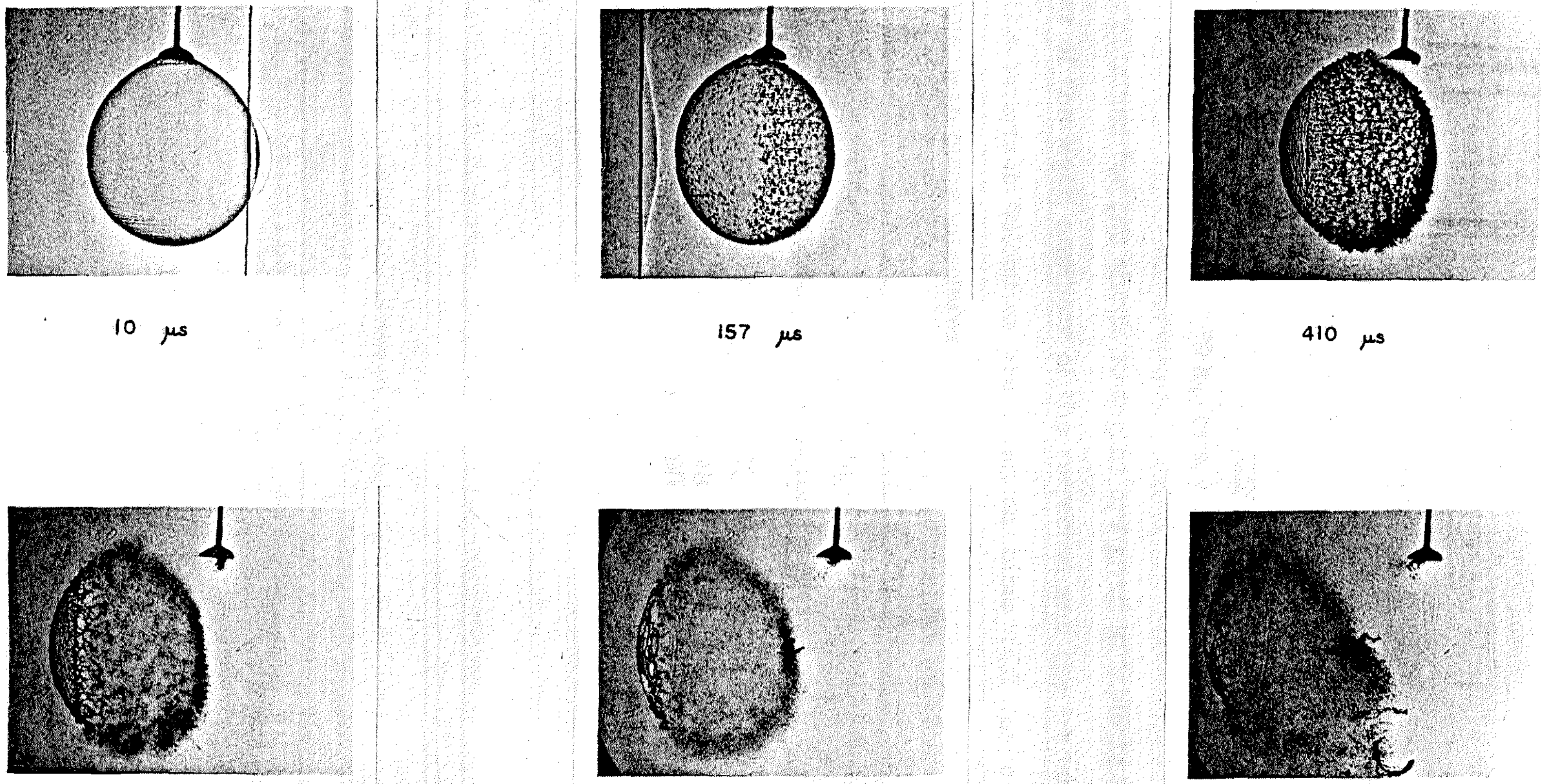

10 μs

157 μs

410 μs

810 μs

1010 μs

1309 μs

transmitted wave does not focus.

14.2.3. *Velocities from the x-t diagrams.* The acoustical properties of argon are:

speed of sound a = 320 m/s,

index of refraction n = 1.068,

density ρ = 1.78 kg/m^{3}s,

acoustical impedance ρa = 569 kg/m^{2}s.

The velocities obtained for two shock strengths are given in table 14.2. The calculated values of the Mach numbers of the refracted and the transmitted waves and of the interface velocities are given in table 14.3 for a "one-dimensional bubble" with plane interfaces.

Table 14.2. Wave and interface velocities for an argon bubble

M_s	V_s	V_R	V_T	M_R	M_T	V_{u_i}	V_{u_f}	V_{d_i}	V_{d_f}
1.10	379	343	398	1.07	1.16	43	33	--	32
1.25	422	382	481	1.19	1.40	90	111	85	107

Table 14.3. Calculated velocities of the air-argon interfaces

M_s	M_R	M_T	V_s	V_2	V_{u_i}	V_{d_i}
1.10	1.11	1.08	377	54	47	50
1.25	1.26	1.23	429	128	113	118

The measured refracted wave velocity is unexpectedly low (M_R should be larger than M_s), while the transmitted wave velocity V_T seems too strong. For the strong incident shock wave ($M_s = 1.25$), the argon volume accelerates to a final velocity (V_{u_f} and V_{d_f}) nearly equal to V_2 which is the air velocity behind the undisturbed shock. The fact that the measured final velocities for the weaker incident shock ($M_s = 1.10$) are lower than the initial one (V_{u_i}) is not expected and may be due to some imprecision in the measurement.

14.3. Nitrogen and helium-argon bubbles

14.3.1. *Neutral bubbles.* Both nitrogen and the helium-argon mixture have a density and a speed of sound very close to the one of air so the bubble can be called neutral. The only effects observed are the ones due to the soap membrane.

The nitrogen bubbles allow the visualization of the liquid phase and the waves generated by the wave/membrane interaction process. The mixture (1/3 helium, 2/3 argon in volume) has the same density as nitrogen but its speed of sound is 9% higher than the one of nitrogen and 11% higher than the speed of sound of air. Therefore, a mixture-filled bubble is expected to behave very much like the nitrogen bubble. However, since its index of refraction is greatly different from air, the behavior of the gas initially inside the bubble can be visualized later as it is swept downstream by the shock wave.

14.3.2. *Behavior with strong waves.* The shadowgraphs of the interaction with the stronger wave ($M_s = 1.25$) are presented in figures 14.9 and 14.10. The general pattern is similar to the one observed for the argon-filled bubble. In the case of nitrogen (figure 14.9) there appears to be a refracted front slightly behind the incident front (40 and 80 μs) and more so at the bottom of the

FIGURE 14.9

INTERACTION OF A MACH 1.25 SHOCK WAVE AND A NITROGEN FILLED SOAP BUBBLE (43mm diameter)

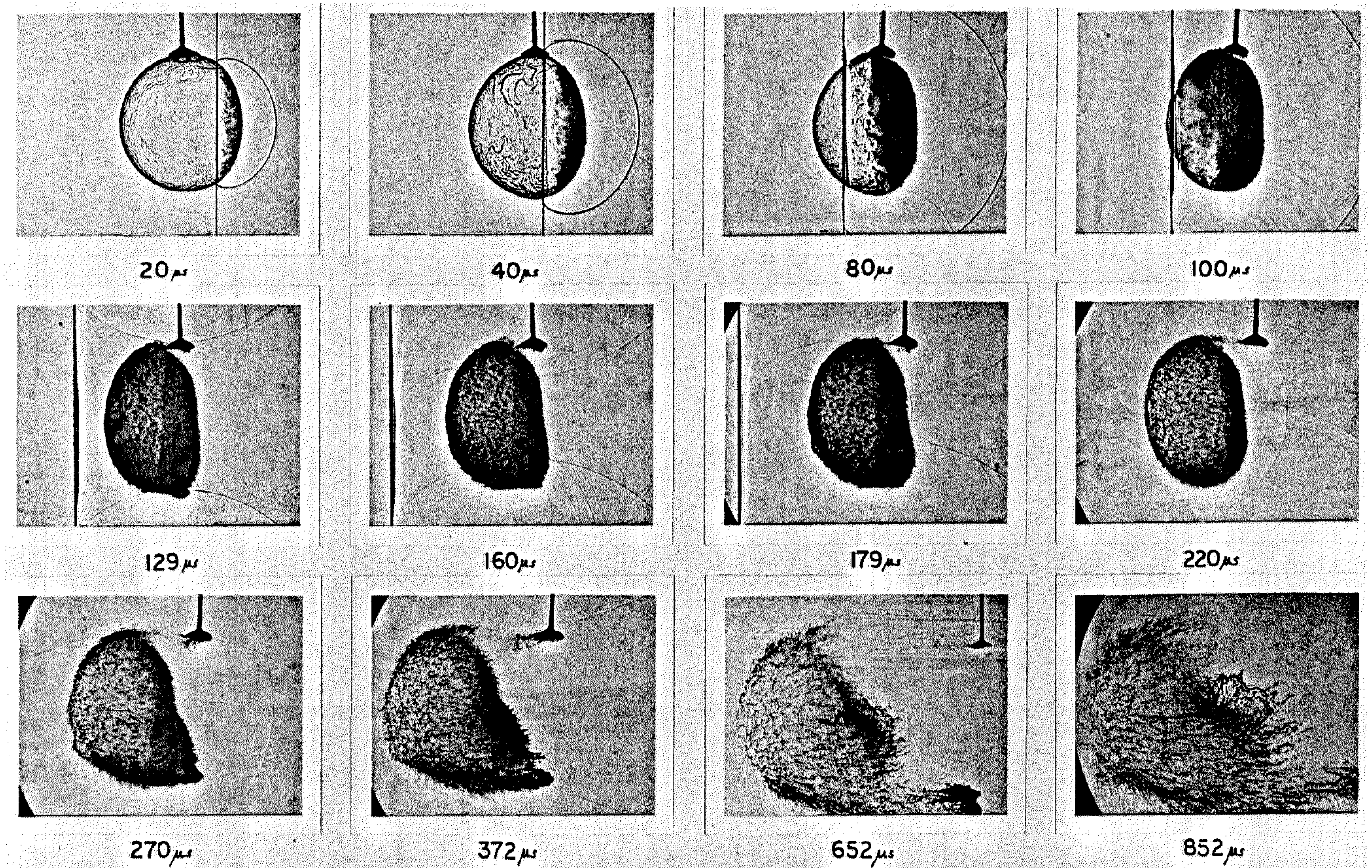

20μs 40μs 80μs 100μs

129μs 160μs 179μs 220μs

270μs 372μs 652μs 852μs

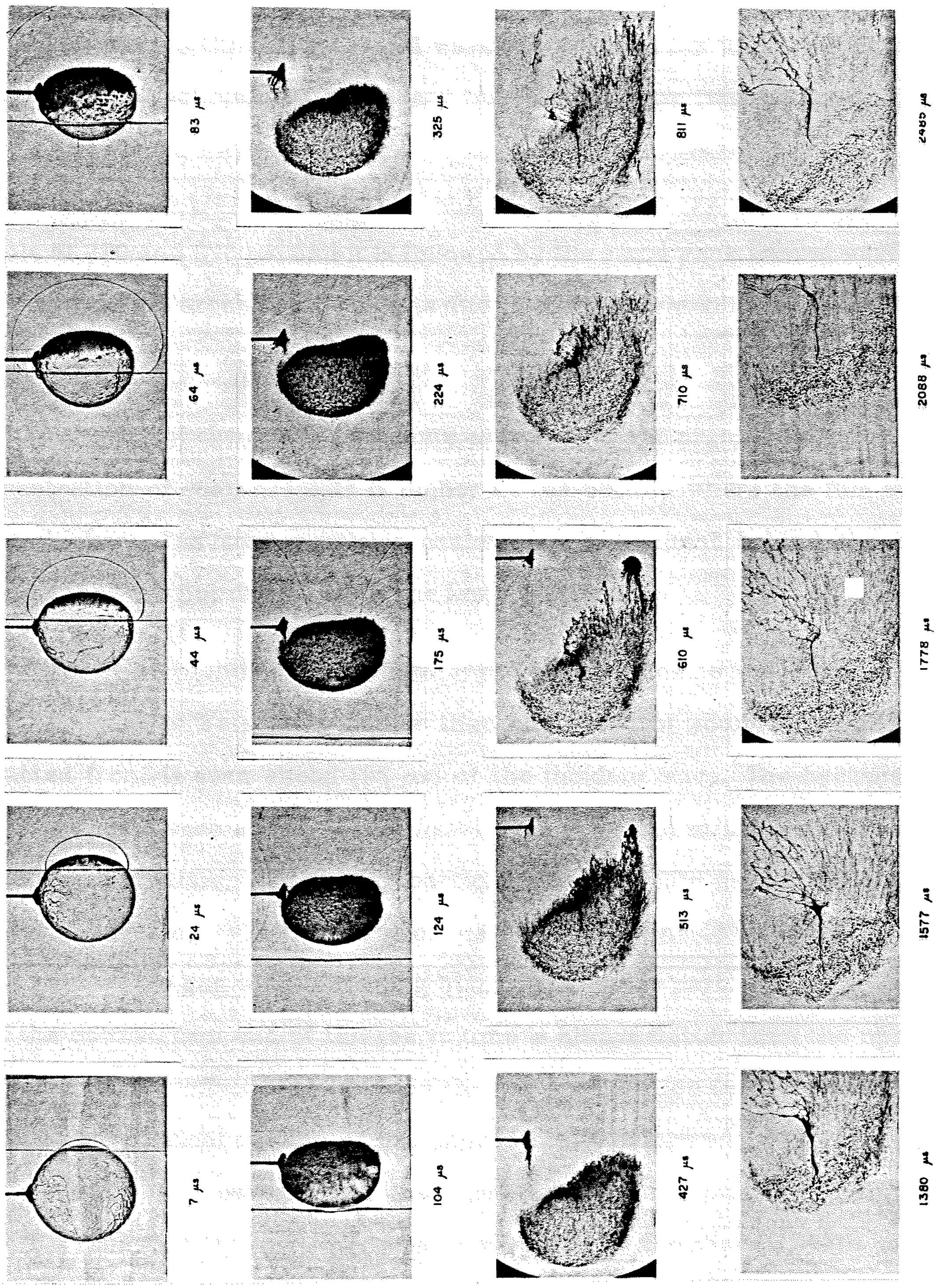

FIGURE 14.10 Interaction of a Mach 1.25 Shock Wave with a Bubble Filled with a Mixture of 1/3 He, 2/3 Ar

bubble, probably due to a thicker film there. On the fourth picture (100 μs), the second front seems to be connected to the wave around the bubble by some branches which outline the toroidal wave due to the rays which have reflected once inside the bubble: that secondary transmitted wave (which is connected to the backscattered wave seen from 129 to 179 μs) catches up with the primary transmitted wave (129 to 179 μs). The backscattered wave appears outside the bubble at 220 and 270 μs, and it is followed by the same weak second wave previously seen in the argon case, which is due to the rays which have reflected *twice* inside.

The behavior of the soap is the same as it was for the argon filled bubble. The concentration of soap droplets is higher at the bottom where the film was initially thicker. The soap particles coalesce in a filament behind the bubble because they are not disturbed by the faster gas motion.

The speed of sound of the helium-argon mixture inside the bubbles (figure 14.10) appears to be slightly higher than the speed of sound of air since the refracted front is seen ahead (83 μs) of the incident wave. The backscattered waves are again seen at 175 to 325 μs. The thicker film at the bottom not only influences the pattern of the soap particles after the film destruction, but also creates an asymmetry in the shape of the gas initially inside the bubble with the lower part of the gas volume trailing behind the upper part. Similarly, the fact that the downstream end of the gas volume is always flatter than the upstream end indicates the effect of the film on the gas acceleration (e.g., at 610 μs) since an initially spherical volume of gas should be transformed in an oval volume with symmetrical upstream and downstream edges. In spite of this imperfection, it is true that the mixing process is very slow as the shadow of the gas mixture does not increase much in size.

14.3.3. *Behavior with weaker waves.* In figures 14.11 (nitrogen, M_s = 1.10) and 14.12 (helium-argon mixture, M_s = 1.08) the behavior of a neutral bubble processed by a weaker shock wave is shown. The destruction of the film, as with the argon bubble, is due to the growth and breaking of waves around the bubble with a sharp transition to the left spherical cap, which is consumed by the growth of the holes (nitrogen bubble, figure 14.11).

The fact that the helium-argon mixture has a speed sound slightly larger than the one of air is apparent at 195 μs on figure 14.12, when the transmitted shock is slightly divergent. The evolution of the shape of the gas volume is similar to the stronger case.

14.3.4. *Velocities from the x-t diagram.* In table 14.4 which shows the velocities of the waves and the gas volume interfaces the notation is as follows : V_G applies to the two gas interface velocities, both upstream and downstream and the subscript *calc* refers to calculated velocities.

Table 14.4. Wave and interface velocities for neutral bubbles

M_s	gas	$V_{s_{calc}}$	$V_{2_{calc}}$	V_s	V_R	V_T	V_G
1.08	He/Ar	371	44	364	394	366	36
1.10	nitrogen	380	55	380	--	--	40
1.25	He/Ar	430	130	420	--	--	118

The table shows that the gas moves slower than the air behind an undisturbed shock does. This is apparently due to the inertia of the film. The refracted waves inside imply a speed of sound of 380 m/s in the helium-argon mixture.

FIGURE 14.11

INTERACTION OF A MACH 1.10 SHOCK WAVE WITH A NITROGEN-FILLED SOAP BUBBLE

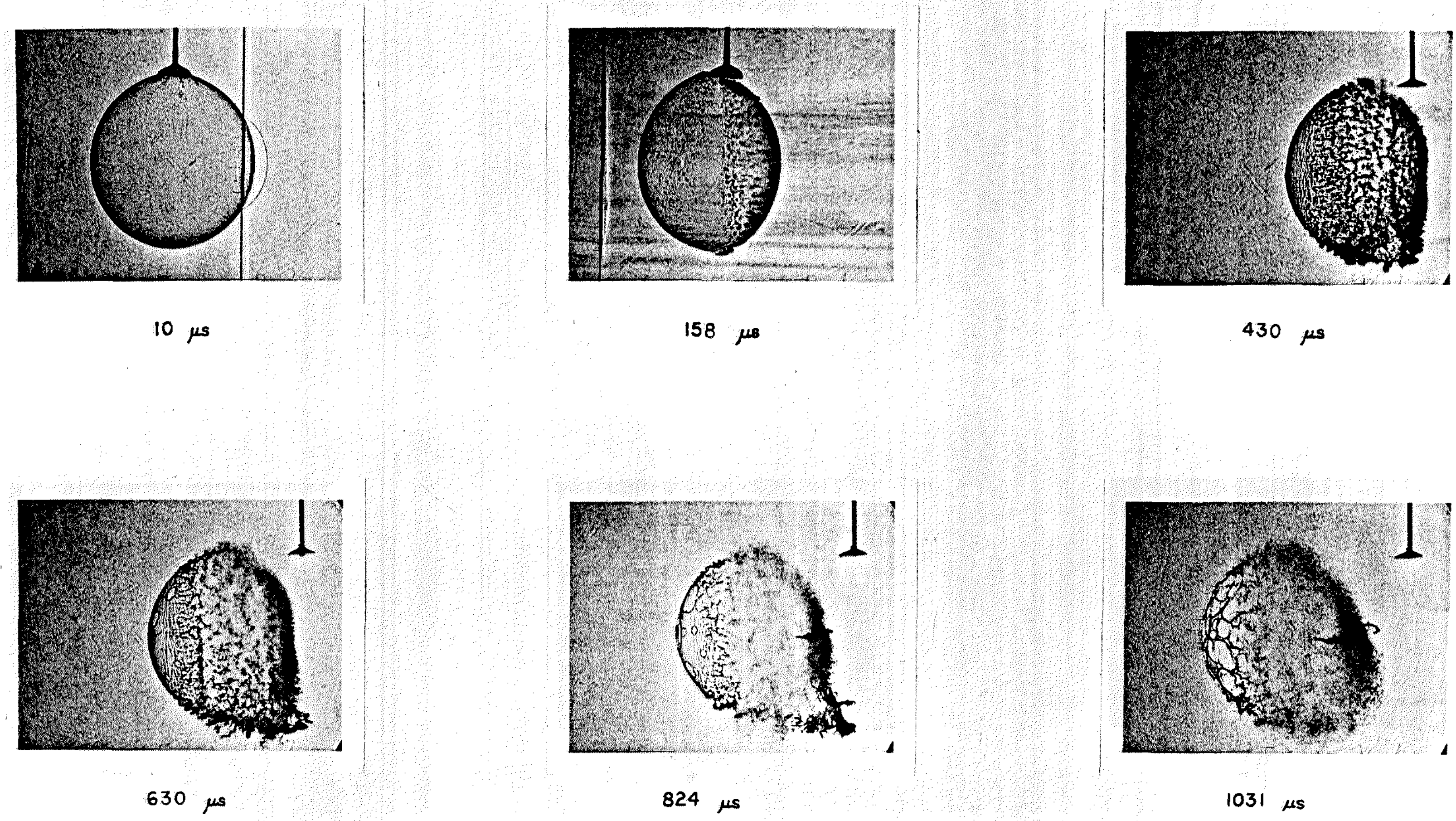

10 μs

158 μs

430 μs

630 μs

824 μs

1031 μs

FIGURE 14.12 INTERACTION OF A MACH 1.08 SHOCK WAVE WITH A SOAP BUBBLE FILLED WITH A MIXTURE OF 1/3 He, 2/3 Ar

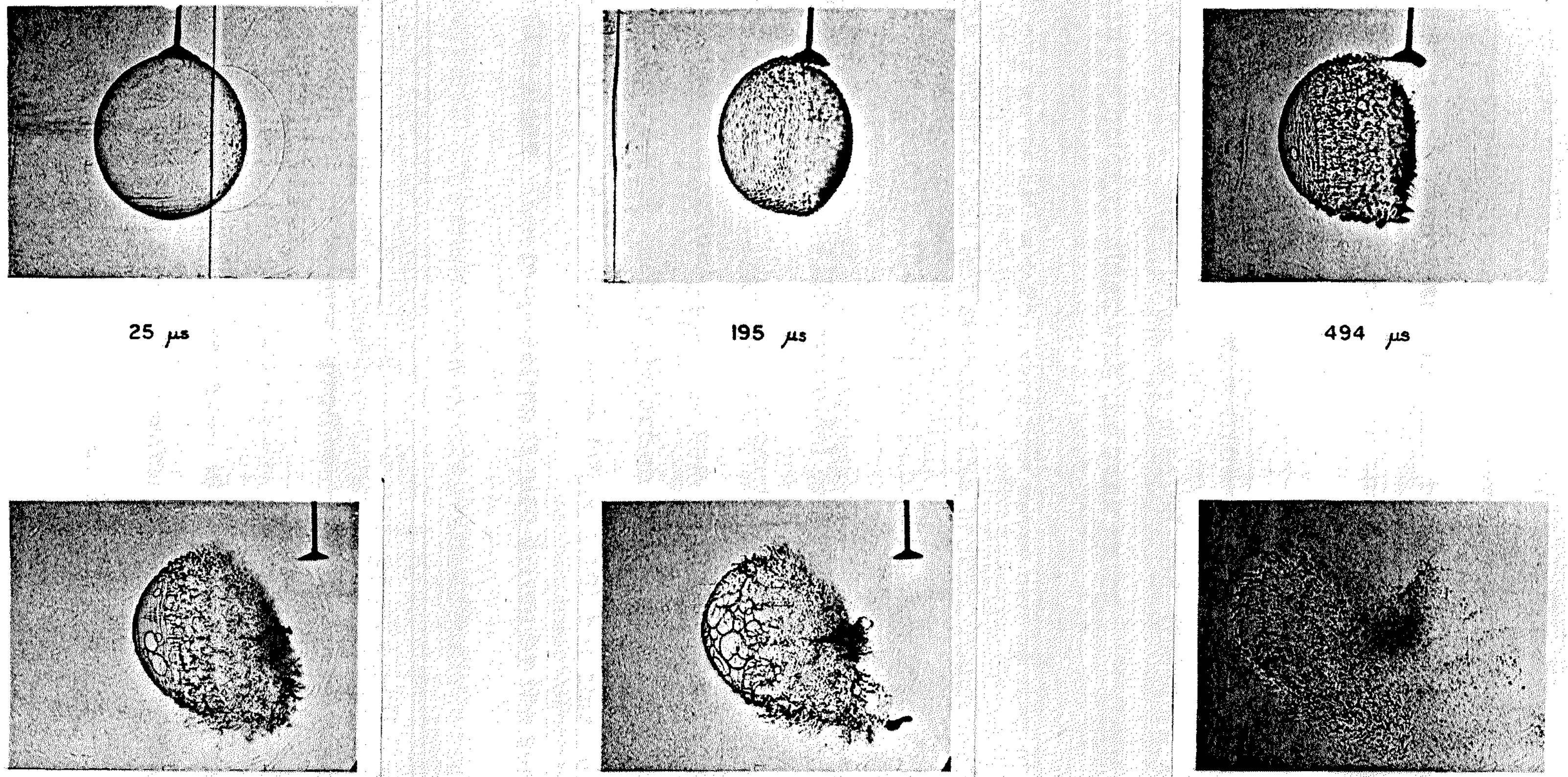

25 µs

195 µs

494 µs

820 µs

1118 µs

2270 µs

14.3.5. *Reflected light photographs: nitrogen bubble.* The film behavior for weak shocks (M_s = 1.05) is characterized by waves of wavelength 1 to 2 mm growing all around the bubble with the film being destroyed first on the upstream side. The waves never propagate to the downstream limit, which is only destroyed by the holes (figure 14.13).

For waves of intermediate strength (M_s = 1.10), the waves forming on the film have a shorter wavelength. More holes are created and, therefore, their final size is smaller than the holes obtained with the weak waves.

Finally, for strong waves (M_s = 1.25), very fine waves can be seen at the transition between the unperturbed left side and the broken, rough looking right side which eventually expands to the complete bubble surface (figure 14.14).

The growth of the holes on the left spherical cap was measured to be about 13 m/s. The corresponding film thickness from (13.8) would be .33 μm. The propagation of the right rim of that spherical cap, in the moving bubble coordinate, is also about 13 m/s when seen in projection on the shadowgraph pictures recorded for the weaker incident shock wave (M_s = 1.10) but this becomes 18 m/s on the soap film plane. This propagation is also driven by the surface tension.

14.3.6. *Pressure profiles.* Pressure profiles recorded just behind the mixture-filled bubbles are shown in figure 14.15. The incoming shock wave is Mach 1.25. The sequence of six profiles taken at 1, 4, 14, 24, 34 and 44mm behind the bubble illustrate how the various waves (transmitted, diffracted and secondary transmitted) merge. In the profile at 1 mm, the initial rise is the transmitted wave, the first peak is the diffracted wave, while the subsequent very large, N-shaped, profile is evidently the signature of the secondary transmitted

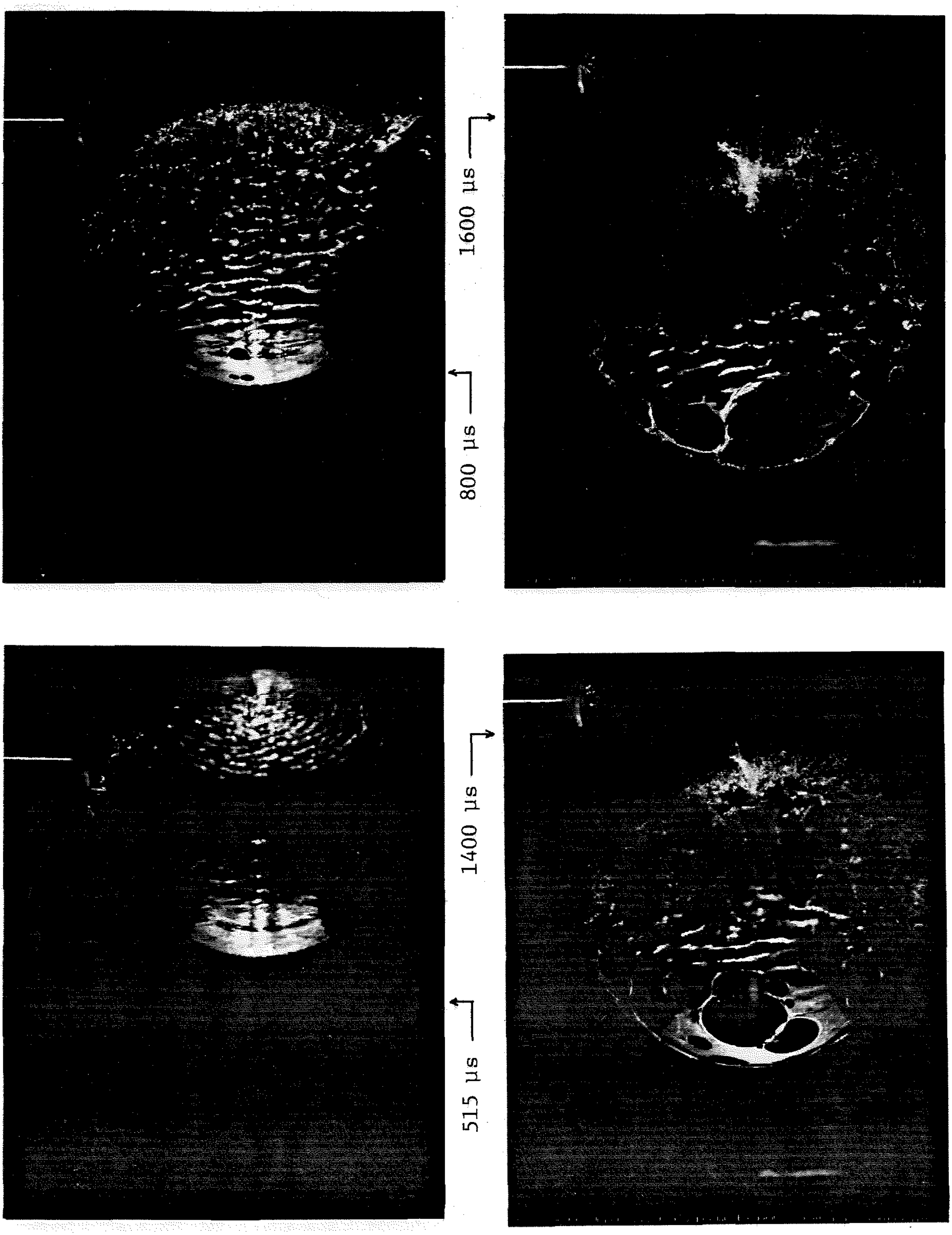

FIGURE 14.13 Disintegration of the Soap Film (Nitrogen Bubble, M_s= 1.05)

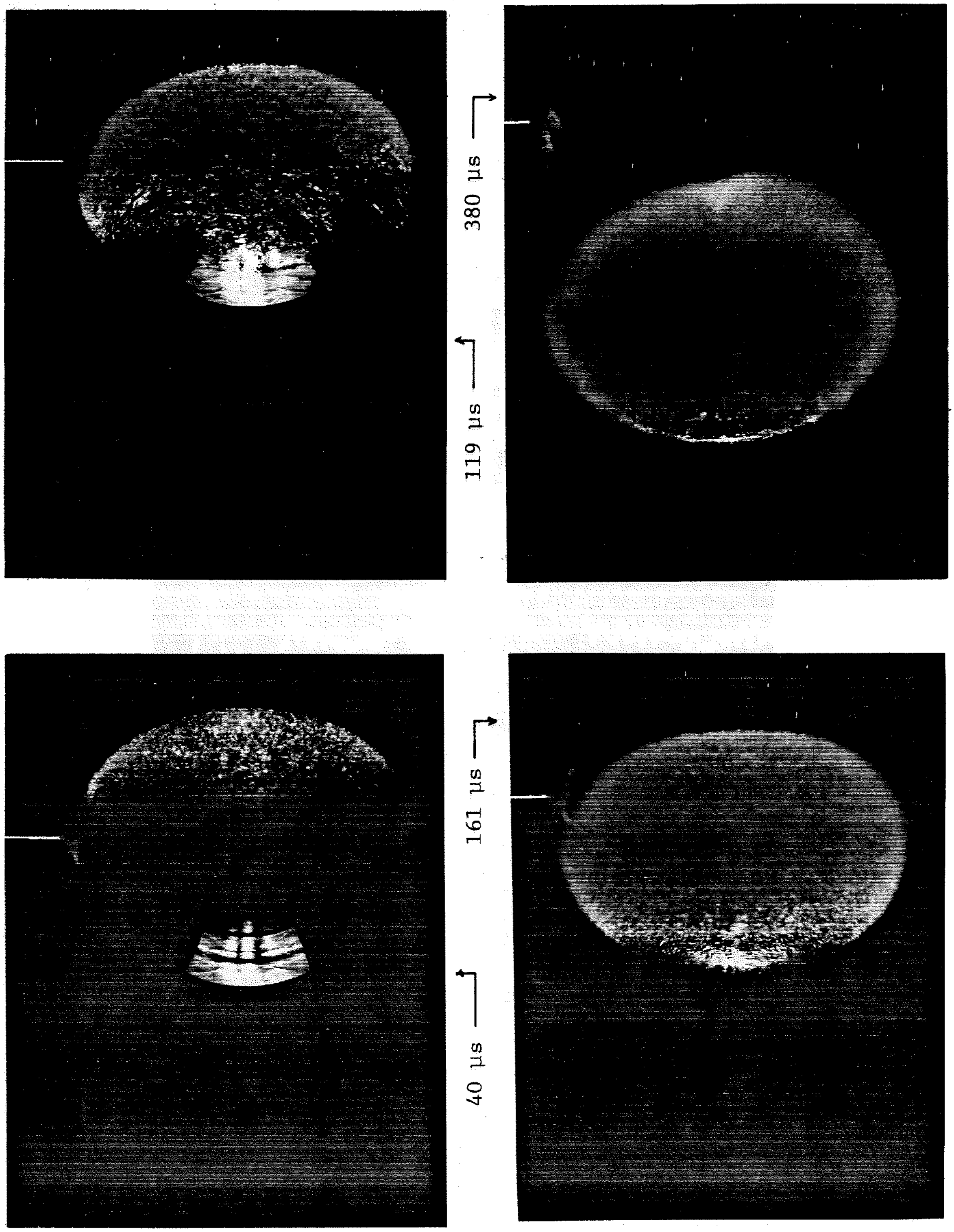

FIGURE 14.14 Disintegration of the Soap Film (Nitrogen Bubble, $M_S = 1.25$)

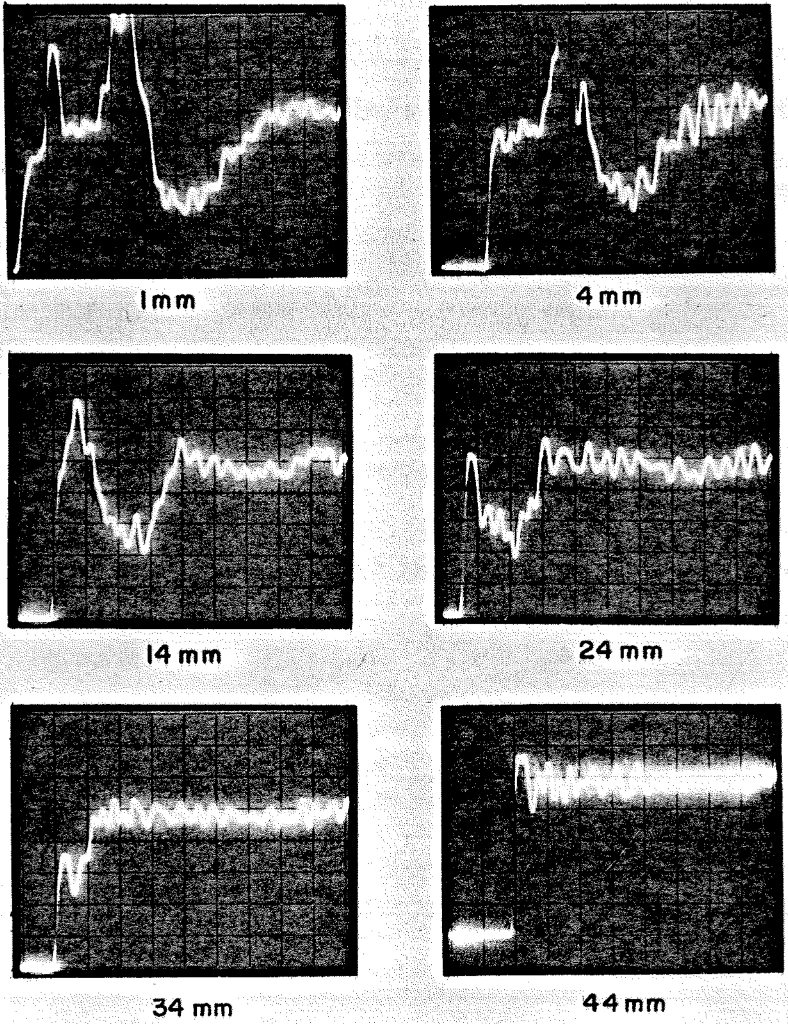

1mm 4mm

14mm 24mm

34mm 44mm

Horizontal Scale 5 μs/div.
Vertical Scale .38 bar/div.

FIGURE 14.15 Pressure Profiles behind the Helium-Argon Bubble (M_s = 1.25) wave (resulting from the rays which have had one internal reflection). The width of the pulse can be attributed to the facts that the wave arrives obliquely on the finite size transducer and that it may be combined with the following (tertiary etc.) transmitted waves. At 4 mm, only the secondary transmitted wave is seen behind the initial front and its merging with the primary transmitted shock is shown at three positions: 14, 24 and 34 mm. At 44 mm, the merging process is completed and the pressure profile is very similar to the profile of an undisturbed shock wave.

Chapter 15

DISCUSSION ON THE INTERFACE VELOCITIES

15.1. Shock-induced acceleration of curved interfaces

15.1.1. *Scope.* The interaction of a shock with a curved interface occurs under many different conditions in this experiment:

i. The geometry of the interface is either spherical or cylindrical.
ii. Two gas pairs are considered, air-helium and air-Freon 22.
iii. Several incident shock strengths are used (1.05 to 1.25).

We will limit our analysis to the simpler configurations, incident shock with upstream interface (air-helium and air-Freon 22), and refracted shock with downstream air-helium interface. In these cases the geometrical configuration allows us to use the results of one-dimensional gasdynamics as a starting point.

15.1.2. *Impulsive acceleration of a wavy interface.* When a plane interface between two different gases is accelerated by a shock wave of velocity V_s perpendicular to its plane, it instantaneously acquires a velocity V which can be calculated once the strength of the refracted wave downstream or the strength of the reflected waves upstream are determined. This calculation was carried out for the upstream and downstream interface of a one-dimensional inhomogeneity in Chapters 10, 13 and 14. For a slow-fast interface, V is larger than V_2, the velocity of the upstream gas behind the incident wave. The refracted wave is weaker than the incident shock and the reflected wave is an expansion. For a fast-slow interface, V is less than V_2, the refracted wave is stronger than the incident shock and the reflected wave is also a shock. An homogeneous volume of gas is compressed in the direction parallel to the shock propagation by a factor $1-V_2/V_s$. Similarly the region near the upstream interface of a gas inhomogeneity is initially compressed by a factor $1-V/V_s$.

The following is a development of the impulsive theory (Markstein, 1957 a, Richtmyer, 1960) to a three dimensional corrugated interface. The geometry of the interface is defined in figure 15.1. The shape of the interface $\eta(y,z,t)$ is given in the relative coordinate system which has started moving at t=0 in the positive x direction at a velocity V. The initial shape is defined by:

$$\eta(y,z,t=0) = \eta_0 \cos K_y y \quad \cos K_z z \tag{15.1}$$

where η_0 is the initial amplitude and K_y and K_z the wave numbers in the two directions y and z. The gradients of the interface should be small, hence,

$$K\,\eta_0 = \sqrt{(K_y^2 + K_z^2)}\ \eta_0 \quad << 1 \tag{15.2}$$

The acceleration b caused by the shock lasts only for a short time τ and creates on the interface the velocity V :

$$V = b\ \tau \tag{15.3}$$

According to the Taylor instability theory (Taylor,1950), the interface is stable or unstable depending on whether the growth rate parameter β is real or imaginary,

$$\beta = \left[K \frac{V}{\tau} \frac{\rho_2 - \rho_1}{\rho_2 + \rho_1} \right]^{1/2} . \tag{15.4}$$

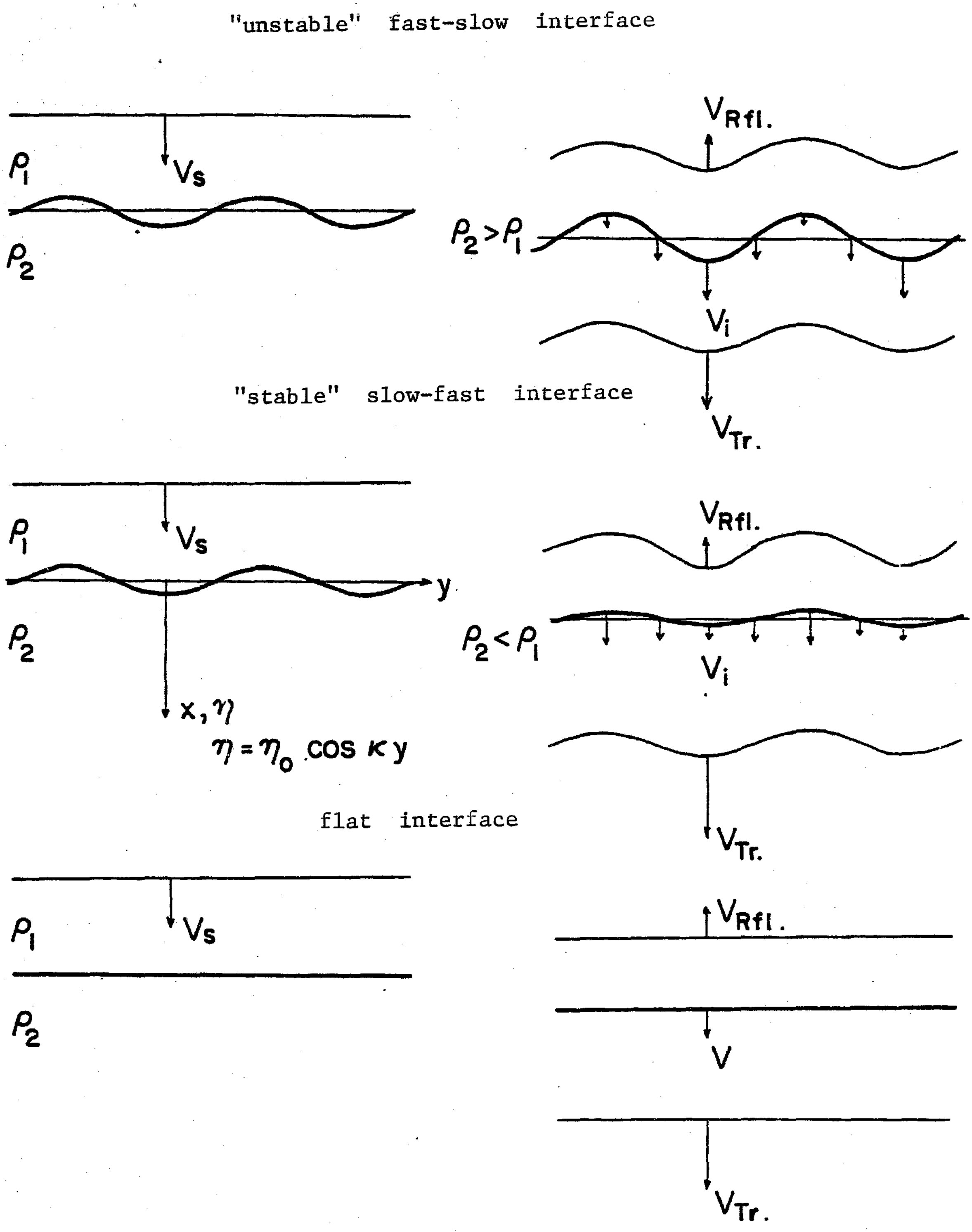

"unstable" fast-slow interface

"stable" slow-fast interface

flat interface

FIGURE 15.1 Shock-Induced Acceleration of a Wavy Interface

$\beta\,\tau$ should be small compared to 1, hence

$$\left[K\,V\,\tau\,\frac{\rho_2-\rho_1}{\rho_2+\rho_1} \right]^{1/2} << 1\,. \tag{15.5}$$

During the initial acceleration, the interface has practically not changed its shape but has acquired a perturbation velocity v (which is superposed to V),

$$v\,(y,z,t>\tau) = \eta_0\,K\,V\,\frac{\rho_2-\rho_1}{\rho_2+\rho_1}\cos K_y\,y\;\cos K_z\,z \tag{15.6}$$

As there is no further acceleration later on, the velocity field persists and the interface is distorted at a constant rate.

A fast-slow interface ($V\,\frac{\rho_2-\rho_1}{\rho_2+\rho_1} > 0$) is initially accelerated in a destabilizing way and the undulations grow. For a slow-fast interface ($V\,\frac{\rho_2-\rho_1}{\rho_2+\rho_1} < 0$), the shock acceleration is initially stabilizing, the amplitude of the initial perturbation decreases first but then the interface undergoes a phase reversal and the reversed undulations grow continuously. Therefore, both configurations are equally unstable under shock acceleration.

15.1.3. *Cylindrical or spherical interface.* In an attempt to predict the velocities of the upstream cylindrical or spherical interface, we consider that the upstream edge is the crest of a two or three dimensional corrugation pattern (figure 15.2), with a local radius of curvature equal to the radius of the cylinder or of the sphere.

For a cylinder, the wave length of such a wave is $2\pi R$, the wave number $K = \frac{1}{R}$ and its amplitude $\eta_0 = R$. Since $K\,\eta_0 = 1$, condition (15.2) is not fulfilled.

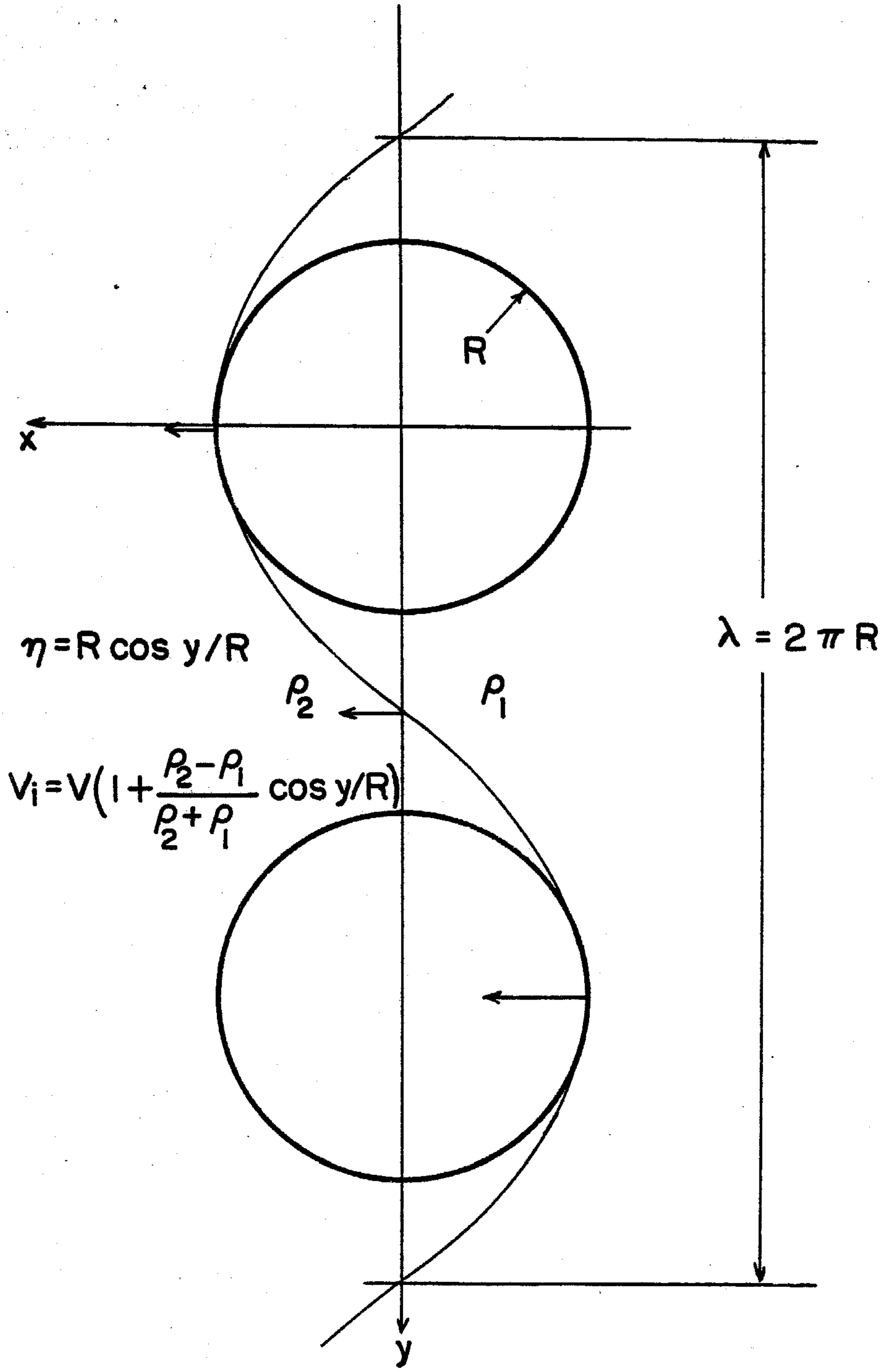

FIGURE 15.2 Shock-Induced Acceleration of a Cylindrical Interface

As it was shown (Meyer and Blewett, 1972) that the relatively high value of this product ($K\eta_0 = 0.3$) in the experiments made by Meshkov (1970) was not the cause of the discrepancy between theory and results, it is assumed that the theory can still be used here as an approximation.

From (15.1), the initial crest position corresponding to the upstream interface is :

$$\eta(\pi R, z, 0) = -R \tag{15.7}$$

and the perturbation velocity is :

$$v(\pi R, z, t) = -V \frac{\rho_2 - \rho_1}{\rho_2 + \rho_1} \quad \text{for } t > \tau \, . \tag{15.8}$$

For a sphere, the wavelength in the two directions is $2\pi R$, the wave number is $K = \frac{\sqrt{2}}{R}$ for the initial amplitude R and $K\eta_0 = \sqrt{2}$. The formulation of the problem in axisymmetric coordinates leads to the same result. The initial upstream interface position is :

$$\eta(\pi R, 0, 0) = -R \tag{15.9}$$

and the perturbation velocity is :

$$v(\pi R, 0, t) = -\sqrt{2}\, V \, \frac{\rho_2 - \rho_1}{\rho_2 + \rho_1} \, . \tag{15.10}$$

The perturbation velocities on the downstream interface are for an initial position $\eta(0,0,0) = R$, the opposite of the ones given by (15.8) and (15.10).

In a fixed coordinate system the interface velocity V_i is $V_i = V + v$. therefore the ratio between the curved interface and plane interface velocities is

$$\frac{V_i}{V} = 1 \pm \alpha \, \frac{\rho_2 - \rho_1}{\rho_2 + \rho_1} , \tag{15.11}$$

where the upper (lower) sign applies to a shock incident on a convex (concave) interface and α is 1 or $\sqrt{2}$ depending on whether the interface is locally cylindrical or spherical.

The condition (15.5) is now :

$$\left[\frac{\alpha V \tau}{R} \, \frac{\rho_2 - \rho_1}{\rho_2 + \rho_1} \right]^{1/2} \ll 1 , \tag{15.12}$$

Which means that the interface perturbation created during the time of shock acceleration is much less than the initial amplitude. For shock induced accelerations, this condition is easily fulfilled.

The question which arises now is whether the initial compression should be taken into account in the calculation of the development of the instability. The velocity associated with the initial compression is V, while the velocity associated with the instability is :

$$v = \eta_0 \, K \, V \, \frac{\rho_2 - \rho_1}{\rho_2 + \rho_1} \tag{15.14}$$

For $\eta_0 \, K \, \frac{\rho_2 - \rho_1}{\rho_2 + \rho_1}$ small compared to 1, the two events can be decoupled and, according to Richtmyer (op.cit.), the initial amplitude of the shape of the interface should be replaced by :

$$\eta_1 = \eta_0 \left(1 - \frac{V}{V_s}\right) \tag{15.15}$$

This is a nonlinear effect and tends to reduce the growth rate of the instability for high Mach numbers. In the present experiment the perturbation velocity v is comparable to V, so the two events cannot be decoupled. The results in § 15.1.4 will tell whether the correction (15.5) should be used or not.

15.1.4. *Comparison between theory and experiments.*

15.1.4.1 *Upstream air-helium interface.* Air is the gas upstream of the interface with a density:

$$\rho_1 = 1.294 \; kg/m^3.$$

and helium is the gas downstream with a density:

$$\rho_2 = 0.178 \; kg/m^3.$$

therefore,

$$\frac{\rho_2 - \rho_1}{\rho_2 + \rho_1} = -0.76.$$

The interface is initially stabilized by the shock. The results for the helium cylinder ($\frac{V_i}{V} = 1.76$) are given in table 15.1, and for the helium sphere ($\frac{V_i}{V} = 2.075$) in table 15.2. The comparison between the calculated values of V_i and the measured values (V_{u_i} and V_j) brings out several points. The flattening

Table 15.1. Upstream interface velocities of the helium cylinder

M_s	V_s	V	$1 - V/V_s$	v	V_i	V_{u_l}	V_j	V_{u_l}/V	V_j/V
1.085	373	52	0.86	39	91	89	123	1.71	2.36
1.22	420	123	0.71	93	216	170	230	1.38	1.87

velocities V_{u_l} are surprisingly very similar for the two geometries and for weak shocks is close to the theoretical value for the cylinder. Possible reasons for the discrepancy between the measurements and this model which predicts higher flattening velocities in the spherical case are: imprecision in the measurement, greater susceptibility of the spherical inhomogeneity to gas contamination, and membrane effect (§ 15.3). The jet velocity V_j is higher than predicted by the model. The fact that it is slightly higher in the spherical case than in the cylindrical case may be the effect of stronger convergence in the axisymmetric configuration. The decrease of the relative velocities for stronger waves, approximately proportional to $1 - \frac{V}{V_s}$, indicates the effect of nonlinearity. Therefore the correction mentioned at the end of § 15.1.3 should be used.

15.1.4.2 *Downstream helium-air interface.* Here helium is the gas upstream of the interface and air the gas downstream, therefore,

$$\frac{\rho_2 - \rho_1}{\rho_2 + \rho_1} = 0.76 \ .$$

This interface is initially destabilized by the shock, as the growth of small scale corrugations on the downstream side of the helium cylinder and sphere suggests (160 μs, figure 9.1 and 145 and 169 μs, figure 13.1). We suppose for the purposes

Table 15.2. Upstream interface velocities of the helium sphere

M_s	V_s	V	$1 - V/V_s$	v	V_i	V_{u_i}	V_j	V_{u_i}/V	V_j/V
1.05	361	31.5	0.91	34	65.4	53	83	1.68	2.63
1.10	378	61.3	0.84	66	127.3	87	140	1.42	2.28
1.25	430	138.2	0.68	148.5	286.8	190	335	1.37	2.42

of this section that the refracted wave is plane. Its Mach number and the velocity to which it accelerates the downstream interface are taken from the one dimensional calculation. The results for the cylinder $(\frac{V_i}{V} = 1.76)$ and for the sphere $(\frac{V_i}{V} = 2.075)$ appear in tables 15.3 and 15.4 .

Table 15.3. Downstream interface velocities of the helium cylinder

M_s	M_R	V	v	V_i	V_{d_i}	V_{d_i}/V
1.085	1.035	28	21	49	69	2.46
1.22	1.085	70	53	123	145	2.07

Again, there is no difference between the results in two dimensions and in three dimensions but the experimental values are now higher than the theoretical ones, indicating that perhaps the interface is further accelerated by the diffracted wave.

15.1.4.3 *Upstream air-Freon 22 interface.* Air is the gas upstream of the interface with a density:

Table 15.4. Downstream interface velocities of the helium sphere

M_s	M_R	V	v	V_i	V_{d_i}	V_{d_i}/V
1.05	1.02	16.5	17.7	34.2	39	2.36
1.10	1.041	33	35.5	68.5	67	2.03
1.25	1.096	79.5	85.5	165	165	2.075

$$\rho_1 = 1.294\ kg/m^3 ,$$

and Freon 22 is the gas downstream with a density:

$$\rho_2 = 4.72\ kg/m^3 ,$$

therefore,

$$\frac{\rho_2 - \rho_1}{\rho_2 + \rho_1} = .57 .$$

The velocities for the Freon 22 cylinder ($\frac{V_i}{V} = 0.43$) and for the Freon 22 sphere ($\frac{V_i}{V} = 0.194$) are presented in tables 15.5 and 15.6. The measured interface velocity is higher than predicted by the model, which means that the real interface distortion velocity v is not large enough. The discrepancy may be due to imprecision in the measurement. The initially unstabilizing effect of the shock on the interface appears qualitatively in its increased curvature (figures 9.5 and 9.6 for the cylinder and figures 14.1 and 14.3 for the bubble). The behavior of the downstream interface cannot be predicted by this model since

Table 15.5. Upstream interface velocities of the Freon cylinder

M_s	V_s	V	$1 - V / V_s$	v	V_i	V_{u_i}	V_{u_i} / V
1.085	368	38	0.90	-20.5	15.5	42	1.10
1.22	430	89	0.79	-50.7	38.3	73	0.82

the refracted shock is near its focus at this point.

15.2. Subsequent behavior of the gas inhomogeneity

15.2.1. *Development of the vortical structures.* The development of vorticity in the shock-accelerated gas volumes appears clearly in the flow visualization photographs. The *cylinders* are deformed into vortex pairs as expected (Rudinger and Somers, 1960). The observation of the deformation of the gas *spheres* does not confirm the corresponding assumptions that these volumes should become vortex rings. The helium bubble is transformed into a two-component structure: an elongated torus containing most of the helium preceded by a vortex ring where most of the circulation initially produced seems to remain, while the aspect of the deformed Freon 22 bubble prevents an unambiguous recognition of a vortex ring.

In a related study of the shock induced acceleration of small cylindrical gas inhomogeneities (H_2, He and SF_6), Rudinger and Somers (1960) developed a simplified theoretical model of the interaction, which leads to the calculation of an initial bubble velocity V_b and a final vortex velocity V_v. While they were prevented by the small scale of the inhomogeneities from observing the details of the development of the structures, it is interesting to see how the velocities measured in this experiment compare to their calculations and measurements.

Table 15.6. Upstream interface velocities of the Freon sphere

M_s	V_s	V	$1 - V/V_s$	v	V_i	V_{u_i}	V_{u_i}/V
1.07	368	30.2	0.92	-24.3	5.9	18	0.6
1.25	430	100	0.77	-80.5	19.5	60	0.6

15.2.2. ***Calculation of the bubble and vortex velocities.*** The gas bubble here refers to a sphere, an infinitely long cylinder or a short cylinder such as used in this experiment. The model of Rudinger and Somers assumes that the bubble processed by the shock initially accelerates to a velocity V_b, different than the surrounding air velocity V_2 and later, after the vortical structure has been developed, acquires a velocity V_v, also different from V_2. The calculation assumes an impulsive, essentially incompressible acceleration. The bubble density is ρ_2 and the air density ρ_1 and their ratio, ρ_2/ρ_1, is σ. The impulse per unit volume I transmitted by the shock to the gas bubble is equal to the one transmitted in air,

$$I = \rho_1 V_2 = \rho_2 V_b + k\ \rho_1 (V_b - V_2) \ . \qquad (15.16)$$

The term $\rho k_1(V_b - V_2)$ represents the impulse transmitted to the air around the bubble due to the bubble motion and k is the inertia coefficient or apparent additional mass fraction. k = 0.5 for a sphere, 1 for an infinitely long cylinder moving at right angles to its axis and approximately 0.7 for a short cylinder (L/D = 1.6) (obtained by assuming the cylinder to be an ellipsoid of elongation 2). From (15.6) the initial bubble velocity is given by,

$$V_b = \frac{1 + k}{\sigma + k} V_2 \ . \qquad (15.17)$$

The subsequent transformation of a gas bubble into a vortex structure implies a decrease of the relative velocity

$$V_v - V_2 = \beta(V_b - V_2) \ . \qquad (15.18)$$

Using a calculation by Taylor (1953) of the generation of a vortex ring by the impulsive acceleration of a disk, and extending it to the formation of a vortex pair, Rudinger chooses $\beta = 0.436$ for the vortex ring and $\beta = 0.203$ for the infinitely long vortex pair. An intermediate value, $\beta = 0.3$ is assumed here for the short vortex pair originating from the short cylinder. The vortex velocity is then given by,

$$V_v = (1 + \beta \frac{1 - \sigma}{\sigma + k}) V_2 \qquad (15.19)$$

15.2.3. *Helium inhomogeneity.* The theoretical results are shown in table 15.7 ($\sigma = 0.138$).

Table 15.7. Predicted helium bubble and vortex velocities

Shape	V_b / V_2	V_v / V_2
Sphere	2.35	1.59
Short cylinder	2.03	1.30
Long cylinder	1.76	1.15

For the experimental values (tables 15.8 and 15.9),we take the initial bubble velocity V_b to be the average of the measured initial upstream and downstream interface velocities V_{u_i} and V_{d_i} from tables 10.1 and 13.1.

Table 15.8. Measured velocities of the short helium cylinder

M_s	V_2	V_{u_i}	V_{d_i}	V_b / V_2	V_v	V_v / V_2
1.085	46.5	89	69	1.70	60	1.29
1.22	114	170	155	1.42	128	1.12

Table 15.9. Measured velocities of the helium sphere

M_s	V_2	V_{u_i}	V_{d_i}	V_b / V_2	V_v	V_v / V_2
1.05	28	53	39	1.64	44	1.57
1.10	44	87	67	1.43	75	1.39
1.25	128	190	165	1.37	165	1.29

The initial bubble velocity, approximately the same for the two configurations, is lower than the value predicted by the Rudinger-Somers model, indicating that acceleration by wave processes (§ 15.1.4.1) is probably a more accurate description than by impulse. Again, the nonlinearity appears as the velocity ratios decrease for stronger shocks. Our vortex velocities agree approximately with the predicted values and Rudinger's experimental results for a long cylinder ($V_v/V_2 \simeq 1.3$ for Mach number 1.12, $V_v/V_2 \simeq 1.15$ for Mach numbers 1.22 and 1.26). Our vortex ring however involves only a small fraction of the volume of the helium bubble and the calculation of the generation of the vortex ring by the piston model (§ 13.3.2) is more appropriate.

15.2.4. *Freon 22 inhomogeneity.* The theoretical results are given in table 15.10 (σ = 2.98). The experimental results appear in table 15.11 for the cylinder and table 15.12 for the sphere. Since in the spherical case the vortex ring cannot be seen, the velocity V_v is the average of the final upstream and downstream edge velocities V_{u_f} and V_{d_f} from table 14.1.

Table 15.10. Predicted Freon bubble and vortex velocities

Shape	V_b / V_2	V_v / V_2
Sphere	0.431	0.75
Short cylinder	0.462	0.84
Long cylinder	0.502	0.90

The data for the cylindrical bubble are too high for both the initial bubble velocity and final vortex pair velocity. As it was discussed earlier (§ 11.2.2), the Freon structure has become so large that it interacts with the shock tube walls. This increase of the size of heavy bubbles was already noticed for SF_6 bubbles by Rudinger who called this an instability. The velocities obtained in the spherical case are closer to the theoretical expectations, even though a well-defined vortex ring can not be identified in our experiments !

Table 15.11. Measured velocities of the Freon 22 cylinder

M_s	V_2	V_{u_i}	V_{u_f}	V_b / V_2	V_v	V_v / V_2
1.085	46.5	42	35	0.83	60	1.29
1.22	114	73	90	0.715	130	1.14

Table 15.12. Measured velocities of the Freon 22 sphere

M_s	V_2	V_{u_i}	V_{d_i}	V_b / V_2	V_{u_f}	V_{d_f}	V_v / V_2
1.07	39	18	27	58	24	27	0.65
1.25	128	60	83	56	99	100	0.78

15.3. Effect of the membrane and of the contamination by air

Rudinger and Somers (1960) had dismissed the use of soap bubbles for precise measurements of the displacement of gas inhomogeneities partly because the mass of the membrane is not negligible compared to the mass of the gas enclosed. This is indeed the case for the small helium scatterers, in the experiment described in Chapters 2 to 6. Despite this, the qualitative behavior of the helium filled bubbles appears to be the same for bubbles of diameter 2 and 45 mm (Chapters 6 and 13). The effect of the membrane on the average bubble density ρ_b is given by the expression

$$\rho_b = \rho_g + n \frac{\delta}{R} \rho_m \tag{15.20}$$

where ρ_g and ρ_m are the gas and membrane densities, δ the membrane thickness, R the bubble radius, and $n = 3$ for a spherical bubble, and 2 for a cylindrical one. A 0.5 μm thick membrane causes an increase of the average density of a cylindrical bubble of 22% (R = 25 mm), and of 40% in the spherical case (R = 22.5 mm). The estimated contamination of the helium in the bubble by air creates similar density increases. Table 15.13 gives the effect of possible density increases on the various velocity ratios previously calculated.

Table 15.13. Effect of density increase on the velocity ratios

Shape of bubble		Cylinder			Sphere		
$\Delta\rho/\rho_2$	ρ_2/ρ_1	V_i/V	V_b/V_2	V_v/V_2	V_i/V	V_b/V_2	V_v/V_2
0	0.138	1.76	2.03	1.30	2.075	2.35	1.59
20	0.166	1.71	1.96	1.29	2.00	2.25	1.54
40	0.193	1.68	1.90	1.27	1.96	2.16	1.51
60	0.221	1.64	1.84	1.25	1.90	2.08	1.47

The velocity ratios do not appear to be very sensitive to large density increases, therefore the mass of the membrane and the contamination by air can account for only a small fraction of the differences between the measured velocities and the (generally higher) calculated ones.

Chapter 16

SUMMARY

The summary of the study of the interaction with a single cylindrical or spherical inhomogeneity is given here first. The concluding remarks about the multiple scattering experiment appear next.

16.1. Interaction with a single discrete inhomogeneity

16.1.1. *Comments on the experimental method.* The method for creating cylindrical gas inhomogeneities has made it possible to observe the wave pattern and the initial deformation of the boundaries of the inhomogeneity as well as the subsequent motion at a later time of the gas structures produced by the interaction.

The microfilm membrane used to separate the two gases, inside and outside the inhomogeneity, did not perturb the geometry of the wave pattern and the motion of the gas interface but had an effect on the strength of the shock waves measured very close to the cylindrical wall.

The precision of the velocity measurements was reduced because of two factors: the gas composition inside and outside the cylindrical cell was not kept within narrow specifications and the method of velocity measurements was based on plotting the positions of the measured feature from series of photographs taken for different runs at different time delays. A better control of the gas composition and the use of a high speed camera will improve the precision of these measurements. Another factor created undesired effects on the motion of the structures. In order to observe the details of the interaction at the initial time, the cylinder diameter was a large fraction of the test section transversal dimension. This resulted in the apparition of reflected waves from the side walls of the shock tube and some perturbation in the development of large structures observed after long time delays. New experiments should have a smaller cylinder size relative to the shock tube (Chapter 10).

16.1.2. *Wave pattern.*

16.1.2.1 *Two-dimensional configuration.* The geometrical features of the interaction of a plane acoustic pulse incident on a cylindrical inhomogeneity are illustrated by computer-generated rays and wave front diagrams. Since the incident shock waves in the experiment are relatively weak, the wave fronts recorded on the photographs are in general similar to the acoustic wave fronts. The interaction with a helium cylinder generates behind it a diverging transmitted wave running ahead of the diffracted wave. Close to the cylinder, a secondary transmitted front is seen just behind the transmitted wave, and in the interior, an internal reflected wave focuses and appears upstream of the cylinder as a backscattered wave which follows the external reflected wave. Pressure profiles recorded behind the cylinder show how the weak transmitted wave is caught up (a few cylinder diameters downstream) by the diffracted wave, which is about as strong as the incident wave.

The wave pattern is more spectacular in the case of a Freon 22 cylinder. Both the internal diffracted wave and refracted wave have caustics and the transmitted wave focuses just behind the cylinder. The higher strength of the converging shock waves in the interior causes some interesting differences between the wave front diagrams obtained for acoustic pulses and the one recorded on the shadowgraphs for finite amplitude shock waves. In addition, the internal reflected waves are rather complicated. A similarity is made between shock wave focusing by a lens or a reflector as the focal hot spot left behind the focus of the transmitted wave is reminiscent of the one obtained behind the focus of a wave which has reflected from a concave cylindrical reflector. After the focus, where it was very strong, the transmitted wave expands, becomes weaker and merges with the diffracted wave, about as strong as the incident wave, at approximately the same distance behind the Freon cylinder as the merging distance behind the helium cylinder (Chapters 9 and 11). A simple conclusion is that light gas inhomogeneities create weak waves ahead of the main shock while heavy gas discontinuities generate weak waves behind the main shock front.

16.1.2.2 *Axisymmetric configuration.* Going from a cylindrical to spherical inhomogeneity does not provide any new information about the shock wave pattern. However, as the experimental procedure was faster, more configurations were tested. The shock wave interaction with an argon filled soap bubble (Chapter 14) creates a slightly converging transmitted wave which does not focus because of non-linear effects. The interaction of shock waves with nitrogen-filled bubbles allows a visualization of the waves which are solely due to the membrane, namely externally and internally reflected waves and secondary transmitted waves which create some strong disturbances on the pressure profiles recorded just behind the bubble. In the case of a helium bubble, the corresponding disturbance created behind the weak primary transmitted wave is proportionally as important. That effect of the membrane is far stronger in the axisymmetric configuration than in the two dimensional one. The shape of the secondary transmitted pulse is not yet understood.

16.1.3. *Effect of the shock wave on the inhomogeneities.*

16.1.3.1 *Initial deformations.* The deformations observed on the upstream edge of a helium sphere or cylinder, namely, a flattening followed by the formation of a spike toward the interior, are approximately confirmed by theoretical estimates based on the shock-induced Taylor instability. Nonlinear effects are demonstrated as the interface deformation velocities become lower in proportion to the velocity V_2 of the air behind an unperturbed shock, for higher Mach numbers. The downstream edge of the helium inhomogeneity becomes more curved and small scale instabilities of the interface are observed.

The observed curvature increase of the upstream edge of a Freon 22 cylinder or sphere is expected under shock-induced instability but the measured velocities are not close to theoretical estimates. The jet of Freon, seen at the downstream edge, is created by the transmitted wave near its focus.

16.1.3.2 *Development of two-dimensional vortices.* The behavior of the helium volume at a later time confirms predictions by other investigators that an inhomogeneity, lighter than the surrounding air, develops into a pair of vortices which stay close to each other and which are moving faster than the surrounding air. This experiment shows how the helium cylinder is turned inside out by the spike or air jet mentioned above. The velocity of the resulting pair of vortices approximately fits theoretical calculations (Chapter 15). The behavior of the Freon 22 volume agrees qualitatively with the prediction that an inhomogeneity, heavier than air, becomes a pair of vortices which tend to diverge from each other and which move slower than the surrounding air. The two vortices obtained from the Freon cylinder soon interact with the top and bottom wall of the test section and the top vortex has to move in front of the lower one in order to increase their separation. Probably because of this interaction, their expected velocities do not confirm theoretical expectations. The above-mentioned need of a smaller cylinder size relative to the shock tube applies especially to that case.

16.1.3.3 *Development of vortex rings.* The observed behavior does not follow earlier expectations. The air jet inside the helium inhomogeneity acts much as an impulsively-driven piston in a cylinder, as it pushes out a small jet of helium which becomes a vortex ring leaving the main body of helium. This behavior is supported by the closeness of the values of the circulation introduced the the "piston" and the circulation deduced from the vortex ring velocity and size (§ 13.5). No vortex ring can be recognized in the large structure obtained from the Freon 22 sphere; however, its measured velocity is consistent with the existence of a vortex ring.

The helium structure can be described qualitatively as an elongated torus preceded by a vortex ring, but the Freon 22 structure is more like a bell with its opening pointing downstream and a large lateral extent.

16.1.4. *Behavior of the soap membrane.* The behavior of the soap membrane accelerated by shocks is qualitatively discussed here (Chapters 13 and 14). It appears to depend mostly on the strength of the shock, and to a lesser extent, on the density of the gas inside the bubble. Theoretically, both the upstream and downstream edges of the bubble are unstable to shock-induced Taylor instability while the membrane on the lateral sides, which separates faster moving gases, is probably deformed by the Kelvin-Helmholtz instability. The main mechanism of membrane break-up is the growth of ripples. Weak waves tend to generate ripples of large wave length which grow slowly, medium strength waves generate shorter wave length ripples which grow and break faster and strong waves generate very fine ripples which break very quickly and give immediately to the membrane a rough, broken texture.

Another mechanism plays in the regions of the membrane, usually on the downstream side, where ripples do not appear. The locally smooth membrane is destroyed by the growth of circular holes driven by surface tension. Weak shock waves trigger the apparition of a few holes which grow to a large size but stronger shock waves cause the formation of many holes which cannot grow to a large size because of their number. This spectacular effect is apparent for helium and nitrogen filled bubbles. The density of the gas inside the bubble influences the pattern of membrane destruction by changing the relative importance of the ripple-dominated and hole-dominated areas and by creating large scale distortions, such as the spike of air on the upstream edge of the helium bubble and the jet appearing on the downstream edge of the Freon bubble, both of which break through the membrane.

16.1.5. *Concluding remarks.* The interaction of shock waves and discrete gas inhomogeneities involves many phenomena which individually deserve specialized investigations of a much more quantitative character than this research effort. The present approach however is far from having exhausted its potential, especially if the above-mentioned experimental shortcomings are corrected. A wider range of incident shock wave Mach numbers and gas densities are clearly needed in order to evaluate the influence of all the parameters involved in both aspects of the interaction: the wave pattern and the motion of the inhomogeneity. A minimum extension of this study should involve gases of intermediate density between air and helium on the light side, and between air and Freon 22 on the heavy side, and a survey of the strength of the diffracted and transmitted waves in the axisymmetric case. The use of a schlieren system might contribute to a better understanding of the features already observed by shadowgraph.

16.2. Multiple scattering of weak shock waves

16.2.1. *Multiple scattering criterion.* This investigation is really a logical extension of the interaction with a single helium inhomogeneity. Multiple scattering occurs when the transmitted wave from one helium scatterer interacts with another scatterer before being caught up by the diffracted wave. The number of bubbles which participate in the multiple scattering process is obtained by multiplying the volume of influence of the scatterer, namely the volume of the region of space where the transmitted and diffracted wave have not yet merged, by the number density of the scatterers. The model given in Chapter 4 allows the calculation of the volume of influence of a helium scatterer and therefore provides a criterion for multiple scattering.

16.2.2. *Influence of the array on the shock.* The experiment described in Chapters 2 to 6 achieved its primary design goal by creating an array dense enough so that very weak shocks are strongly scattered apparently in a manner very similar to the scattering of shock waves by turbulence (Hesselink, 1977). Evidence of strong scattering is obtained here as the rise time in the shock wave pressure profile recorded at the end of the scattering cloud is increased by an order of magnitude (from 1 μs to 10-20 μs) which corresponds to an increase of the thickness of the shock wave by two orders of magnitude (up to 6 mm). This occurred for some of the runs made with very weak incident shocks ($M_s \leq 1.01$) and for a number density of (2 mm diameter) helium scatterers between 0.4 and 0.8 cm^{-3}. The multiple scattering criterion predicts in this case that between 25 and 150 bubbles participate in the scattering process. As no significant tilt of the shock wave is recorded in this experiment, the observed rise time corresponds to a real increase of the shock wave thickness. This points out a difference with the mechanism which caused the increased rise time obtained in the scattering of a wave of similar strength (M_s = 1.07) by the turbulent mixture. In that case, the fact that the rise time was the same within the mixture and 22 cm behind it (at a distance over which a thickened wave would have steepened because of nonlinear effects) led to speculations that the shock was folded or tilted by a large scale inhomogeneity in the mixture. A possible reconciliation of the two different experiments is that several effects, shock thickening and wrinkling due to the inhomogeneities of the size of the microscale (1.5 mm) occur simultaneously with tilting and folding by large scale inhomogeneities in the scattering by turbulence while only shock thickening is created by the interaction with a discrete array.

Most recorded pressure profiles, however, indicate evidence of partial scattering, with a smooth compression preceding the steep pressure rise of the shock. This compression precursor, lasting for a few microseconds and rising to a fraction of the height of the incident shock pressure rise, is usually obtained for the less favorable cases of that sequence of runs where the criterion predicts a lower number of bubbles involved in multiple scattering (25 to 50). In addition to the compression precursors in front of the main shock, some modifications of the pattern of the oscillations after the pressure rise are recorded showing that the interaction also creates some disturbance behind the main shock front.

Weak scattering is obtained for slightly stronger waves (M_s = 1.02) where only a few bubbles are expected to be involved in multiple scattering. For higher Mach number shock waves (1.06 to 1.36) for which only single scattering is expected as the volumes of influence do not overlap any more, the measured shock wave pressure profiles are usually undisturbed. The few cases in which a small precursor is recorded are the ones where a scatterer happens to be in the immediate proximity of the transducer. The effect of the scattering medium on a weak shock wave, as shown on the shadowgraphs, is an apparent thickening of the wave front which becomes very faint and difficult to see for very weak waves. The effect on strong incident waves is heavy but local perturbations of the area of the shock front which has just propagated through a scatterer or a cluster of scatterers.

16.2.3. *Effect of the shock wave on the scatterers.* As the bubbles are very small, the effect of the soap film is expected to be much larger than for large bubbles. For weak and very weak shock waves ($M_s \leq$ 1.02) the instabilities generated by the interaction are overcome by the stabilizing effect of the surface tension. For the incident wave of intermediate strength (M_s = 1.07) the bubbles do break up but some only after being processed again by the reflected wave.

For stronger incident shock waves (M_s = 1.15 to 1.36) the bubbles are deformed much in the same way as it was observed for the large helium bubbles: the jet of air can be seen clearly pushing ahead a secondary structure which should be the vortex ring observed at the larger scale. Later on, the helium structure mixes completely with the air. The whole process takes place behind the incident shock wave over a distance which becomes shorter for higher Mach numbers.

17. References

ABD-EL-FATTAH, A.M., HENDERSON, L.F. & LOZZI, A. 1976 Precursor shock waves at a slow-fast gas interface. *J. Fluid Mech.*, **76**, 157-176.

ABD-EL-FATTAH, A.M. & HENDERSON, L.F. 1978 Shock waves at a fast slow interface. *J. Fluid Mech.*, **86**, 15-32.

ABD-EL-FATTAH, A.M. & HENDERSON, L.F. 1978 Shock waves at a slow fast gas interface. *J. Fluid Mech.*, **89**, 79-95.

BAKER, L. & FREEMAN, J.R. 1981 Heuristic model of the nonlinear Rayleigh-Taylor instability. *J. Appl. Phys.*, **52**, 655-663.

BOYS, C.V. 1911 *Soap bubbles, their colours and the forces which mold them.* Dover (1959).

CULICK, F.E.C. 1960 Comments on a ruptured soap film. *J. Appl. Phys.*, **31(6)**, 1128-1129.

CURTET, R. 1960 Sur l'ecoulement d'un jet entre parois. *Service de documentation et d'information technique de l'aeronautique*, **359**, Paris.

DAVY, B.A. & BLACKSTOCK, D.T. 1971 Measurements of the refraction and diffraction of a short *N* wave by a gas-filled soap bubble. *J. Acoust. Soc. Am.*, **49**, 732-737.

DIDDEN, N. 1979 On the formation of vortex rings : Rolling-up and production of circulation. *Z. f. angew. Math. u. Phys.*, **30**, 101-116.

FRANKEL, S. & MYSELS, K.J. 1969 The bursting of soap films. II. Theoretical considerations. *J. Phys. Chem.*, **73**, 3028-3038.

FRIEDLANDER, F.G. 1958 *Sound Pulses*, Cambridge.

GLEZER, A. 1981 *An experimental study of a turbulent vortex ring*. Ph.D. thesis, California Institute of Technology.

HALE, R.W., TAN, P. & ORDWAY, E. 1969 Experimental investigation of several neutrally-buoyant bubble generators for aerodynamic flow visualization. *SAGE ACTION, Inc.* report no. SAI-RR-6901.

HALE, R.W., TAN, P., STOWELL, R.C. & ORDWAY, D.E. 1971 Development of an integrated system for flow visualization in air using neutrally-buoyant bubbles. *SAGE ACTION, Inc.* report no. SAI-RR-7107.

HESSELINK, L. 1977 *An experimental investigation of propagation of weak shock waves in a random medium.* Ph.D. thesis, California Institute of Technology.

HESSELINK, L. 1978 An experimental investigation of propagation of weak shock waves in a random medium. *Proc. 11th Int. Symp. on Shock Tubes and Waves*, (ed. Hahlborn, Hertzberg and Russel), Univ. Washington Press, 82-90.

JAHN, R.G. 1956 The refraction of shock waves at a gaseous interface. *J. Fluid Mech.*, 1, 457-459.

JONES, D.S. 1978 Acoustic tunneling. *Proc. Royal Soc. Edinburgh* **81-A**, 1-21.

KELLER, J.B. 1955 Diffraction by a convex cylinder. *URSI Mich. Symp. on Electro Magnetic Wave Propagation*

KELLER, J.B. 1958 "A geometrical Theory of Diffraction" *Proc. Sym. App. Math.* **Vol VIII** *Calculus of Variations and its Applications*. McGraw-Hill

McENTEE, W.R. & MYSELS, K.J. 1969 The bursting of soap films. I. An experimental study. *J. Phys. Chemistry*, **73. 9.**, 3018-3028.

MARKSTEIN, G.H. 1957a Flow disturbances induced near a slightly wavy contact surface, or flame front, traversed by a shock wave. *J. Aero. Sci.*, **24**, 238.

MARKSTEIN, G.H. 1957b A shock tube study of flame front-pressure wave interactions. *6th Int. Symp. Comb.* Reinhold, New York 387-398.

MARSTON, P.L. & KINGSBURY, D.L. 1981 Acoustic scattering from fluid spheres: diffraction and interference near the critical scattering angle. *J. Acou. Soc. Am.*, **70(5)**, 1488-1495.

MAXWORTHY, T. 1977 Some experimental studies of vortex rings. *J. Fluid Mech.*, **81**, 465-495.

MEYER, K.A. & BLEWETT, P.J. 1972 Numerical investigation of the stability of a shock accelerated interface between two fluids. *Phys. Fluids*, **15**, 753-759.

MESHKOV, Y.Y. 1970 Instability of a shock wave accelerated interface between two gases. *NASA TT* **F-13**, 074.

PIERCE, A.D. 1981 *Acoustics* McGraw-Hill.

RICHTMYER, R.D. 1960 Taylor instability in shock acceleration of compressible fluids. *Com. Pu. App. Math*, **23**, 297-319.

RUDINGER, G. 1958 Shock wave and flame interactions. *Combustion and Propulsion*, **153-82**, Third AGARD Coll. London. Pergamon.

RUDINGER, G. & SOMERS, L. 1960 Behavior of small regions of different gases carried in accelerated gas flows. *J. Fluid Mech.*, **7**, 161-176.

SMITH, J.A., COLES, D., ROSHKO, A. & PRASAD, A.J. 1967 A description of the GALCIT 6-inch shock tube. *GALCIT report FM-67-1*, California Institute of Technology,.

STONG, C.L. 1969 How to blow soap bubbles that last for months and even years. *Scientific American, May 1969* , 128-134.

STURTEVANT, B. & KULKARNY, V.A. 1976 The focusing of weak shock waves. *J. Fluid Mech.*. **73**, 651-671.

STURTEVANT, B., HESSELINK, L. & HAAS, J.F. 1980 Propagation of shock waves through nonuniform and random media. *Proc. 12th Int. Symp. on Shock Tubes and Waves*, (ed. Lifshitz and Rom). The Magnes Press, Jerusalem, 359-369.

STURTEVANT, B., HESSELINK, L., WHITE, B.S., KULKARNY, V. & CATHERASOO, C. 1981 Propagation of shock waves in random media. *13th Int. Symp. on Shock Tubes and Waves*, Niagara Falls, New York.

TAYLOR, G.I. 1950 The instability of liquid surfaces when accelerated in a direction perpendicular to their plane. I. *Proc. Roy. Soc.*, **A, 201**, 192-196.

TAYLOR, G.I. 1953 Formation of a vortex ring by giving an impulse to a circular disk and then dissolving it away. *J. App. Phys.*, **24. 1**, 104.

Appendix A

MODEL OF BUBBLE POPULATION

In this model of the evolution of the bubble population in an enclosed volume V, the bubbles are continuously created at a rate P but they are destroyed by collisions among themselves at a rate D_1 or with the walls at a rate D_2. The differential equation for the number of bubbles N, which varies with time is therefore:

$$\frac{dN}{dt} = P - D_1 - D_2 \tag{A.1}$$

The values of the death rates D_1 and D_2 are obtained from the number of collisions per unit time: N_1 for interbubble collisions and N_2 for bubble wall collisions. N_1 and N_2 are in turn derived using the physical principles underlying the kinetic theory of gases. It is assumed that the bubbles, which have a radius r, a cross sectional area $A = \pi r^2$ have a mean velocity $\bar{c}$ and that they propagate along straight lines between their birth and their death at the first collision. This is of course very different from the actual behavior of the bubbles in the test section, but this model allows us to estimate the influence of various parameters such as P, V or $\bar{c}$. The bubble mean-free path is defined by the formula

$$L = \frac{V}{NA} \tag{A.2}$$

The number of collisions is

$$N\frac{\bar{c}}{L} = N^2\frac{A\bar{c}}{V} \tag{A.3}$$

and the death rate D_1 is

$$D_1 = 2N^2\frac{A\bar{c}}{V} \tag{A.4}$$

with the assumption that the two bubbles involved are destroyed. The enclosed volume V, chosen to be aproximately the volume of the dense cloud in the experiment is supposed to be a sphere of radius R. This radius can be thought of as the mean distance between a bubble and the wall of the enclosure. Therefore the number of the bubbles colliding with the wall is

$$N_2 = D_2 = N\frac{\bar{c}}{R} \tag{A.5}$$

The differential equation becomes:

$$\frac{dN}{dT} = R - N\frac{\bar{c}}{R} - 2N^2\frac{A\bar{c}}{B}\,. \tag{A.6}$$

When the bubble production is started, the bubble population increases initially at a rate P and reaches an asymptotic value Nf given by the formula:

$$Nf = \frac{V}{4AR}\left[\sqrt{1 + \frac{8PAR^2}{V\bar{c}}} - 1\right] \tag{A.7}$$

or with the substitution $V = \frac{4}{3}\pi R^3$; $A = \pi r^2$

$$Nf = \frac{R^2}{3r^2}\left[\sqrt{1 + \frac{6Pr^2}{R\bar{c}}} - 1\right] \tag{A.8}$$

The time T to reach the steady state value Nf is inversely proportional to P, therefore T is given by the approximation

$$T = k\,\frac{Nf}{P} \tag{A.9}$$

where the factor k lies between 1 and 5. The value of the parameters entering in this model are taken from the experiment with one bubble generator and the model is used to estimate the performance of four generators.

From experiment: V = 8.9 x 8.9 x 50 cm^3 = 3960 cm^3
therefore r = 1 mm , R = 9.8 cm , P = 500

An estimate of the bubble population Nf in the dense section of the cloud was 1000 - 1500, therefore the calculated value of the mean free path L: 84 - 126 cm is one order of magnitude larger than R ; this means that at this concentration most collisions occur with the walls.

From the observation of the streak photographs the mean velocity is on the order of a few cm/s, thus the calculations are done with the values 1 , 4 and 10 cm/s.

The table below shows the values of Nf , v volume available per bubble and d : the diameter of a sphere of volume v which is an approximation of the mean distance between bubbles

$\bar{c}$ cm/s	Nf	v_{cm^3}	d_{cm}
1	3333	1.49	1.41
4	1076	3.68	1.91
10	467	8.48	2.53

With the experimentally deduced value of Nf near 1000 the estimate $\bar{c}$ = 4 cm/s seems reasonable. T was observed to be around 5 s, the factor k can therefore be estimated near 2.3.

With four generators the production rate becomes 2000 but except for V and R, which should be somewhat lower because of the observed shorter length of the dense cloud in the square tube, all the other parameters are kept the same. Assuming first that V and R should be kept the same because of the large number of bubbles migrating in the tube beyond the dense recirculation eddy the estimated values of Nf , v and d become

$\bar{c}$ cm/s	Nf	v_{cm^3}	d_{cm}
1	8180	.456	.95
4	3330	1.49	142
10	1610	246	1.67

with k = 2.3 and $\bar{c}$ = 4 cm/s , T should be 3.8 s.

Assuming now that because the recirculation eddy should theoretically be twice as short, the bubble cloud volume V should now be near 2000 cm^3 and R near 7.9 cm, the new table becomes:

$\bar{c}$ cm/s	Nf	v_{cm^3}	d_{cm}
1	6160	.32	.85
4	2430	.81	1.15
10	1200	1.05	1.26

again with $k = 2.3$ and $\bar{c} = 4$ cm/s, T should be 2.8 s. A reasonable assumption lies between the two given above. This model was used initially to justify the use of four bubble generators. As a comparison tool it was relatively successful: it predicted a decrease of v from 3.7 to 1.15 cm^3 when switching from one generator to four. In the experiment the best performances observed in each case were 3 cm^3 for one generator and 1.2 cm^3 for four generators.

Appendix B

MEAN PROPERTIES OF A MIXTURE OF SEVERAL GASES

The speed of sound of a mixture of two gases is given by

$$a_m = \sqrt{\gamma_m R_m T} \tag{B.1}$$

where

$$\gamma_m = \frac{\alpha_1 C_{p_1} + \alpha_2 C_{p_2}}{\alpha_1 C_{v_1} + \alpha_2 C_{v_2}} \tag{B.2}$$

and

$$R_m = \alpha_1 R_1 + \alpha_2 R_2 \quad . \tag{B.3}$$

α_1 and α_2 are the mass fractions of gas 1 and 2. R_1 and R_2 are the gas constants of the gases. C_p and C_v are specific heats of the gases, γ is their ratio, and T the absolute temperature. With

$$a_i = \sqrt{\gamma_i R_i T} \tag{B.4}$$

$$a_m{}^2 = \frac{\alpha_1 C_{p_1} + \alpha_2 C_{p_2}}{\alpha_1 C_{v_1} + \alpha_2 C_{v_2}} \left(\frac{\alpha_1}{\gamma_1} a_1{}^2 + \frac{\alpha_2}{\gamma_2} a_2{}^2 \right) \quad . \tag{B.5}$$

For air: $a_{air} = 20.93\sqrt{T}$, $\gamma_{air} = 1.4$, and $R_{air} = 286.7$. For helium: $a_{He} = 58.86\sqrt{T}$,

$\gamma_{He} = 1.67$, and $R_{He} = 2078.6$ in SI units.

Assuming that the volume concentration of helium is small, its mass concentration is even much smaller and the relation between the mass fraction α_{He} and the volume fraction C_{He} can be derived simply:

$$\alpha_{He} = \frac{M_{He}}{M_{He} + M_{air}} = \frac{M_{He}}{M_{air}} = \frac{\rho_{He} V_{He}}{\rho_{air} V_{air}} \tag{B.6}$$

as

$$C_{He} = \frac{V_{He}}{V_{He} + V_{air}} = \frac{V_{He}}{V_{air}},\ \alpha_{He} = \frac{\rho_{He}}{\rho_{air}} C_{He} = .138 C_{He}. \tag{B.7}$$

The expression for γ_{mix} can be linearized for small values of α_{He}:

$$\gamma_{mix} = \frac{C_{p_{air}} + (C_{p_{He}} - C_{p_{air}})\alpha_{He}}{C_{v_{air}} + (C_{v_{He}} - C_{v_{air}})\alpha_{He}}$$

$$= \gamma_{air}[1 + (\frac{C_{p_{He}}}{C_{p_{air}}} - \frac{C_{v_{He}}}{C_{v_{air}}})\ \alpha_{He}] \quad \text{for} \quad \alpha_{He} << 1. \tag{B.8}$$

With $C_{p_{air}} = 1003.5$, $C_{v_{air}} = 716.8$, $C_{P_{He}} = 5196.5$ and $C_{V_{He}} = 3117.9$ in SI units,

$$\gamma_m = 1.4(1 + 0.828\alpha_{He}) = 1.4(1 + 0.114 C_{He}) \tag{B.9}$$

$$\frac{\alpha_{He}}{\gamma_{He}} a_{He}{}^2 + \frac{\alpha_{air}}{\gamma_{air}} a_{air}{}^2 = \frac{\alpha_{He}}{\gamma_{He}} a_{He}{}^2 + \frac{1-\alpha_{He}}{\gamma_{air}} a_{air}{}^2$$

$$= \frac{a_{air}{}^2}{\gamma_{air}}(1 + 0.625\, \alpha_{He}) = \frac{a_{air}{}^2}{1.4}(1 + 0.826\, C_{He}). \qquad \text{(B.10)}$$

Hence,

$$a_m = a_{air}\,(1+3.54\, \alpha_{He}) = a_{air}(1 + 0.488\, C_{He}). \qquad \text{(B.11)}$$

A mixture of air (mass fraction α_{air}) and nitrogen (mass fraction α_{N_2}) has an average speed of sound given by

$$a_m = (1.4 R_m T)^{1/2} \qquad \text{(B.12)}$$

where

$$R_m = \alpha_{N_2} R_{N_2} + (1-\alpha_{N_2})\, R_{air}, \qquad \text{(B.13)}$$

with

$$a_{air} = \sqrt{1.4 R_{air} T} \quad \text{and} \quad \Delta R = R_m - R_{air}$$

$$a_m = a_{air}\left[1 + \alpha_{N_2}\, \frac{\Delta R}{R_{air}}\right]^{1/2}. \qquad \text{(B.14)}$$

$R_{air} = 286.7$, $R_{N_2} = 296.9$ in SI units.

When the nitrogen mass fraction is small

$$a_m = a_{air}(1+0.0178\alpha_{N_2}) \tag{B.15}$$

as $\alpha_{N_2} = \frac{28}{29} C_{N_2}$, where C_{N_2} is the volume concentration of nitrogen,

$$a_m = a_{air}\,(1+0.0172\;C_{N_2}). \tag{B.16}$$

For a mixture of air, helium and nitrogen, the average speed of sound a_{mix} for low concentration of helium and nitrogen is

$$a_{mix} = a_{air}(1+0.488C_{He} + 0.0172C_{N_2}). \tag{B.17}$$

The average density is obtained directly:

$$\rho_{mix} = (1-\alpha_{He}-\alpha_{N_2})\rho_{air} + \alpha_{He}\rho_{He} + \alpha_{N_2}\rho_{N_2} \tag{B.18}$$

For low helium and nitrogen concentration:

$$\rho_{mix} = \rho_{air}(1-0.862C_{He} - 0.034C_{N_2}). \tag{B.19}$$

The average acoustic impedance is:

$$(\rho a)_{mix} = (\rho a)_{air}\;(1 - 0.374\;C_{He} - 0.0168\;C_{N_2})\;. \tag{B.20}$$